

https://dspace.org/

Use of the cone penetration test to assess the liquefaction potential of tailings storage facilities

Torres Cruz, Luis Alberto

2016

http://hdl.handle.net/10539/22007

Torres Cruz, Luis Alberto (2016) Use of the cone penetration test to assess the liquefaction potential of tailings storage facilities, University of Witwatersrand, Johannesburg, <http://wiredspace.wits.ac.za/handle/10539/22007>

Downloaded from a DSpace repository. https://dspace.org/

USE OF THE CONE PENETRATION TEST TO ASSESS THE LIQUEFACTION POTENTIAL OF TAILINGS STORAGE FACILITIES

Luis Alberto Torres Cruz

A dissertation submitted to the Faculty of Engineering and the Built Environment, University of the Witwatersrand, Johannesburg, in fulfilment of the requirements for the Degree of Doctor of Philosophy.

Johannesburg, 2016

Declaration

I declare that this thesis is my own unaided work. It is being submitted to the Degree of Doctor of Philosophy to the University of the Witwatersrand, Johannesburg. It has not been submitted before for any degree or examination to any other University.

_____

(Signature of the Candidate)

15th day of September 2016

Abstract

The performance in tailings storage facilities (TSFs) of three methods based on the cone penetration test (CPT) to assess liquefaction potential is explored. For two of these methods the investigation highlights potential limitations mostly related with the experimental data that supports some of the equations used by the methods. However, the methodologies yielded mostly correct performance predictions when implemented on TSF case histories in which an undrained response is believed to have occurred. The positive performance of both methodologies must be tempered by the limitations identified in the methods.

The steady state line (SSL) is an input of the third method considered. Accordingly, the correlation between the SSL and soil index parameters was investigated using a database of 151 non-plastic soiltypes compiled from data previously reported in the literature. The SSLs were modelled in void ratio (e) - mean effective stress (p') space, using a logarithmic equation. The y-intercept of the SSL is termed Γ, and the slope is termed λ. A direct, and linear (R^2 = 0.74) correlation between the minimum void ratio (e_{min}) and Γ was found. Although previous research has explored the effect of non-plastic fines on the SSL, the analysis presented herein shows that the Γ-e_{min} correlation is independent of fines content. The correlation is also independent of the angularity of the particles provided that these are bulky, as opposed to platy. A direct λ-e_{min} correlation was also found; however this correlation is much weaker and probably obscured by uncertainties in void ratio measurements.

Triaxial testing was conducted to determine the SSLs of three tailings soiltypes obtained from a single TSF. The trends observed in the resulting SSLs are in agreement with the Γ-e_{min} and λ-e_{min} correlations from the database.

An assessment was made of the sensitivity of the third method, which is based on a state parameter (ψ), to variations in λ throughout a single TSF. It was found that in some TSFs, the variations of λ are small enough to be disregarded without significantly affecting the accuracy of ψ. However, in other TSFs it is necessary to estimate how λ varies throughout the deposit.

To the people of South Africa.

Acknowledgements

I gratefully acknowledge the assistance of the following individuals and institutions:

- My late supervisor Prof Geoffrey Eustace Blight for his kind and patient guidance and for sharing with me his joy for geotechnical engineering.
- My co-supervisors Dr Irvin Luker (Wits University) and Dr Peter Day (Jones & Wagener Engineering and Environmental Consultants) for taking on the task of providing me with the guidance and encouragement needed after the passing of Prof Blight.
- My Head of School Prof Mitchell Gohnert for his firm support of my work and for granting me the time to work on my investigation.
- Prof Eben Rust (University of Pretoria) for facilitating digitised versions of CPTu results.
- Prof Gerhard Heymann (University of Pretoria) for most useful advice in conducting the triaxial tests.
- Dr Nico Vermeulen (Jones & Wagener Engineering and Environmental consultants) for insightful and challenging discussions, and for proofreading manuscripts.
- Mr. Tinus Grobler and Mr. Marno Gagiano (Soillab) for their assistance with the inspection of triaxial testing equipment.
- SRK Consulting, Jones & Wagener Engineering and Environmental Consultants, and Impala Platinum Holdings Ltd., for facilitating information to document some of the case histories described herein.
- Finally, I cannot thank my family enough for their exceptional support throughout my studies.

Table of Contents

1 Introduction 1

1.1 Topic overview 1

1.2 Research objectives 2

1.3 Organization of the thesis 3

2 Conceptual framework 5

2.1 The mechanics of soil liquefaction 5

2.2 The cone penetration test (CPT) 8

2.2.1 Standard measurements, corrections and typical geometry of the probe 8

2.2.2 Normalised parameters and soil classification 9

2.2.3 Dissipation tests 12

2.3 The Olson and Stark method 12

2.3.1 General comments 12

2.3.2 Susceptibility analysis 12

2.3.3 Triggering analysis 13

2.3.4 Post-triggering analysis 14

2.3.5 Assessment of seismic effects 15

2.3.6 General outline of the method 16

2.4 The Robertson-based method 17

2.4.1 General comments 17

2.4.2 Susceptibility analysis 18

2.4.3 Assessment of the cyclic resistance ratio (CRR) 19

2.4.4 Triggering analysis of sand-like soils ($I_c \leq 2.6$) 19

2.4.5 Triggering analysis of clay-like soils ($I_c > 2.6$) 22

2.5 The Jefferies and Been method 23

2.5.1 General comments 23

2.5.2 Determining the state parameter (ψ) in situ 24

2.6 Comparisons between methodologies 27

2.6.1 Stages of liquefaction analyses considered in this study 27

2.6.2 Input requirements of the different methodologies 27

2.7 Conclusions 28

2.8 Tables and figures 30

3 Case histories: description and idealisations 39

3.1 Introduction 39

3.2 Hokkaido Dam – Japan, 1968 40

3.2.1 Description 40

3.2.2 Assumptions and idealisations 40

3.3 Mochikoshi Dam (Dykes 1 and 2) – Japan, 1978 40

3.3.1 Description 40

3.3.2 Assumptions and idealisations 41

3.4 Dashihe Iron Tailings Dam (Beach and outer wall) – China, 1990 42

3.4.1 Description 42

3.4.2 Assumptions and idealisations 43

3.5 Sullivan Tailings Dam – Canada, 1991 44

3.5.1 Description 44

3.5.2 Assumptions and idealisations 44

3.6 Merriespruit gold tailings dam – South Africa, 1994 45

3.6.1 Description 45

3.6.2 Assumptions and idealisations 46

3.7 Impala Platinum TSF – South Africa 46

3.7.1 Description 46

3.7.2 Assumptions and idealisations 47

3.8 Summary 48

3.9 Tables and Figures 49

4 Implementation of the Olson & Stark and Robertson-based methods 65

4.1 The Olson and Stark method 65

4.1.1 General comments 65

4.1.2 Hokkaido Dam – Japan, 1968 65

4.1.3 Mochikoshi Dam (Dykes 1 and 2) – Japan, 1978 65

4.1.4 Dashihe Iron Tailings Dam (Beach and outer wall) – China, 1990 66

4.1.5 Sullivan Tailings Dam – Canada, 1991 66

4.1.6 Merriespruit gold tailings dam – South Africa, 1994 67

4.2 The Robertson-based method 67

4.2.1 General comments 67

4.2.2 Hokkaido Dam – Japan, 1968 67

4.2.3 Mochikoshi Dam (Dykes 1 and 2) – Japan, 1978 67

4.2.4 Dashihe Iron Tailings Dam (Beach and outer wall) – China, 1990 68

4.2.5 Sullivan Tailings Dam – Canada, 1991 68

4.2.6 Merriespruit gold tailings dam – South Africa, 1994 69

4.3 Conclusions 69

4.4 Tables and figures 71

5 Processing of the CPTu data of the Impala Platinum TSF 79

5.1 Introduction 79

5.2 Initial considerations *79*

5.3 Estimation of the in situ pore water pressure profiles *80*

5.4 Calculation of parameters Q and B_q *82*

5.5 A soil behaviour type index for the Q-B_q classification chart *82*

5.6 Summary *83*

5.7 Tables and Figures *85*

6 The correlation between the SSL and the minimum void ratio 92

6.1 Introduction *92*

6.2 A literature review of correlations between index properties and SSL parameters *93*

6.2.1 Correlations between the SSL and FC 93

6.2.2 Correlations between the SSL and particle shape 96

6.2.3 Correlations between the SSL and descriptors of the shape of the GSD curve 98

6.2.4 Correlations between the SSL and void ratio limits. 99

6.2.5 Justification to further consider e_{min} and e_{max} as predictors of Γ and λ. 100

6.3 A database to assess the correlation of SSL parameters with void ratio limits *102*

6.4 Correlations between void ratio limits and SSL parameters *104*

6.4.1 Trends identified in the entire database 104

6.4.2 Trends identified in sub-sets of the database obtained from a single reference 106

6.5 Discussion *106*

6.6 Concluding remarks *108*

6.7 Tables and figures *110*

7 Experimental determination of the SSLs of Impala platinum tailings 145

7.1 Introduction *145*

7.2 Soiltypes used to characterise the tailings from the Impala TSF *146*

7.3 Triaxial testing programme *149*

7.3.1 Rationale 149

7.3.2 Triaxial testing procedure 151

7.3.3 Results of the triaxial tests 157

7.4 Discussion and concluding remarks *159*

7.5 Tables and Figures *161*

8 Sensitivity of the state parameter to uncertainty on λ 185

8.1 Introduction *185*

8.2 The sensitivity of ψ to variations in λ *186*

8.2.1 Description of the procedure 186

8.2.2 Resulting values of $\Delta\psi_\lambda$ 188

8.3 A tentative path from CPT results to λ in TSFs 190

8.4 Concluding remarks 193

8.5 Tables and Figures 194

9 Conclusions and recommendations 204

9.1 Summary of main findings 204

9.2 Recommendations for future research 207

Appendix A Slope stability models used to implement the Olson and Stark method 208

A.1 Introduction 208

A.2 Hokkaido Dam – Japan, 1968 208

A.3 Mochikoshi Dam – Japan, 1978 209

A.4 Dashihe Iron Tailings Dam – China, 1990 209

A.5 Sullivan Tailings Dam – Canada, 1991 210

A.6 Merriespruit Tailings Dam – South Africa, 1994 210

A.7 Tables and Figures 210

Appendix B Additional inputs and results corresponding to the Robertson-based method 223

B.1 Hokkaido TSF 223

B.2 Mochikoshi TSF 224

B.3 Dashihe Iron TSF 227

B.4 Sullivan TSF 234

B.5 Merriespruit TSF 235

Appendix C Values of mean effective stress (p'), deviator stress (q), and void ratio (e) used to calculate the SSL parameters in Table 6.3 236

C.1 Soiltypes ARM 236

C.2 Soiltypes ASM 236

C.3 Soiltypes CP 237

C.4 Soiltype DUZ 237

C.5 Soiltypes GB 238

C.6 Soiltypes HCM 238

C.7 Soiltypes HOS 239

C.8 Soiltypes MLM 240

C.9 Soiltypes MER *240*

C.10 Soiltype MIZ *241*

C.11 Soiltype OTM *241*

C.12 Soiltype PAY *242*

C.13 Soiltype RIM *242*

C.14 Soiltypes SIM *242*

C.15 Soiltypes STA *242*

C.16 Soiltypes TOM *243*

C.17 Soiltypes CDS 1 ..... *244*

C.18 Soiltypes CDS 2 ..... *244*

C.19 Soiltypes JB1 ..... *244*

C.20 Soiltypes JB2 ..... *245*

Appendix D Correlations of Γ_n vs e_{min} in which each soiltype was included **246**

10 References **249**

List of figures

Figure 2.1 Idealisation of the critical or steady state line. 31

Figure 2.2 SSLs of foundry sand and Ottawa Sand. Data from: (a) Thevanayagam et al. (2002) and (b) Murthy et al. (2007). 32

Figure 2.3 Liquefaction mechanisms in saturated, undrained, contractive soil (Olson and Stark 2003). 32

Figure 2.4 Typical geometry of a CPTu probe (Lunne et al. 1997) 32

Figure 2.5 Correlations between I_c, *FC*, and *PI,* after Robertson and Wride (1998). Dashed curve indicates the extrapolation made in this study. 33

Figure 2.6 CPT-based SBT charts. a) Q_{tn} vs F_r chart (Robertson and Wride 1998), b) Q vs B_q chart (Robertson 1991). Soiltypes: 1, sensitive, fine grained; 2, peats; 3, silty clay to clay; 4, clayey silt to silty clay; 5, silty sand to sandy silt; 6, clean sand to silty sand; 7, gravelly sand to dense sand; 8, very stiff sand to clayey sand (heavily overconsolidated or cemented); 9, very stiff, fine grained (heavily overconsolidated or cemented). OCR, overconsolidation ratio. $F = F_r$. *Note:* For part (a): $Q = Q_{tn}$. 33

Figure 2.7 Comparison of contractive-dilative boundaries. 34

Figure 2.8 YSR and LSR correlations with q_{c1}. Data from Olson and Stark (2002) and (2003). Note: Labels indicate case history according to the numbering used by Olson and Stark. 34

Figure 2.9 Profile of r_d as per Youd et al. (2001) (Eq. 2.26), and mean and ±1 standard deviation of the r_d profiles reported by Cetin and Seed (2004). 35

Figure 2.10 Susceptibility criteria of Robertson (2010). a) Inclined shaded areas form the liquefaction susceptibility boundary. b) Supporting "Class A" case-history data and contour of $Q_{tn,cs} = 70$ which conservatively approximates the susceptibility boundary. 35

Figure 2.11 CPT-based liquefaction boundary curve (Robertson 2009b) 36

Figure 2.12 Stress paths of sands Kogyuk 350/2 and Kogyuk 350/10 for different values of D_r and ψ (Jefferies and Been 2006). 36

Figure 2.13 Experimentally determined correlations between k, m, and λ (Been et al. 1987). 37

Figure 2.14 Relationship between λ ($=\lambda_{10}$) and F_r (=F). a) Original data presented by Plewes et al. (1992), b) Updated data set presented by Reid (2012). 37

Figure 2.15 Relationship between λ ($=\lambda_{10}$) and I_c suggested by Been and Jefferies (1992). Figure from Jefferies and Been (2006). 38

Figure 3.1 Plan view of Hokkaido tailings dam with flow failure outlined (Ishihara et al. 1990). 52

Figure 3.2 Pre and post-failure cross section of Hokkaido tailings dam (Ishihara et al. 1990). 52

Figure 3.3 Cone resistance profiles at Hokkaido tailings dam. Data from Ishihara et al. (1990). 53

Figure 3.4 FE model of Hokkaido Dam. Dashed vertical line indicates alignment along which τ_h was computed. 53

Figure 3.5 Plan view of the Mochikoshi tailings dam (Okusa and Anma 1980). 54

Figure 3.6 Pre and post-failure geometry of Dykes 1 (upper) and 2 (lower) of the Mochikoshi tailings dam (Ishihara et al. 1990). 54

Figure 3.7 Double tube cone penetration test at Mochikoshi tailings dam. Data from Ishihara et al. (1990). 55

Figure 3.8 FE model of Mochikoshi Dyke 1. Dashed vertical line indicates alignment along which τ_h was computed. 55

Figure 3.9 FE model of Mochikoshi Dyke 2. Dashed vertical line indicates alignment along which τ_h was computed. 56

Figure 3.10 1990 pre-failure geometry of the Dashihe tailings dam and approximate location of the CPT soundings. After Amante (1993). 56

Figure 3.11 CPT soundings on the beach of Dashihe tailings dam. Data from Lee et al. (1992). 57

Figure 3.12 CPT*s* through the outer wall of the Dashihe tailings dam. Data from Lee et al. (1992). 57

Figure 3.13 FE model of the Dashihe outer wall. Dashed vertical line indicates alignment along which τ_h was computed. 58

Figure 3.14 Soil behaviour type from the CPT soundings made on the Dashihe tailings dam beach. 58

Figure 3.15 Cone resistance (q_c) profiles from the crest and toe of the Sullivan tailings dam. Replotted from Jefferies and Been (2006). 59

Figure 3.16 Pre and post-failure geometry of the Sullivan tailings dam and location of two CPT soundings (Jefferies and Been 2006). 59

Figure 3.17 f_s and I_c (Eq. 2.11) profiles for sounding CP91-29 at the Sullivan tailings dam. f_s values from Jefferies and Been (2006) 60

Figure 3.18 Most likely sequence of failure of the Merriespruit tailings dam (Papageorgiou 2004) 61

Figure 3.19 Cone penetration resistance (q_c) profiles of CPTu soundings made on the beach of the Merriespruit tailings dam. 62

Figure 3.20 Fourth stage of retrogressive failure in Merriespruit Tailings Dam as modelled by Jones & Wagener Consulting Civil Engineers (from J&W files). 63

Figure 3.21 Aerial view of the Impala TSF. Dots indicate approximate location of CPTu soundings. Labels indicate numbering of CPTu. Image extracted from Google Earth. 63

Figure 3.22 GSD curves of 49 samples recovered from the Impala TSF during the midlife investigation. Note: Dashed line indicates 75 µm. 64

Figure 4.1 Liquefaction susceptibility at Hokkaido, Mochikoshi and Dashihe dams using the Olson & Stark method. Notes: CDB = Contractive-dilative boundary (Eq. 2.22). The numbers in parenthesis in the legends of parts c) and d) indicate the σ'_{vo} value in kPa at which the water table is located. 72

Figure 4.2 Liquefaction susceptibility at the Sullivan Tailings Dam using the Olson & Stark method. CDB = Contractive-dilative boundary (Eq. 2.22). Notes: Water table depth for sounding CP91-29 was 2 m ($\sigma'_{vo} \approx 45$ kPa). Water table depth was assumed equal for all other soundings. 73

Figure 4.3 Liquefaction susceptibility at the Merriespruit tailings dam using the Olson & Stark method. Note: CDB = Contractive-dilative boundary (Eq. 2.22). 73

Figure 4.4 Factors of safety from the triggering analysis of the Olson and Stark method. HOK = Hokkaido, MKD1 = Mochikoshi Dyke 1, MKD2 = Mochikoshi Dyke 2, DASB = Dashihe Beach, DASOW = Dashihe Outer Wall, SUL = Sullivan, MER = Merriespruit. 74

Figure 4.5 Factors of safety from the post-triggering analysis of the Olson and Stark method. HOK = Hokkaido, MKD1 = Mochikoshi Dyke 1, MKD2 = Mochikoshi Dyke 2, SUL = Sullivan Dam, MER = Merriespruit Dam 74

Figure 4.6 Results for Hokkaido dam of the Robertson-based method. (a) $Q_{tn,cs}$, (b) Factor of safety against triggering of liquefaction. Note: Code after hyphen indicates CPT sounding. 75

Figure 4.7 $Q_{tn,cs}$, profiles at the Mochikoshi Dam. Note: Code after hyphen indicates CPT sounding. 75

Figure 4.8 Profiles of factor of safety determined with the Robertson-based method. (a) Mochikoshi Dyke 1 (MKD1), (b) Mochikoshi Dyke 2 (MKD2). Note: Code after hyphen indicates CPT sounding. 76

Figure 4.9 Results of the Robertson-based method for Dashihe Beach. (a) Profiles of $Q_{tn,cs}$, (b) profiles of factor of safety. Note: Code after hyphen indicates CPT sounding.....76

Figure 4.10 Results of the Robertson-based method for Dashihe Outer Wall. (a) Profiles of $Q_{tn,cs}$, (b) profiles of factor of safety. Note: Code after hyphen indicates CPT sounding. 77

Figure 4.11 $Q_{tn,cs}$, profiles at Sullivan dam computed from CPT sounding CP91-29.....77

Figure 4.12 $Q_{tn,cs}$ profiles at Merriespruit Dam calculated using I_c = 2.2. Note: Code after hyphen indicates CPTu sounding. 78

Figure 4.13 $Q_{tn,cs}$ profiles at Merriespruit Dam calculated using I_c = 2.8. Note: Code after hyphen indicates CPTu sounding. 78

Figure 5.1 Q vs. B_q classification chart proposed by Robertson (1991) with superimposed contours of $I_{Q\text{-}Bq}$. Soiltypes: 1, sensitive, fine grained; 2, peats; 3, silty clay to clay; 4, clayey silt to silty clay; 5, silty sand to sandy silt; 6, clean sand to silty sand; 7, gravelly sand to dense sand.....85

Figure 5.2 Example of the exclusion of q_c values measured immediately after rotary drilling. 86

Figure 5.3 Example of the effect of pauses for dissipation tests on q_c profile. 86

Figure 5.4 Typical results of dissipations test performed in the clay and decomposed norite that underlies the Impala tailings. 87

Figure 5.5 Typical results of dissipations test performed in the Impala tailings: a) PWP increases to a stable value. b) After an initial increase, PWP decreases to a stable value. 87

Figure 5.6 Logarithmic extrapolation used to estimate u_0 from incomplete dissipation tests. 88

Figure 5.7 Check of the logarithmic extrapolation on dissipation records that stabilised: a) u_{0E}/u_0 is closer to 1 than u_{0T}/u_0, b) u_{0T}/u_0 is closer to 1 than u_{0E}/u_0. 88

Figure 5.8 Comparison of ratios u_{0E}/u_0 and u_{0T}/u_0 to assess accuracy and merit of the extrapolation procedure.....89

Figure 5.9 Dissipation test results exhibiting zigzag pattern and interpreted as an indication that the soil was not fully saturated. 89

Figure 5.10 Results of a dissipation test in which transducer malfunction is suspected. 89

Figure 5.11 Sample profile of u_0. Note: Interruptions in the profile are due to cemented layers on which rotary drilling was used. 90

Figure 5.12 Histogram of B_q. 90

Figure 5.13 Sample profile of $I_{Q\text{-}Bq}$. 91

Figure 6.1 SSLs corresponding to four different GSDs of gold tailings from the Merriespruit TSF (Fourie and Papageorgiou 2001). 122

Figure 6.2 SSLs for Kogyuk 350 sand with different silt contents (Been and Jefferies 1985). 122

Figure 6.3 Lower stress portions of SSLs of non-plastic soils. Data from Thevanayagam et al. (2002). 123

Figure 6.4 SSLs for micaceous sands (Hird and Hassona 1990). Notes: 1) LBS = Leighton Buzzard Sand. 2) Number after slash indicates percentage of mica. 123

Figure 6.5 Correlations between FC and λ, Γ_1 (= Γ_{cs}), and M (= M_{cs}) (Bouckovalas et al. 2003).....124

Figure 6.6 Correlations λ vs FC and Γ_1 vs FC shown in Figure 6.5 but excluding the data point at FC = 48%. Data from Bouckovalas et al. (2003). 124

Figure 6.7 Correlation between λ and FC (Jefferies and Been 2006). 125

Figure 6.8 Rationale adopted by Thevanayagam et al. (2002). 125

Figure 6.9 SSLs in terms of $(e_c)_{eq}$ and $(e_f)_{eq}$ Thevanayagam et al. (2002).....125

Figure 6.10 Unification of SSLs in $(e_c)_{eq}$ vs p' space for soils with FC < TFC. (a) Rahman and Lo (2008), (b) Rahman and Lo (2012). Note: $e^* = (e_c)_{eq}$. 126

Figure 6.11 Assembly of photoelastic and rubber discs. Note: Dashed squares enclose particles that do not contribute to the force chains (Original photograph from Dodds (2003)) 126

Figure 6.12 Gold tailings retained on sieve aperture: (a) 300 µm, (b) 150 µm, (c) 63 µm; and settled in water after: (d) 4 minutes or >20 µm, (e) 30 minutes or >8 µm, (f) 4 hours or >3µm. (Original micrographs from Vermeulen (2001)).....127

Figure 6.13 Influence of particle shape and GSD on the slope and vertical position of the SSL, respectively (Poulos et al. 1985).....127

Figure 6.14 Effect on λ of void ratio range and particle shape (Cubrinovski and Ishihara 2000).....128

Figure 6.15 Correlations between SSL and particle shape (Cho et al. 2006). *Note:* $e_{cs100} = \Gamma_{100}$.....128

Figure 6.16 SSLs obtained from a 2D-DEM of assemblies with identical GSD but different particle shape (Maeda et al. 2009). 129

Figure 6.17 Particle shapes of the assemblies whose SSLs are shown in Figure 6.16. Note: a) cl01, b) cl03, and d) cl06 (Maeda et al. 2009).....129

Figure 6.18 a) GSD curves used with Hostun Sand and glass balls. b) Parallel GSD curves of Hostun Sand (Li 2013).....129

Figure 6.19 Effect of particle shape and GSD on the SSL (Li 2013).....130

Figure 6.20 Comparison of SSL parameters of soils with identical mineralogy and GSD but different particle shape. Data from Li (2013). 130

Figure 6.21 SSLs of 2D DEM disc assemblies with different GSDs (Muir-Wood and Maeda 2008). ..131

Figure 6.22 SSLs of Hostun sand with parallel GSDs. a) C_u = 1.1 and b) C_u = 1.4. Data from Li (2013). 131

Figure 6.23 Correlation between D_{r0} and $(e_{max} - e_{min})$. R^2 value calculated in present work (Cubrinovski and Ishihara 2000). 131

Figure 6.24 Effect of particle shape on void ratio limits (Cho et al. 2006). 132

Figure 6.25 Correlations of Γ_1 (=Γ) and λ with limiting void ratios. Filled symbols represent regularity (ρ) < 0.6, empty symbols represent regularity > 0.6, and line symbols represent soils with no particle shape information. R^2 values were calculated in the current work (Cho et al. 2006).....132

Figure 6.26 Correlations of e_{min} and e_{max} with Γ_1. Data from Table 2.1 of Jefferies and Been (2006).132

Figure 6.27 Effect of FC on: a) Γ_{100} (= e_{100}) (Rahman and Lo 2008), and b) e_{max} and e_{min} (Lade et al. 1998). 133

Figure 6.28 Effect of GSD (C_u) on e_{max} and e_{min} (Li 2013). 133

Figure 6.29 Correlation between emax and emin of different natural soiltypes (Cubrinovski and Ishihara 2002). 134

Figure 6.30 Correlations of e_0 with e_{max} and e_{min}. Data from Cubrinovski and Ishihara (2000).....134

Figure 6.31 Plots of Γ_{50}, λ, and M vs e_{min}.....135

Figure 6.32 Plots of Γ_{50}, λ, and M vs e_{max}. 136

Figure 6.33 Plots of Γ_{50}, λ, and M vs $(e_{max} - e_{min})$. 137

Figure 6.34 Plots of Γ_{50} vs e_{min} grouped by FC. The line in each plot is the best fit line for the entire database (Figure 6.31a). 138

Figure 6.35 Γ_{50} vs e_{min} for a) rounded to sub-rounded soiltypes and b) angular to sub-angular soiltypes. The solid line is the best fit line for the entire database (Figure 6.31a). 138

Figure 6.36 Correlations between e_{min} and Γ_n for n = 50, 90, 150, 250, 450, and 800 kPa. Note: Appendix D indicates which soiltypes were included in each correlation. 139

Figure 6.37 SSLs predicted as a function of e_{min} using the correlations in Figure 6.36. 139

Figure 6.38 Relationship between e_{min} and λ as inferred from the SSLs in Figure 6.37 (Eq. 6.4). 140

Figure 6.39 Comparison between Equation 6.4 (Figure 6.38) and the datapoints in Figure 6.31b. .. 140

Figure 6.40 λ vs e_{min} for a) rounded to sub-rounded soiltypes and b) angular to sub-angular soiltypes. 140

Figure 6.41 Plots of SSL parameters vs e_{min} using data from a single reference. Labels next to each data point indicate FC(%). Figure continues below. 141

Figure 6.42 Potential effect on SSL parameters of error in void ratio measurements. 144

Figure 7.1 Nonstandard (450 mm diameter) and standard (200 mm diameter) sieves. 163

Figure 7.2 GSD curves of the fine, medium, and coarse categories into which the Impala tailings were initially separated. 163

Figure 7.3 GSDs of laboratory mixes and in situ samples of Impala tailings. Note: Vertical dotted line indicates sieve aperture = 75 µm. In situ GSD curves were extracted from Figure 3.22. 164

Figure 7.4 Compaction curves from the modified Proctor procedure - ASTM D1557. 164

Figure 7.5 Particle density (ρ_s) of the different soiltypes used in the experimental programme. 165

Figure 7.6 Void ratio limits of Impala tailings. 165

Figure 7.7 Equipment used to conduct nonstandard e_{min} determinations: a) compaction mould, b) extension sleeve, c) overburden weight, and d) rubber mallet. 165

Figure 7.8 Repeatability of the nonstandard procedure to determine e_{min}. 166

Figure 7.9 Correlation between e_{min} values obtained using the nonstandard procedure and using ASTM D1557. 166

Figure 7.10 Mechanical responses reported by Verdugo and Ishihara (1996) for undrained triaxial tests. a) Dilatant response, b) contractive response in curves labelled σ'_o = 3.0 MPa and σ'_o = 2.0 MPa. 167

Figure 7.11 Comparison between local and global void ratios measured using computer tomography (Desrues et al. 1996). Note: Annotations in italic were added in the current work. 167

Figure 7.12 The SSL of Toyoura sand defined by drained and undrained triaxial tests. Note: Annotation in italic was added in the current work. 168

Figure 7.13 Steady state line defined from contractive and dilatant specimens tested under undrained conditions (Verdugo and Ishihara 1996). 168

Figure 7.14 a) Instruments used to tamp the triaxial test specimens. b) Setup adopted when tamping. 169

Figure 7.15 Specimen on the base of the triaxial cell. 169

Figure 7.16 Triaxial testing Setup 2: automated system. 170

Figure 7.17 Triaxial testing Setup 1. a) Temperature control booth closed and on table: power supply for transducers, laptop computer, and data logger. b) Temperature control booth open with triaxial cell inside. 170

Figure 7.18 Components of the temperature control system used in setup 2: a) fan heater, b) temperature controller, c) Solid state relay, d) thermocouple. 171

Figure 7.19 Temperature effects on PWP readings under undrained conditions. 171

Figure 7.20 Non-uniform radial strains in specimens tested with enlarged and lubricated end platens. Original pictures from Rees (2010). 172

Figure 7.21 Extrapolation scheme to infer the steady state values of p' and q (Carrera et al. 2011). 173

Figure 7.22 Accounting for shear bands in the estimation of steady state values of p' and q (Carrera et al. 2011). 174

Figure 7.23 Deviator stress and q/p' values calculated with Eq. 7.6 (right circular cylinder) and with Eq. 7.7 (barrel-type deformation). Results correspond to Test 1. 175

Figure 7.24 Typical barrel-like geometry of sheared specimens. 175

Figure 7.25 Results of a CU triaxial test on mix 30/53 (Test 9) in which the steady state was reached. 176

Figure 7.26 Results of a CD triaxial test on mix 10/70 (Test 5) in which the steady state was reached. 176

Figure 7.27 Results of a CU test on mix 81/63 (Test 14) in which the steady state was not reached. 177

Figure 7.28 Implementation of the extrapolation method suggested by Carrera et al. (2011) on a CU test on mix 81/63 (Test 14). 177

Figure 7.29 Results of CD test on mix 30/53 (Test 13) in which a shear band developed. 178

Figure 7.30 Development of a shear band during Test 13. 178

Figure 7.31 Implementation of extrapolation procedure on a CD test of mix 30/53 (Test 13). Notes: Arrows in parts (b) and (c) indicate direction of shear. M value indicated in part (d) was measured in triaxial tests on the same soiltype. 179

Figure 7.32 State and stress paths of the triaxial tests on mix 10/70. 179

Figure 7.33 State and stress paths of the triaxial tests on mix 30/53. 180

Figure 7.34 State and stress paths of the triaxial tests on mix 81/63. 180

Figure 7.35 SSLs of Impala tailings in e-p' space with best fits of the form of Eq. 2.1. 180

Figure 7.36 SSLs in q-p' space of Impala platinum tailings. 181

Figure 7.37 Γ_{50} vs e_{min} plot of Impala platinum tailings. Note: The code in parenthesis indicates e_{min} method. PR = Modified Proctor (ASTM D1557), and NS = Nonstandard method (Section 7.2). 181

Figure 7.38 Γ_{50} vs e_{min} data points of Impala platinum tailings compared with the database of non-plastic soils from Chapter 6. Note: IMP stands for Impala tailings. 182

Figure 7.39 Γ_{50} vs e_{min} data of tailings compared with the database of non-plastic soils from Chapter 6. Note: Soiltypes in the legend are abbreviated as per Table 6.2. 182

Figure 7.40 λ vs e_{min} plot of Impala platinum tailings. 183

Figure 7.41 λ vs e_{min} data points of Impala platinum tailings compared with the database of non-plastic soils from Chapter 6. 183

Figure 7.42 λ vs e_{min} data of tailings compared with the database of non-plastic soils from Chapter 6. 184

Figure 8.1 λ_{10} vs F_r (Reid 2014). Note: $\lambda_{10} = \lambda$ (Eq. 2.1). 194

Figure 8.2 $I_{c,BJ}$ vs $1/\lambda_{10}$ (Reid 2014). Note: $I_{c,BJ} = I_c$ (Eq. 2.20); and $\lambda_{10} = \lambda$ (Eq. 2.1). 195

Figure 8.3 Increase of ψ with increase of λ at low Q_p and large λ. Note: Eq. 8.1 was computed with M = 1.35 and $B_q = 0$. 195

Figure 8.4 Dependence of $\Delta\psi_\lambda$ on $\Delta\lambda$ for $B_q = 0$ 196

Figure 8.5 Dependence of $\Delta\psi_\lambda$ on $\Delta\lambda$ for $B_q = 0.2$ 197

Figure 8.6 Variation of $\Delta\psi_\lambda$ with Q_p for the five TSFs in Table 8.1. Note: $\Delta\psi_\lambda$ is annotated at $Q_p = 10$ and $Q_p = 320$ 198

Figure 8.7 Uncertainty on ψ estimated from Eq. 8.1 due to $\Delta\lambda$ and the intrinsic uncertainty. 199

Figure 8.8 Site-specific λ-e_{min} and Γ_{50}-e_{min} correlations for the Impala TSF. Note: e_{min} determined using the non-standard method described in Section 7.2. 199

Figure 8.9 Profiles of estimated and measured FC (Yi 2014) 200

Figure 8.10 Profiles of estimated and measured FC (Boone and Freitas 2010). 200

Figure 8.11 GSD curves of samples from the Impala TSF grouped by FC. 201

Figure 8.12 GSD curves of samples from the Merriespruit TSF grouped by FC. Data from Williams and Strydom (1994). 202

Figure 8.13 Poor correlation between C_u and C_c, and FC for samples from the Impala TSF. 203

Figure 8.14 Hypothetical e_{min}-FC correlation for the Impala TSF. Note: e_{min} determined using the non-standard method described in Section 7.2. 203

Figure 8.15 Tentative approach to estimate λ and Γ in situ using CPT results and laboratory data. . 203

Figure A.1 Hokkaido Dam: Geometry of model used in scenario 1 213

Figure A.2 Hokkaido Dam: Geometry of model used in scenario 2 213

Figure A.3 Hokkaido Dam: Geometry of model used in scenario 3 213

Figure A.4 Hokkaido Dam: Geometry of model used in scenario 4 214

Figure A.5 Hokkaido Dam: Geometry of model used in scenario 5 214

Figure A.6 Hokkaido Dam: Geometry of model used in scenario 6 214

Figure A.7 Hokkaido Dam: Geometry of model used in scenario 7 215

Figure A.8 Mochikoshi Dyke 1: Geometry of model used in scenario 1 215

Figure A.9 Mochikoshi Dyke 1: Geometry of model used in scenario 2 215

Figure A.10 Mochikoshi Dyke 1: Geometry of model used in scenario 3 215

Figure A.11 Mochikoshi Dyke 1: Geometry of model used in scenario 4 216

Figure A.12 Mochikoshi Dyke 2: Geometry of model used in scenario 1 216

Figure A.13 Mochikoshi Dyke 2: Geometry of model used in scenario 2 216

Figure A.14 Mochikoshi Dyke 2: Geometry of model used in scenario 3 217

Figure A.15 Mochikoshi Dyke 2: Geometry of model used in scenario 4 217

Figure A.16 Mochikoshi Dyke 2: Geometry of model used in scenario 5 217

Figure A.17 Dashihe Beach: Geometry of model used in scenario 1. 218

Figure A.18 Dashihe Beach: Geometry of model used in scenarios 2. 218

Figure A.19 Dashihe Beach: Geometry of model used in scenario 3. 218

Figure A.20 Dashihe Beach: Geometry of model used in scenario 4. 218
Figure A.21 Dashihe Outer Wall: Geometry of model used in scenario 1. 219
Figure A.22 Dashihe Outer Wall: Geometry of model used in scenario 2. 219
Figure A.23 Dashihe Outer Wall: Geometry of model used in scenario 3. 219
Figure A.24 Dashihe Outer Wall: Geometry of model used in scenario 4. 220
Figure A.25 Sullivan Dam: Geometry of model used in scenario 1. 220
Figure A.26 Sullivan Dam: Geometry of model used in scenario 2. 220
Figure A.27 Sullivan Dam: Geometry of model used in scenario 3. 221
Figure A.28 Sullivan Dam: Geometry of model used in scenario 4. 221
Figure A.29 Merriespruit Dam: Geometry of model used in scenario 1. 221
Figure A.30 Merriespruit Dam: Geometry of model used in scenario 2. 222
Figure A.31 Merriespruit Dam: Geometry of model used in scenario 3. 222
Figure A.32 Merriespruit Dam: Geometry of model used in scenario 4. 222
Figure B.1 σ'_v, σ_v, $Q_{tn,cs}$, and τ_h profiles of the Hokkaido TSF. 223
Figure B.2 K_α, τ_h/S_u, CSR, CRR_α, and FS profiles of the Hokkaido TSF. 223
Figure B.3 σ'_v, σ_v, $Q_{tn,cs}$, and τ_h profiles of the Mochikoshi TSF - Dyke 1. 224
Figure B.4 K_α, τ_h/S_u, CSR, CRR_α, and FS profiles of the Mochikoshi TSF - Dyke 1. Values computed using CPT sounding SY1. 224
Figure B.5 K_α, τ_h/S_u, CSR, CRR_α, and FS profiles of the Mochikoshi TSF - Dyke 1. Values computed using CPT sounding SY2. 225
Figure B.6 σ'_v, σ_v, $Q_{tn,cs}$, and τ_h profiles of the Mochikoshi TSF - Dyke 2. 225
Figure B.7 K_α, τ_h/S_u, CSR, CRR_α, and FS profiles of the Mochikoshi TSF - Dyke 2. Values computed using CPT sounding SY1. 226
Figure B.8 K_α, τ_h/S_u, CSR, CRR_α, and FS profiles of the Mochikoshi TSF - Dyke 2. Values computed using CPT sounding SY2. 226
Figure B.9 σ'_v, σ_v, $Q_{tn,cs}$, F_r, and I_c profiles of the Dashihe TSF beach. Values computed with CPT sounding I8. 227
Figure B.10 CSR, CRR, and FS profiles of the Dashihe TSF beach. Values computed with CPT sounding I8. 227
Figure B.11 σ'_v, σ_v, $Q_{tn,cs}$, F_r, and I_c profiles of the Dashihe TSF beach. Values computed with CPT sounding I9. 228
Figure B.12 CSR, CRR, and FS profiles of the Dashihe TSF beach. Values computed with CPT sounding I9. 228
Figure B.13 σ'_v, σ_v, $Q_{tn,cs}$, F_r, and I_c profiles of the Dashihe TSF beach. Values computed with CPT sounding II6. 229
Figure B.14 CSR, CRR, and FS profiles of the Dashihe TSF beach. Values computed with CPT sounding II6. 229
Figure B.15 σ'_v, σ_v, $Q_{tn,cs}$, I_c, and τ_h profiles of the Dashihe TSF outer wall. Values computed with CPT sounding I4. 230
Figure B.16 K_α, τ_h/S_u, CSR, CRR_α, and FS profiles of the Dashihe TSF outer wall. Values computed with CPT sounding I4. 230

Figure B.17 σ'_v, σ_v, $Q_{tn,cs}$, I_c, and τ_h profiles of the Dashihe TSF outer wall. Values computed with CPT sounding I5.....231

Figure B.18 K_α, τ_h/S_u, CSR, CRR_α, and FS profiles of the Dashihe TSF outer wall. Values computed with CPT sounding I5.....231

Figure B.19 σ'_v, σ_v, $Q_{tn,cs}$, I_c, and τ_h profiles of the Dashihe TSF outer wall. Values computed with CPT sounding II2.....232

Figure B.20 K_α, τ_h/S_u, CSR, CRR_α, and FS profiles of the Dashihe TSF outer wall. Values computed with CPT sounding II2.....232

Figure B.21 σ'_v, σ_v, $Q_{tn,cs}$, I_c, and τ_h profiles of the Dashihe TSF outer wall. Values computed with CPT sounding II4.....233

Figure B.22 K_α, τ_h/S_u, CSR, CRR_α, and FS profiles of the Dashihe TSF outer wall. Values computed with CPT sounding II4.....233

Figure B.23 σ'_v, σ_v, F_r, I_c, and $Q_{tn,cs}$ profiles of the Sullivan TSF. Values computed with CPT sounding CP91-29.....234

Figure B.24 Profiles of total vertical stress (σ_v) and effective vertical stress (σ'_v) for the different CPTu soundings conducted at the Merriespruit TSF.....235

List of tables

Table 2.1 I_c ranges for different SBTs. Data from: Robertson and Wride (1998) and Jefferies and Been (2006). 30

Table 2.2 Magnitude scaling factors (Youd et al. 2001). 30

Table 2.3 References that address the different stages of liquefaction considered in this study 30

Table 2.4 Data requirements to implement the analyses considered in this study. 31

Table 3.1 Summary of case histories. 49

Table 3.2 Total unit weight (γ_t) and Poisson's ratio (v) values used in the finite element models. 50

Table 3.3 Average f_s values at the Dashihe dam beach. Data from Henian et al. (1990). 50

Table 3.4 Soiltypes probed by the CPT*s* on the Dashihe outer wall. Data from Amante (1993) 51

Table 3.5 Typical *FC* and *PI* values of the soiltypes in the Dashihe dam reported by Lee et al. (1992). I_c values were estimated in the current study using Figure 2.5. 51

Table 4.1 Summary of the validity of the predictions made by the methods. 71

Table 5.1 Soil behaviour type from classification index $I_{Q\text{-}Bq}$. 85

Table 6.1 Correlations between soil index parameters and the SSL. 110

Table 6.2 Index properties of soils in the database. 111

Table 6.3 SSL parameters of the different soiltypes. 118

Table 7.1 Index properties and SSL parameters of the laboratory mixes of Impala tailings. 161

Table 7.2 Shearing rates in axial strain per hour adopted in investigations with non-plastic soils. 161

Table 7.3 Transducers used in triaxial testing setups 1 and 2. 161

Table 7.4 Summary of the triaxial testing programme 162

Table 8.1 Soil behaviour type from classification index $I_{Q\text{-}Bq}$ and FC from site-specific calibration. 194

Table A.1 Scenarios used to analyse Hokkaido Dam. 211

Table A.2 Scenarios used to analyse Mochikoshi Dyke 1 211

Table A.3 Scenarios used to analyse Mochikoshi Dyke 2. 211

Table A.4 Scenarios used to analyse Dashihe Beach. 212

Table A.5 Scenarios used to analyse Dashihe Outer Wall. 212

Table A.6 Scenarios used to analyse Sullivan Dam. 212

Table A.7 Scenarios used to analyse Merriespruit Dam. 212

Table D.1 Correlations of Γn vs emin in which each soiltype was included. 246

List of Symbols

The equation or figure number in which the less common symbols are defined or used is given in parenthesis.

A	Angular particle *OR* Cross sectional area of a triaxial test specimen *OR* $Q_p/[M(1-B_q)]$
a	CPT unequal area ratio (Eq. 2.6)
A_c	Projected area of the CPT cone (Figure 2.4) *OR* Cross sectional area of triaxial test specimen at the end of consolidation
a_{max}	Maximum horizontal acceleration at ground surface due to seismic action
A_n	Cross sectional area of the shaft of the CPT probe (Figure 2.4)
APC	Automatic pressure controller
b	Fraction of fines that contributes to the active intergrain contacts (Eq. 6.1)
BP	Back pressure
B_q	CPT normalised excess pore water pressure (Eq. 2.16)
c	Soil cohesion
c'	Soil effective cohesion
C_c	Coefficient of curvature (GSD descriptor, $D_{30}^2/(D_{60}\cdot D_{10})$)
CD	Consolidated drained
CP	Cell pressure
CPT	Cone penetration test
CPTu	CPT with dynamic pwp readings
CRR	Cyclic resistance ratio (Eq. 2.31)
$CRR_{7.5}$	Cyclic resistance ratio adjusted to an earthquake of magnitude 7.5 (Eq. 2.30)
CSL	Critical state line
CSR	Cyclic stress ratio (Eq. 2.25)
CSSM	Critical state soil mechanics
C_u	Coefficient of uniformity (GSD descriptor, D_{60}/D_{10})
CU	Consolidated undrained
DEM	Discrete element method
D_n	Diameter at which *n*% of the soil is finer
e	Void ratio
e_c	Critical void ratio (Eq. 2.5)
$(e_c)_{eq}$	Equivalent intergranular void ratio (Eq. 6.1)
e_f	Post-shearing void ratio
$(e_f)_{eq}$	Equivalent interfine void ratio (Eq. 6.2)
e_{is}	In situ void ratio
e_{max}	Maximum index void ratio
e_{min}	Minimum index void ratio
FC	Fines content
FE	Finite element
F_r	CPT sleeve friction ratio (Eq. 2.12)
f_s	CPT sleeve friction
FS	Factor of safety
FS_{flow}	Factor of safety against flow failure (Eq. 2.29)
$FS_{triggering}$	Factor of safety against the triggering of liquefaction (Eq. 2.28)
g	Acceleration due to gravity
G	Small strain shear modulus
GLU	Glaciolacustrine
G_s	Specific gravity of a soil particle
GSD	Grain size distribution
H	Hardening modulus
H_c	Consolidated height of triaxial test specimen
I_c	CPT soil behaviour type index (Eqs. 2.11 and 2.20)
I_G	Grading state index (GSD descriptor)
$I_{Q\text{-}Bq}$	CPT soil behaviour type index (Eq. 5.1)
I_R	Rigidity modulus
k	Inversion parameter to calculate ψ (Eq. 2.43)

k'	Effective inversion parameter to calculate ψ (Eq. 2.46)
K_0	Coefficient of lateral stress at rest
K_c	Correction factor used in the calculation of $Q_{tn,cs}$ (Eq. 2.14)
K_α	Static shear stress correction factor (Eq. 2.32)
LSR	Liquefied strength ratio (Eq. 2.24)
M	Steady state friction ratio (Eq. 2.2)
m	Inversion parameter to calculate ψ (Eq. 2.44)
m'	Effective inversion parameter to calculate ψ (Eq. 2.47)
M_s	Mass of solids
MSF	Earthquake magnitude scaling factor
M_w	Earthquake moment magnitude
n	Stress exponent used in the calculation of $Q_{tn,cs}$ (Eq. 2.10)
N_{kt}	Empirical cone factor used to infer shear strength from q_t
OCR	Overconsolidation ratio
P	Axial load in triaxial test
p'	Mean effective stress (Eq. 2.4)
p	Mean total stress (Eq. 7.13)
p_a	Atmospheric pressure
PI	Plasticity index
p'_{is}	In situ mean effective stress
pwp	Pore water pressure
q	Deviator stress (Eq. 2.3 and 7.15)
Q	CPT tip resistance normalised by the vertical stress (Eq. 2.15)
q_c	CPT tip resistance
q_{c1}	CPT tip resistance normalised by atmospheric pressure (Eq. 2.8)
q_{c1}*	Representative value of q_{c1}
Q_p	CPT tip resistance normalised by the mean stress (Eq. 2.17)
q_t	CPT tip resistance corrected for unequal area effects (Eq. 2.6)
Q_{tn}	CPT tip resistance normalised by atmospheric pressure using the stress exponent n (Eq. 2.9)
$Q_{tn,cs}$	Clean sand equivalent of Q_{tn} (Eq. 2.13)
R	Rounded
r_d	Depth reduction factor used in the calculation of CSR (Eq. 2.26)
SA	Sub-angular
SBT	Soil behaviour type
SPT	Standard penetration test
SR	Sub-rounded
SSL	Steady state line
S_u(LIQ)	Liquefied (residual) shear strength
S_u(yield)	Yield (peak) shear strength
TFC	Threshold fines content
TSF	Tailings storage facility
U	Normalised pore pressure ratio (Eq. 2.21)
u_0	In situ pwp
u_{0E}	Value of u_0 as extrapolated from an incomplete CPTu dissipation test
u_{0T}	Last pwp value of a truncated CPTu dissipation test
u_i	Initial pwp value in a CPTu dissipation test
u_n	Dynamic pwp recorded by the CPTu. *n* varies from 1 to 3 depending on the location of the pwp sensor.
u_t	PWP at time t
V_s	Volume of solids (Eq. 7.3)
V_{wf}	Volume of water after consolidating a triaxial test specimen
w	Water content (mass of water divided by the mass of solids)
YSR	Yield strength ratio (Eq. 2.23)
z	Depth below ground level
ε_a	Axial strain (Eq. 7.4)
ε_s	Shear strain
ε_v	Volumetric strain

Γ_n	Void ratio value of the SSL in e-p' space at a mean stress level of *n* kPa (Eq. 2.1)
γ_t	Total unit weight
λ	Slope of the SSL in e-$\log_{10}$(p') space (Eq. 2.1)
ν	Poisson's ratio
ρ_{dry}	Dry soil density
ρ_s	Particle density
σ_d	Deviator stress (Eq. 2.3 and 7.15)
σ_i	Major (i=1), intermediate (i=2), and minor (i=3) principal stress.
σ'_v	Vertical effective stress
σ'_{v0}	Initial vertical effective stress
σ_v	Vertical total stress
σ_{v0}	Initial total effective stress
$\tau_{ave,seismic}$	Average seismic shear stress (Eq. 2.25)
$\tau_{driving}$	Static shear stress
τ_h	Horizontal static shear stress
τ_{other}	Other shear stresses
ϕ'	Effective friction angle
ϕ_{cs}	Friction angle at critical state
ψ	State parameter (Eq. 2.41)

1 Introduction

1.1 Topic overview

Several well documented disasters serve to confirm the destructive potential of improperly managed mining activities. Tailings storage facilities (TSFs) are associated with only a fraction of these disasters, but the failure of these structures generally leads to considerable social, environmental, and economical losses. Davies et al. (2001) reviewed a database of instabilities in TSFs from 1970 to 1999 and estimated an annual probability of failure rate between 1 in 700 and 1 in 1,750. They further pointed out that this rate is significantly higher than the estimated 1 in 10,000 probability of failure of conventional dams. These figures leave little doubt about the role played by TSF failures in fostering a negative image of the mining industry. As an example of how relevant this issue remains, one has to look no further back than August 4, 2014 for news of a catastrophic TSF failure that featured in international media. On that day the embankment of a tailings pond at the Mount Polley copper and gold mine in the Canadian state of British Columbia was breached generating a sudden loss of containment. The breach resulted in a surge of tailings slurry flowing to the nearby Polley and Quesnel Lakes. The magnitude of the breach has been estimated to exceed 10×10^6 m^3 of water and 4.5×10^6 m^3 of tailings (www.mountpolleyreviewpanel.ca). An independent review panel of the Mount Polley disaster concluded that the failure was caused by insufficient strength of a glaciolacustrine (GLU) layer underneath a section of the embankment. The panel determined that "*the GLU deposit had properties that became increasingly contractive when sheared*" and that made the GLU layer "*disposed to undrained failure*" (Morgenstern et al. 2015). As will be seen in Section 2.1, the implication of these findings is that liquefaction could have contributed to the Mount Polley disaster.

Considering the magnitude of disasters such as the one at Mount Polley, it is not surprising that the topic of soil liquefaction has received significant attention by the geotechnical profession. Some of the methods proposed to assess liquefaction potential have relied on the recovery of undisturbed samples to determine in situ density e.g. (Poulos et al. 1985). However, given the difficulties of undisturbed sampling, especially in cohesionless soils, many methods have also relied on in situ testing. This trend of reliance on in situ testing can be traced back to the simplified procedure for evaluating soil liquefaction potential proposed by Seed and Idriss (1971) which correlated results from the standard penetration test (SPT) to the maximum seismic action that a soil can resist without undergoing liquefaction. Both Seed and Idriss were linked to the University of California in Berkeley, so methods that adopt the framework proposed by Seed and Idriss (1971) are often collectively referred to as the Berkeley School.

With the development of in situ tests that are more reliable than the SPT, methods that make use of the newer tests also emerged. Examples of such methods are Olson and Stark (2002) and (2003), Jefferies and Been (2006), and Robertson (2009b) and (2010). All three of these methods rely on the cone penetration test (CPT) as their main in situ test. The current thesis is an investigation into the performance of these CPT-based methods in TSFs. It is worth asking what sets TSFs apart

from other soil deposits. Several distinguishing features can be mentioned. Unlike natural deposits, TSFs are geologically young as they only appeared with large scale mining. Consequently, tailings are generally cohesionless and exhibit low plasticity due to limited chemical weathering. Hydraulic deposition is commonly used in the construction of TSFs and this implies that the water table often lies close to the beach surface and an important portion of the tailings is in a fully saturated condition. These are features that favour the occurrence of liquefaction (Robertson 2010) if the TSF is not properly managed. Additionally, since tailings are the result of an ore crushing process, individual particles have a highly angular shape which is distinctly different to the sub-rounded particle shape characteristic of alluvial soils.

The three methods mentioned above were selected for study as they adopt different approaches to assess liquefaction potential and are often cited in technical literature. The method proposed by Olson and Stark (2002) and (2003) is anchored on a database of case histories of liquefaction induced failures. The method is applicable to level and sloping ground, and seismic and static loading. The method proposed by Jefferies and Been (2006) was initially developed from the analysis of CPT calibration chamber data (Been et al. 1986; Been et al. 1987) with more recent developments also using constitutive models to refine the interpretation of CPT results (Shuttle and Jefferies 1998). The method was not developed using a case history database and is applicable to level and sloping ground, and seismic and static loading. As will be shown in Chapter 2, the steady state line (SSL) of a soil is a key input for the implementation and verification of the Jefferies and Been (2006) method. For this reason, the investigation of how the method is affected by the variation of SSL parameters within a soil deposit was amongst the objectives of the thesis. The method proposed by Robertson (2009b) and (2010) is anchored on a case history database and on laboratory results. It can be applied to level and sloping ground. The correlations developed by Robertson (2009b) are applicable to seismic loading only, whereas those developed by Robertson (2010) are applicable to both static and seismic loading. Some of the procedures recommended by Robertson (2009b) adopt the concepts of the Berkeley School.

1.2 Research objectives

Against this background, the thesis has two general objectives:

1. Assess the applicability to TSFs of the methods proposed by Olson and Stark (2002) and (2003), and Robertson (2009b) and (2010).
2. Assess the sensitivity of the state parameter, ψ (defined in Section 2.5), as estimated from a method proposed by Jefferies and Been (2006), to variations of soil properties in TSFs.

The following specific objectives were pursued in order to meet the first general objective:

- Conduct a critical review of the data that supports the equations of the Olson and Stark (2002) and (2003) method. This review will include the susceptibility, triggering and post-triggering analyses.

- Implement the Olson and Stark (2002) and (2003) method on a database of TSF case histories to determine the capability of the method to predict performance.
- Conduct a critical review of the data that supports the equations of the Robertson (2009b) and (2010) method. This review will include the susceptibility and triggering analyses.
- Implement the susceptibility and triggering analyses of Robertson (2009b) and (2010) on a database of TSF case histories to determine the capability of the method to predict performance.

The following specific objectives were pursued in order to meet the second general objective:

- Process the raw data corresponding to CPTu soundings made at a South African TSF to establish representative parameters to be used when assessing the sensitivity of ψ to soil variability.
- Investigate the correlations between the index parameters of a soil and the SSL. These correlations provide guidance for the selection of representative soiltypes from a given deposit to evaluate SSL parameters. Evaluation of these parameters is an essential first step for the implementation of the Jefferies and Been (2006) methodology.
- Conduct a triaxial testing programme to characterise the variability of SSLs at the South African TSF for which CPTu soundings were available. The design of this testing programme was based on the previously mentioned investigation of the correlations between the SSL and index parameters.
- Quantify, for TSF-like conditions, the sensitivity of the state parameter (ψ) to variations in the SSL, when implementing one of the methods proposed by Jefferies and Been (2006).
- Highlight characteristics of the grain size distribution curves corresponding to two hydraulically deposited TSFs which may be useful in improving estimates of SSL parameters from a combination of CPT data and triaxial testing results. These improved estimates may be necessary in certain cases to reduce the uncertainty on ψ.

1.3 Organization of the thesis

The remainder of this thesis has been organised as follows. Chapter 2 describes the conceptual framework of the thesis. This includes an overview of the basic principles of soil liquefaction, a brief description of the CPT, and a description and review of the three liquefaction assessment methodologies being considered: Olson and Stark (2002) and (2003), Jefferies and Been (2006), and Robertson (2009b) and (2010). Importantly, this chapter also describes modifications made by the author to the procedures outlined by Robertson (2009b) and (2010) to make them applicable to the case history database compiled for this thesis. Chapter 3 describes the case histories on which the different methodologies were implemented and presents the idealisations that were made for each case history. Chapter 4 presents the results of the implementation of the Olson and Stark (2002) and (2003), and Robertson (2009b) and (2010) methodologies on the case history database compiled for

this study. Chapter 5 describes the processing of the raw CPTu data corresponding to soundings performed at a South African platinum TSF named the Impala TSF, and presents a CPTu-based soil behaviour type index that does not rely on sleeve friction. Chapter 6 explores correlations between the index properties of soils and the SSL. Emphasis is placed on non-plastic soils as this is generally the nature of tailings. Chapter 6 concludes that there is a correlation between the minimum void ratio (e_{min}) and the vertical location of the SSL in void ratio (e) vs mean effective stress (p') space. Data is also presented indicating that there might be a correlation between e_{min} and the slope of the SSL in e-p' space. Chapter 7 describes the experimental programme undertaken to characterise the variability of SSLs in the Impala TSF. The results of the experimental programme are compared with the correlations identified in Chapter 6. Chapter 8 investigates the sensitivity of ψ, as estimated with a simplified method proposed by Jefferies and Been (2006), to variations in the slope of the SSL in e-p' space. Additionally, Chapter 8 also proposes a tentative approach to calculate profiles of SSL parameters using a combination of CPTu and laboratory results. However, further research is required to validate the proposed approach. Lastly, Chapter 9 presents a summary of the most salient findings of the study.

2 Conceptual framework

2.1 The mechanics of soil liquefaction

Soil liquefaction is a process in which a tendency for undrained volumetric contraction of a saturated soil mass causes an increase in pore water pressure that in turn leads to a loss of shear strength (i.e. strain softening). Although liquefaction is possible in unsaturated soils (Unno et al. 2008), it is generally acknowledged that saturated soils are more susceptible to this phenomenon (Ishihara 1993; Robertson 2010). Depending on the site conditions, liquefaction can be manifested in a variety of ways such as sand boils, sudden collapse of foundations, vertical settlements and flow failures (Ishihara 1993). Given that the increase in pore water pressure that leads to liquefaction affects only the frictional component of soil strength, soils able to develop significant cohesive strength such as clays are less vulnerable to the effects of liquefaction. Conversely, in soils that derive their shear strength mostly from the frictional contacts between particles, such as sands and non-plastic silts, the consequences of liquefaction can be more serious. A good example of this second type of soil is mining tailings, as the fines contained in tailings are typically cohesionless.

The nature of the volume changes that a saturated soil undergoes when sheared is central to understanding liquefaction. If the volume changes are contractive, there will be a tendency to pore water pressure (pwp) increase and consequent reduction in strength when the soil is sheared under undrained conditions. That is, a contractive tendency is needed for liquefaction. Conversely, if the tendency is dilative, undrained shearing will lead to a reduction of pwp which will strengthen the soil. In other words, liquefaction cannot occur in dilatant soils. Casagrande (1936) addressed the question of whether a soil will contract or dilate when sheared. Through a series of shear box tests he found that for a given soiltype, loose specimens contracted and dense specimens dilated until reaching approximately the same ultimate void ratio (e). Casagrande referred to this ultimate void ratio as the critical void ratio (e_c). He noted that upon shearing, a soil specimen will contract if e is greater than e_c, and will dilate if e is lower than e_c.

Schofield and Wroth (1968) proposed the theory of Critical State Soil Mechanics (CSSM) which was based on the critical void ratio concept of Casagrande. They described the kernel of their ideas as *"the concept that soil and other granular material, if continuously distorted until they flow as a frictional fluid, will come into a well defined critical state determined by"*

$$\mathrm{e}_c = \Gamma_1 - \lambda \cdot \log_{10} p' \qquad 2.1$$

$$\mathrm{q} = M \cdot p' \qquad 2.2$$

where the deviator stress (q) and the mean effective stress (p') are defined as:

$$q = \sigma_1 - \sigma_3 \qquad 2.3$$

$$p' = (\sigma'_1 + \sigma'_2 + \sigma'_3)/3 \qquad 2.4$$

and σ_i and σ'_i are the total and effective stresses, respectively, in the principal direction i. The constants Γ_1, and λ are properties that vary from one soiltype to another, whereas M varies both with soiltype and mode of loading. Figure 2.1 illustrates the meaning of Γ_1 and λ. The sub-index 1 for Γ indicates that it is the void ratio of the critical state line (CSL) at a mean stress of 1 kPa. This notation was further generalised in the current work so that Γ_n denotes the void ratio of the CSL at a mean stress of *n* kPa. For clarity, the meaning of Γ_{100} is also illustrated in Figure 2.1. Additionally Γ alone, without a sub-index, will be used herein to refer to the vertical location of the CSL in e-p' space in general. It is worth noting that some authors (e.g. Cho et al. 2006) prefer to express the ratio M = q/p' as a friction angle termed the critical state friction angle (ϕ_{cs}). In the current work the dimensionless parameter M has been preferred to characterise the state of stresses at critical state.

Castro (1969) used a series of stress-controlled triaxial tests to study the state reached by sands when deformed continuously. He found that his tests led to a well-defined line correlating e_c and p'. He termed this line the steady state line (SSL). Casagrande (1975) made a distinction between the line representing the ultimate (e-p') conditions of drained and undrained triaxial tests. He defined the CSL as the line obtained through drained tests and the SSL as the line obtained through undrained tests. However, extensive testing programmes on Erksak sand (Been et al. 1991) and Toyoura sand (Verdugo and Ishihara 1996), among others, suggest that the SSL and the CSL are the same. This equivalence between CSL and SSL has been adopted in the current work. The term SSL was preferred over CSL, as the word “steady” is more descriptive of the fact that, when sheared to its ultimate condition, the stresses and void ratio of a soil remain constant.

The SSLs of a great variety of soils have been reported in the literature (e.g. Table 6.3 compiled by the present author). In general, it has been found that Eq. 2.2 is a suitable representation of the SSL in the q-p' plane. However the ability of Eq. 2.1 to represent the SSL in the e-p' space is known to be more limited. The main limitation is that the SSL generally exhibits some degree of curvature in e-log(p') space. To accommodate such curvature, higher order alternatives to equation 2.1 have been proposed. For instance, Li and Wang (1998) adopted:

$$\mathrm{e}_c = \mathrm{e}_{ref} - \lambda\left(\frac{p'}{p_{at}}\right)^{\xi} \qquad 2.5$$

Where e_{ref} is the critical void ratio when p' = 0 kPa, and ξ together with λ, determine the slope of the SSL.

Jefferies and Been (2006) argued that there is no fundamental reason to choose one equation of SSL over the other, and that the choice depends only on the characteristics of the data at hand. This is illustrated in Figure 2.2 which shows the SSLs extending to about p' = 1000 kPa of four silica sands: two foundry sands and two Ottawa sands. Also shown in the figure are the best fit lines obtained using equations 2.1 and 2.5. Due to the curvature in the data of the foundry sands, the resulting best

fit line is quite different depending on the equation used to make the fit. However, for the Ottawa sands the best fit line is largely independent of the adopted equation.

The observations of Casagrande (1936), Schofield and Wroth (1968), and Castro (1969) indicate that, if sheared under undrained conditions, a soil whose state plots below the SSL will tend to dilate to reach its steady state. Conversely, a soil whose state plots above the SSL will tend to contract to reach its steady state. That is, the SSL can be thought of, for a first approximation, as a boundary between states conducive to strain softening (contractive) and states conducive to strain hardening (dilative) (Figure 2.1). This concept is referred to as an approximation because it is known to be inapplicable to states that plot above, but close to, the SSL. For instance, Ishihara (1993) reported experimental data showing that, after an initial drop in strength, such states still strain harden when sheared to steady state. Notwithstanding this limitation, the SSL is generally considered a suitable boundary to distinguish between strain softening and strain hardening states (Cubrinovski and Ishihara 2000; Fourie and Papageorgiou 2001; Robertson 2010).

It follows from the previous observations that in order for liquefaction to occur, the first condition that must be met is that the soil must exist in a contractive state. If this condition is met, there must be a triggering mechanism that shears the soil and leads to an increase in pwp. Figure 2.3 (Olson and Stark 2003) schematically represents three triggering mechanisms that may lead a contractive cohesionless soil to liquefy. Point A represents the result of applying a static shear stress smaller than the peak strength of the soil. The shear stress could be increased sufficiently (e.g. by an increase in surcharge load) to reach the maximum available shear strength (S_u(yield)), at B. Thereafter, any attempt to increase the shear stress can only result in a decrease of available shear strength to its residual value (S_u(LIQ)), and substantial straining from B to C. Alternatively, if at point A, the static shear stress induces creep deformation, this will result in an increase of pwp and a corresponding movement from A to D and a subsequent strain softening to C. A third possibility is that cyclic stresses (e.g. vibration induced by machinery or seismic action), together with their accompanying irreversible strains, will move a point such as A' to point E. Once again, the soil will strain-soften and the strain and stress diagrams will move towards C.

In accordance with the mechanisms described in the previous paragraph the assessment of liquefaction potential and its consequences can be broken down into a three-step analysis (Ishihara 1993; Olson and Stark 2003). The first step is a susceptibility analysis in which the aim is to determine whether a soil is in a contractive state, i.e., susceptible to liquefaction. The second step is a triggering analysis in which the shear stresses acting on the soil mass are compared to the available undrained peak strength (S_u(yield)). Finally, a post-triggering analysis is done in which the permanent stresses acting on the soil are compared to the residual shear strength (S_u(LIQ)). If the permanent stresses are greater than S_u(LIQ), then liquefaction can be expected to result in large deformations which will modify the geometry of the soil deposit until its internal shear stresses are equal to or smaller than S_u(LIQ). These large deformations are generally referred to in technical literature as flow failure or flow liquefaction (Ishihara 1993; Robertson 2010).

The authors of the three methods considered in the current study have addressed all three of the steps described above. However, considering the field data available and the laboratory data

that could be obtained for this study, the current thesis focused on the following steps of the different methods. For the method proposed by Olson and Stark (2002) and (2003), all three steps of the liquefaction analysis were considered. For Robertson (2009b) and (2010), the susceptibility and the triggering analyses were considered. As for the method proposed by Jefferies and Been (2006), the focus was on determining how the estimation of the state parameter (ψ), which is defined in Eq. 2.41 and is the base of the method, is affected by the variability of λ throughout the deposit.

2.2 The cone penetration test (CPT)

2.2.1 Standard measurements, corrections and typical geometry of the probe

A typical CPT probe measures tip resistance (q_c), sleeve friction (f_s) and dynamic pore pressure (u_n), where n adopts the value of 1, 2, or 3 depending on the location of the pwp transducer (Figure 2.4a). The term "dynamic" is used to indicate that this is not an in situ water pressure (u_0), but rather the water pressure generated as the cone is pushed into the soil. The abbreviation CPTu is commonly used to emphasise that u_n has been measured and will be used in this thesis. However, the abbreviation CPT, as used herein, does not preclude u_n readings. The standardised geometric characteristics of a CPT probe as specified by ISSMFE (1989) are a projected cone area of 10 cm^2 with an apex angle of 60°. Additionally, although not standardised, ISSMFE (1989) refers to u_2 as the preferred location of the pore pressure transducer.

An unequal area effect correction is generally made to q_c to account for the action of the dynamic pore water pressure on the shoulder behind the cone (Figure 2.4b). The pressure acting on this shoulder exerts a downward force and relieves some of the load that the cone would take if the shoulder were not there. The corrected q_c value is termed the total cone resistance (q_t) and is calculated as:

$$q_t = q_c + u_2(1 - a) \tag{2.6}$$

where *a* is called the unequal area ratio and is defined as the ratio of the cross sectional area of the shaft (A_n) to the projected area of the cone (A_c) (Figure 2.4b). A similar unequal area correction can also be made to f_s. The corrected f_s value is termed f_t and is calculated as:

$$f_t = f_s - \frac{(u_2 \cdot A_{sb} - u_3 \cdot A_{st})}{A_s} \tag{2.7}$$

where A_{sb} and A_{st} are the bottom and top cross sectional areas of the friction sleeve, respectively (Figure 2.4b). Lunne et al. (1997) point out that since u_3 is seldom measured, it is not generally possible to calculate f_t, and that this is one of the reasons why sleeve friction readings are generally regarded as less reliable than tip resistance readings. None of the CPT datasets reviewed in this

study included u_3 values and therefore f_s was used instead of f_t. It is also worth noting that the unequal area corrections of q_c and f_s are directly proportional to the magnitude of the dynamic pore pressure. Accordingly, unequal area corrections are often negligible when the CPT is drained (e.g. sandy soils) but significant when the CPT is partially drained (e.g. clays).

2.2.2 Normalised parameters and soil classification

It is known that for a constant soil density, tip resistance increases with effective overburden stress. For this reason, it is common to convert q_c or q_t values into normalised parameters that account for the total and effective stresses acting at the depth of interest. Several equations have been proposed to achieve this. The equations used by the methodologies considered in this study will now be presented. Olson and Stark (2002) adopt the following equation:

$$q_{c1} = q_c \cdot \frac{1.8}{0.8 + \sigma'_{vo}/p_a} \tag{2.8}$$

where p_a is the atmospheric pressure (≈100 kPa), σ'_v is the vertical effective stress in the same units as p_a, and the sub-index 0 is added to emphasise reference to pre-CPT conditions. Robertson (2009b) adopted a normalised penetration parameter defined as:

$$Q_{tn} = \left(\frac{q_t - \sigma_{vo}}{p_a}\right)\left(\frac{p_a}{\sigma'_{vo}}\right)^n \tag{2.9}$$

where σ_v is the vertical total stress, with the sub-index 0 emphasising pre-CPT conditions. The constant n is a stress exponent whose value depends on the soiltype and which is calculated with the following equations:

$$n = 0.381 \cdot (I_c) + 0.05 \cdot (\sigma'_{vo}/p_a) - 0.15 \quad where\ n \leq 1.0 \tag{2.10}$$

$$I_c = \sqrt{(3.47 - \log Q_{tn})^2 + (\log F_r + 1.22)^2} \tag{2.11}$$

$$F_r = \left(\frac{f_s}{q_t - \sigma_{vo}}\right) \cdot 100\% \tag{2.12}$$

where I_c is a soil behaviour type (SBT) index proportional to fines content (FC) and plasticity (Figure 2.5), and F_r is the sleeve friction ratio. Given the interdependence between Q_{tn}, n, and I_c an iteration process is required to find their final values. Eq. 2.11 was proposed by Robertson and Wride (1998) as a means of identifying SBT using CPT results. The definition of I_c is linked to the Q_{tn} vs F_r classification chart proposed by Robertson and Wride (1998) (Figure 2.6a) and to the observation of

Jefferies and Davies (1993) that the boundaries between zones 2-7 of the chart can be approximated as concentric circles. Equation 2.11 is therefore the radius of a circle concentric with these boundaries. The SBTs that correspond to different ranges of I_c as defined by Eq. 2.11 are shown in Table 2.1. The following criteria given by Robertson and Wride (1998) were also considered in this study when using the Q_{tn} vs F_r classification chart:

1. I_c does not apply to regions 1, 8 or 9.
2. Very loose clean sands may be confused with denser sands containing fines in the region defined by $1.64 < I_c < 2.36$ and $F_r < 0.5\%$. Therefore, soils plotting in this zone should be conservatively treated as clean sand.
3. Soils that fall in the region defined by $I_c > 2.6$ and $F_r \leq 1.0\%$ can be very sensitive and susceptible to liquefaction. Soils in this region require additional testing to determine their liquefaction potential.

Equation 2.10 was initially proposed by Robertson (2009a) and is supported mostly on qualitative observations that centre around two facts: First, cone resistance varies linearly (n = 1) with depth in fine grained soils, very loose sands and dense sands subjected to pressures that are high enough to suppress dilatancy. Second, cone resistance in coarse grained soils varies nonlinearly with depth and the average stress exponent to capture this change is close to 0.5. Robertson (2009a) further states that Eq. 2.10 "*is not an arbitrary approach, but is based on experimental observations…*" However none of these experimental observations are reproduced in Robertson (2009a) to allow an assessment of the suitability of applying Eq. 2.10 to tailings storage facilities (TSF).

Robertson and Wride (1998) proposed a clean sand equivalent of Q_{tn} (termed $Q_{tn,cs}$) which is defined by Eqs. 2.13 and 2.14. The rationale behind $Q_{tn,cs}$ is to account for the higher resistance to liquefaction that Robertson and Wride (1998) attribute to soils with higher I_c values, i.e. soils with higher FC and/or higher plasticity.

$$Q_{tn,cs} = Q_{tn} \cdot K_c \tag{2.13}$$

$$\begin{aligned} &if\ I_c \leq 1.64, \qquad K_c = 1.0 \\ &if\ I_c > 1.64, \qquad K_c = -0.403 \cdot I_c^4 + 5.581 \cdot I_c^3 - 21.63 \cdot I_c^2 + 33.75 \cdot I_c - 17.88 \end{aligned} \tag{2.14}$$

Robertson and Wride (1998) state that Eq. 2.14 is approximate but that it provides a useful guide for small projects or for initial screening of larger projects. However, no experimental data is presented to support Eq. 2.14.

Robertson (1990) adopted the following normalised tip resistance parameter:

$$Q = (q_t - \sigma_{v0})/\sigma'_{v0} \tag{2.15}$$

Robertson (1991) proposed a Q vs B_q classification chart that does not require f_s for its implementation (Figure 2.6b). B_q is the normalised excess pore pressure defined as:

$$B_q = (u_2 - u_0)/(q_t - \sigma_{v0}) \quad 2.16$$

Jefferies and Been (2006) noted that normalising with respect to a reference pressure (e.g. p_a in Eqs. 2.8 and 2.9) is an attempt to calculate the q_t value that would have been measured if the soil had been at the same relative density but at an in situ stress of p_a. They objected to this approach as it assumes that relative density is well correlated to soil behaviour and this is known to be incorrect (Been and Jefferies 1985). Instead, Jefferies and Been (2006) propose a normalisation of q_t with respect to the initial mean effective stress (p') using the following equation:

$$Q_p = (q_t - p_0)/p'_0 \quad 2.17$$

where p is the mean total stress defined as:

$$p = (\sigma_1 + \sigma_2 + \sigma_3)/3 \quad 2.18$$

and the sub-index 0 has been added to p and p' to emphasise pre-CPT conditions. A difficulty in using Eq. 2.17 is that it requires knowledge of stress in all three principal directions. For geostatic stress conditions this reduces to two directions since $\sigma'_1 = \sigma'_v$, and $\sigma'_2 = \sigma'_3 = \sigma'_h$. Accordingly, p'_0 can be expressed as:

$$p'_0 = (\sigma'_v + 2 \cdot \sigma'_h)/3 = (\sigma'_v + 2 \cdot K_0 \cdot \sigma'_v)/3 \quad 2.19$$

Where $K_0 = \sigma'_h/\sigma'_v$ is the coefficient of lateral stress at rest and σ'_h is the effective horizontal stress. Estimation of p'_0, and therefore of Q_p, poses a challenge because unlike σ'_v, σ'_h cannot be readily estimated from total unit weights and pwp. Instead, reliable determination of σ'_h requires additional in situ testing as discussed in Section 2.6.2.

Jefferies and Been (2006) also make use of I_c, however their definition of I_c is different from that of Eq. 2.11 and is given by:

$$I_c = \sqrt{\left(3 - \log\left(Q\left(1 - B_q\right) + 1\right)\right)^2 + (1.5 + 1.3\log(F_r))^2} \quad 2.20$$

Jefferies and Been (2006) justify their preference of Eq. 2.20 over Eq. 2.11 by noting that Eq. 2.20 incorporates information regarding the dynamic pore water pressure which can assist in identifying soiltype. It should also be noted that Q, and not Q_p, is used in Eq. 2.20. Jefferies and Been (2006) explain that although Q_p is more fundamentally sound as it considers the effect of horizontal

stresses, the soil classification chart on which I_c (Eq. 2.20) is based uses Q. The SBTs that correspond to different ranges of I_c as defined by Eq. 2.20 are shown in Table 2.1.

2.2.3 Dissipation tests

It was noted above that the dynamic pore water pressure (u_n) measured during a CPTu sounding is different from the in situ water pressure (u_0). In order to measure u_0, the probe has to be brought to a full stop to allow for u_n to dissipate. Once u_n reaches a constant value, this reading can be interpreted as u_0 and used to compute B_q (Eq. 2.16). When presenting the results of dissipation tests, it is common to express the decay in pore water pressure using a normalised pore pressure ratio (U) which is defined as:

$$U = \frac{u_t - u_0}{u_i - u_0} \qquad 2.21$$

where u_t is the pore pressure at time t, and u_i is the pore pressure at the start of the dissipation test. The value of U indicates the fraction of dissipation that is yet to occur. Accordingly, U = 1 at the start of dissipation and U = 0 when dissipation is complete.

2.3 The Olson and Stark method

2.3.1 General comments

Olson and Stark (2002) and (2003), proposed a methodology to assess the liquefaction potential of sloping and level ground subjected to monotonic or seismic loading. The methodology is based on the back analyses of flow failure case histories and was implemented in this study without any deviations from the procedures outlined by Olson and Stark (2002) and (2003). A detailed description of all the case histories and the different sources of uncertainty involved in their analysis is presented in Olson (2001).

2.3.2 Susceptibility analysis

For the susceptibility analysis, Olson and Stark (2003) propose a boundary that establishes the minimum values of q_{c1} (Eq. 2.8) that a soil at a given σ'_{vo} must exhibit to be dilative. This boundary is expressed as:

$$(\sigma'_{vo})_{boundary} = 1.10 \times 10^{-2}(q_{c1})^{4.79} \qquad 2.22$$

where $(\sigma'_{vo})_{boundary}$ and q_{c1} have units of kPa and MPa respectively and $(\sigma'_{vo})_{boundary}$ has an upper bound value of about 350 kPa. Equation 2.22 was proposed by Olson and Stark (2003) as a

contractive-dilative boundary applicable to all types of soils. Olson and Stark (2003) explain that this boundary was first presented (in terms of SPT) by Fear and Robertson (1995). However, Fear and Robertson (1995) presented this boundary as being applicable specifically to Ottawa Sand for K_0 = 0.5, where K_0 is the coefficient of lateral stress at rest. Some of the specific characteristics of Ottawa Sand are (Robertson et al. 1995): D_{50} = 0.35 mm, uniformly graded, FC = 0, sub-rounded particles, and composed primarily of quartz. The simplification made by Olson and Stark (2003) by applying a single contractive-dilative boundary in q_{c1}-σ'_{vo} space to all soiltypes is inconsistent with the CSSM framework presented by Fear and Robertson (1995) in which different soils have different contractive-dilative boundaries. For instance, Figure 2.7 compares Equation 2.22 with the contractive-dilative boundary for Alaska Sand as calculated from Cunning et al. (1995). Alaska Sand is an angular sand from a marine tailings deposit, with D_{50} = 0.12mm and a FC of about 32%. Figure 2.7 shows that for a given σ'_{v0}, the boundary for Alaska Sand requires a significantly lower q_{c1} value than Equation 2.22 for the soil to be considered dilative. This comparison indicates that Eq. 2.22 is too conservative for generalised use on TSFs. Following a different approach, Robertson (2010) also concluded that the susceptibility boundary proposed by Olson and Stark (2003) was only adequate for clean sands. Olson (2009) also questioned the generalised use of Eq. 2.22 and suggested that it be modified to account for the compressibility of different soiltypes.

2.3.3 Triggering analysis

For the triggering analysis, Olson and Stark (2003) proposed a method to compute S_u(yield) from q_{c1} that was based on the back analysis of liquefaction case histories on sloping ground. Although Olson and Stark (2003) presented a database of 33 case histories, only eight of these were used to establish the correlations between S_u(yield) and q_{c1}. The remaining case histories were considered to have a pre-failure geometry that was not representative of failure conditions and therefore their analyses did not allow estimations of S_u(yield). Olson and Stark (2003) normalised the value of S_u(yield) with σ'_{vo} and thus obtained the yield strength ratio (YSR) (Eq. 2.23). Figure 2.8a shows best estimates of YSR vs. mean q_{c1} as reported by Olson and Stark (2003) for the eight case histories. Due to an overlap at (3 MPa; 0.265), only seven points are visible. The q_{c1} values of two of the eight case histories were based on CPT readings. For the other six Olson and Stark (2003) inferred q_{c1} values from SPT results, relative density measurements, or otherwise estimated them. Referring to the data points in Figure 2.8a, Olson and Stark (2003) stated that "*despite the uncertainties, a trend of increasing yield strength ratio with increasing penetration resistance is observed.*" The equation they proposed to describe this trend is:

$$\text{YSR} = \frac{S_u(yield)}{\sigma'_{vo}} = 0.205 + 0.0143(q_{c1}) \pm 0.04 \quad \text{for} \quad q_{c1} \leq 6.5 \text{ MPa} \qquad 2.23$$

where q_{c1} has units of MPa. The term ±0.04 represents the upper and lower boundaries suggested to account for data scatter, however only the mean line was used in the present study. The mean line

and the upper and lower bounds of equation 2.23 are also plotted in Figure 2.8a. A linear regression was made in the present study on the eight data points in Figure 2.8a. The poor fit (R^2 = 0.15) indicates that the conclusion of a direct correlation between YSR and q_{c1} cannot be reached considering only these points. It is also noted that the best fit line is different from the mean line of Equation 2.23.

Olson and Stark (2003) state that Eq. 2.23 should be implemented using the mean penetration resistance value or that alternatively "*the desired level of conservatism can be incorporated by using a penetration resistance larger or smaller than the mean value…*" In the present study the representative q_{c1} (q_{c1}*) of each case history was taken as the 66th percentile of the q_{c1} values found to be contractive in the susceptibility analysis, i.e. q_{c1}* was smaller than 66% of the contractive q_{c1} values. This approach to determining q_{c1}* was recommended by Anderson et al. (2007).

2.3.4 Post-triggering analysis

For the post-triggering analysis, Olson and Stark (2002) proposed a method to compute S_u(LIQ) from q_{c1} that was based on the back analysis of 21 of the 33 liquefaction case histories on sloping ground included in their database. Olson and Stark (2002) normalised the value of S_u(LIQ) with σ'_{vo} and thus obtained the liquefied strength ratio (LSR) (Eq. 2.24). Figure 2.8b shows the plot of best estimate of LSR vs. mean q_{c1} as reported by Olson and Stark (2002) for the 21 case histories. The q_{c1} values of seven of the 21 case histories were based on CPT readings. For the other 14 case histories q_{c1} values were inferred from SPT results, relative density measurements, or otherwise estimated. Referring to the data points in Figure 2.8b Olson and Stark (2002) stated that "*despite the uncertainties for each case, a reasonable trend in the data is apparent...*" The equation they proposed to describe this trend is:

$$\mathrm{LSR} = \frac{S_u(LIQ)}{\sigma'_{vo}} = 0.03 + 0.0143(q_{c1}) \pm 0.03 \quad \text{for} \quad q_{c1} \leq 6.5 \text{ MPa} \qquad 2.24$$

where q_{c1} has units of MPa. The term ±0.03 represents the upper and lower boundary lines suggested to account for data scatter, however only the mean line was used in the present study. The mean line and the upper and lower bounds of equation 2.24 are also plotted in Figure 2.8b. A linear regression was made in the present study on the 21 data points in Figure 2.8b. The poor fit (R^2 = 0.21) indicates that the conclusion of a direct correlation between LSR and q_{c1} cannot be reached considering only these points. It is also noted that the best fit line is different from the mean line of Eq. 2.24. In the present study, Eq. 2.24 was used with the same q_{c1}* value that was used in Eq. 2.23, i.e., the 66th percentile of the contractive q_{c1} values for each case history.

2.3.5 Assessment of seismic effects

The Olson and Stark (2002) and (2003) method allows the consideration of both static and seismic shear stresses. The determination of the static stresses will be addressed below. For the seismic stresses, the method adopts the simplified approach proposed by Seed and Idriss (1971):

$$CSR = \frac{\tau_{ave,seismic}}{\sigma'_{vo}} = 0.65\left(\frac{a_{max}}{g}\right)\left(\frac{\sigma_{vo}}{\sigma'_{vo}}\right)r_d \qquad 2.25$$

where CSR stands for cyclic stress ratio, $\tau_{ave,seismic}$ is the average cyclic shear stress induced by seismic action, a_{max} is the maximum horizontal acceleration at ground surface, g is the acceleration due to gravity, and r_d is a depth reduction factor that accounts for the deformability of the soil deposit.

Estimation of both a_{max} and r_d involves considerable uncertainty. For instance, in none of the five seismic case histories considered in this study, were acceleration readings available at the location of the tailings dam. Thus, attenuation relationships or other means described in Chapter 3 were used to estimate a_{max} at the natural ground level of the site being analysed. Furthermore, the "ground level" at a tailings dam is not the natural ground level, but rather the surface of the tailings beach. Therefore the relevant a_{max} is the maximum horizontal acceleration at the top of the tailings deposit. Given the flexibility of a tailings deposit, the maximum acceleration at the base can be different from the acceleration at the crest. This difference is dependent on the specific ground motion and site and materials characteristics of each case history. However, as a working simplification, a_{max} in the present work was taken as equal to the maximum acceleration estimated for the natural ground level.

The depth reduction factor r_d, has a maximum value of one at ground surface and reduces with depth, with lower values of r_d implying lower seismic stresses on the soil (Eq. 2.25). Olson and Stark (2003) suggest the use of a formula proposed by Youd et al. (2001) to estimate r_d:

$$r_d = 1.0 - 0.00765z \quad for\ z \leq 9.15m \qquad 2.26a$$

$$r_d = 1.174 - 0.0267z \quad for\ 9.15m < z \leq 23m \qquad 2.26b$$

$$r_d = 0.744 - 0.008z \quad for\ 23m < z \leq 30m \qquad 2.26c$$

$$r_d = 0.5 \quad for\ z > 30m \qquad 2.26d$$

where z is depth in meters below ground level. It is important to realise that contrary to what Eq. 2.26 suggests, r_d is known to not only be a function of depth. As pointed out by Cetin and Seed (2004), several authors have conducted studies showing that r_d is nonlinearly dependent on other variables such as ground motion frequency, maximum acceleration, earthquake magnitude and site stiffness. To study the nature of this dependence, Cetin and Seed (2004) performed 2153 site response analyses to study the variation of r_d profiles with different site conditions and ground motion characteristics. Figure 2.9 compares Eq. 2.26 with the mean and ±1 standard deviation of the r_d profiles obtained by Cetin and Seed (2004). The lines corresponding to the ±1 standard deviation

highlight the variability of r_d. It is also apparent that at any depth, Eq. 2.26 yields higher r_d values than the mean profile obtained by Cetin and Seed (2004). That is, Eq. 2.26 has a tendency to yield conservative estimates of r_d. Such conservativism seems warranted for a simplified method as the one proposed by Olson and Stark.

2.3.6 General outline of the method

The equations thus far presented in this sub-section are used according to the following procedure which is mostly an excerpt from Olson and Stark (2003):

1. Conduct a slope stability back analysis of the pre-failure geometry to estimate the static shear stress ($\tau_{driving}$) in the contractive (liquefiable) soils. A trial value of shear strength is assumed for the liquefiable soils, and this value is modified until a factor of safety of unity is achieved. Fully mobilised drained or undrained shear strengths are assigned to the non-liquefiable soils. The slope stability analysis should consider both circular and non-circular potential failure surfaces that cross the liquefiable soils at different locations and depth.
2. Divide the critical failure surface into a number of segments. Ten to fifteen segments are satisfactory.
3. Determine the weighted average value of σ'_{vo} (Eq. 2.27) along the critical failure surface and calculate the average static shear stress ratio, $\tau_{driving}/\sigma'_{vo}(ave)$.

$$\sigma'_{vo}(ave) = \frac{\sum_{i=1}^{n} \sigma'_{v,i} \cdot L_i}{\sum_{i=1}^{n} L_i} \qquad 2.27$$

   where n is the number of segments into which the slip surface has been divided; $\sigma'_{v,i}$ is the σ'_{vo} acting on segment i; and L_i is the length of segment i.
4. Estimate the average seismic shear stress ($\tau_{ave,seismic}$) applied to each segment of the critical failure surface using Eq. 2.25 and divide it by the appropriate magnitude scaling factor (MSF) to account for earthquake magnitude. MSFs are further discussed below.
5. If applicable, estimate other shear stresses (τ_{other}) applied to each segment of the critical failure surface using appropriate analyses.
6. Determine the value of *YSR* as a function of the characteristic q_{c1} (q_{c1}*) from Eq. 2.23.
7. Calculate the values of $S_u(yield)$ and $\tau_{driving}$ for each segment of the critical failure surface by multiplying the values of *YSR* and $\tau_{driving}/\sigma'_{vo}(ave)$ by the σ'_{vo} for the segment.
8. The factor of safety against the triggering of liquefaction in each segment is then estimated as

$$FS_{Triggering} \approx \frac{S_u(yield)}{\tau_{driving} + \tau_{ave,seismic} + \tau_{other}} \qquad 2.28$$

Segments with $FS_{Triggering} \leq 1$ are likely to liquefy and should be assigned S_u(LIQ) for the post-triggering analysis. Segments with $FS_{Triggering} > 1$ should be assigned $S_u(yield)$ value in a post-triggering analysis. If all segments have $FS_{Triggering} > 1$, a post-triggering analysis is unnecessary as this means that liquefaction would not be triggered under undrained conditions.

9. The value of S_u(LIQ) for segments with $FS_{Triggering} \leq 1$ is computed as the product of σ'_{vo} and LSR (Eq. 2.24). New factors of safety are then computed for all segments as:

$$FS_{Flow} = \frac{S_u}{\tau_{static}} \qquad 2.29$$

where S_u may be equal to $S_u(yield)$ or $S_u(LIQ)$ depending on whether or not the segment was predicted to liquefy in step 8, and τ_{static} are all static shear stresses acting along the slip surface. If the average FS_{Flow} is smaller than 1, flow failure is expected to occur; if the average FS_{Flow} is greater than 1.1, flow failure is unlikely; and if the average FS_{Flow} is between 1 and 1.1, some deformation is expected to occur and the analysis must be repeated assigning $S_u(LIQ)$ to all segments with $FS_{Triggering}$ smaller than 1.1.

Step 4 of the procedure described above mentions the use of MSFs. Seed and Idriss (1982) implemented MSFs in their simplified SPT-based procedure of liquefaction assessment because their database of case histories involved only earthquakes with magnitudes near 7.5. So for a given penetration resistance their method would use this database to predict the resistance of the site to seismic loading. However, the resistance had to be increased if the magnitude of the design earthquake was smaller than 7.5, or decreased if the magnitude was greater than 7.5. The MSF is the coefficient through which this adjustment in resistance is made. Youd et al. (2001) reported several ways of estimating the MSF. The Olson and Stark (2002) and (2003) method adopts the lower bound of the range of MSFs recommended by Youd et al. (2001) (Table 2.2).

2.4 The Robertson-based method

2.4.1 General comments

Robertson (2009b) proposed a CPT-based simplified method to assess the potential of triggering of liquefaction due to seismic action. The methodology is intended for use in sand-like soils with level ground and in clay-like soils with level or sloping ground. Additionally, Robertson (2010) proposed procedures applicable to a wide range of soils (sand- and clay-like) to perform preliminary assessments of liquefaction susceptibility and of liquefied shear strength (S_u(LIQ)). A strict implementation of the methods proposed by Robertson (2009b) and (2010) requires CPTs with readings of q_c and f_s (Robertson (2010) refers to these as “Class A” CPT records). Since the CPT data of some of the case histories used in the present study do not include f_s readings, some minor modifications had to be made to the methods to allow their implementation in all case histories.

Modifications were also introduced to the triggering analysis of Robertson (2009b) to make it applicable to sand-like soils with sloping ground. The modifications will be described in detail in this section. Given that the method has not been implemented exactly as prescribed by Robertson (2009b) and (2010), it will be referred to herein as the Robertson-based method.

Both the susceptibility analysis proposed by Robertson (2010) and the triggering analysis proposed by Robertson (2009b) will be reviewed in this section and will be implemented on the case histories described in Chapter 3. Regarding the post-triggering analysis, Robertson (2010) pointed out that the calculation of S_u(LIQ) values from the back-analysis of flow failure case histories is "*often approximate at best*". Under this consideration, it was deemed inadequate to implement the post-triggering analysis of Robertson (2010) on the case history database compiled for this research, as the inherent uncertainty of the method would have been compounded by the absence of Class A CPT records in most of the TSF case histories analysed in the present study (Chapter 3). This situation would have made it difficult to arrive at conclusive results when assessing the suitability of Robertson's post-triggering analysis to TSFs.

2.4.2 Susceptibility analysis

Robertson (2010) suggests a zone in the Q_{tn} vs F_r chart that can be interpreted as an approximate boundary between contractive and dilative soils (Figure 2.10a). This boundary zone is meant to represent soils with a state parameter (ψ) smaller than -0.05 (ψ is defined in section 2.5) and normally consolidated clays with a sensitivity of 1. Robertson (2010) noted that the upper bound of this zone could be approximated by a contour of $Q_{tn,cs}$ = 70, thus he proposed $Q_{tn,cs} \leq 70$ as a conservative screening criteria to detect soils susceptible to flow liquefaction (Figure 2.10b).

In order to validate the proposed susceptibility criteria, Robertson (2010) used the case history database of Olson and Stark (2002) and (2003) plus three additional liquefaction case histories. Although his resulting database had a total of 34 case histories, Robertson (2010) used mostly case histories with Class A CPT records, which he regarded as the most reliable, to verify the susceptibility criteria. The results of this verification (Figure 2.10b) show that the CPT data of all the Class A case histories plots underneath the $Q_{tn,cs}$ = 70 contour. The dots in Figure 2.10b represent the mean values of the CPT data corresponding to the zone considered to have liquefied, while the elliptical shapes represent ±1 standard deviation of the data.

Despite the agreement between the case histories and the $Q_{tn,cs} \leq 70$ criterion it should be noted that this criterion is partly based on the idea that $Q_{tn,cs}$ can be taken as a proxy for ψ. While the data of Robertson (2010) suggests that in some instances this might be true, it is important to realise that there are fundamental differences between the methods proposed by Jefferies and Been (2006) to infer ψ from the CPTu (section 2.5.2) and the methods proposed by Robertson (2010) to calculate $Q_{tn,cs}$. A key difference is that the inference of ψ is dependent on the SSL parameters λ and M. The database presented in Chapter 6 (see Table 6.1) suggests that for non-plastic soils both of these parameters are largely independent of fines content. On the other hand, $Q_{tn,cs}$ is dependent on I_c (Eqs. 2.13 and 2.14) which is correlated to the fines content (Figure 2.5). The fact that $Q_{tn,cs}$ depends

on FC, while ψ does not, highlights the fact that $Q_{tn,cs}$ cannot be a suitable proxy for ψ under all circumstances.

Eqs. 2.13 and 2.14 indicate that I_c is a required input to calculate $Q_{tn,cs}$. In turn I_c requires f_s as one of its inputs. However, f_s readings were unavailable for six of the eight case histories described in Chapter 3. Thus two alternative means of calculating I_c were also used in this study. The first alternative approach was based on the correlation given by Robertson and Wride (1998) between I_c, FC, and plasticity index (PI) (Figure 2.5). A second alternative approach was used for one case history (Hokkaido Dam) for which no f_s, FC or PI were found in the literature. In this case the estimation of I_c was based on the qualitative soil description provided by the references and the corresponding I_c range suggested by Robertson and Wride (1998) and reproduced here in Table 2.1. Due to the greater uncertainty of this second alternative approach, both the upper and lower bound values of the I_c range were used to estimate $Q_{tn,cs}$. Both of these alternative approaches were also used by Robertson (2010) to analyse case histories that did not have Class A CPT data.

2.4.3 Assessment of the cyclic resistance ratio (CRR)

In order to assess the shear stresses due to seismic action, Robertson (2009b) prescribes the use of Eq. 2.25 to compute CSR, with r_d estimated as per Eq. 2.26. Uncertainties involved in the estimations of a_{max} and r_d in TSFs were already mentioned in Section 2.3. Robertson (2009b) adopted the maximum value of CSR that a soil can withstand without liquefaction being triggered as the parameter to quantify a soil's resistance to seismic action. This maximum value of CSR is termed the cyclic resistance ratio (CRR). The method to calculate CRR depends on whether the soil is classified as sand- or clay-like. This classification is based on I_c which is calculated with Eq. 2.11 or using one of the alternative approaches described in Section 2.4.2. Once I_c has been calculated, the soil is classified into sand-like ($I_c \leq 2.6$) or clay-like ($I_c > 2.6$).

2.4.4 Triggering analysis of sand-like soils ($I_c \leq 2.6$)

Estimation of CRR in sand-like soils follows the Berkeley school and is based on a chart originally proposed by Robertson and Wride (1998). The chart is a plot (Figure 2.11) of data points representing liquefaction or non-liquefaction case histories on level or gently sloping ground subjected to seismic action. The horizontal coordinate is the value of $Q_{tn,cs}$ corresponding to the critical layer of each case history, and the vertical axis is the earthquake-induced CSR. A curve is traced as a boundary between the liquefaction and non-liquefaction case histories. The resulting curve correlates $Q_{tn,cs}$ with $CRR_{7.5}$. The sub-index 7.5 is added because the case histories plotted in Figure 2.11 either involved earthquakes of magnitude 7.5 or had their seismic stresses adjusted through an MSF to make them comparable to the shear stresses that would have been induced by an earthquake of magnitude 7.5. That is, $CRR_{7.5}$ represents the maximum CSR value that a soil can resist when subjected to an earthquake of magnitude 7.5. The curve that correlates $CRR_{7.5}$ to $Q_{tn,cs}$

(Figure 2.11) can be represented with the following equations proposed by Robertson and Wride (1998):

$$if\ Q_{tn,cs} < 50, \quad CRR_{7.5} = 0.833\left[\frac{Q_{tn,cs}}{1000}\right]^3 + 0.05 \qquad 2.30a$$

$$if\ 50 \leq Q_{tn,cs} \leq 160, \quad CRR_{7.5} = 93\left[\frac{Q_{tn,cs}}{1000}\right]^3 + 0.08 \qquad 2.30b$$

Since $Q_{tn,cs}$ is directly proportional to I_c, Eq. 2.30 implies that there is a direct correlation between a soil's resistance to liquefaction and I_c. In turn, I_c is directly correlated to FC and plasticity (Figure 2.5). Given that tailings are generally non-plastic, the application of Eq. 2.30 in TSFs will yield a value of $CRR_{7.5}$ which will be directly correlated to the FC of the tailings. TSFs typically have significant amounts of fines, thus Eq. 2.30 will lead to higher estimations of $CRR_{7.5}$. Such higher (unconservative) estimations of $CRR_{7.5}$ will be the result of using Eq. 2.14 which is approximate and for which there is no supporting experimental data. Furthermore, the analysis presented in Chapter 6 indicates that for non-plastic soils it is the packing efficiency and not FC per se, that has the greatest influence on mechanical behaviour. This brings into question the validity of assigning a greater liquefaction resistance to a non-plastic soil based on its FC alone.

Robertson and Wride (1998) explained that the rationale for the use of K_c (Eqs. 2.13 and 2.14) was to take into account that for a given $CRR_{7.5}$, the "*CPT penetration resistance in silty sands is smaller because of the greater compressibility and decreased permeability of silty sands*" as compared to clean sands. Nonetheless, it will be shown in later chapters that CPTu penetration can be virtually drained (i.e. $B_q \approx 0$) even in tailings deposits with significant amounts of fines (e.g. Figure 5.13) and that for non-plastic soils, the experimental evidence does not support any correlation between FC and compressibility indicators such as λ (e.g. Olson 2001 and Figure 6.41 of this thesis). Furthermore, Reid (2014), referring specifically to tailings reported that "*fines content in itself does not provide a useful correlation to compressibility*". It is relevant to acknowledge that in Robertson (2010) the emphasis shifts from FC to soil plasticity, with plastic soils being presented as less prone to strength-loss than non-plastic soils. This change in logic seems a step in the right direction, as it is known that plasticity is directly correlated to λ (Schofield and Wroth 1968). Nonetheless, the fact remains that Eqs. 2.14 and 2.30 imply that a higher FC, even for non-plastic soils, results in a higher resistance to liquefaction.

Once $CRR_{7.5}$ has been determined from Eq. 2.30 it must be adjusted by an MSF. This allows comparisons of $CRR_{7.5}$ with the CSR calculated with Eq. 2.25 which may correspond to an earthquake with a magnitude other than 7.5. For sand-like soils Robertson (2009b) adopts the MSFs suggested by Youd et al. (2001) (Table 2.2). Once the MSF has been determined, CRR of sand-like soils is computed as:

$$CRR = CRR_{7.5} \cdot MSF \qquad 2.31$$

This value of CRR must now be reduced to account for the horizontal static shear stresses (τ_h) induced by the slope of the outer wall of the TSFs. Robertson (2009b) does not suggest any particular procedure of accounting for sloping ground in sand-like soils, only for clay-like soils. Therefore in this study, the procedure suggested by Robertson (2009b) to account for static stresses in clay-like soils was also used for sand-like soils. This approach was employed here because there is no widely accepted method to account for the effect of sloping ground on the liquefaction potential of sand-like soils (Youd et al. 2001).

Accounting for the effect of sloping ground requires the estimation of τ_h induced by the slope. Robertson (2009b) does not prescribe any particular method to estimate τ_h. In this study, τ_h profiles were calculated with drained in situ stress analyses of finite element models the details of which are presented in Chapter 3. The profiles of τ_h were used to calculate a static shear stress correction factor (K_α). Seed (1981) introduced the K_α factor to account for the reduction of a soil's resistance to cyclic loading due to initial static shear stresses. Robertson (2009b) suggests the use of the expression for K_α proposed by Boulanger and Idriss (2007):

$$K_\alpha = 1.344 - \frac{0.344}{\left(1 - \frac{\tau_s}{S_u(yield)}\right)^{0.638}} \quad \text{for } 0 \le \tau_s/S_u(yield) \le 0.88 \qquad 2.32a$$

$$K_\alpha = 0 \quad \text{for } \tau_s/S_u(yield) > 0.88 \qquad 2.32b$$

where τ_s is the initial static shear stress acting on the plane of interest (horizontal in this case). Eq. 2.32 was developed with experimental results from Drammen Clay (PI = 27), however Boulanger and Idriss (2007) suggested its generalised use in soils with PI ≥ 7 based on the observation that it was reasonably representative of their overall data set. Robertson (2009b) noted that for clay-like soils S_u(yield) can be expressed as:

$$S_u(yield) = \frac{q_t - \sigma_{vo}}{N_{kt}} \qquad 2.33$$

where N_{kt} is an empirical cone factor with an average value of 15 recommended by Robertson (2009b). Replacing Eq. 2.33 in Eq. 2.32 yields the expression for K_α used in this study:

$$K_\alpha = 1.344 - \frac{0.344}{\left(1 - \frac{15 \cdot \tau_h}{q_t - \sigma_{vo}}\right)^{0.638}} \quad \text{for } 0 \le \tau_s/S_u \le 0.88 \qquad 2.34a$$

$$K_\alpha = 0 \quad \text{for } \tau_s/S_u > 0.88 \qquad 2.34b$$

K_α is then used to calculate CRR_α which is the value of CRR reduced to account for τ_h and is computed as:

$$CRR_\alpha = CRR \cdot K_\alpha \quad (2.35)$$

The factor of safety against the triggering of liquefaction was then determined as:

$$FS = \frac{CRR_\alpha}{CSR} \quad (2.36)$$

where CRR_α = CRR (i.e. K_α = 1) for cases that only involve level or gently sloping ground (i.e. $\tau_h \approx 0$).

It is noted that although Eq. 2.33 is intended for use with clay-like soils, its use on tailings is not without precedent. For example Fourie et al. (2001) applied this equation to CPT results made on the Merriespruit TSF and obtained S_u(yield) values that were consistent with those from vane shear tests. It is also convenient to explore the suitability of adopting N_{kt} = 15 in Eq. 2.33 when applied to TSFs. Blight (2010) analysed N_{kt} values obtained by Thomas (1965), and Marsland and Quarterman (1982) for soils with different plasticity. Plotting the N_{kt} values against PI Blight (2010) found that, despite considerable scatter, the data roughly extrapolates to N_{kt} = 15 for non-plastic soils, e.g. tailings. Due to the uncertainties in the estimation of N_{kt} Blight (2010) does not recommend the use of Eq. 2.33. However his results show that in the absence of additional tests, N_{kt} = 15 is a sensible alternative.

2.4.5 Triggering analysis of clay-like soils (I_c > 2.6)

In order to calculate the $CRR_{7.5}$ of clay-like soils, Robertson (2009b) uses the expression suggested by Boulanger and Idriss (2007):

$$CRR_{7.5} = 0.8\frac{S_u(yield)}{\sigma'_{vo}} \quad (2.37)$$

However, Boulanger and Idriss (2007) also suggest that for tailing slimes, Eq. 2.37 should be reduced by approximately 20%, thus yielding the expression:

$$CRR_{7.5} = 0.64\frac{S_u(yield)}{\sigma'_{vo}} \quad (2.38)$$

Robertson (2009b) substituted for S_u(yield) from Eq. 2.33 into Eq. 2.37 to arrive at a CPT-based expression for $CRR_{7.5}$. The same has been done here, but Eq. 2.38 was used instead of Eq. 2.37. The resulting expression for $CRR_{7.5}$ for clay-like soils that was used in the present study is:

$$CRR_{7.5} = 0.043 \cdot Q \qquad 2.39$$

Similar to sand-like soils, $CRR_{7.5}$ must be adjusted by MSF to allow comparisons to the CSR calculated with Eq. 2.25 which does not necessarily correspond to an M = 7.5 earthquake. Such adjustment was done with Eq. 2.31, but for clay-like soils Robertson (2009b) recommends calculating MSF with the following expression proposed by Boulanger and Idriss (2007):

$$MSF = 1.12 \cdot exp\left(\frac{-M_w}{4}\right) + 0.828 \qquad 2.40$$

The initial static horizontal shear stresses induced by the outer walls are accounted for as already described for sand-like soils, i.e. using Eqs. 2.34 and 2.35. The factor of safety against the triggering of liquefaction is then determined by Eq. 2.36.

2.5 The Jefferies and Been method

2.5.1 General comments

Jefferies and Been (2006) describe a CPTu interpretation method anchored in critical state soil mechanics (CSSM). The most important parameter within their method is the state parameter (ψ), which was defined by Been and Jefferies (1985) as the void ratio difference between the initial sand state and the steady state line (Figure 2.1):

$$\psi = e - e_{ss} \qquad 2.41$$

where e is the current void ratio of the soil and e_{ss} is the void ratio of the steady state at the same mean effective stress (p') (Figure 2.1). Although Been and Jefferies (1985) initially proposed ψ for use in sands, Jefferies and Been (2006) have shown that the behaviour of non-plastic silts (e.g. tailings) is also strongly correlated to ψ.

Been and Jefferies (1985) noted that a key element in the definition of ψ is that it is measured with respect to the SSL. Since the steady state is defined by the stresses and void ratio that a soil attains after being significantly sheared, it follows that ψ is a direct measure of how much a soil will have to dilate or contract to reach the steady state. Noting that Rowe (1962) found that the mechanical response of a soil is determined by the volume changes it undergoes when sheared, and not by the stress level or density alone, Been and Jefferies (1985) stated that there is a fundamental basis to correlate ψ to soil behaviour. They also presented experimental data supporting their hypothesis that ψ could be correlated to several behavioural aspects of soils. Considering limitations of ψ, Been and Jefferies (1985) pointed out that given that ψ does not account for fabric, it is not possible to correlate ψ to those aspects of soil behaviour that are affected by fabric. However, they showed that ψ could be used to normalise large strain behaviours (e.g. liquefaction) where the

effect of initial fabric is small. For instance, Figure 2.12 shows six stress paths corresponding to consolidated undrained triaxial tests made on two different soiltypes. It is observed that specimens with an initial negative ψ (test numbers 103, 108, and 113) exhibit strain hardening at large deformations, whereas specimens with an initial positive ψ (37, 45, and 112) exhibit strain softening at large deformations. Jefferies and Been (2006) explored the question of what is the limiting value of ψ below which a soil will not lose strength when sheared. They noted that the answer depended on the specific characteristics of the problem (e.g. soil properties and stress path), but that in general ψ <≈ -0.08 was indicative of a soil that dilated continuously under monotonic loading regardless of the stress path.

2.5.2 Determining the state parameter (ψ) in situ

Since the potential of a soil mass liquefying (strain softening) can be correlated to ψ, the methodology of liquefaction assessment proposed by Jefferies and Been (2006) relies on the inference of ψ in situ from CPTu readings. The method to infer ψ from CPTu has evolved over the years. The original method, described in Been et al. (1986) and (1987), was based on the analysis of experimental data from CPT calibration chambers from which they concluded that for sands in general there exists a correlation between ψ and Q_p which can be represented as:

$$Q_p = k \cdot exp(-m \cdot \psi) \qquad 2.42$$

where the values of k and m vary from one sand to another. Been et al. (1987) noted that it was reasonable to expect Q_p to be a function not only of the initial state of the sand (characterised by ψ) but also to the sand's response to the additional stresses imposed by the CPT, i.e. the sand's compressibility. They further stated that this compressibility can be captured by λ and on that basis proposed the following equations for k and m (Figure 2.13):

$$k = 8 + \frac{0.55}{\lambda - 0.01} \qquad 2.43$$

$$m = 8.1 - 2.3 \log_{10} \lambda \qquad 2.44$$

Sladen (1989) showed that the values of k and m varied systematically with p' for the same soiltype. This was contrary to the approach of Been et al. (1987) in which k and m were treated as material properties. To account for this stress level bias, the methodology for calculating k and m was updated by Shuttle and Jefferies (1998). The updated equations to calculate k and m (not reproduced here) were no longer functions of λ only as was initially suggested by Been et al. (1987) (Figure 2.13), but were also functions of additional parameters such as the small strain shear modulus (G), the mean effective stress (p'), the critical friction ratio (M), and the hardening modulus (H).

The methodology developed by Shuttle and Jefferies (1998) is applicable to any soil in which cone penetration is drained (i.e. $B_q \approx 0$). In order to expand the applicability of Eq. 2.42 to undrained penetration, the normalised tip resistance Q_p has to be replaced by $Q_p/(1-B_q)$ and the inversion coefficients k and m must be replaced by their effective stress equivalents k' and m' (Jefferies and Been 2006):

$$Q_p/\left(1 - B_q\right) = k' \cdot exp(-m' \cdot \psi) \quad 2.45$$

where k' and m' are calculated according to the following approximate correlations:

$$k' = M \cdot (3 + 0.85/\lambda) \quad 2.46$$

$$m' = 11.9 - 13.3 \cdot \lambda \quad 2.47$$

It is clear that regardless of the method used to infer ψ from CPT results, it is necessary to determine the SSL of the soil being probed. Namely, the slope λ is an input of the methods proposed by Been et al. (1987), Shuttle and Jefferies (1998), and Jefferies and Been (2006); and the friction ratio M is an input of the methods proposed by the two most recent of these three references. Additionally, the experimental validation of the inferred values of ψ, e.g. by comparing the inferred ψ with the void ratio of an undisturbed sample, also requires knowledge of Γ_1. Adopting Eq. 2.1 to represent the SSL in e-p' space, this experimental validation would imply that the following equation must be met:

$$\psi = e_{is} - \Gamma_1 + \lambda \cdot \log_{10}(p'_{is}) \quad 2.48$$

where e_{is} is the in situ void ratio as determined from an undisturbed specimen, and p'_{is} is the in situ mean effective stress. Direct and reliable measurement of e_{is} generally involves ground freezing either before or after sampling (Wride et al. 2000). This greatly limits the number of situations in which Eq. 2.48 can be used, as ground freezing is not routinely done in geotechnical practice. However, there are some situations in which Eq. 2.48 might be useful. For example, Jefferies and Been (2006) report that despite the costs involved, ground freezing and coring is a practice that may be contemplated on important projects. Additionally, Shuttle and Cunning (2007) provide an example of how Eq. 2.48 may be useful even when high quality undisturbed samples are not available. They made comparisons between ψ values inferred from CPTu, and ψ values estimated from the SSL and e_{is} as inferred from disturbed saturated samples. The disturbance of the samples introduced uncertainties in e_{is} and therefore in ψ. However, despite the uncertainties, this comparison allowed Shuttle and Cunning (2007) to make an approximate check on the ψ values estimated from CPTu. It is worth noting that e_{is} in itself is not very useful to predict soil behaviour because, contrary to ψ, it does not consider the effect of stress levels or the location of the SSL.

However, as shown in Eq. 2.48, e_{is} and the SSL can be used together to validate the ψ values inferred from CPTu using the Jefferies and Been (2006) method.

It is known that TSFs typically contain a wide variety of soiltypes and it is not realistic to assume that all these soiltypes can be characterized by a single SSL (Fourie and Papageorgiou 2001). Therefore the SSL of the different soiltypes in the TSF must somehow be determined. Jefferies and Been (2006) suggest several approaches to do this. At a "screening-level" analysis, λ can be estimated as a function of CPT measurements and M can be linked to λ "*as high values of M do not normally occur in clays, and low values do not normally occur in sands*" (Jefferies and Been 2006).

Jefferies and Been (2006) present two ways in which λ can be correlated to CPT data. The first method was proposed by Plewes et al. (1992) and correlates λ with F_r (Figure 2.14a). However, Jefferies and Been (2006) raised two objections to this approach. First, the data that supports the correlation is clustered in two distinct groups and thus there is significant reliance on interpolation and extrapolation. Second, constant F_r does not indicate constant soiltype in CPT classification charts (e.g. Figure 2.6a) and on this basis the attempt to correlate F_r with a soiltype parameter such as λ is questionable. The first of these objections was addressed by an update to the Plewes method presented by Reid (2012) (Figure 2.14b). However Reid (2012) highlighted the high scatter in the data and the approximate nature of the method. The second objection was addressed by Been and Jefferies (1992) by correlating λ to I_c which by definition is meant to be constant for a given soiltype. The equation for the proposed λ vs I_c correlation is:

$$1/\lambda = 34 - 10 \cdot I_c \qquad 2.49$$

where I_c is defined by Eq. 2.20. The data supporting Eq. 2.49 is shown in Figure 2.15. As noted by Jefferies and Been (2006), the data points continue to be clustered in two portions of the graph and there is heavy reliance on interpolation. Additionally, whereas I_c is dependent on particle size, it will be shown in Chapter 6 that there is no systematic correlation between grain size (as characterised by FC) and λ in non-plastic soils. Reid (2014) evaluated the performance of the methods proposed by Plewes et al. (1992) (Figure 2.14a) and Been and Jefferies (1992) (Eq. 2.49) to estimate λ. He noted that I_c provided qualitatively better fits to λ than F_r, but that important difficulties are evident when attempting to use I_c to infer λ of relatively incompressible soils (λ < ≈0.1). Perhaps more importantly, the results from Reid (2014) highlight the significant scatter involved in both methods.

Jefferies and Been (2006) state that for a more precise inference of ψ, the correlations of λ with CPT results should be calibrated using site specific data. This implies that the SSLs of two or three soiltypes within the soil deposit must be experimentally determined and the resulting λ and M values correlated to CPT parameters. Characteristics regarding the grain size distribution (GSD) curves of tailings samples that may assist in correlating λ to CPT readings, complemented with SSLs measured in the laboratory, will be presented in Chapter 8.

2.6 Comparisons between methodologies

2.6.1 Stages of liquefaction analyses considered in this study

Table 2.3 summarises the different stages of liquefaction analysis that are addressed by the methodologies reviewed herein. The table also shows which of these analyses are used in this study. It should be noted that the susceptibility analysis of Jefferies and Been (2006) will only be partially considered herein. That is because the present study will assess the effect of the variability of λ on the uncertainty of the estimated values of ψ (Chapter 8). However, no attempt will be made to assess the accuracy of these estimations. Additional field data, namely in situ void ratio measurements, would be needed for this purpose.

2.6.2 Input requirements of the different methodologies

Table 2.6 lists the inputs required to implement the methodologies. The listed inputs are limited to those required by the stages of analyses implemented in this study. For instance, the listed inputs under the Olson and Stark column correspond to the inputs required to implement the susceptibility, triggering, and post-triggering analyses of Olson and Stark (2002) and (2003) as all three of these analyses were implemented in this study. Whereas the inputs listed under the Jefferies and Been column correspond to the inputs required to implement the susceptibility analysis of Jefferies and Been (2006) as only the susceptibility analysis of this reference was investigated in this study.

It is clear from the table that the input requirements for the Jefferies and Been (2006) methodology are considerably greater than those of the other two methodologies. The time and cost implications that these additional data requirements imply is now briefly discussed:

Dynamic pore water pressure (u_2): This information is routinely measured in CPT testing (CPTu) so it is likely to be available at no extra cost or time.

Horizontal stresses: Jefferies and Been (2006) suggest that horizontal stresses be measured either with a self-bored pressuremeter (SBP) or with a CPT fitted with an additional channel to measure radial stress. Both of these tests would normally imply an additional cost. However, the CPT option has the advantage that it does not require additional time as the radial stresses would be measured simultaneously with q_c, f_s and u_2. This convenience is somewhat offset though by the need to convert the measured radial stress to the in situ horizontal stress that existed prior to the soil being disturbed by the CPT probe.

SSL parameters M and λ: Experimental determination of these parameters requires a series of triaxial tests on two or three soiltypes representative of the deposit being studied. Clearly this implies additional costs and time.

Additional soil parameters G & H: Jefferies and Been (2006) indicate two possible methods to measure the elastic shear modulus (G) in situ. One is to use pressuremeter testing to measure local values. This implies additional costs and time. The other is to use geophysical tests which allow the calculation of average G values over a given distance, typically 1 m to 5 m. If the geophysical test is done with a CPT that has a geophone fitted on it, time and costs will typically be lower than those associated with pressuremeter testing. As for the hardening modulus (H) Jefferies and Been (2006) do not specify any particular method to measure this parameter in situ. Presumably it can be determined by fitting the results of a constitutive model that includes H as a model variable, to the triaxial test results of a soil specimen whose fabric resembles the in situ fabric.

Jefferies and Been (2006) developed their method around concepts of CSSM and analyses of CPT calibration chamber data, without any reliance on case histories. This theoretical soundness does have the disadvantage that the data inputs required for the thorough implementation of their methodology have higher cost and time implications than the inputs required to implement the methodologies of Olson and Stark (2002) and (2003) and Robertson (2009b) and (2010). Of course, the true merit of any method lies not in the simplicity of its data inputs, but in the reliability with which it can predict mechanical behaviour over a wide variety of scenarios.

2.7 Conclusions

This chapter laid out the conceptual framework that will be used throughout the thesis. A literature review was conducted to explain the most salient aspects of the mechanics of soil liquefaction, and the CPT. The review identified variations in the way different authors normalise CPT readings, and also in how these normalised parameters are used to identify soiltypes (e.g. compare Eq. 2.9 to Eq. 2.17 or Eq. 2.11 to Eq. 2.20).

The liquefaction assessment methods that will be used in the current study were also reviewed and critiqued. With regards to the Olson and Stark method, it was noted that it proposes a unique contractive-dilative boundary (Eq. 2.22) in q_{c1}-σ'_{v0} space and that this is inconsistent with CSSM which indicates that this boundary is soil-specific. It was also noted that the triggering and post-triggering analyses are based on correlations between q_{c1} and undrained shear strength (Eqs. 2.23 and 2.24) for which the supporting data exhibits a significant amount of scatter (Figure 2.8). Furthermore, it was noted that for both correlations no more than one third of the data points corresponded to actual CPT readings. For the remaining data points, q_{c1} was inferred from SPT results, relative density measurements, or otherwise estimated. These inferences introduce uncertainty to the method and probably contribute the large scatter of the data.

The review of the methods proposed by Robertson (2009b) and Robertson (2010) showed that the reliance of the method on I_c (Eq. 2.11) to make estimations of ψ and, more generally, to make tip resistance corrections (Eqs. 2.13 and 2.14) may be unjustified and unconservative. This is because I_c is directly correlated to FC in both plastic and non-plastic soils (Figure 2.5), however, experimental

data from this thesis and from other authors shows that the mechanical behaviour of non-plastic soils such as tailings is not fundamentally correlated to FC (e.g. Figure 6.41). Robertson (2010) suggested plasticity, as opposed to FC, as the parameter which may be correlated to a soil's susceptibility to liquefaction. However, he did not suggest a modification to the direct correlation between I_c and FC for non-plastic soils. The absence of supporting experimental data for Eqs. 2.10 and 2.14 was also noted. Finally, modifications made to the methods proposed by Robertson to make them applicable to the case histories reviewed in this study were described. Due to these modifications, the method will be referred to in the remainder of the thesis as the "Robertson-based" method.

In reviewing the liquefaction assessment method proposed by Jefferies and Been (2006) it was noted that the direct correlation between λ and I_c (and therefore between λ and FC) that Eq. 2.49 suggests, is not supported by the database for non-plastic soils that will be presented in Chapter 6. Additionally, upon comparing the data inputs required for the different methods (Table 2.4), it was clear that the greater theoretical soundness of the Jefferies and Been (2006) method implies that its data requirements are greater than those of the other two methods considered. Nonetheless, it must be kept in mind that the merit of any given method does not lie only in the simplicity of its data requirements but also, and more importantly, in the accuracy with which it can explain soil behaviour.

The following chapter will present a description of the eight TSF case histories that will be used to study the liquefaction assessment methods. The chapter will present both known facts and the idealisations adopted in this study.

2.8 Tables and figures

Table 2.1 I_c ranges for different SBTs. Data from: Robertson and Wride (1998) and Jefferies and Been (2006).

Soil behaviour type	I_c range (Eq. 2.11)	I_c range (Eq. 2.20)	Zone (Figure 2.6)
Gravelly sand to dense sand	$I_c < 1.31$	$I_c < 1.25$	7
Sands: clean sand to silty sand	$1.31 < I_c < 2.05$	$1.25 < I_c < 1.80$	6
Sand mixtures: silty sand to sandy silt	$2.05 < I_c < 2.60$	$1.80 < I_c < 2.40$	5
Silt mixtures: clayey silt to silty clay	$2.60 < I_c < 2.95$	$2.40 < I_c < 2.76$	4
Clays: silty clay to clay	$2.95 < I_c < 3.60$	$2.76 < I_c < 3.22$	3
Organic soils: peats	$I_c > 3.60$	$I_c > 3.22$	2

Table 2.2 Magnitude scaling factors (Youd et al. 2001).

Earthquake Magnitude, M_w	Magnitude scaling factor	
	Lower bound	Upper bound
5.5	2.20	2.8
6.0	1.76	2.1
6.5	1.44	1.6
7.0	1.19	1.25
7.5	1.00	
8.0	0.84	
8.5	0.72	

Table 2.3 References that address the different stages of liquefaction considered in this study

Authors	Stage of liquefaction analysis:		
	Susceptibility	Triggering	Post-triggering
Olson & Stark	**Olson and Stark (2003)**	**Olson and Stark (2003)**	**Olson and Stark (2002)**
Robertson	**Robertson (2010)**	**Robertson (2009b)**	Robertson (2010)
Jefferies & Been	**Jefferies and Been (2006)**	Jefferies and Been (2006)	Jefferies and Been (2006)

Note: Bold font indicates that the analysis has been used in this study.

Table 2.4 Data requirements to implement the analyses considered in this study.

Olson & Stark	Robertson-based	Jefferies & Been
1. Tip resistance (q_c or q_t) for Eq. 2.8 **2.** Total unit weights and u_0 to compute σ_{vo} and σ'_{vo} for Eqs. 2.8 and 2.25. **3.** External analysis to compute $\tau_{driving}$ for Eq. 2.28 and τ_{static} for Eq. 2.29. **4.** Seismic loading characteristics for Eq. 2.25. **Comments:** q_c normalised with respect to reference stress level (p_a). Based on a case-history database.	**1.** Tip resistance (q_c or q_t) for Eqs. 2.9 and 2.11. **2.** Sleeve friction (f_s) for Eqs. 2.11 and 2.12. **3.** Total unit weights and u_0 to compute σ_{vo} and σ'_{vo} for Eqs. 2.9, 2.10, 2.11, 2.12 and 2.25. **4.** External analysis to compute τ_h for Eq. 2.34. **5.** Seismic loading characteristics for Eq. 2.25. **Comments:** q_c normalised with respect to reference stress level (p_a). Analysis of sand-like soils is based on a case-history database. Analysis of clay-like soils is based on laboratory results.	**1.** Tip resistance (q_c or q_t) for Eqs. 2.15, 2.17, 2.20, 2.42, and 2.45. **2.** Sleeve friction (f_s) for Eqs. 2.12 and 2.20. **3.** Dynamic pore water pressure for Eqs. 2.16 and 2.20. **4.** Total unit weights and u_0 to compute σ_{vo} and σ'_{vo} for Eqs. 2.12, 2.15, 2.16, and 2.17. **5.** Horizontal stresses to compute p_0 and p'_0 for Eq. 2.17. **6.** M and λ are required when inferring ψ using Eqs. 2.46 and 2.47. **7.** Additional soil parameters G & H are required when inferring ψ using the approach proposed by Shuttle and Jefferies (1998). **Comments:** q_c normalised with respect to mean effective stress (p'_0). Anchored on CSSM.

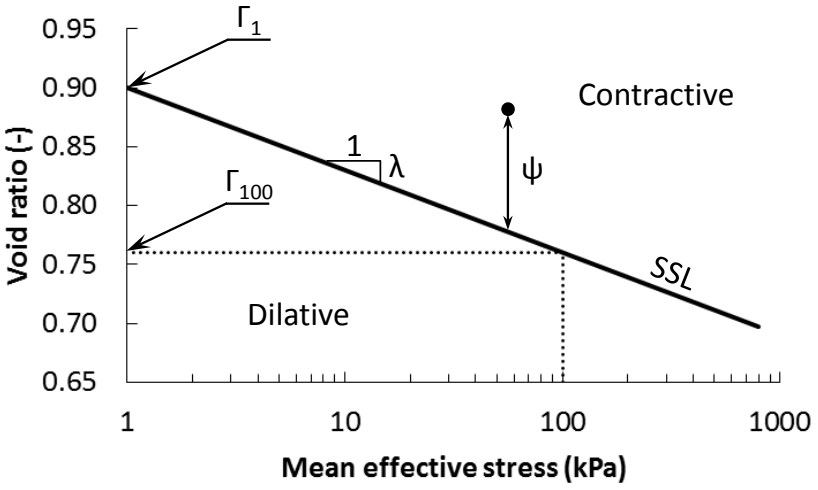


Figure 2.1 Idealisation of the critical or steady state line.

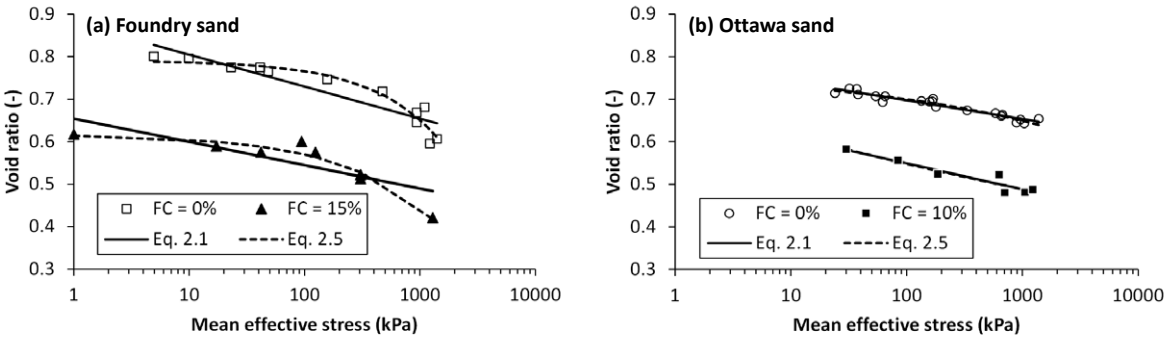


Figure 2.2 SSLs of foundry sand and Ottawa Sand. Data from: (a) Thevanayagam et al. (2002) and (b) Murthy et al. (2007).

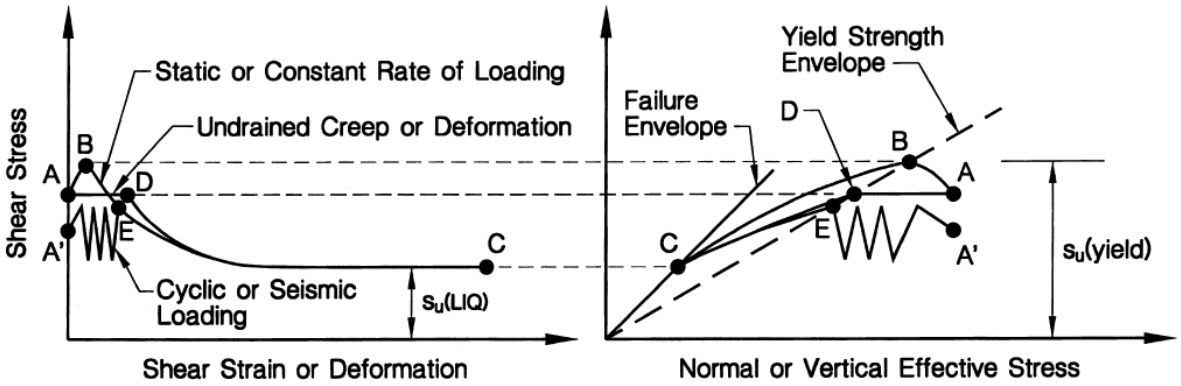


Figure 2.3 Liquefaction mechanisms in saturated, undrained, contractive soil (Olson and Stark 2003).

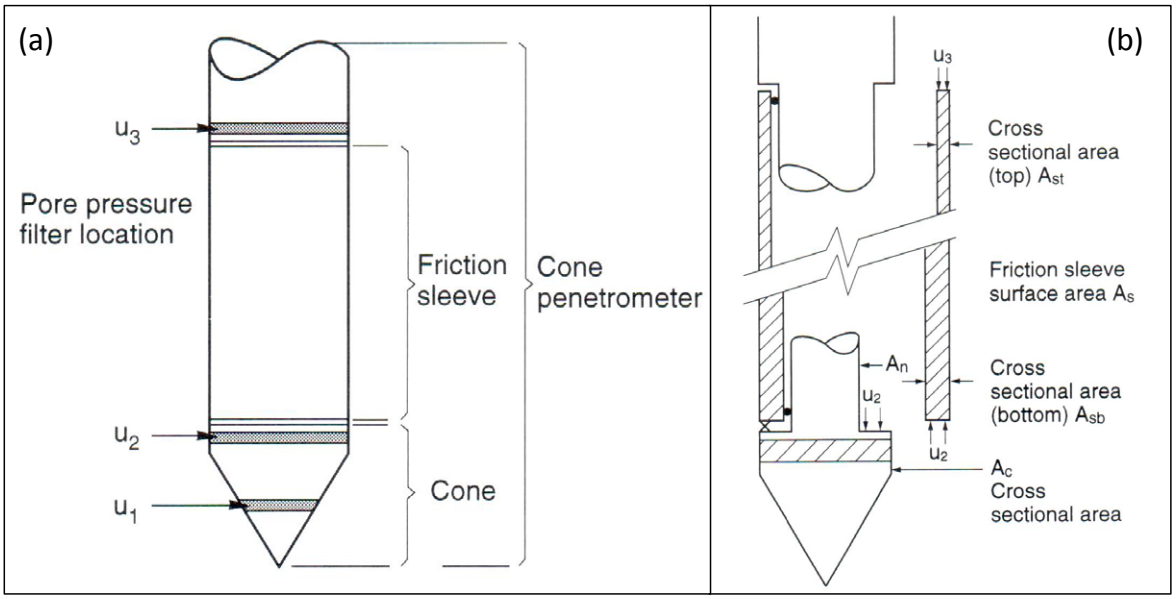


Figure 2.4 Typical geometry of a CPTu probe (Lunne et al. 1997).

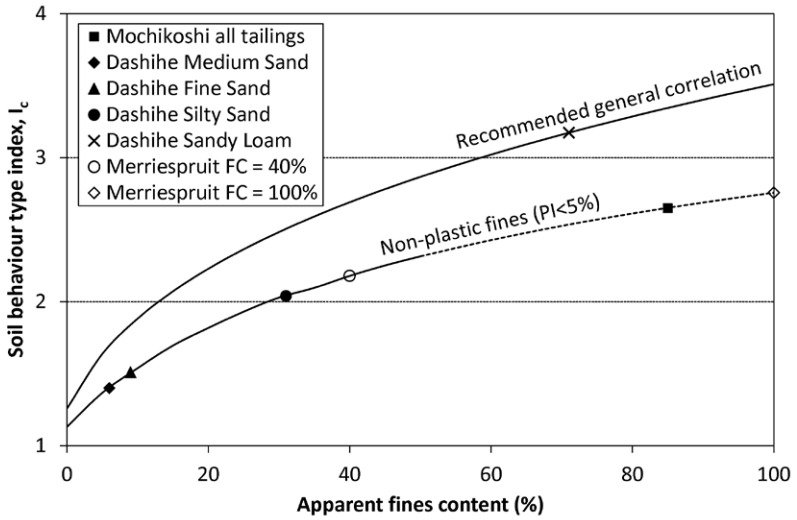


Figure 2.5 Correlations between I_c, *FC*, and *PI,* after Robertson and Wride (1998). Dashed curve indicates the extrapolation made in this study.

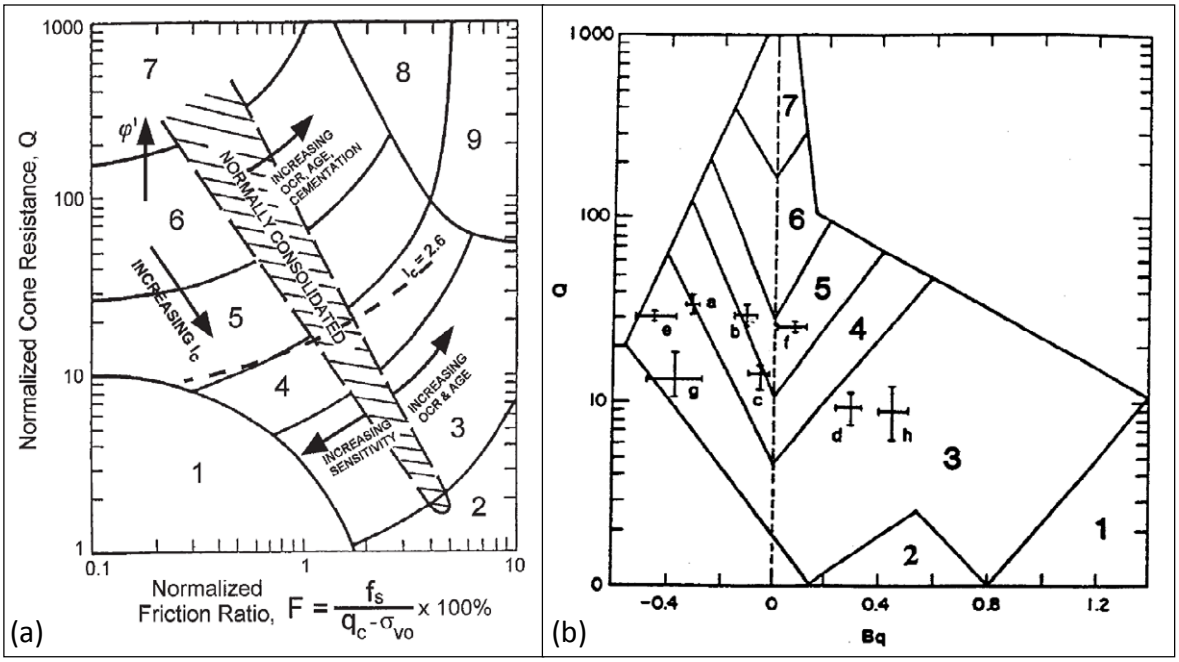


Figure 2.6 CPT-based SBT charts. a) Q_{tn} vs F_r chart (Robertson and Wride 1998), b) Q vs B_q chart (Robertson 1991). Soiltypes: 1, sensitive, fine grained; 2, peats; 3, silty clay to clay; 4, clayey silt to silty clay; 5, silty sand to sandy silt; 6, clean sand to silty sand; 7, gravelly sand to dense sand; 8, very stiff sand to clayey sand (heavily overconsolidated or cemented); 9, very stiff, fine grained (heavily overconsolidated or cemented). OCR, overconsolidation ratio. F = F_r. *Note:* For part (a): Q = Q_{tn}.

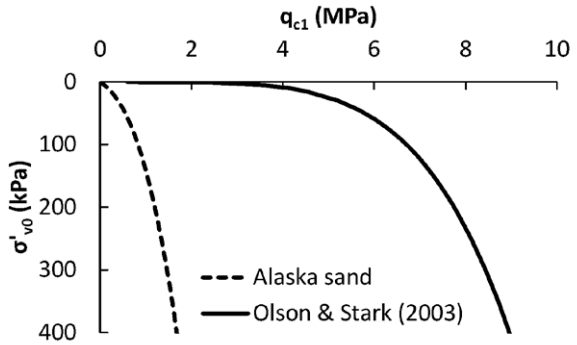


Figure 2.7 Comparison of contractive-dilative boundaries.

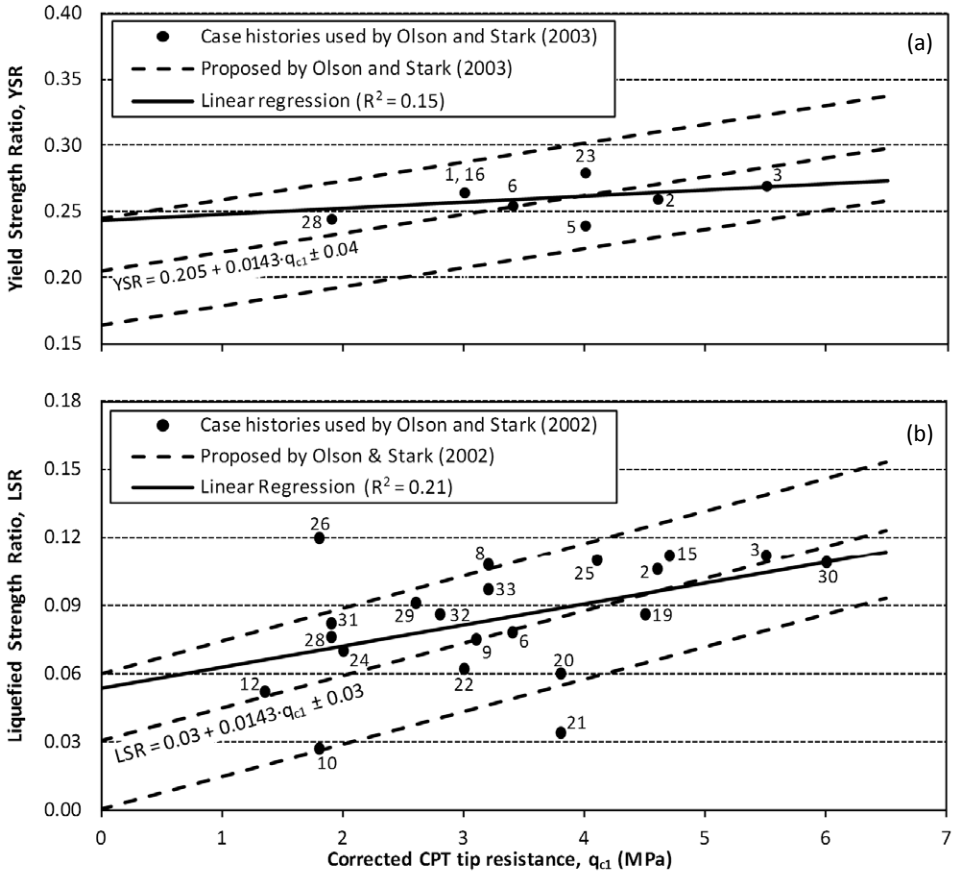


Figure 2.8 YSR and LSR correlations with q_{c1}. Data from Olson and Stark (2002) and (2003). Note: Labels indicate case history according to the numbering used by Olson and Stark.

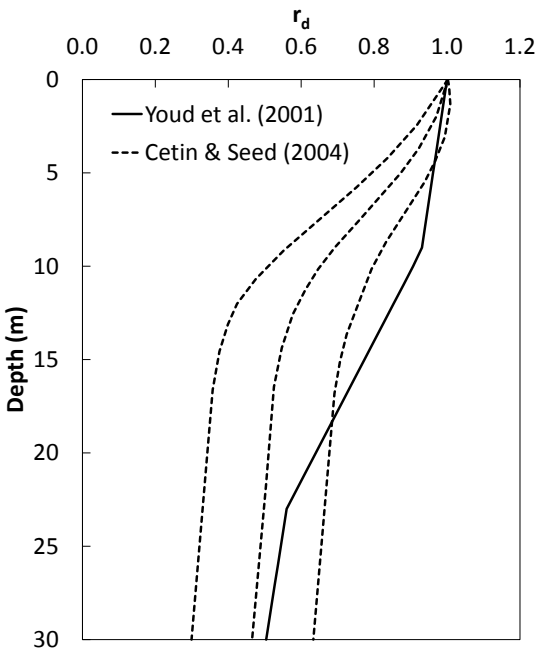


Figure 2.9 Profile of r_d as per Youd et al. (2001) (Eq. 2.26), and mean and ±1 standard deviation of the r_d profiles reported by Cetin and Seed (2004).

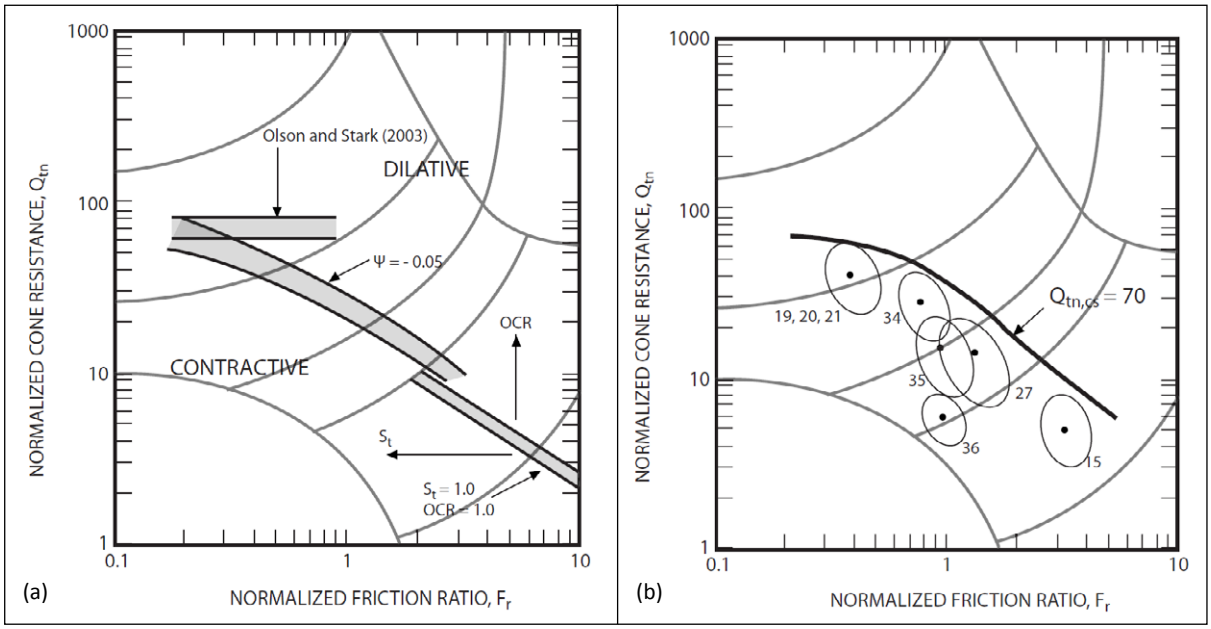


Figure 2.10 Susceptibility criteria of Robertson (2010). a) Inclined shaded areas form the liquefaction susceptibility boundary. b) Supporting "Class A" case-history data and contour of $Q_{tn,cs}$ = 70 which conservatively approximates the susceptibility boundary.

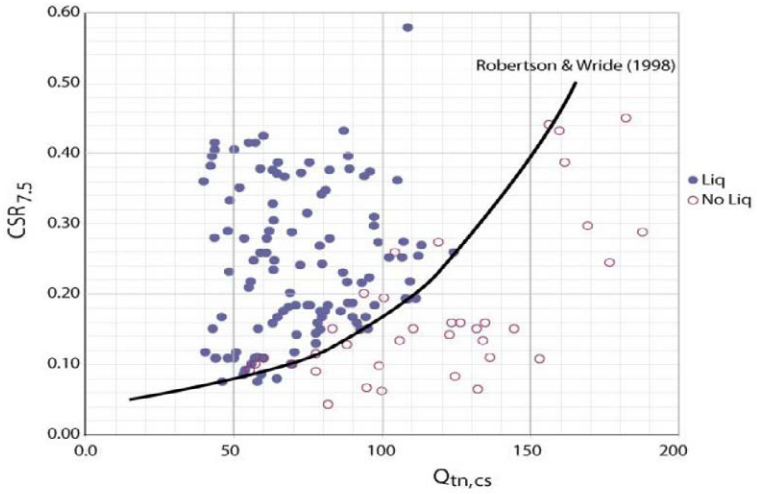


Figure 2.11 CPT-based liquefaction boundary curve (Robertson 2009b).

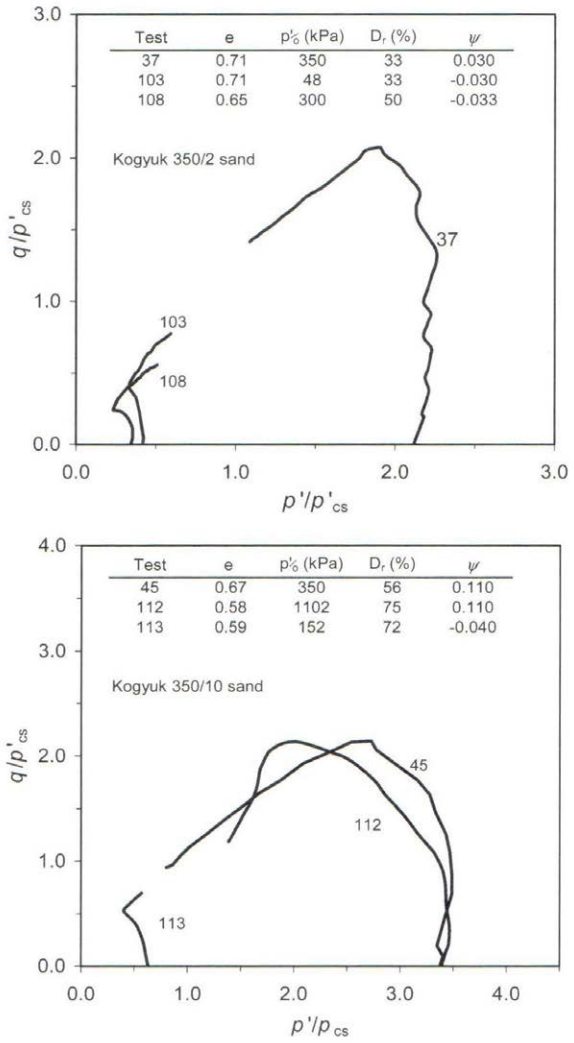


Figure 2.12 Stress paths of sands Kogyuk 350/2 and Kogyuk 350/10 for different values of D_r and ψ (Jefferies and Been 2006).

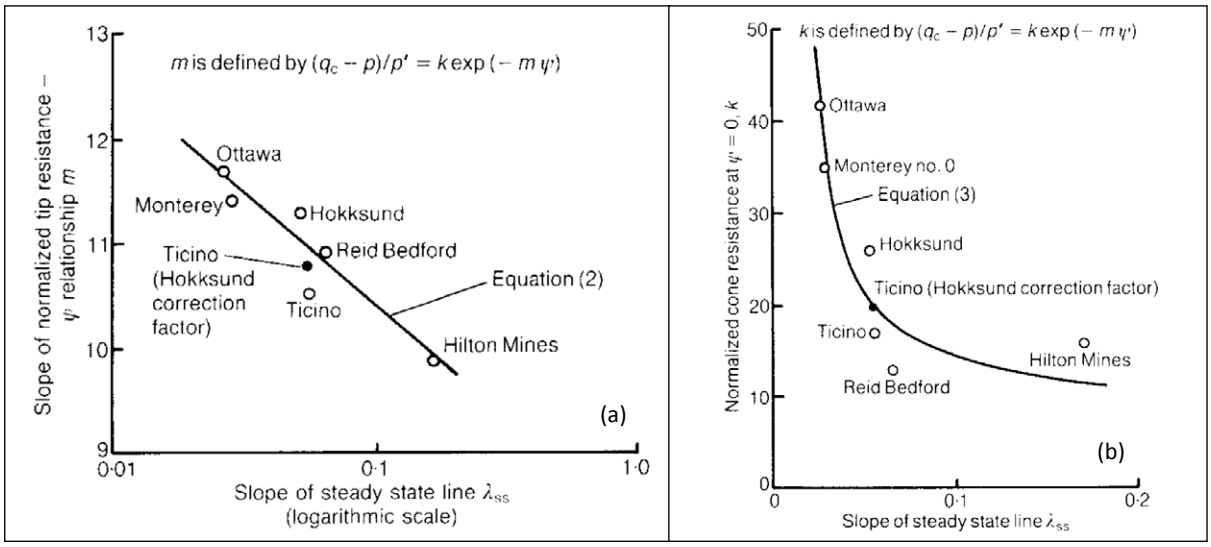


Figure 2.13 Experimentally determined correlations between k, m, and λ (Been et al. 1987).

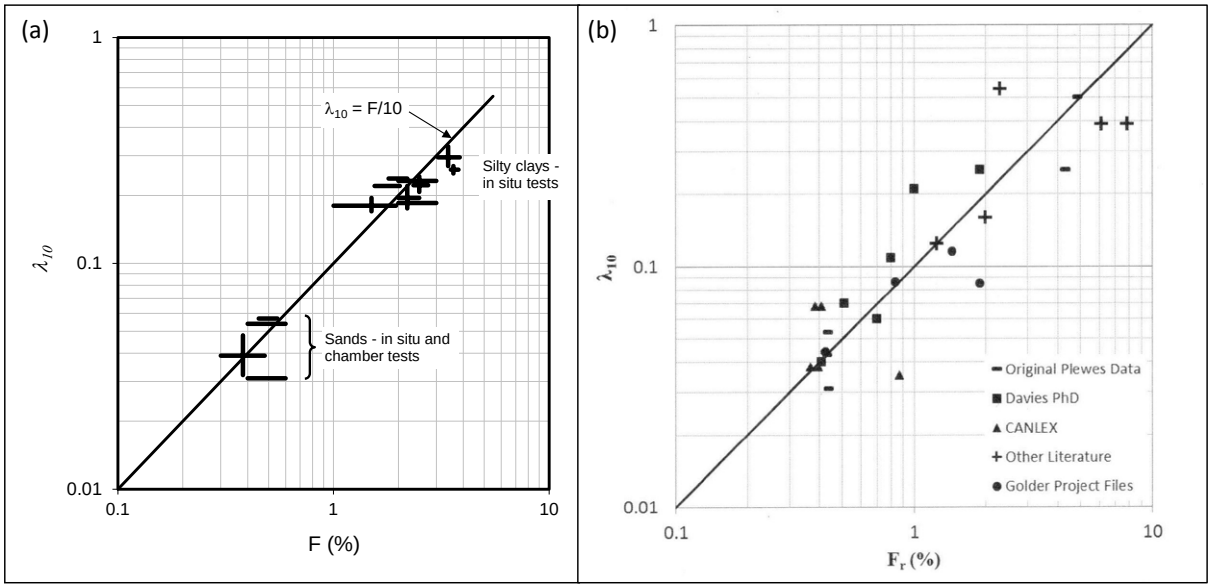


Figure 2.14 Relationship between λ (=λ_{10}) and F_r (=F). a) Original data presented by Plewes et al. (1992), b) Updated data set presented by Reid (2012).

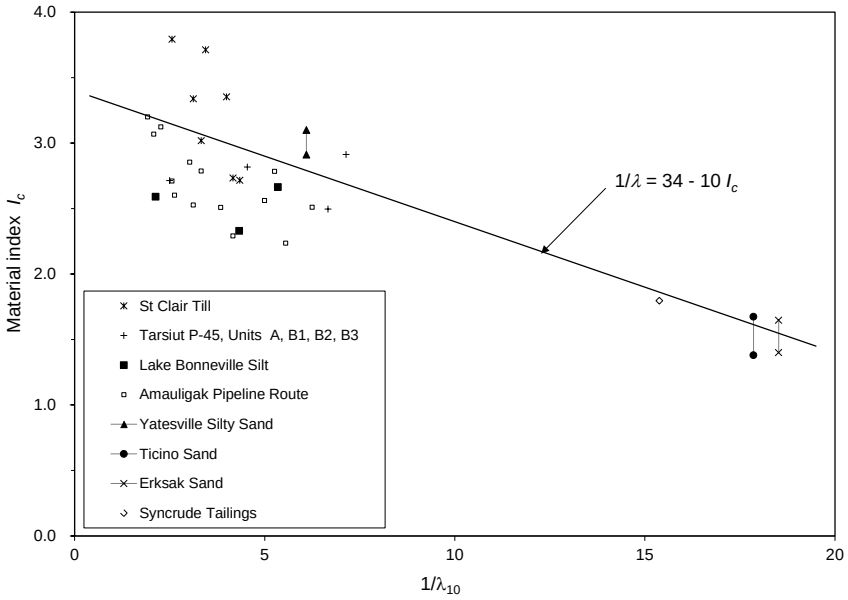


Figure 2.15 Relationship between λ (=λ_{10}) and I_c suggested by Been and Jefferies (1992). Figure from Jefferies and Been (2006).

3 Case histories: description and idealisations

3.1 Introduction

This chapter describes the eight case histories on which the CPT-based liquefaction assessment methods were implemented. The idealisations used to build the slope stability and finite element (FE) models required to implement the Olson and Stark and Robertson-based methods, respectively, are described. All but one of the case histories has either exhibited liquefaction-induced failure or has withstood a seismic event. The exception is the Impala Platinum TSF which at the time of writing (2015) is an operational dam in South Africa in which no signs of liquefaction have been observed. The Impala TSF was used in this study only to assess the influence of the variability in λ on the predicted values of ψ when using the Jefferies and Been (2006) method (Chapter 8). As there are no events that can be deemed likely to have triggered an undrained response in the Impala TSF, the Olson and Stark and Robertson-based methods were not applied to this case history. The main features of each case history are presented in Table 3.1.

The geometry, total unit weights (γ_t), water table location, and soil strength parameters of each case history were used to build the slope stability models required to implement the Olson and Stark method. The module Slope/W of the GeoStudio 2007 (Geo-Slope International Ltd.) software was used to build the slope stability models and their detailed description is presented in Appendix A. Additionally, FE models were built to compute the horizontal shear stresses (τ_h) necessary to implement the Robertson-based method. The FE models were 2-dimensional, linear-elastic, and isotropic. The module Sigma/W of the GeoStudio 2007 (Geo-Slope International Ltd.) software was used to build the models. Triangular and quadrilateral elements, of three and four nodes respectively, were used in the meshes. The meshes were refined until further refinements did not result in significant changes in τ_h values. Both horizontal and vertical displacements were constrained at the base of the models, whereas only horizontal displacements were constrained on the lateral borders. The resulting τ_h profiles depended on two material properties: total unit weight (γ_t) and Poisson's ratio (ν). For simplicity, each case history was modelled with a single soiltype, since including additional soiltypes did not significantly alter the τ_h profiles. The γ_t value used for each case history was based on the soil descriptions found in the literature. Values of ν were not reported for any of the case histories so ν = 0.3 was assumed for all cases. This ν value is similar to that adopted in other FE models of TSFs. E.g. Zardari (2011) used 0.33, Zandarín et al. (2009) used 0.35, and Psarropoulos and Tsompanakis (2008) used 0.3. The γ_t and ν values used in the FE models are presented in Table 3.2. The resulting profiles of τ_h are presented in Appendix B.

3.2 Hokkaido Dam – Japan, 1968

3.2.1 Description

The Tokachi-Oki earthquake struck the northern Pacific coast of Japan on May 16, 1968. It had a moment magnitude M_w = 8.0 (Kanamori 2004), and a_{max} = 2.3 m/s^2 recorded in Hachinohe (Yoshimi and Akagi 1968). The earthquake caused 50 deaths, collapsed 676 buildings, and triggered 78 slope failures (Yoshimi and Akagi 1968). A liquefaction induced flow failure triggered at a tailings dam in Hokkaido (Figure 3.1 and Figure 3.2) was described by Ishihara et al. (1990). The average depth of the sliding surface was estimated to be from 2 m to 5 m (Ishihara et al. 1990). The q_c readings of two CPT soundings performed after the failure at an intact location near the slide are shown in Figure 3.3. Ishihara et al. (1990) describes the tailings as cohesionless silty sand with a γ_t = 19.8 kN/m^3. No other information on soiltype was found in the literature.

3.2.2 Assumptions and idealisations

The literature does not provide a precise location of the Hokkaido Dam. It is therefore uncertain how close it was to Hachinohe which is the location where a_{max} was measured. It will be assumed herein that the a_{max} measured at Hachinohe was equal to that at the location of the Hokkaido Dam.

The general geometry and water table location shown in Figure 3.2 were adopted in the slope stability (Appendix A.2) and the FE (Figure 3.4) models. The depth of the water table at the locations of the CPT soundings is not reported in the literature, so it was assumed to be equal to 1 m for both soundings. The pore water pressure regime was assumed to be hydrostatic. Since f_s readings and soiltype characteristics were not available, the estimation of I_c was based on the "silty sand" description provided by Ishihara et al. (1990). According to Table 2.1 the range of I_c values that correspond to this soiltype can be taken as $2.05 < I_c < 2.60$. Therefore calculations of n (Eq. 2.10) and K_c (Eq. 2.14) were made for both I_c = 2.05 and I_c = 2.60.

Olson (2001) assumed that φ' of the tailings is between 30˚ to 35˚, and this same range was used in the current study for the slope stability analyses. As the starter dyke was not affected by the failure, it was taken as impenetrable bedrock in the models.

3.3 Mochikoshi Dam (Dykes 1 and 2) – Japan, 1978

3.3.1 Description

The Izu-Ohshima-Kinkai earthquake struck the Izu peninsula of Japan on 14 January 1978. It had a Richter scale magnitude M_L = 7.0, and caused 25 deaths and extensive material damage (Okusa and Anma 1980). A flow failure was triggered at the Mochikoshi tailings dam, about 40 km away from the epicentre, where three dykes had been built. Accounts of the flow failure are given by Okusa and Anma (1980) and Ishihara et al. (1990). Dyke No. 1, the tallest, failed almost immediately

after the earthquake struck, developing a breach 73 m wide and 14 m high through which approximately 80,000 m^3 of liquefied silver and gold tailings flowed between 7 km to 8 km down the valley and killed one person. Dyke No. 2, the second tallest, withstood the main shock but subsequently failed due to an aftershock on 15 January. Plan views and cross sections of both dikes are shown in Figure 3.5 and Figure 3.6, respectively. Liquefaction is estimated to have occurred at depths between 6 m to 7 m. Ishihara and Nagao (1983) reported approximate contours of a_{max} derived from the analyses of overturned tombstones in cemeteries in the region. From these contours, a_{max} for Mochikoshi was estimated to be 2.5 m/s^2. Ishihara et al. (1990) report q_c results of two soundings performed with a portable cone penetrometer on the intact part of the tailings impoundment adjacent to the failure scar (Figure 3.7).

Okusa and Anma (1980) described the tailings as alternating layers of silt and sandy silt of 3 cm to 7 cm in thickness. The PI of the silt was reported as 10% and the sandy silt was described as non-plastic. FC = 85% was measured by Okusa and Anma (1980) on a sample of tailings recovered from the valley below Dike No. 1. Ishihara et al. (1990) report that the tailings had an approximate γ_t of 17.6 kN/m^3. Okusa and Anma (1980) report that the γ_t of the dyke material for Dykes 1 and 2 were 16.6 kN/m^3 and 15.1 kN/m^3, respectively.

3.3.2 Assumptions and idealisations

In accordance with the $M_L - M_w$ correlation suggested by Youd et al. (2001), an equivalent moment magnitude M_w = 7.7 was used here for this case history. Given that acceleration estimates are only available for the main shock, and that there is great uncertainty on the prevailing pore water pressure conditions in the dykes when the aftershock struck, only the main shock was considered in this study. Furthermore, even though Dyke 2 did not exhibit flow failure immediately after the main shock, it will be assumed herein that liquefaction was triggered. This assumption is based on the fact that Dyke 2 did eventually exhibit flow failure following an aftershock, so it seems likely that the main shock left Dyke 2 in a state of incipient failure.

The geometry of Dykes 1 and 2 presented in Figure 3.6 was adopted in the slope stability (Appendix A.3) and FE (Figure 3.8 and Figure 3.9) models. No information was found in the literature regarding the location of the water table. Given that the Mochikoshi tailings dam was in operation when it failed, and that Okusa and Anma (1980) reported degrees of saturation of 100% for tailings recovered from both slides, the water table was assumed to be near the ground surface in the slope stability and FE models. Similarly, the water table was assumed to be 1 m below ground level at the locations were the CPT soundings were made. The pore water pressure regime was assumed to be hydrostatic. An average PI value of 5% was taken as representative of the whole dam. This PI value was used together with the measured FC = 85% and the 'non-plastic fines' curve of Figure 2.5 to estimate an I_c value of 2.65 for both dykes.

No formal measurements of shear strength parameters are reported in the literature. In this study all the tailings were considered to be liquefiable and therefore their strength was determined through the back-analysis of the slope stability models. As for the dyke material, Olson (2001)

assumes that, due to its likely angular particle shape, the effective friction angle of the dyke material is 35˚; this same value was adopted herein.

3.4 Dashihe Iron Tailings Dam (Beach and outer wall) – China, 1990

3.4.1 Description

Amante (1993) presents a synthetic case history in which the finite element (FE) computer codes TARA-3 and TARA-3FL are used to predict the performance of the major tailings dam at the Dashihe iron mine in China (Figure 3.10) in its 1990 configuration, subjected to the Tangshan earthquake of 28 July, 1976. Kanamori (1977) estimated the moment magnitude of the earthquake to be M_w = 7.5. Using an attenuation relationship, Amante (1993), estimated the peak acceleration at the dam site to be 1.2 m/s^2.

Amante performed both a triggering and post-triggering analysis to study the stability of the beach and outer wall of the Dashihe dam. The triggering analysis, which Amante refers to as 'seismic response analysis', predicts triggering of liquefaction in the tailings that lie under the pond and in the beach area near the pond. As for the outer wall, the analysis predicts the triggering of liquefaction only in a very limited portion close to the crest of the starter dyke. The post-triggering analysis, which Amante refers to as 'post-liquefaction analysis' predicts that the tailings in the beach would exhibit flow failure and estimates deformations of 2 m to 13.5 m, i.e. a rather small flow. Since these tailings would flow downslope, deeper into the pond, the only predicted consequence is extensive cracking in the beach due to loss of support. The post-triggering analysis did not predict significant displacements in any portion of the outer wall.

Amante confirmed the results of the post-triggering analysis with a detailed pseudo-static analysis of the beach and outer wall. The pseudo-static analysis confirmed the occurrence of a flow failure in the beach tailings. As for the outer wall, given the more serious consequences that a flow failure of this portion of the dam would imply, the pseudo-static analysis considered the uncertainties in the response acceleration of the outer wall and the reduction in strength of a thin clay layer underlying the tailings. From the triggering analysis, Amante determined that the response acceleration of the tailings in the outer wall varied from 0.08 g to 0.24 g with an average of 0.13 g. Based on previously published experimental data Amante determined that the lower bound of the cyclic yield strength of clay could be taken as 80% of the static undrained strength. Considering these value ranges for response acceleration and clay weakening, Amante performed the pseudo static analysis for response accelerations ranging from 0.10 g to 0.17 g with increments of 0.01 g, and strength reductions of the clay layer of 5%, 10%, 15% and 20%. The resulting factors of safety varied from 0.87 to 1.3. The lowest response acceleration that led to a factor of safety smaller than 1.0 was 0.14 g and it occurred when considering a strength reduction of the clay layer of 20%. Given that the average response acceleration expected in the outer wall is 0.13 g and that the FE-based post-triggering analysis did not predict significant displacements in the outer wall, Amante concluded that flow failure of the outer wall was unlikely.

Three CPT soundings were used in this research to characterise the beach tailings. Henian et al. (1990) present average f_s values of these three CPT soundings and Lee et al. (1992) present the corresponding continuous q_c profiles (Table 3.3 and Figure 3.11). Four CPT soundings were used in this research to characterise the tailings on and underneath the outer wall. Continuous q_c profiles of the four soundings are presented by Lee et al. (1992) (Figure 3.12). No f_s readings were found in the literature for the CPTs on the outer wall.

Amante (1993) shows a cross sectional cut of the outer wall illustrating the location of the different soil layers as inferred from collected samples. The four CPT outer wall soundings were approximately located on this cut (Figure 3.10) to determine the soiltypes penetrated by each CPT (Table 3.4). The values of FC and PI that corresponds to each of these soiltypes are shown in Table 3.5.

Average values of γ_t of 19.6 kN/m^3 and 15.9 kN/m^3 are reported for the tailings below and above the water table, respectively, and γ_t = 18.9 kN/m^3 for the clay underlying the tailings (Amante 1993; Lee et al. 1992). Amante (1993) reported the following shear strength parameters: Average values of ϕ' = 37˚ and ϕ' = 39˚ for tailings below and above the water table, respectively, and a total strength parameter c = 164 kPa for the clay underlying the tailings. The tailings were reported to be cohesionless.

3.4.2 Assumptions and idealisations

The first assumption to be discussed is whether the FE analysis of Amante (1993) can be considered reliable enough to test the Olson and Stark, and Robertson-based methods. Two considerations have led the author to conclude that it is. First, the main FE programme used by Amante, TARA-3 (Finn et al. 1986), had already been used by other researchers to successfully model the response of the Dashihe tailings dam, in its 1976 configuration, to the Tangshan earthquake and its Luanxian aftershock. And second, the input parameters of the FE model were of high quality, as they were drawn from comprehensive field and laboratory studies made on the Dashihe tailings, e.g. Gao et al. (1991) and Lee et al. (1992).

The general geometry and water table location shown in Figure 3.10 were adopted in the slope stability (Appendix A.4) and the FE (Figure 3.13) models. Given the gentle slope of the beach (≈3%), values of τ_h were assumed to be small and therefore an FE model of the beach was not necessary. A hydrostatic pore water pressure distribution was assumed for the models and to process the CPT data.

The I_c values of the soiltypes found in the CPT soundings made on the beach were calculated using Eq. 2.11 together with the f_s and q_c profiles reported in Table 3.3 and Figure 3.11 respectively. The resulting classification of the beach tailings is shown in Figure 3.14. It is seen that several data points fall in the region defined by $1.64 < I_c < 2.36$ and $F_r < 0.5\%$. As prescribed by Robertson and Wride (1998), these data points were conservatively treated as clean sands, i.e. $K_c = 1$. The I_c values for the outer wall were calculated from the PI and FC values reported in Table 3.5 together with Figure 2.5. The resulting I_c values are shown on Figure 2.5 and on Table 3.5.

3.5 Sullivan Tailings Dam – Canada, 1991

3.5.1 Description

Accounts for this case history are given by Davies (1999) and Jefferies and Been (2006). The Sullivan tailings dam is located in the Canadian province of British Columbia. On 23 August 1991 a 300 m section of the 21 m high dyke slumped suddenly, causing a predominantly horizontal displacement of up to 45 m in the toe region. Despite these downstream movements, and the involvement of 75,000 m^3 of tailings, the failure did not have major economic or environmental consequences, nor did it cause loss of human lives because the involved tailings slid into an adjacent siliceous pond. Given that: the failure occurred as a 2.4 m raise was being placed, it happened quickly, and sand boils were observed after the failure; it was concluded that this was a case of static liquefaction. Figure 3.16 illustrates the pre- and post-failure geometry of the tailings dam.

Jefferies and Been (2006) published q_c results of six CPT soundings (Figure 3.15) made through the failed soil mass beneath the original location of the dykes. Three of these soundings were made on the crest of the dam, at the location marked as CP91-29 on Figure 3.16, and the other three were made on the toe of the dam, at the location marked as CP91-31 on Figure 3.16. The f_s profile corresponding to the CPT sounding CP91-29 was also reported by Jefferies and Been (2006) and is reproduced here in Figure 3.17. The analyses of Davies (1999) and Jefferies and Been (2006) indicate that liquefaction took place on the old iron tailings on which the dyke was founded, at an approximate depth of 10 m to 12 m of the soundings performed on the crest (Figure 3.16).

The tailings are classified as non-plastic silt or silty fine sand, with $FC \geq 50\%$. Jefferies and Been (2006) reported γ_t of 22.4 kN/m^3 and 24.0 kN/m^3 for the compacted fill (dyke material) and iron tailings respectively. They also reported that standpipe piezometers that had been operating at the site before the failure indicate that the water table was "*generally within a few feet of ground surface*" and "*above ground level at the dyke toe*", but that a declining trend had been detected a month before the failure. Regarding the position of the water table after the failure when the CPT soundings were performed, Jefferies and Been (2006) indicate that for the sounding CP91-29, the water table was located 2 m below ground surface.

3.5.2 Assumptions and idealisations

Davies (1999) states that although the 2.4 m rise and dynamic loads due to construction equipment may have contributed to trigger liquefaction, there is stronger evidence indicating that failure would have occurred even if the raise had not been built nor dynamic loads been present. Consequently, the 2.4 m raise was not included in the slope stability analyses (Appendix A.5) made in this research. The pre-failure geometry presented in Figure 3.16 was adopted in the slope stability models. In agreement with the observations of Jefferies and Been (2006), the water table was placed close to ground level in the slope stability models. As no seismic loads were involved, the triggering

analysis of the Robertson-based method was not implemented. Consequently, no FE model was built for this case history.

The water table location for the CPTs is only reported for sounding CP91-29. For the remaining five soundings, the water table depth was taken to be equal as that of CP91-29, that is, 2 m below ground level.

I_c values (Figure 3.17) were only calculated using sounding CP91-29, as this is the only sounding for which f_s readings were available. The remaining five CPT soundings were not used for the susceptibility analysis of the Robertson-based method, only to calculate the q_{c1} values of the Olson and Stark method.

The references do not provide any shear strength parameters of the soils involved in the failure, therefore in the slope stability models the strength of the dyke material was estimated to range from c' = 5 kPa and ϕ' = 30˚, to c' = 15 kPa and ϕ' = 35˚. The tailings were taken as liquefiable so their strength was obtained through back analysis.

3.6 Merriespruit gold tailings dam – South Africa, 1994

3.6.1 Description

On 22 February 1994 the 31 m high northern outer wall of a gold tailings dam upslope of Merriespruit, a suburb of the town of Virginia, South Africa, collapsed producing a flow failure. The failure resulted in a breach of approximately 600,000 m^3 of gold tailings that caused the death of 17 people, extensive destruction of property and environmental damage (Wagener et al. 1997).

Fourie and Papageorgiou (2001) performed a series of consolidated undrained (CU) triaxial compression tests on reconstituted Merriespruit tailings to determine the SSL of four different grain size distributions (GSD). Comparing these SSLs to the void ratio of undisturbed samples, Fourie et al. (2001) concluded that the failure had occurred due to static liquefaction of the impounded tailings. The accepted sequence of events (Figure 3.18) is that overtopping at a section of the dam caused considerable erosion of the outer wall, and triggered a series of retrogressive slope failures that left the impounded tailings without confinement. Under this scenario, the impounded tailings were subjected to a static shear stress large enough to trigger liquefaction (Papageorgiou 2004). Strydom and Williams (1999) presented satellite imagery that shows that at least three weeks before the failure, the pond was already lying against the section of the outer wall that eventually failed.

The q_c profiles of five CPTu soundings (Figure 3.19) made on the beach were obtained from the files of Jones and Wagener Consulting Civil Engineers (J&W), a firm that conducted an investigation to determine the causes of the failure. These soundings were made 22 to 35 days after the failure at locations close to the failure scar.

Based on the GSDs of 41 samples obtained from different locations around the failure scar Fourie et al. (2001) found that the FC varied from 40% to 100%. Wagener et al. (1998) reported PI values varying between 1% and 8%. Strydom and Williams (1999) indicate that the in situ γ_t of the

impounded tailings was close to 20 kN/m^3. The triaxial tests reported by Fourie and Papageorgiou (2001) indicate that the tailings were cohesionless.

3.6.2 Assumptions and idealisations

In agreement with the sequence of events described by (Papageorgiou 2004), the geometry adopted for the slope stability models was that of the eroded outer wall after overtopping had occurred (Figure 3.20). This eroded geometry was taken from the files of J&W and is based on the accounts of eye witnesses. Additionally, based on the satellite images presented by Strydom and Williams (1999), high water table conditions were assumed in the slope stability models (Appendix A.6).

The tailings probed by the J&WWEST1 CPTu sounding were above the water table (Figure 3.19). The implication is that, despite possible capillary effects, these tailings were likely not saturated and therefore not prone to liquefaction. However, the results of this sounding have been included here to help characterise the penetration resistance of the tailings.

Since no f_s values were measured during the CPTu soundings, estimates of I_c were made by considering the range of FC reported by Fourie et al. (2001) (i.e. 40% to 100%), the low plasticity values reported by Wagener et al. (1998), and the correlations shown in Figure 2.5. This led to the estimation of upper and lower bounds for I_c of 2.2 and 2.8. The susceptibility analysis of the Robertson-based method was implemented with both of these I_c values.

J&W conducted slope stability analyses as part of the post-failure investigation. In their analyses they adopted c' = 40 kPa and ϕ' = 40˚ for the natural soil underlying the tailings. It is not clear though whether these strength parameters were assumed or measured. These same strength parameters were adopted in the slope stability analyses made in this research.

3.7 Impala Platinum TSF – South Africa

3.7.1 Description

The Impala platinum TSF (Figure 3.21) is located in the North West Province of South Africa. It is a ring dyke TSF built using the conventional upstream spigotted tailings method. The TSF serves two plants, each of which treats a different ore body. With a perimeter of 9 km, and an average height of the outer wall of 55 m, it is one of the largest TSFs in South Africa. Considering that the Impala TSF is currently halfway through its operational life, the managers of the facility commissioned a midlife investigation in the year 2009 in order to, among other objectives, assess liquefaction susceptibility. The results of the midlife investigation are found in a private report to which the author has been granted access.

Fourteen CPTu soundings, made along two alignments, were conducted as part of the midlife investigation. Twelve of these CPTu were made on Dam No. 4 and two on Dam No. 3 (Figure 3.21). Besides recording q_c and u_2, the CPTu soundings included pwp dissipation tests (Section 2.2.3) that

were made approximately every 1 m. The CPTu soundings did not include f_s readings. For the 12 soundings made on Dam No.4, there was refusal of the cone due to the presence of hard cemented layers. In such cases the CPTu contractor used rotary drilling to get through the hard layer and the CPTu resumed once softer material was encountered. This sequence was repeated in each sounding until natural ground level was reached. The processing of the CPTu results is described in further detail in Chapter 5. Boreholes were drilled next to the location of each CPTu to obtain samples using Shelby tubes. These disturbed samples were mostly used for G_s measurements and in situ void ratio estimations. The borehole records show that the tailings are underlain by clay and decomposed norite.

As part of the midlife investigation, the GSD curves of 49 samples from Dam No. 4 were determined by sieving and hydrometer analysis. 45 of these samples were taken at surface and were collected from points that were distributed every 50m on alignments 1, 2, and 3 (Figure 3.21). The remaining four samples were extracted from boreholes at depths ranging from 18 to 40 m below the beach surface. The purpose of collecting samples from different locations in the beach was to ensure representation of all particle sizes, from the coarse material that settles close to the point of deposition to the finer material which tends to concentrate closer to the pool. The resulting GSD curves (Figure 3.22) indicate that fines content (FC) varies from 33% to 95%, with an average value of FC = 64%, and 39 samples having FC ≥ 50%. The present author made an attempt to measure the liquid limit of the fine fraction (<75 μm) of the tailings using the Casagrande cup (ASTM D4318) and found the tailings to be non-plastic. Accordingly, the 49 samples classify as either silty sands (SM) or low plasticity silts (ML) according to standard ASTM D2487, with a predominance of silts (FC ≥ 50%). Chapter 7 presents the experimental determination of the SSLs corresponding to three soiltypes of Impala tailings.

The report of the midlife investigation contained several measurements of particle density (ρ_s), however, the ρ_s values used in this research were determined independently by the author (Chapter 7). In situ values of ρ_s depended on the GSD of the sample and varied from 3.43 g/cm^3 to 3.61 g/cm^3. A value of 3.54 g/cm^3 was chosen as representative of all the tailings as this is the value of mixes that had an average FC of 64% (Figure 7.5). The report of the midlife investigation indicates the ρ_s of the underlying clay and decomposed norite varies between 2.6 and 2.9 g/cm^3. The results of the midlife investigation further suggest γ_t = 25 kN/m^3 for saturated tailings and γ_t = 23 kN/m^3 for partially saturated tailings.

3.7.2 Assumptions and idealisations

No formal measurements of K_0 have been made at the Impala TSF, so a value of K_0 = 0.7 was assumed here. This value is similar to the average value reported by Graham and Jefferies (1986) for a normally consolidated hydraulic fill.

3.8 Summary

Eight TSF case histories have been described in this chapter. The main features and idealisations of each case history are summarised in Table 3.1. Seven of the TSFs were subjected to loading conditions in which an undrained response is expected to have occurred. Accordingly, the Olson and Stark, and the Robertson-based methods were implemented on these seven case histories to determine whether the methods were able to predict the performance of the TSFs. The results of these implementations are presented in the following chapter. Additionally, the Impala TSF was also described. The Merriespruit and Impala TSFs are the only case histories described in this study for which SSLs were available. Accordingly, both case histories will be used in Chapter 8 to study the effect of the variability in λ on the predicted values of ψ when using the Jefferies and Been (2006) method. As an undrained response is not expected to have occurred at the Impala TSF, the Olson and Stark, and the Robertson-based methods were not implemented in this case history.

The failure case histories illustrate the variety of scenarios that can lead to catastrophic flows, and in particular that these flows can be triggered by either static or dynamic conditions. It is important to note that the failure case histories listed in this chapter do not represent a comprehensive list of TSF failures, as only failure case histories with CPT results and involving liquefaction were included. Davies (2002) makes reference to commonly used databases that provide a much more comprehensive list of incidents at TSFs. Interestingly, Davies (2002) also points out that many TSF failures, and the lessons that could be learnt from them, remain unpublished.

3.9 Tables and Figures

Table 3.1 Summary of case histories.

Case history	Static or seismic?	Liquefaction triggered?	Flow failure?	Magnitude (M_w)	a_{max} (m/s^2)	q_{c1}* (MPa)	FC (%)	D_{50} (mm)	Height of dam (m)	Average Slope[a]	I_c (--)
Hokkaido, 1968	Seismic	Yes	Yes	8.0	2.3	0.47	n/a[b] - Described as containing silt sized grains.		9.2	1V:3H	2.05 & 2.6
Mochikoshi Dyke 1, 1978	Seismic	Yes	Yes	7.7	2.5	0.23	85	0.04	≈28	1V:3H	2.65[c]
Mochikoshi Dyke 2, 1978	Seismic	Yes	No	7.7	2.5	0.23	85	0.04	22	1V:3H	2.65[c]
Dashihe beach, 1990	Seismic	Yes	Yes	7.5	1.2	4.5	9 - 31	0.09 - 0.19	70	1V:5H	1.4 - 3.2[d]
Dashihe outer wall, 1990	Seismic	No	No	7.5	1.2	5.6	6 - 71	0.05 - 0.32	n/a	≈1V:33H	1.4 - 2.95[c]
Sullivan, 1991	Static	Yes	Yes	n/a	n/a	1.4	> 50	< 0.075	11	1V:2H	1.4 - 3.3[e]
Merriespruit, 1994	Static	Yes	Yes	n/a	n/a	0.92	40 - 100	0.009 - 0.09	31	1V:2.4H	2.2 & 2.8[c]
Impala, 2009	n/a	n/a	n/a	n/a	n/a	n/a	33 - 95	0.01 - 0.1	55	n/a	n/a

Notes: a) Refers to global slope, including benches or step-ins where applicable. b) n/a = not applicable or not available. c) Value(s) shown in Figure 2.5. d) Values shown in Figure 3.14. e) Values shown in Figure 3.17.

Table 3.2 Total unit weight (γ_t) and Poisson's ratio (ν) values used in the finite element models.

Case history	γ_t (kN/m^3)	ν
Hokkaido	19.8	0.3
Mochikoshi dyke 1	17.1	
Mochikoshi dyke 2	16.4	
Dashihe outer wall	17.8	

Table 3.3 Average f_s values at the Dashihe dam beach. Data from Henian et al. (1990).

CPT Sounding	Depth of layer (m)	Average f_s (kPa)
I8	0.0 - 5.0	15
	5.0 - 10.6	36
	10.6 - 17.4	65
	17.4 - 21.0	102
	21.0 - 31.4	93
I9	0.0 - 2.3	6
	2.3 - 9.4	26
	9.4 - 15.0	56
	15.0 - 24.1	55
	24.1 - 31.5	50
II6	0.0 - 4.5	9
	4.5 - 8.1	22
	8.1 - 16.0	30
	16.0 - 20.4	46
	20.4 - 28.0	58
	28.0 - 33.5	68

Table 3.4 Soiltypes probed by the CPT*s* on the Dashihe outer wall. Data from Amante (1993).

CPT Sounding	Thickness of layer (m)	Soiltype
I4	11.0	Medium sand
	12.5	Fine sand
	4.5	Silty sand
	2.0	Sandy loam
I5	24.0	Medium sand
	4.0	Fine sand
	3.5	Sandy loam
II2	16.0	Fine sand
	5.0	Silty sand
II4	24.0	Medium sand
	4.0	Fine sand
	3.5	Sandy loam

Table 3.5 Typical *FC* and *PI* values of the soiltypes in the Dashihe dam reported by Lee et al. (1992). I_c values were estimated in the current study using Figure 2.5.

Soiltype	FC (%)	PI (%)	I_c
Medium sand	6	0	1.4
Fine sand	9	0	1.5
Silty sand	31	0	2.0
Sandy loam	71	8.6	3.2

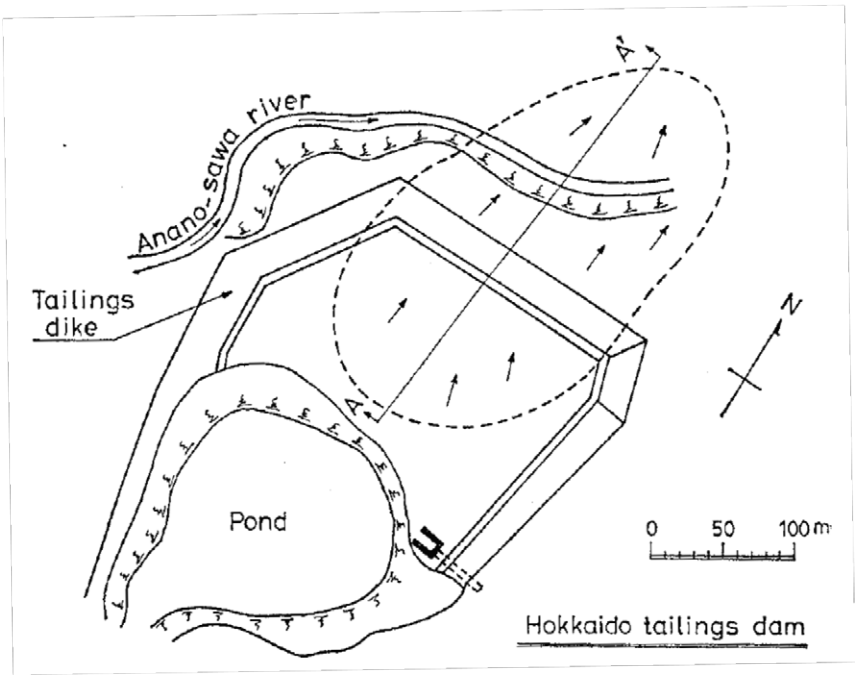


Figure 3.1 Plan view of Hokkaido tailings dam with flow failure outlined (Ishihara et al. 1990).

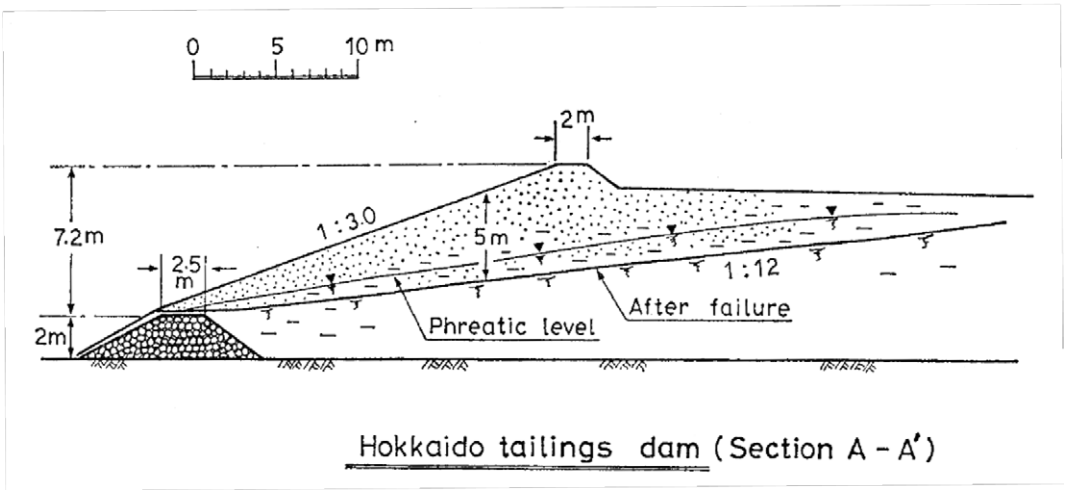


Figure 3.2 Pre and post-failure cross section of Hokkaido tailings dam (Ishihara et al. 1990).

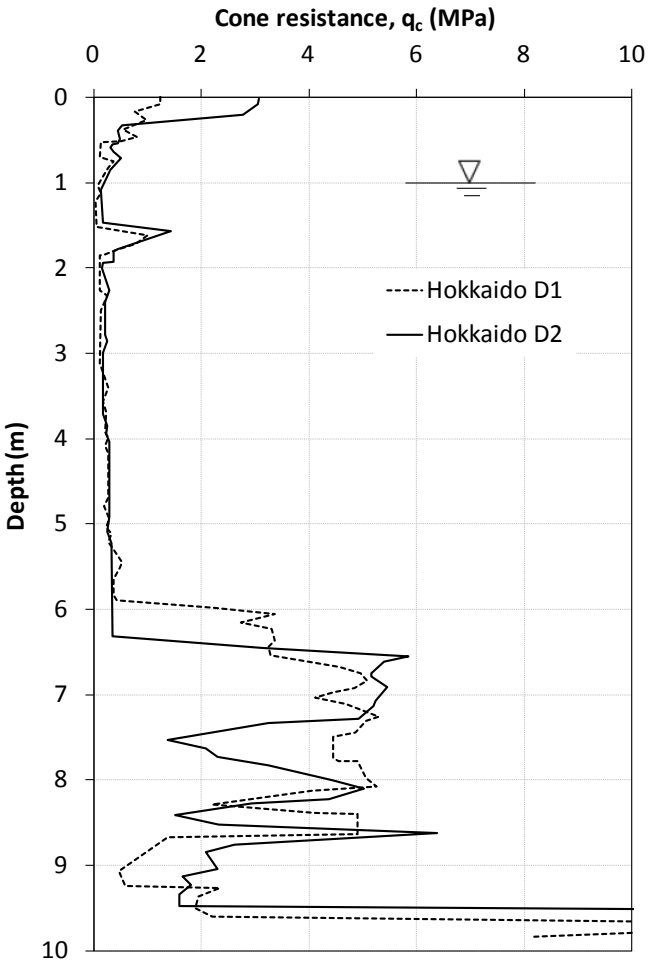


Figure 3.3 Cone resistance profiles at Hokkaido tailings dam. Data from Ishihara et al. (1990).

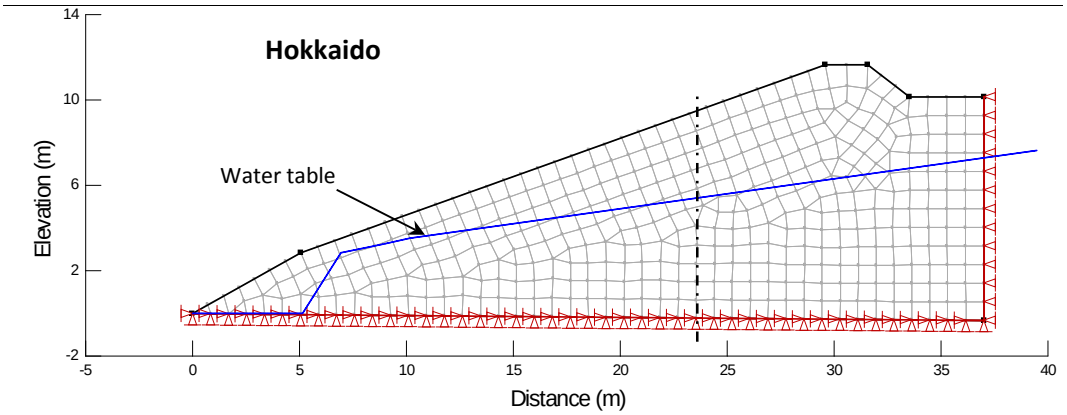


Figure 3.4 FE model of Hokkaido Dam. Dashed vertical line indicates alignment along which τ_h was computed.

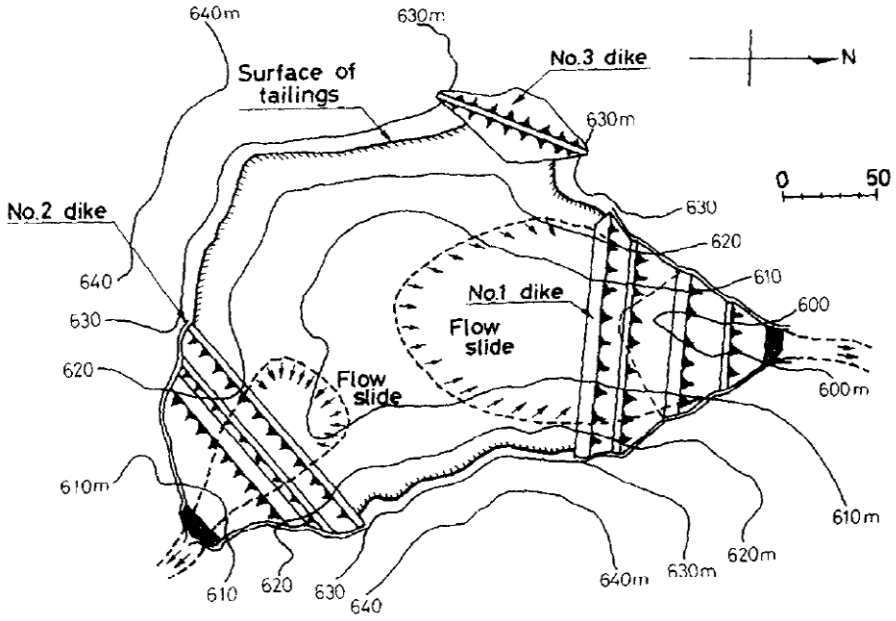


Figure 3.5 Plan view of the Mochikoshi tailings dam (Okusa and Anma 1980).

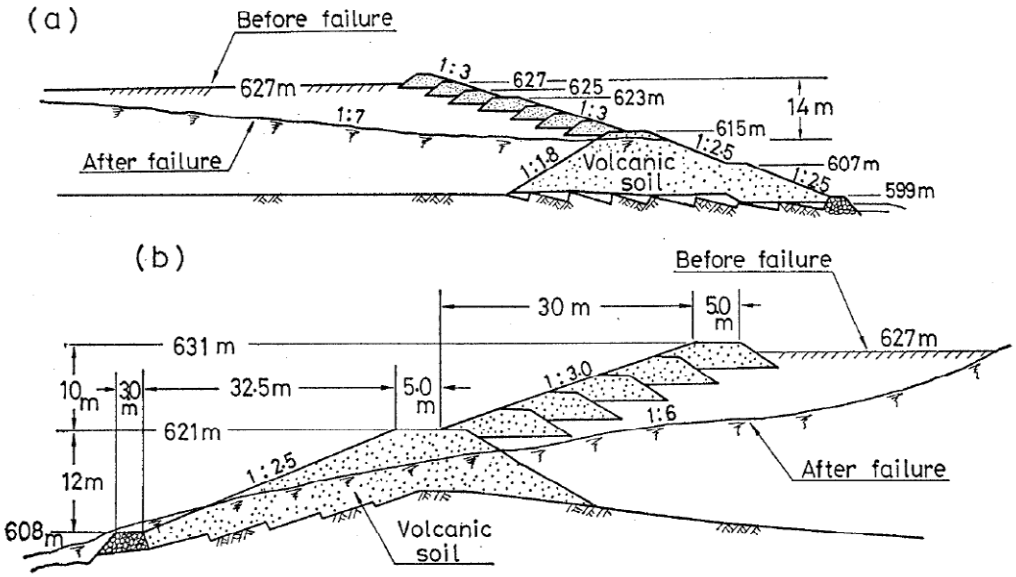


Figure 3.6 Pre and post-failure geometry of Dykes 1 (upper) and 2 (lower) of the Mochikoshi tailings dam (Ishihara et al. 1990).

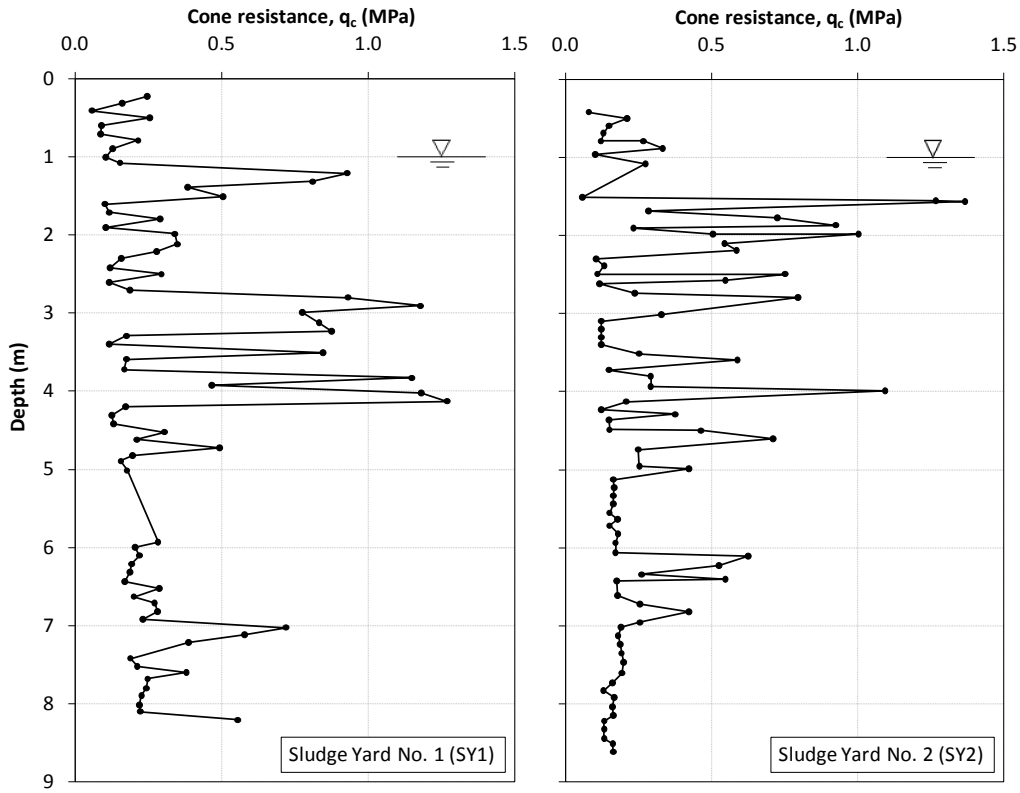


Figure 3.7 Double tube cone penetration test at Mochikoshi tailings dam. Data from Ishihara et al. (1990).

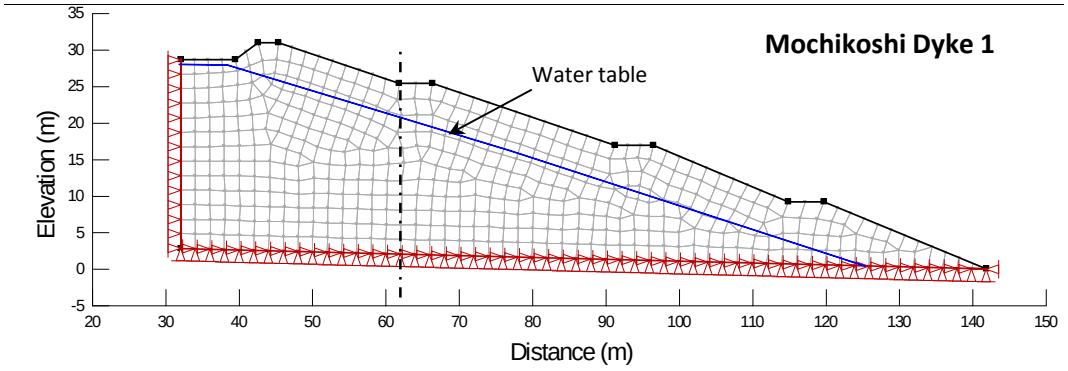


Figure 3.8 FE model of Mochikoshi Dyke 1. Dashed vertical line indicates alignment along which τ_h was computed.

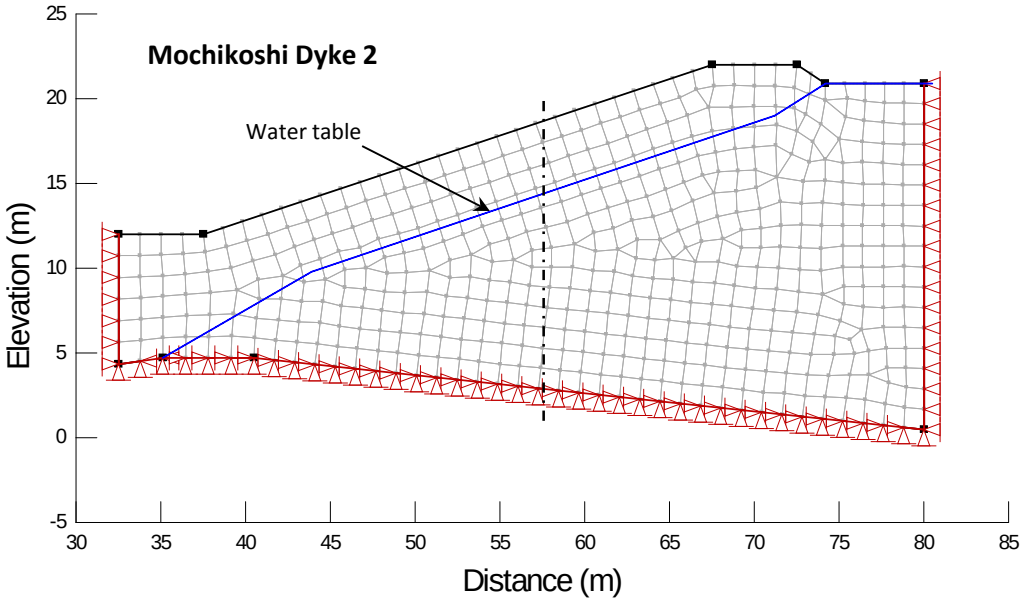


Figure 3.9 FE model of Mochikoshi Dyke 2. Dashed vertical line indicates alignment along which τ_h was computed.

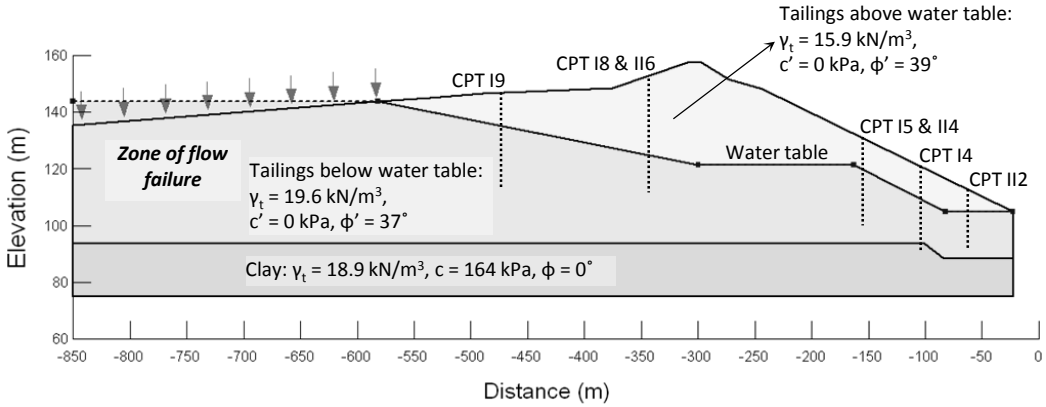


Figure 3.10 1990 pre-failure geometry of the Dashihe tailings dam and approximate location of the CPT soundings. After Amante (1993).

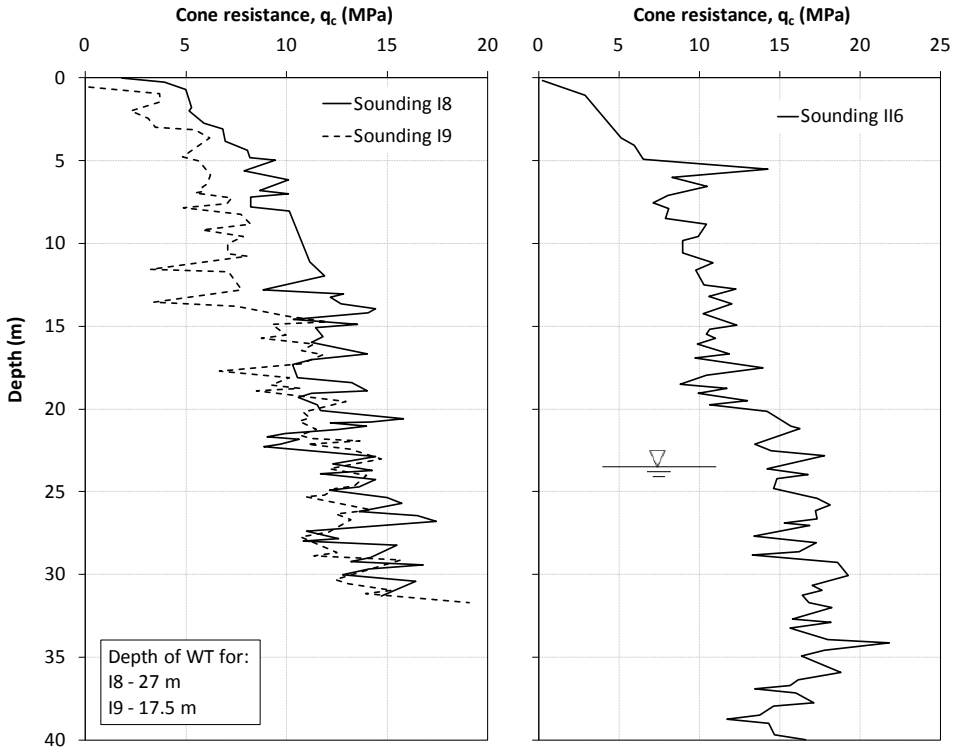


Figure 3.11 CPT soundings on the beach of Dashihe tailings dam. Data from Lee et al. (1992).

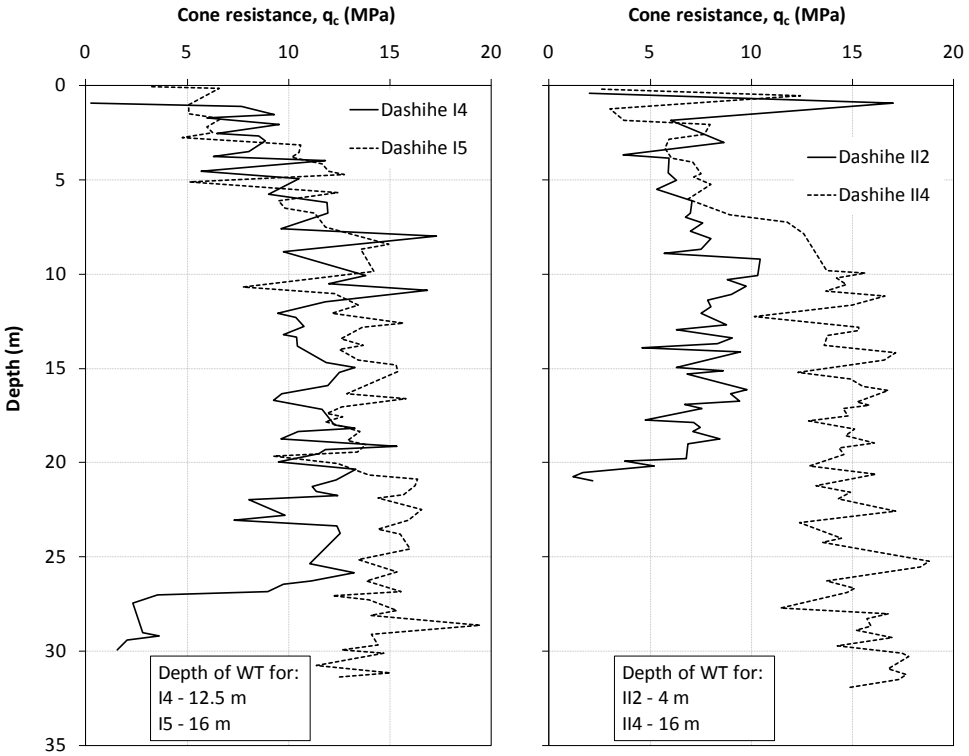


Figure 3.12 CPT*s* through the outer wall of the Dashihe tailings dam. Data from Lee et al. (1992).

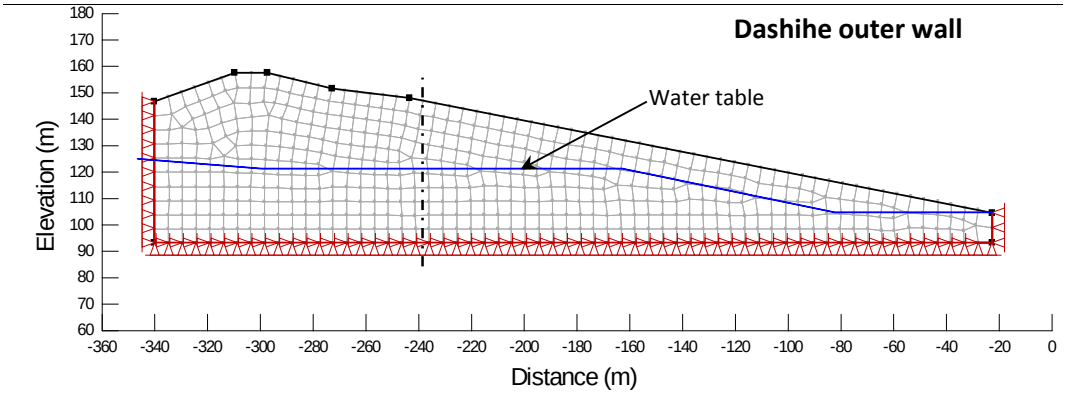


Figure 3.13 FE model of the Dashihe outer wall. Dashed vertical line indicates alignment along which τ_h was computed.

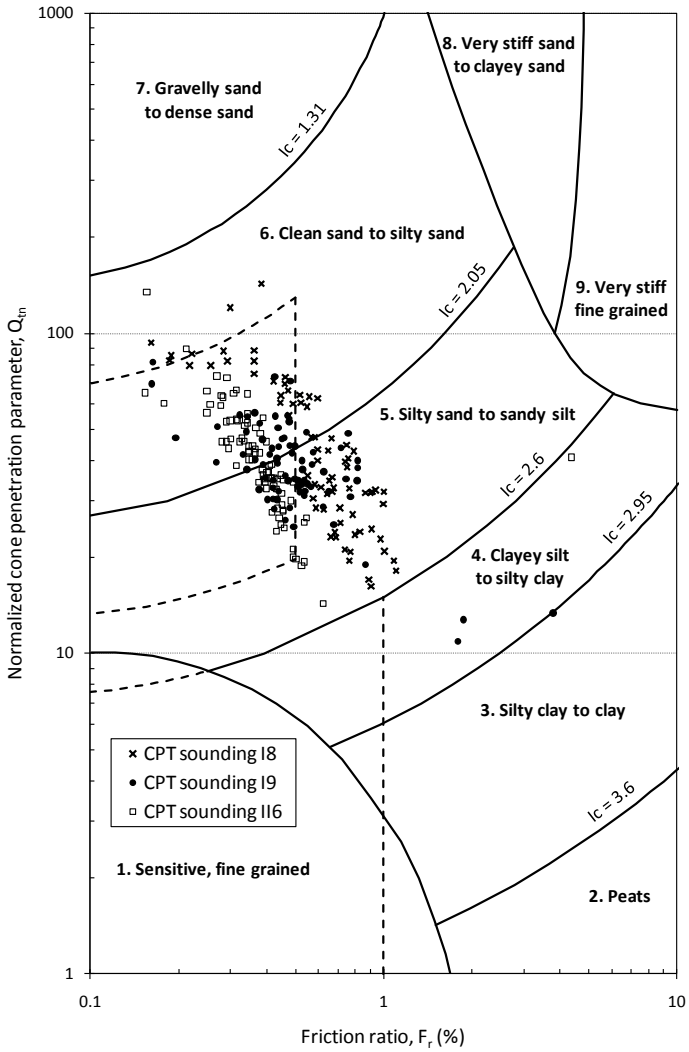


Figure 3.14 Soil behaviour type from the CPT soundings made on the Dashihe tailings dam beach.

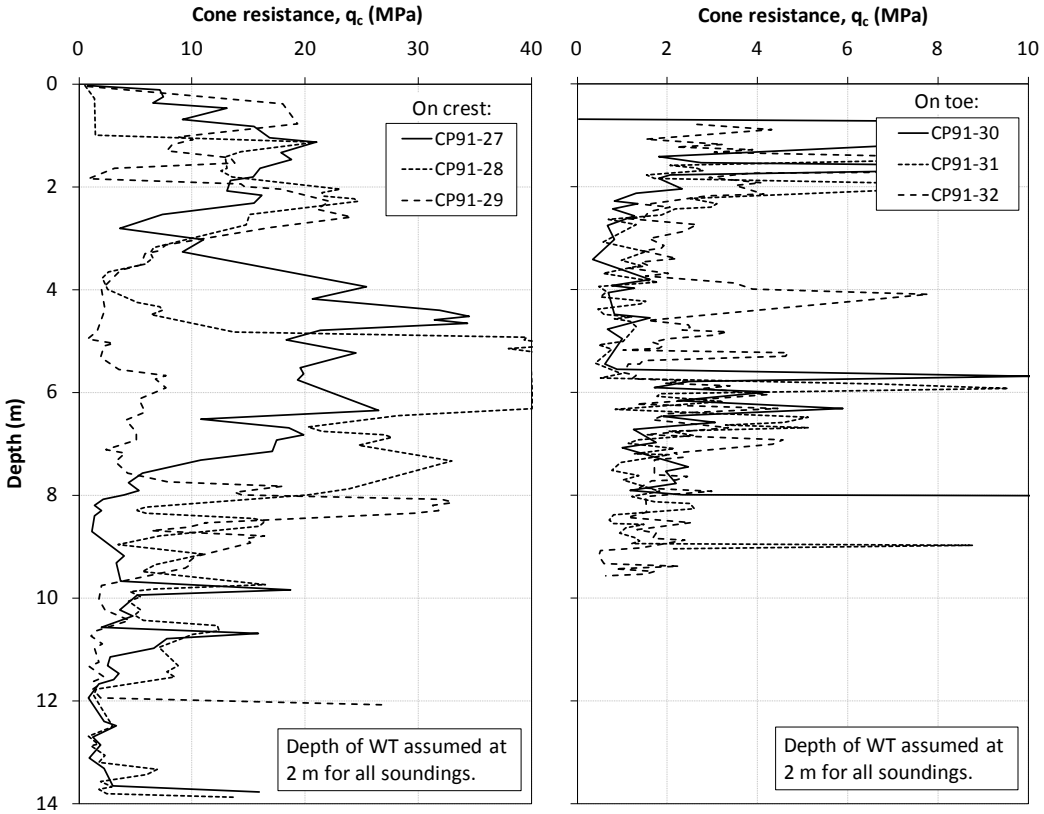


Figure 3.15 Cone resistance (q_c) profiles from the crest and toe of the Sullivan tailings dam. Replotted from Jefferies and Been (2006).

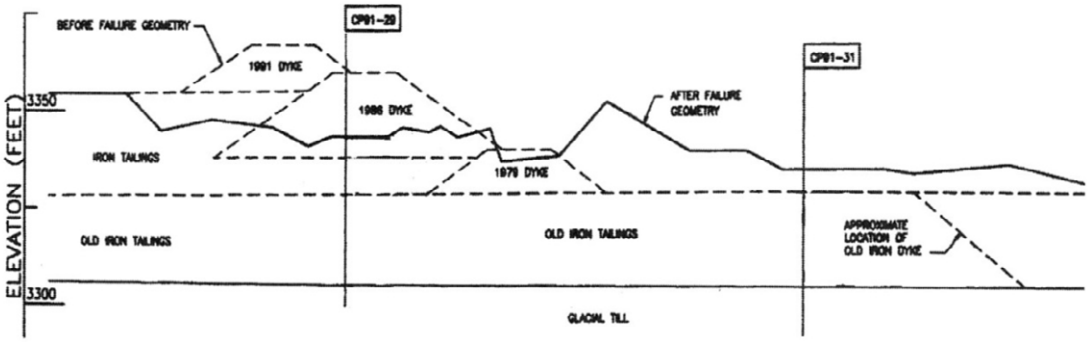


Figure 3.16 Pre and post-failure geometry of the Sullivan tailings dam and location of two CPT soundings (Jefferies and Been 2006).

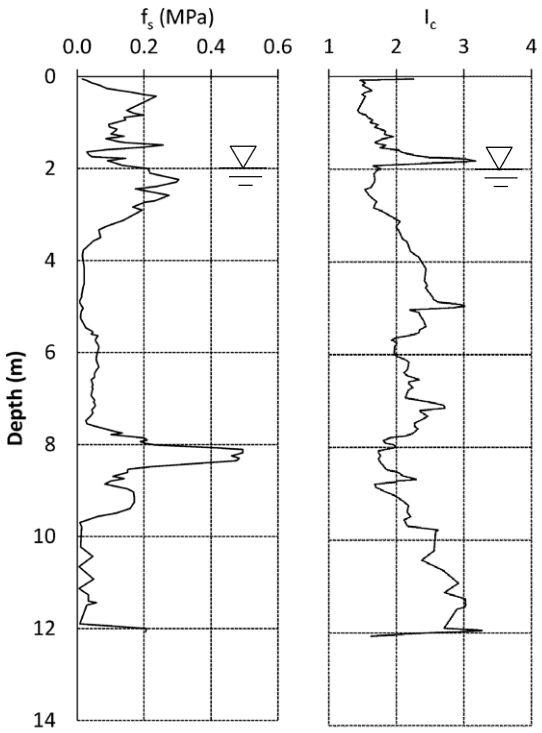
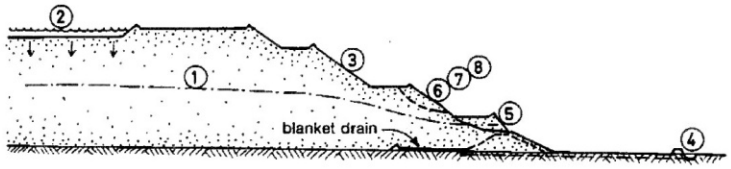
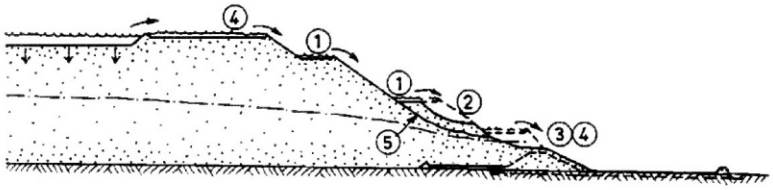


Figure 3.17 f_s and I_c (Eq. 2.11) profiles for sounding CP91-29 at the Sullivan tailings dam. f_s values from Jefferies and Been (2006)



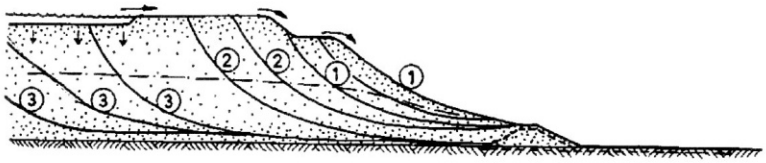
CRITICAL SECTION PRIOR TO FAILURE

1. High phreatic surface.
2. Pool against daywall.
3. Irrigation of grass on slope.
4. Effluent drain choked with slime and mud blocking blanket drain outlet pipe.
5. Seep on slimes buttress.
6. Sloughing and seep on lower slope.
7. New slips on lower slope.
8. Local slips repaired with dry slime.



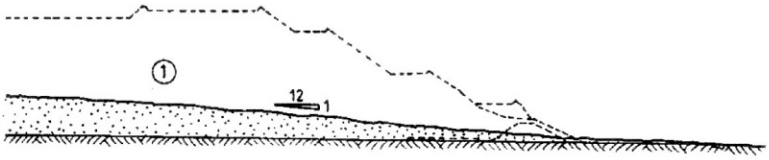
CRITICAL SECTION DURING EARLY STAGES OF FAILURE

1. Berms overtop after thunderstorm.
2. Loose infill to earlier failures on lower slope erodes.
3. Slimes buttress starts to fail.
4. Pool commences overtopping and erodes slopes and slimes buttress.
5. Unstable lower slope fails and is washed away.



CRITICAL SECTION DURING FAILURE

1. Lower slopes fail and are washed away.
2. Domino effect of local slope failures which are washed away due to eroding force of water from pool.
3. Major slope failure with massive flow of slime and water engulfing town.



CRITICAL SECTION AFTER FAILURE

1. 530 000 m^3 of slime washed out through breach area.

Figure 3.18 Most likely sequence of failure of the Merriespruit tailings dam (Papageorgiou 2004).

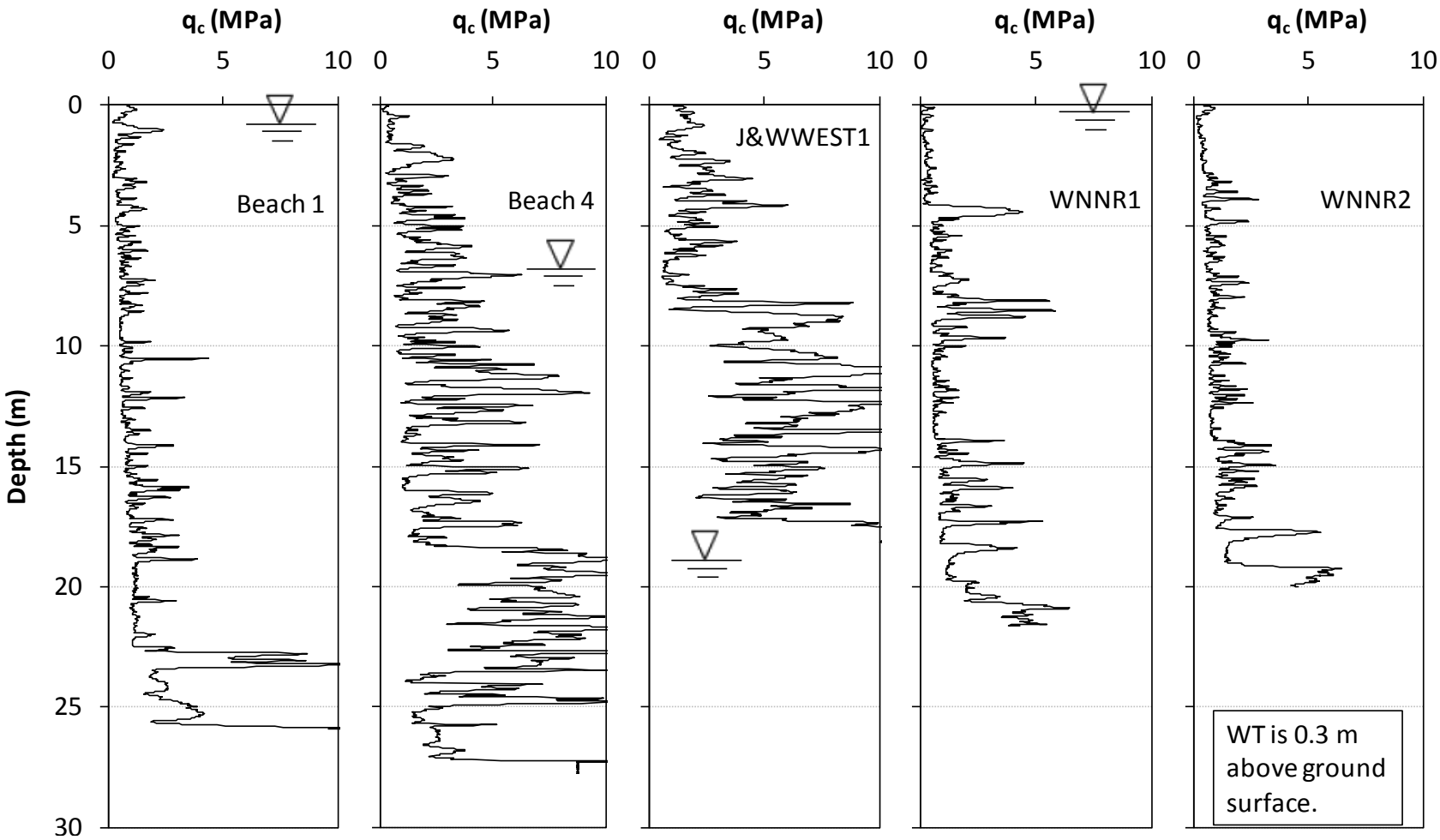


Figure 3.19 Cone penetration resistance (q_c) profiles of CPTu soundings made on the beach of the Merriespruit tailings dam.

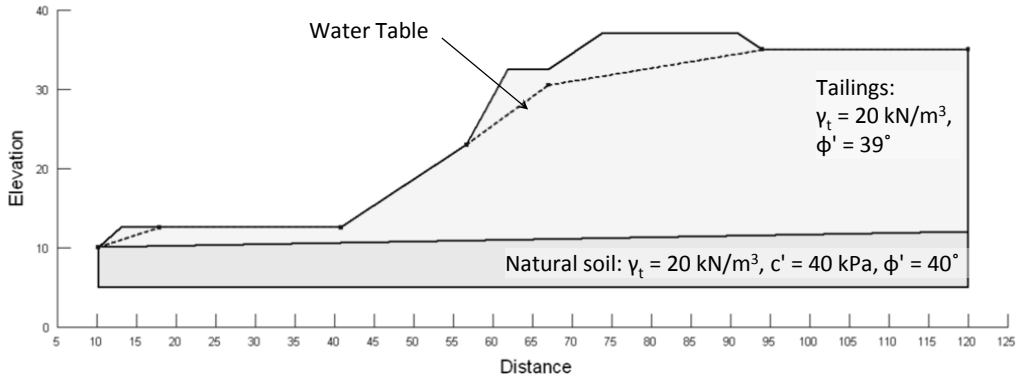


Figure 3.20 Fourth stage of retrogressive failure in Merriespruit Tailings Dam as modelled by Jones & Wagener Consulting Civil Engineers (from J&W files).

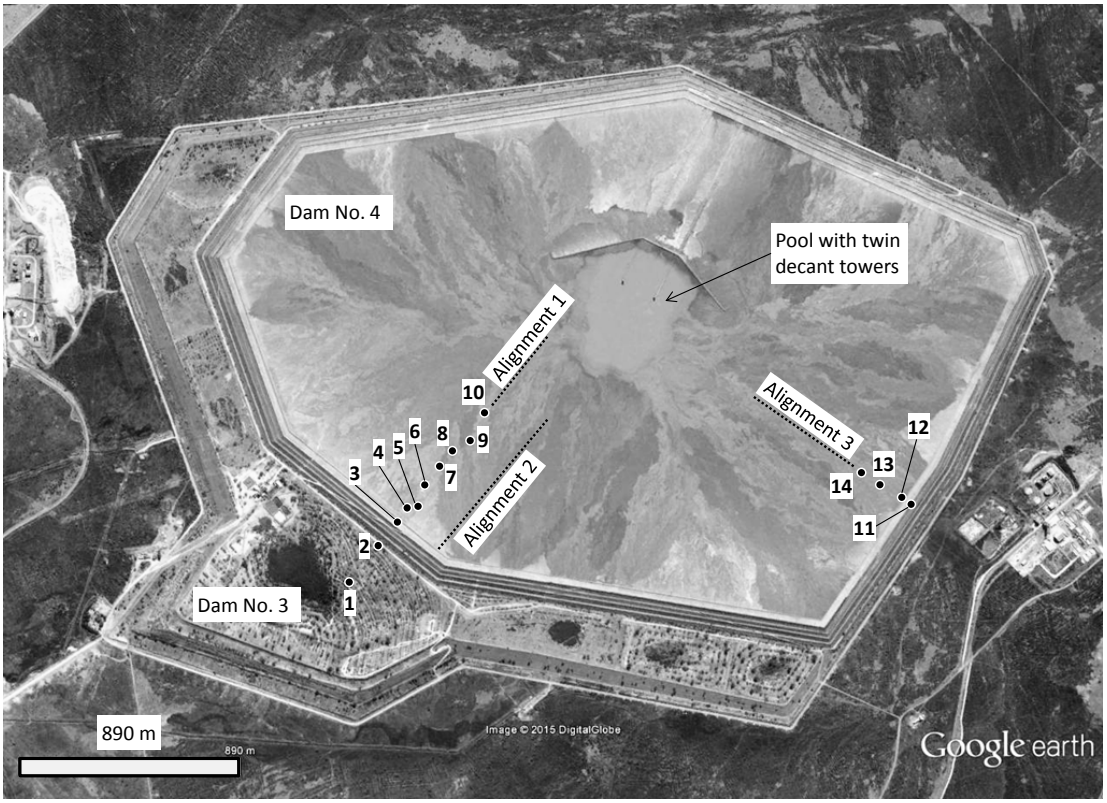


Figure 3.21 Aerial view of the Impala TSF. Dots indicate approximate location of CPTu soundings. Labels indicate numbering of CPTu. Image extracted from Google Earth.

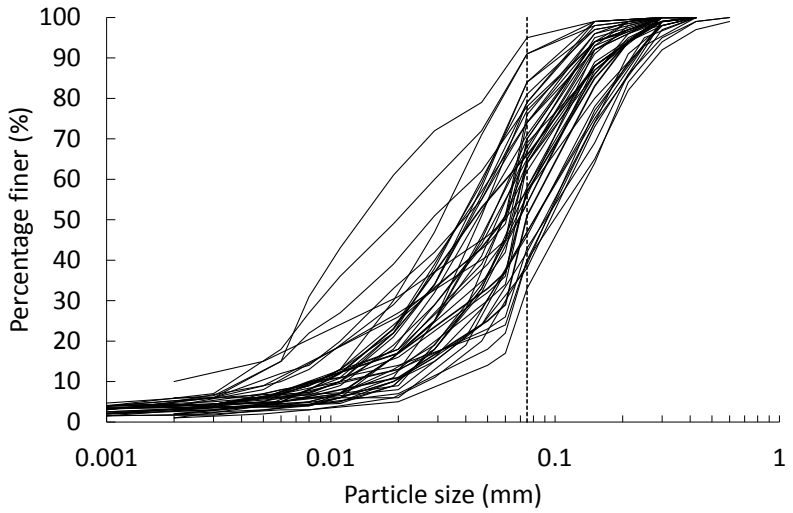


Figure 3.22 GSD curves of 49 samples recovered from the Impala TSF during the midlife investigation. Note: Dashed line indicates 75 µm.

4 Implementation of the Olson & Stark and Robertson-based methods

4.1 The Olson and Stark method

4.1.1 General comments

The results of the Olson and Stark method are presented in the following sections. Implementation of the first step, i.e. the susceptibility analysis (Section 2.3.2), allowed the identification of liquefiable and non-liquefiable soils. This information was incorporated into the slope stability models required to implement the method. Detailed descriptions of the slope stability models, including which soiltypes were identified as liquefiable, are presented in Appendix A. Given the uncertainties involved, and following the approach used by Olson (2001), several scenarios were analysed for each case history. In applying the method, focus was placed on the saturated soils (typically below the water table) as these are the soils most susceptible to liquefaction.

4.1.2 Hokkaido Dam – Japan, 1968

Figure 4.1a compares the q_{c1} (Eq. 2.8) profiles calculated for Hokkaido Dam with the liquefaction susceptibility boundary (Eq. 2.22). Virtually the entire depth of probed tailings is predicted to be susceptible to liquefaction, i.e. the q_{c1} profiles plot below and to the left of the susceptibility boundary. $FS_{Triggering}$ (Eq. 2.28) and FS_{Flow} (Eq. 2.29) values were found to be smaller than 1 for all the slope stability models considered (Figure 4.4 and Figure 4.5). Given that a flow failure developed at this site, the results of the three steps of the method are correct.

4.1.3 Mochikoshi Dam (Dykes 1 and 2) – Japan, 1978

Figure 4.1b compares the q_{c1} profiles calculated for Mochikoshi Dam with the liquefaction susceptibility boundary. The entire depth of probed tailings is predicted to be susceptible to liquefaction. $FS_{Triggering}$ and FS_{Flow} values were found to be smaller than 1 for the four slope stability models considered for Dyke 1 and the five slope stability models considered for Dyke 2 (Figure 4.4 and Figure 4.5). The results of all three steps of the liquefaction analysis are correct for Dyke 1, as a flow failure was induced by the main shock of the Izu-Ohshima-Kinkai earthquake. As for Dyke 2, the method's prediction of liquefaction being triggered is in all likelihood correct as Dyke 2 seems to have been left in a state of incipient failure by the main shock (Section 3.3). However, the prediction of flow failure is incorrect because Dyke 2 only exhibited flow failure a day after the main shock when it was subjected to an aftershock.

4.1.4 Dashihe Iron Tailings Dam (Beach and outer wall) – China, 1990

The q_{c1} profiles measured at the Dashihe Beach are mostly indicative of a contractive state (Figure 4.1c). Only sounding I8 is unambiguously indicative of a dilative state for σ'_{vo} values smaller than 150 kPa, which is approximately equivalent to a depth of 7.5 m. Therefore, as a conservative assumption, the entire profile of the beach was taken as contractive. In the Dashihe Outer Wall, the q_{c1} profiles (Figure 4.1d) indicate the presence of contractive tailings at σ'_{vo} values greater than 200 kPa, 270 kPa, 140 kPa and 270 kPa for soundings I4, I5, II2 and II4 respectively. The depths associated with these levels of stress are 12 m, 17 m, 13.5 m and 17 m respectively. Comparison of these depths with the water table depths reported in Figure 3.12 indicates that, except for sounding II2, there is a close correspondence between the depth of the water table and the depth at which contractive tailings are detected. Therefore, all tailings below the water table of the Dashihe outer wall were taken here as contractive.

$FS_{Triggering}$ values (Figure 4.4) were found to be greater than 1 for the four slope stability models considered for the beach and the two slope stability models considered for the outer wall. As triggering of liquefaction was not predicted, a post-triggering analysis was not carried out.

Given that the analysis of Amante (1993) showed that liquefaction could be triggered at both the beach and outer wall (although very limited at the outer wall), the predictions regarding liquefaction susceptibility made by the method are considered to be correct. The prediction of $FS_{Triggering} > 1$ for the beach is incorrect because Amante's analysis showed that a small flow failure does develop at that location. However, the prediction of $FS_{Triggering} > 1$ for the outer wall is considered correct because Amante's analysis showed that liquefaction would be triggered on only a very limited portion of the outer wall. An $FS_{Triggering} > 1$ for the beach also means that the method did not predict the small flow failure of tailings towards the pond.

4.1.5 Sullivan Tailings Dam – Canada, 1991

The q_{c1} profiles from the crest of the Sullivan Dam indicate contractive states at different depths, whereas the soundings made at the toe indicate mostly contractive states (Figure 4.2). The interpretation of these results is further complicated by the fact that the soundings were performed through the post-failure geometry of the dam, making it virtually impossible to determine the pre-failure depth at which tailings can be expected to be contractive. As a simplifying assumption, it was considered in the slope stability models that the dyke tailings were dilative, whereas the impounded tailings were contractive. $FS_{Triggering}$ and FS_{Flow} values were found to be smaller than 1 for the four slope stability models considered (Figure 4.4 and Figure 4.5). Given that a flow failure did occur at the Sullivan Tailings Dam, the results of the Olson and Stark method are correct.

4.1.6 Merriespruit gold tailings dam – South Africa, 1994

The five q_{c1} profiles (Figure 4.3) of the Merriespruit dam indicate that the tailings are contractive. $FS_{Triggering}$ and FS_{Flow} values were found to be smaller than 1 for the four slope stability models considered (Figure 4.4 and Figure 4.5). Given that a flow failure did occur at Merriespruit, the results of the Olson and Stark method are correct. It is worth reiterating that in the slope stability analyses conducted for the Merriespruit tailings dam, it was the eroded geometry of the dam that was considered (Section 3.6 and Appendix A.6).

4.2 The Robertson-based method

4.2.1 General comments

The results of the susceptibility and triggering analyses of the Robertson-based method are presented in the following sections. As explained in Section 2.2.1 the post-triggering analysis was not implemented as the data available for most of the case histories was of insufficient quality to arrive at meaningful results. Furthermore, due to its characteristics, the triggering analysis can only be implemented on seismic case histories (Sections 2.4.4 and 2.4.5). Only the profiles of $Q_{tn,cs}$ and factors of safety are presented in the figures herein. Appendix B contains figures with profiles of additional parameters such as: σ'_v, σ_v, τ_h, K_α, CSR, and CRR_α. In applying the method, focus was placed on the saturated soils (typically below the water table) as these are the soils most susceptible to liquefaction.

4.2.2 Hokkaido Dam – Japan, 1968

The $Q_{tn,cs}$ profiles of Hokkaido Dam (Figure 4.6a) indicate that, regardless of the I_c value used, the tailings at depths between 1 m to 6 m are susceptible to liquefaction (i.e. $Q_{tn,cs} < 70$). The profiles of factor of safety (Eq. 2.36) calculated using $I_c = 2.6$ indicate that triggering of liquefaction occurred at depths between 1 m to 6 m (Figure 4.6b). An even more widespread triggering of liquefaction is predicted when using $I_c = 2.05$. This outcome is a result of the greater resistance to liquefaction that Robertson (2009b) attributes to finer grained (higher I_c) soils. The predictions of the method with regards to susceptibility and triggering of liquefaction are correct, as they are in agreement with the flow failure that developed at Hokkaido.

4.2.3 Mochikoshi Dam (Dykes 1 and 2) – Japan, 1978

The $Q_{tn,cs}$ profiles (Figure 4.7) at Mochikoshi dam indicate that virtually the entire depth of probed tailings was susceptible to liquefaction. This is especially true for tailings at depths greater than about 4 m. The profiles of factor of safety (Figure 4.8) indicate triggering of liquefaction of virtually the entire depth of tailings below 5 m for both dykes. The predictions of the method with

regards to susceptibility and triggering of liquefaction are correct, as they are in agreement with the flow failure that developed at Dyke 1 immediately after the main shock of the earthquake, and the flow failure that developed at Dyke 2 after receiving an aftershock.

For both dykes there are considerable segments of the profile for which the factor of safety is zero (Figure 4.8). This is caused by τ_h/S_u estimations that are greater than 0.88 and thus lead to K_α (Eq. 2.32) and CRR_α (Eq. 2.35) equal to zero. The implication of this is that the methodology would have predicted an FS = 0 (Eq. 2.36) regardless of the earthquake characteristics (M_w, a_{max}), i.e. regardless of the value of *CSR*.

4.2.4 Dashihe Iron Tailings Dam (Beach and outer wall) – China, 1990

The results corresponding to the beach of the Dashihe Dam will be presented first. The profiles of $Q_{tn,cs}$ (Figure 4.9a) show that for the three CPTs considered, the tailings below the water table are susceptible to liquefaction. As for the profiles of factor of safety against triggering (Figure 4.9b), the three CPTs considered indicate values very close, and in some instances smaller than, one. These predictions regarding susceptibility and triggering of liquefaction are correct, as they are consistent with the triggering of liquefaction predicted by Amante (1993) for the tailings under the pond and the beach area near the pond.

With regards to the outer wall of the Dashihe Dam, the $Q_{tn,cs}$ profiles (Figure 4.10a) indicate the presence of tailings below the water table that are marginally liquefiable ($Q_{tn,cs} \approx 70$) in soundings I5 and II4, and soils that are liquefiable ($Q_{tn,cs} < 70$) in soundings I4 and II2. As for the profiles of factor of safety against triggering of liquefaction (Figure 4.10b), the values calculated from soundings I5 and II4 are greater than 1 (close to 2) for virtually the entire depth of tailings, whereas the values calculated from soundings I4 and II2 were smaller than one for significant portions of the profile. The prevalence of values of factor of safety smaller than one is especially noticeable in profile II2. The predictions regarding susceptibility to liquefaction for the outer wall are considered correct because the analysis made by Amante (1993) concluded that triggering of liquefaction was possible in the outer wall. However, in Amante's analysis liquefaction was only predicted to be triggered in a very limited portion of the outer wall. This is inconsistent with the more widespread triggering of liquefaction predicted by the Robertson-based method when using sounding II2.

4.2.5 Sullivan Tailings Dam – Canada, 1991

The $Q_{tn,cs}$ profile (Figure 4.11) indicates the presence of two layers susceptible to liquefaction. The first one extends between depths of 4 m and 5.5 m, and the second one between depths of approximately 10 m to 12 m. These results are consistent with the manifestations of soil liquefaction that took place in the dam. Triggering of liquefaction was not assessed as this case history did not include seismic loading.

4.2.6 Merriespruit gold tailings dam – South Africa, 1994

The $Q_{tn,cs}$ profiles calculated with I_c = 2.2 (Figure 4.12) and I_c = 2.8 (Figure 4.13) show that the tailings are mostly predicted to be liquefiable. As expected, the susceptibility to liquefaction is greater when $Q_{tn,cs}$ is calculated with I_c = 2.2. These results are consistent with the flow failure that took place in the Merriespruit tailings dam. Triggering of liquefaction was not assessed as this case history did not include seismic loading.

4.3 Conclusions

Two methods for assessing the liquefaction potential of soils using the CPT were implemented on seven TSF case histories, five of which involved seismic loads. One of the methods corresponds to the procedures outlined by Olson and Stark (2002), and Olson and Stark (2003) and the other method is based on the procedures outlined by Robertson (2009b) and Robertson (2010).

The susceptibility, triggering, and post-triggering analyses of the Olson & Stark method were implemented on the seven case histories. The susceptibility analysis correctly predicted that the tailings involved in all the case histories were susceptible to liquefaction. However it is noted that these correct predictions could be the result of the susceptibility criteria being too conservative for a generalised implementation in TSFs (Section 2.3.2). The triggering analysis correctly predicted the onset, or not, of liquefaction in six of the seven case histories. The single incorrect performance prediction was made for the Dashihe beach, in which the method failed to identify the triggering of liquefaction predicted by the analysis of Amante (1993). Regarding the post-triggering analysis, the method made incorrect predictions for two of the case histories. These were the Mochikoshi dyke 2, for which a flow failure was predicted, and Dashihe beach, for which a flow failure was not predicted because triggering had also not been predicted in the triggering analysis. A post-triggering analysis was not conducted on the Dashihe outer wall because the method correctly predicted that liquefaction had not been triggered in this case history, thus making the post-triggering analysis unnecessary.

The susceptibility analysis of the Robertson-based method was implemented on the seven case histories and the triggering analysis was implemented on the five seismic case histories. The susceptibility analysis correctly predicted that the tailings involved in all the case histories were susceptible to liquefaction. The triggering analysis correctly predicted the performance of four of the five seismic case histories on which it was implemented. The incorrect prediction was made for the Dashihe outer wall, for which the method predicted triggering of liquefaction.

Table 4.1 presents a summary of the validity of the predictions made by the Olson and Stark, and the Robertson-based methods. The susceptibility analysis of both methods performed equally well: all tailings deposits were correctly classified as susceptible to liquefaction. Similarly, when considering the triggering analysis of the seismic case histories, both methods made four out of five correct predictions. In general the performance of both methods seems acceptable, with the Olson and Stark method erring on only 3 out of 21 predictions and the Robertson-based method erring on

only 1 out of 12 predictions. The positive performance of the methods is somewhat surprising considering the criticisms that were made to some of their underlying equations (Sections 2.3, 2.4, and 2.7). A possible explanation is that the TSF case histories on which the methods were implemented involved tailings in such a loose state that a correct prediction was inevitable. Additionally, given that liquefaction was triggered in six of the seven case histories considered in this chapter (Table 3.1), any undue conservatism of the methods would have favoured their performance. It is likely that a more fair assessment of the methods could have been achieved by considering more border-line cases and, in particular, TSFs in which an undrained response is suspected but in which liquefaction was not triggered (e.g. TSFs that successfully withstood an earthquake). However, a difficulty with the latter type of case history, is that TSFs in which liquefaction was not triggered are seldom documented in public technical literature.

The results of this chapter emphasise that making correct performance predictions does not necessarily equate to the validation of a method. Instead, it is imperative to make a critical assessment of the physics and the experimental data on which the method is based, as was done in Chapter 2. Such an assessment can help identify situations in which the ability of the methods to properly predict liquefaction related phenomena may be compromised.

In the remainder of the thesis, the focus will shift to studying the sensitivity of the state parameter ψ, as estimated from CPT results using Eq. 2.45, to the variability of λ within a TSF. The Impala TSF (Section 3.7) will be one of the TSFs used to assess this sensitivity. Accordingly, the next chapter will explain how the data of the CPTu soundings conducted at the Impala TSF was processed.

4.4 Tables and figures

Table 4.1 Summary of the validity of the predictions made by the methods.

	Olson and Stark method			**Robertson-based method**	
	Susceptibility	Triggering	Post-Triggering	Susceptibility	Triggering
Hokkaido[a]	✓	✓	✓	✓	✓
Mochikoshi dyke 1[a]	✓	✓	✓	✓	✓
Mochikoshi dyke 2[a]	✓	✓	×	✓	✓
Dashihe beach[a]	✓	×	×	✓	✓
Dashihe outer wall[a]	✓	✓	n/a	✓	×
Sullivan	✓	✓	✓	✓	n/a
Merriespruit	✓	✓	✓	✓	n/a

Note: a) Seismic case history. n/a = not applicable. ✓ = correct prediction. × = incorrect prediction.

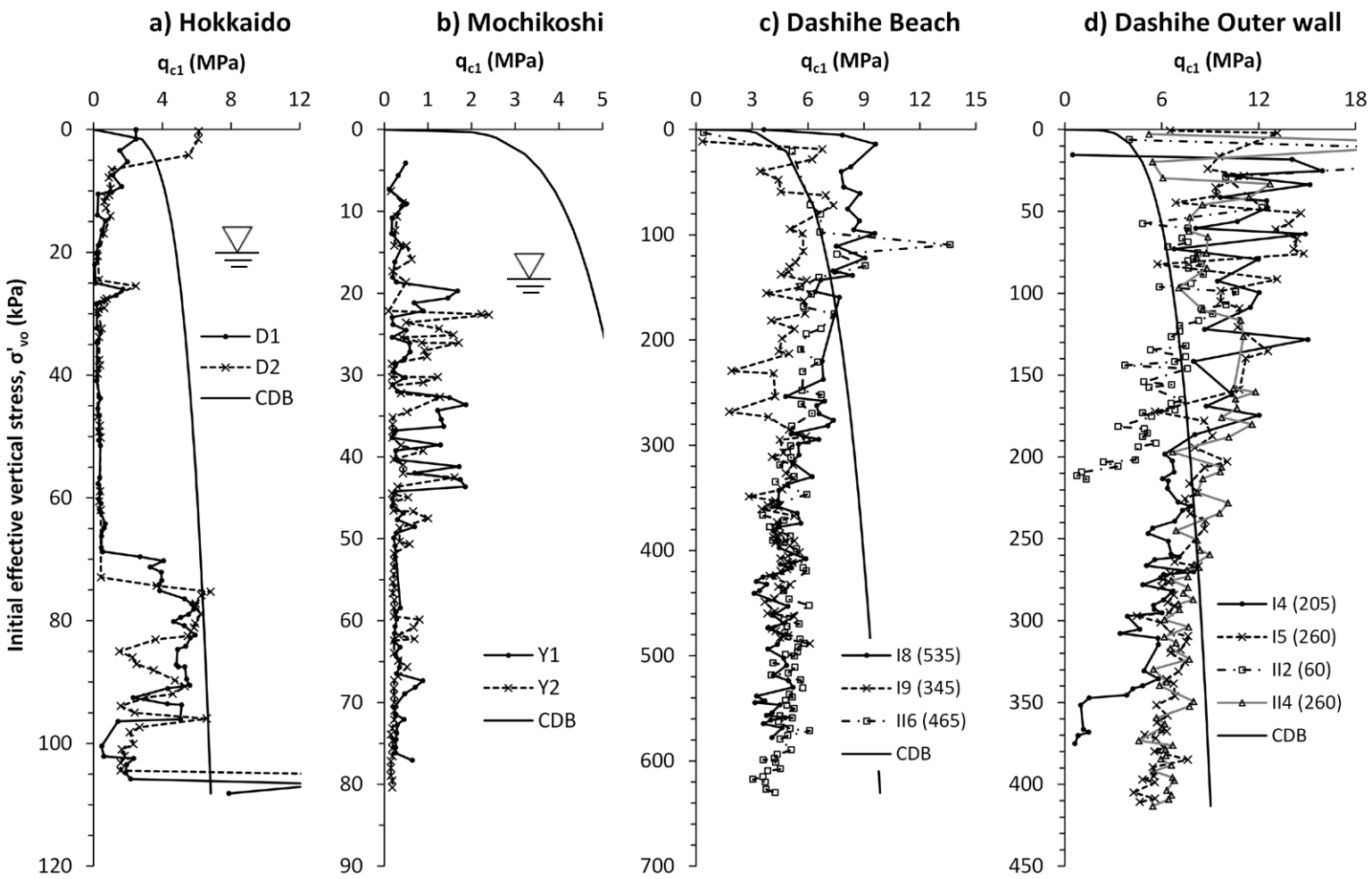


Figure 4.1 Liquefaction susceptibility at Hokkaido, Mochikoshi and Dashihe dams using the Olson & Stark method. Notes: CDB = Contractive-dilative boundary (Eq. 2.22). The numbers in parenthesis in the legends of parts c) and d) indicate the σ'_{vo} value in kPa at which the water table is located.

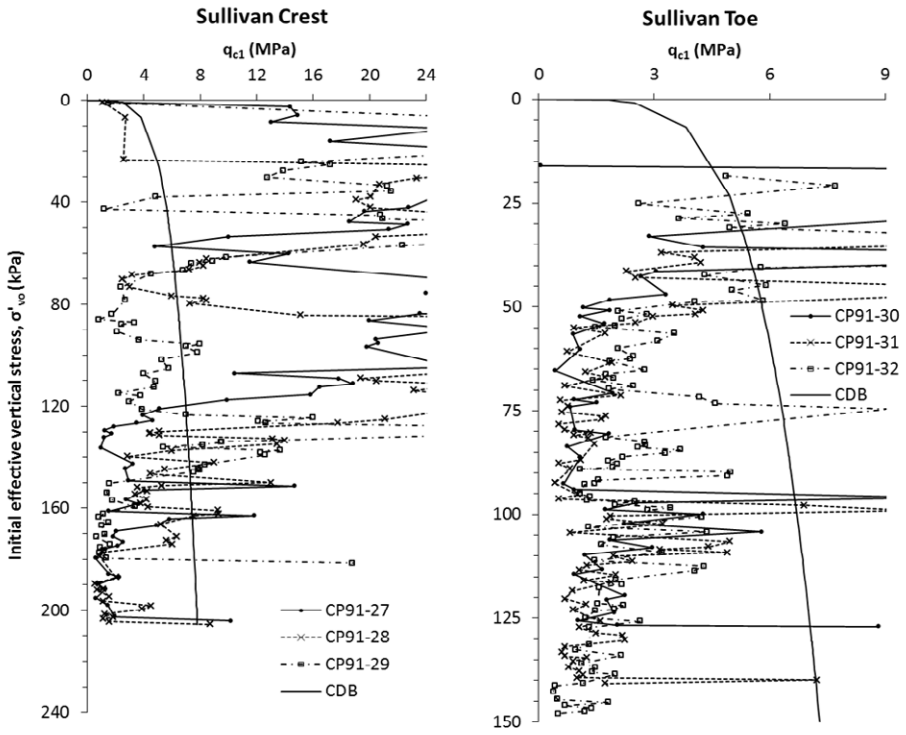


Figure 4.2 Liquefaction susceptibility at the Sullivan Tailings Dam using the Olson & Stark method. CDB = Contractive-dilative boundary (Eq. 2.22). Notes: Water table depth for sounding CP91-29 was 2 m (σ'_{vo} ≈ 45 kPa). Water table depth was assumed equal for all other soundings.

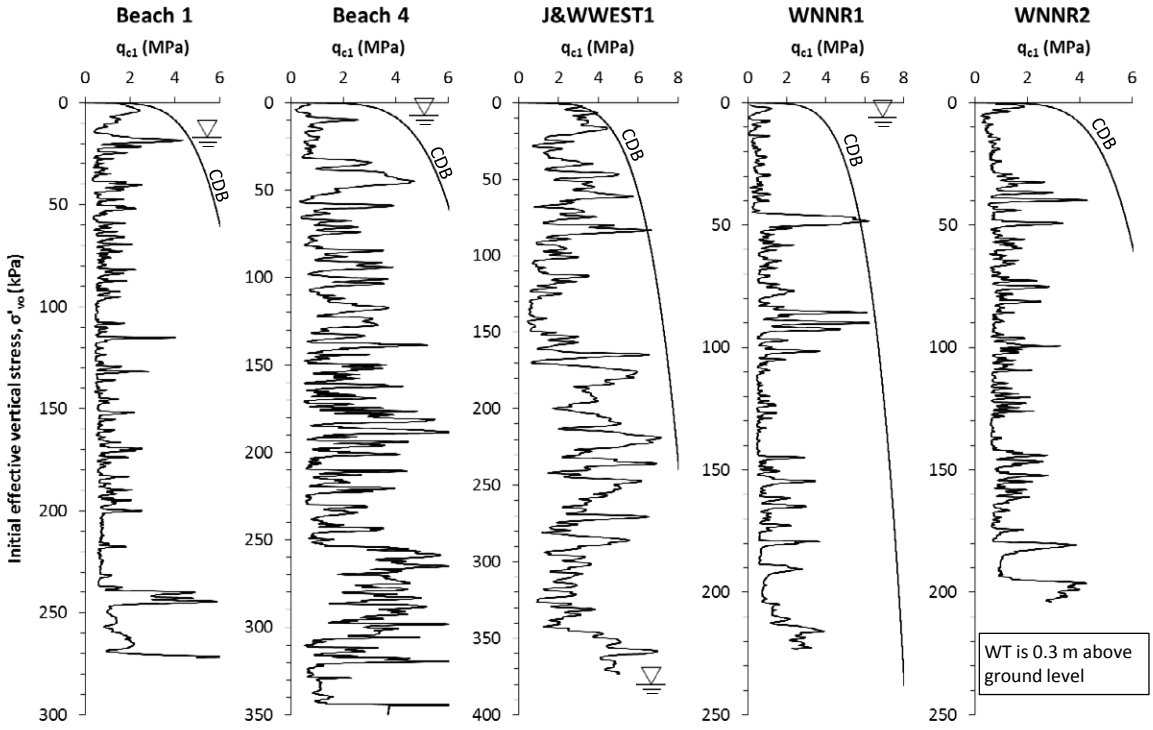


Figure 4.3 Liquefaction susceptibility at the Merriespruit tailings dam using the Olson & Stark method. Note: CDB = Contractive-dilative boundary (Eq. 2.22).

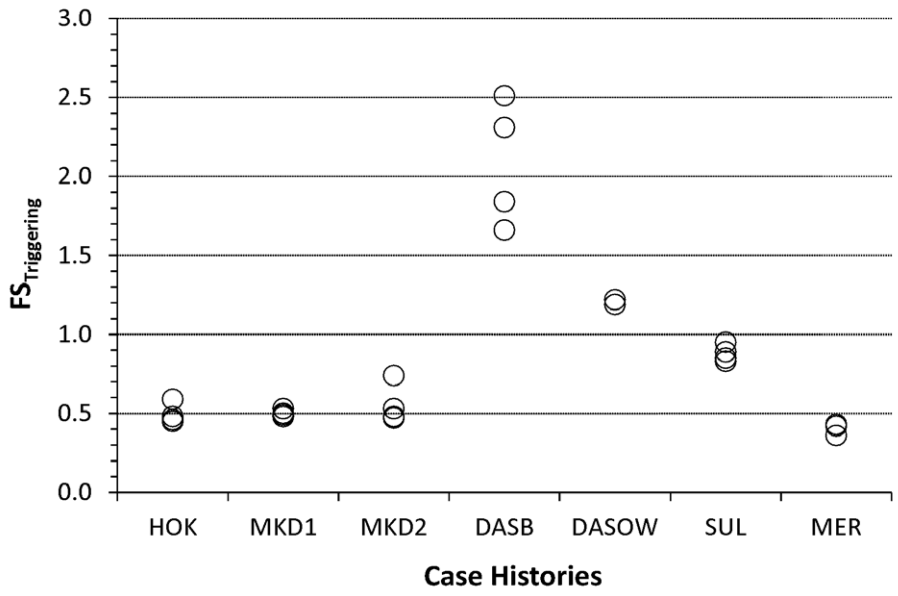


Figure 4.4 Factors of safety from the triggering analysis of the Olson and Stark method. HOK = Hokkaido, MKD1 = Mochikoshi Dyke 1, MKD2 = Mochikoshi Dyke 2, DASB = Dashihe Beach, DASOW = Dashihe Outer Wall, SUL = Sullivan, MER = Merriespruit.

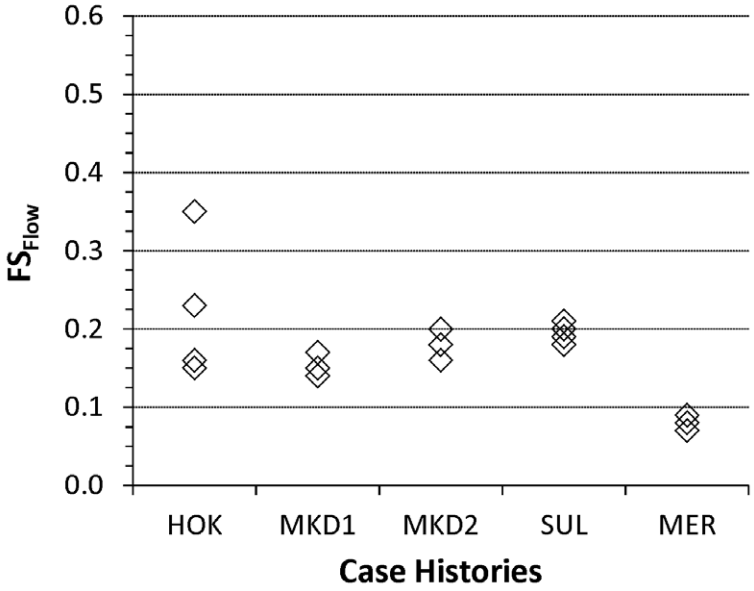


Figure 4.5 Factors of safety from the post-triggering analysis of the Olson and Stark method. HOK = Hokkaido, MKD1 = Mochikoshi Dyke 1, MKD2 = Mochikoshi Dyke 2, SUL = Sullivan Dam, MER = Merriespruit Dam.

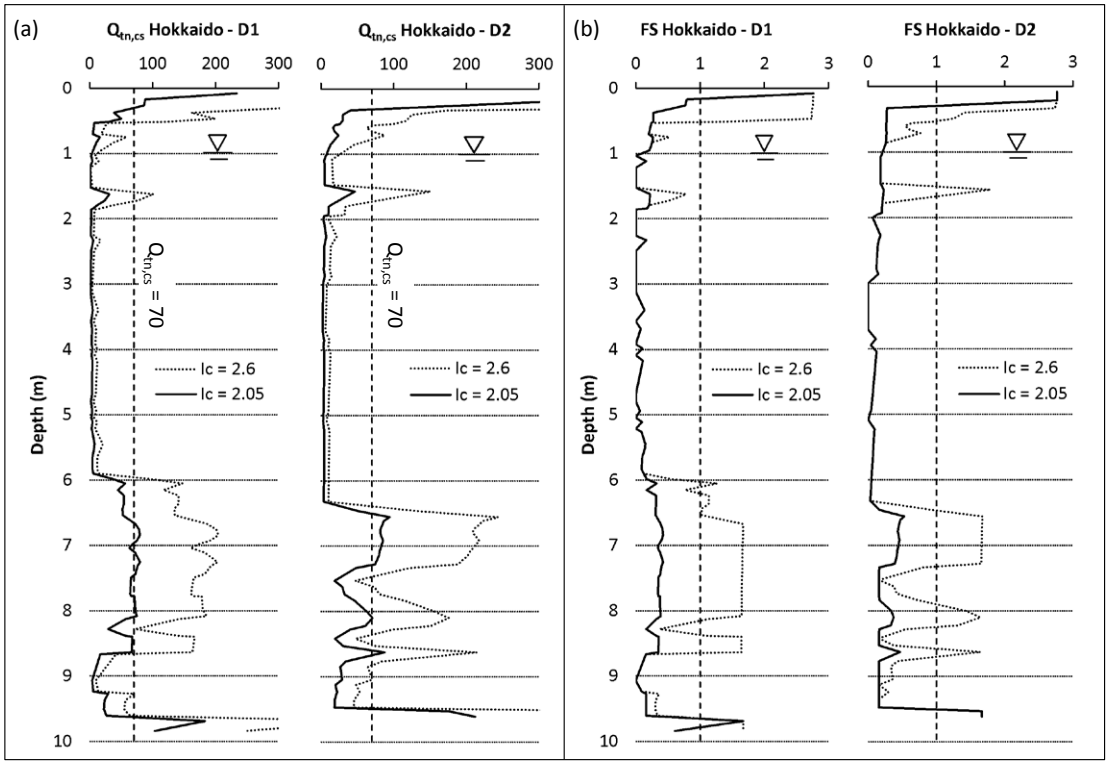


Figure 4.6 Results for Hokkaido dam of the Robertson-based method. (a) $Q_{tn,cs}$, (b) Factor of safety against triggering of liquefaction. Note: Code after hyphen indicates CPT sounding.

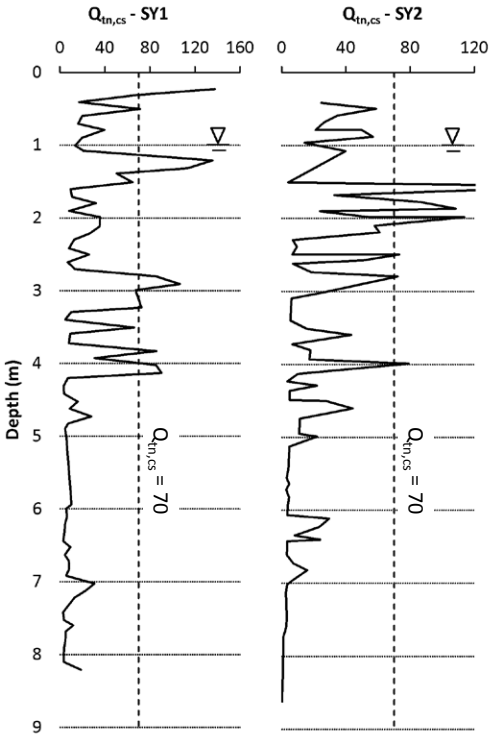


Figure 4.7 $Q_{tn,cs}$, profiles at the Mochikoshi Dam. Note: Code after hyphen indicates CPT sounding.

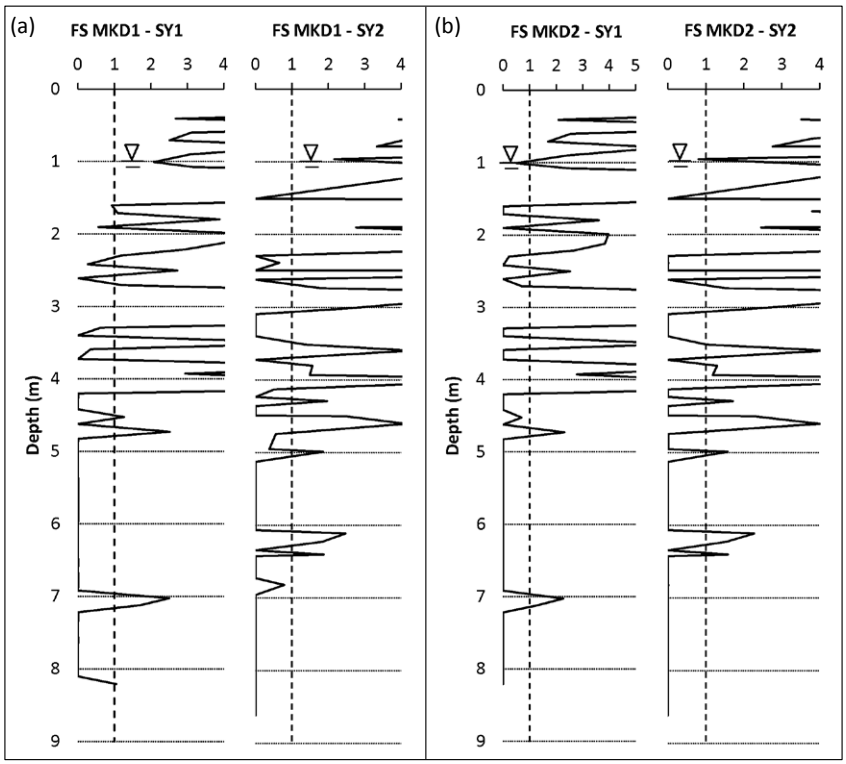


Figure 4.8 Profiles of factor of safety determined with the Robertson-based method. (a) Mochikoshi Dyke 1 (MKD1), (b) Mochikoshi Dyke 2 (MKD2). Note: Code after hyphen indicates CPT sounding.

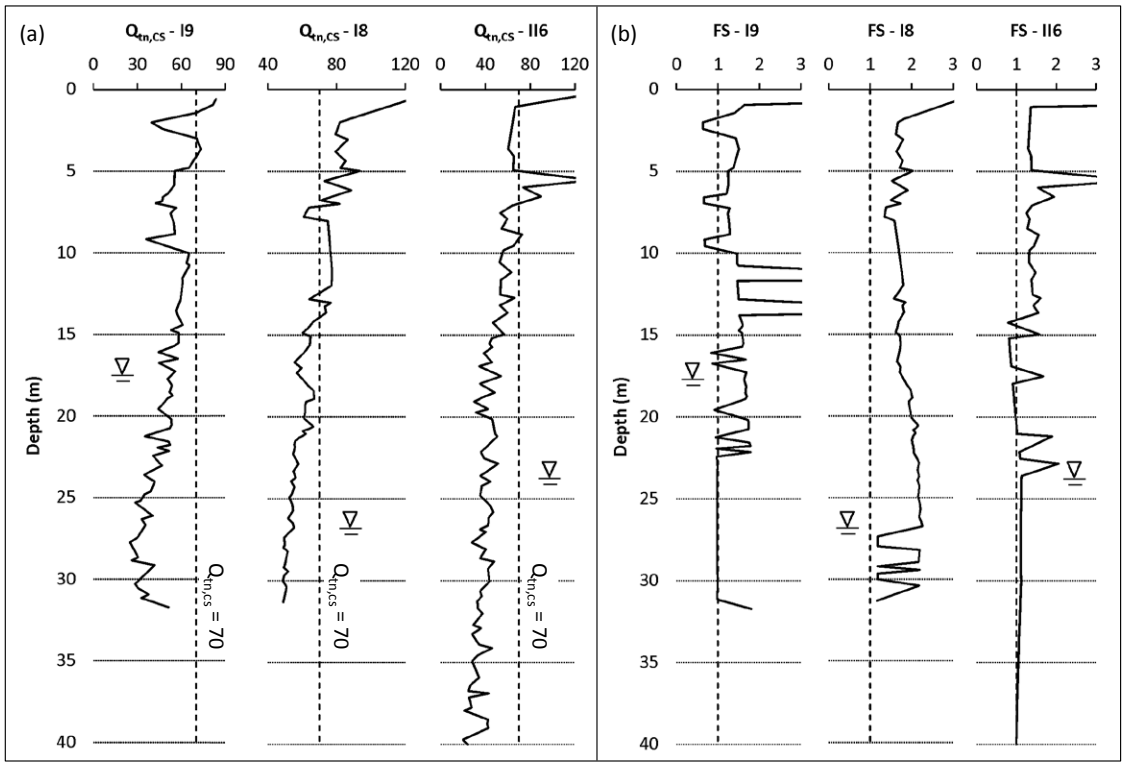


Figure 4.9 Results of the Robertson-based method for Dashihe Beach. (a) Profiles of $Q_{tn,cs}$, (b) profiles of factor of safety. Note: Code after hyphen indicates CPT sounding.

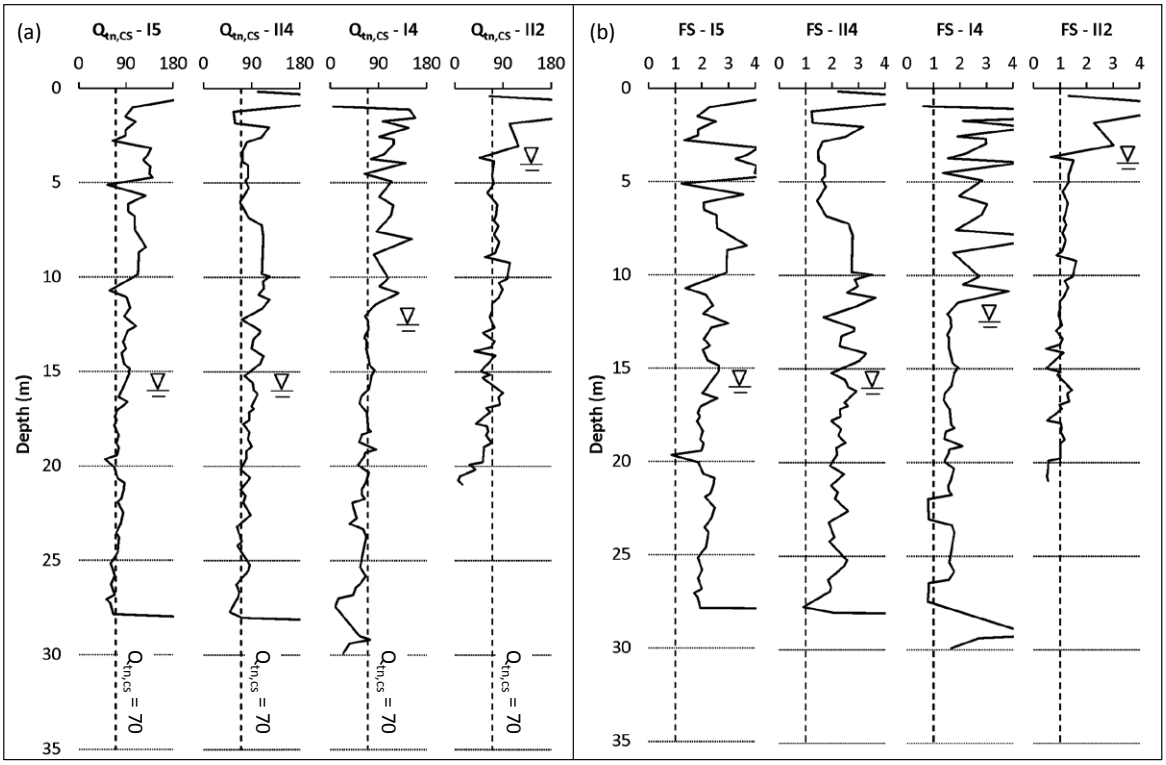


Figure 4.10 Results of the Robertson-based method for Dashihe Outer Wall. (a) Profiles of $Q_{tn,cs}$, (b) profiles of factor of safety. Note: Code after hyphen indicates CPT sounding.

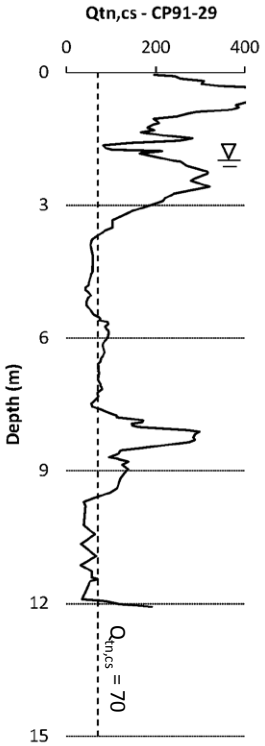


Figure 4.11 $Q_{tn,cs}$, profiles at Sullivan dam computed from CPT sounding CP91-29.

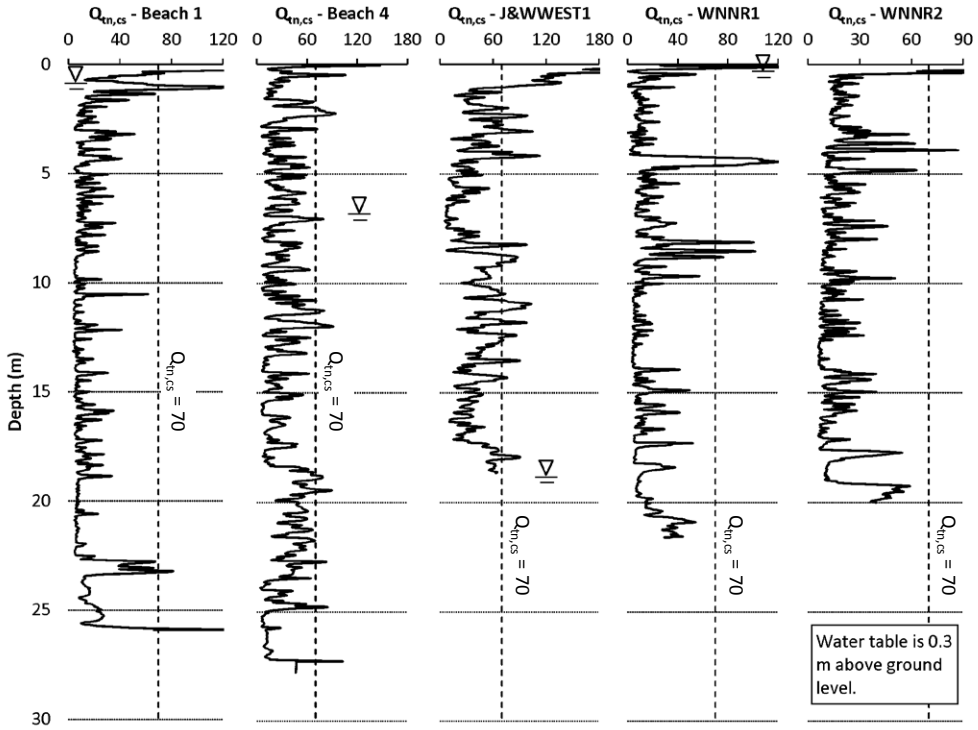


Figure 4.12 $Q_{tn,cs}$ profiles at Merriespruit Dam calculated using I_c = 2.2. Note: Code after hyphen indicates CPTu sounding.

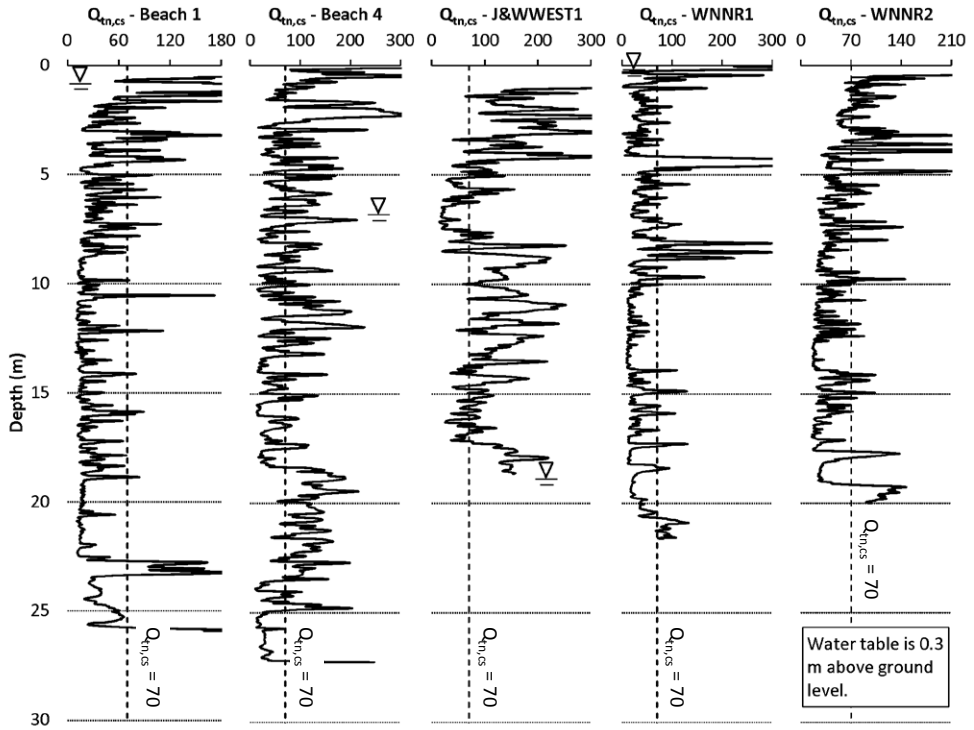


Figure 4.13 $Q_{tn,cs}$ profiles at Merriespruit Dam calculated using I_c = 2.8. Note: Code after hyphen indicates CPTu sounding.

5 Processing of the CPTu data of the Impala Platinum TSF

5.1 Introduction

As will be shown in Chapter 8, the sensitivity of ψ to variations in λ is a function of the normalised excess pore pressure B_q (Eq. 2.16). Accordingly, a reliable assessment of this sensitivity in the Impala TSF, requires the processing of the raw CPTu data to determine an applicable average B_q value. The current chapter describes in detail how 14 CPTu soundings made at the Impala Platinum TSF were processed. Additionally, since this CPTu data does not include f_s readings, a new SBT index ($I_{Q\text{-}Bq}$) independent of f_s, is presented. The proposed $I_{Q\text{-}Bq}$ is based on the Q-B_q classification chart proposed by Robertson (1991) (Figure 5.1). $I_{Q\text{-}Bq}$ is likely to be particularly useful in the South African context, where historical CPTu data do not commonly include f_s readings. The numbering of the CPTu soundings used in this chapter corresponds to that shown in Figure 3.21.

5.2 Initial considerations

Jefferies and Davies (1991) noted that care should be taken when using the Q-B_q chart in dilatant soils, because in such cases the cut-off value of B_q will be governed by cavitation and B_q becomes decoupled from soiltype. Accordingly, the CPTu data from the Impala TSF was checked for cavitation. It was found that the smallest value of u_2 measured during all the soundings was -53kPa. This value was deemed sufficiently above from -90 kPa which is the pressure at which cavitation can be expected to occur provided that the pore water temperature does not exceed 50 °C. Having ruled out cavitation, the Q-B_q chart was considered adequate to interpret the CPTu data. It should also be noted that use of B_q, and thus of the chart itself, is only meaningful in saturated soils. Accordingly, only those portions of tailings that were deemed to be saturated were classified using the Q-B_q chart. Detection of saturated soils is addressed Section 5.3.

As mentioned in Section 3.7, a particularity of the CPTu soundings at the Impala TSF is that 12 of the 14 soundings involved an alternation of CPTu probing and rotary drilling due to the presence of hard cemented layers. In some instances, the depth probed by the CPTu in between runs of rotary drilling was as thin as 0.5 m. It is known that CPT results are affected by the properties of soils above and below the depth being probed (Jefferies and Been 2006; Lunne et al. 1997). Therefore it is questionable whether the CPT results of thin layers should be deemed acceptable, or disregarded due to the potentially misleading effects of the nearby hard layers. Jefferies and Been (2006) indicated that despite several research efforts, there is no standard method to allow for layering effects and recommended "*to neglect confinement or layering effects and develop estimates of liquefaction potential from data obtained away from the transition between strata.*" They further stated that this approach will yield satisfactory results provided that the layers are thicker than 0.6 m. Accordingly, in this research, all runs of CPTu that were smaller than 1.0 m were not considered in the analysis as their results could have been unduly affected by the proximity of the hard layers.

Several runs of CPTu made after drilling a hard layer had unusually low q_c values for the first half metre or so (Figure 5.2). It is believed that the tailings that exhibited these low q_c values were disturbed during the preceding drilling operation or could have fallen to the bottom of the borehole during drilling. As such, these low q_c values are not representative of the in situ condition of the tailings and were therefore excluded from the analysis.

Atypically low q_c values were also observed during the first 100 to 150 mm probed after a pause for a dissipation test (Figure 5.3). These drops in q_c readings are typical of the rod breaks or pauses in testing that have to be made approximately every metre to add a rod and perform dissipation tests. This is why the drops of q_c are seen to coincide with the depths of dissipation tests in Figure 5.3. Campanella and Robertson (1988) explained that at these pauses the tip load reduces due to creep effects in the soil. It thus follows that upon reloading to resume the test, the rods are recompressed and it takes some movement to mobilise the full resistance of the soil again. Due to these irregularities, Campanella and Robertson (1988) recommend that the CPTu data affected by pauses in the penetration is either identified or removed from the profiles. The latter approach was adopted herein.

Given that the objective of interpreting the CPTu results was to characterise the tailings, the results corresponding to the clay and decomposed norite underlying the tailings (Section 3.7.1) were excluded from the analysis. The records from the boreholes that were made next to each CPTu sounding and the CPTu data itself were used to distinguish the clay from the tailings. In some instances, the borehole logs contained qualitative soil descriptors such as “clay” and “weathered norite” that indicated the depth of the natural ground. In other cases, the specific gravity (G_s) of recovered samples was reported. Since the G_s of the tailings (≈3.5 g/cm^3) was significantly higher than the G_s of the clay (≈2.8 g/cm^3), distinction between the two soiltypes was straightforward. Additionally, a sudden decrease in q_t or increase in u_2 readings was also interpreted as an indicator of the CPTu probe having reached the clay layer. This is because clays are typically characterised by low q_t and high u_2 values (Robertson 1990). Another indicator that the CPTu probe had reached the clay layer was that the dissipation tests (Section 2.2.3) would take considerably longer (over 15 minutes) to reach equilibrium than they did in the tailings. Figure 5.4 and Figure 5.5 show examples of dissipation test results in clays and tailings, respectively.

5.3 Estimation of the in situ pore water pressure profiles

Use of the Q-B_q classification chart requires the determination of the profile of in situ water pressure (u_0) of each CPTu sounding. This was done with the results from the dissipation tests described in Section 2.2.3. Essentially, the value at which the pore water pressure (pwp) readings stabilised during a dissipation test was interpreted as the in situ water pressure. Figure 5.5 shows examples of dissipation tests in tailings that attained a stable value. It is observed that in some cases (e.g. Figure 5.5a) the pwp increased to a stable value, whereas in others (e.g. Figure 5.5b) the pwp decreased to a stable value. It is also noted that in some of the cases in which the pwp decreased to

its stable value, the pwp readings exhibited an initial peak. These different types of behaviours are normal and have been previously reported in the literature by Sully et al. (1999).

Several dissipation tests ended before pwp had stabilised. In such cases the last value of the series could have been used as an estimate of u_0, however it was found convenient to refine this estimate by performing an extrapolation procedure. Several theoretical methods have been proposed to perform such an extrapolation (Kim and Lee 2000; Rust and Clayton 1999; Teh and Houlsby 1991), however the implementation of these methods was not possible for this work because they require soil parameters such as the rigidity modulus (I_R), and the coefficient of lateral stress (K_0), which have not been measured at Impala. Accordingly, in the present study an empirical approach was adopted based on the observation of Rust and Clayton (1999) that the last part of the slope of the curve of an incomplete dissipation test can be used to estimate the unrecorded part of the dissipation curve. The adopted procedure, illustrated in Figure 5.6, was as follows:

1. The slope of the last portion of the recorded dissipation curve was interpolated with a logarithmic function.
2. The logarithmic function was extended until its value reached zero.
3. The extended portion of the logarithmic function was then numerically integrated to calculate the unrecorded part of the dissipation curve. The last value of the extrapolated dissipation curve (u_{0E}) was then taken as the u_0 estimate.

In cases in which the incomplete dissipation tests did not have enough data to interpolate the slope of the dissipation curve, u_0 was estimated by considering the results of neighbouring dissipation tests that had stabilised. Likewise, whenever the extrapolation yielded a value of u_{0E} that did not agree with the results of neighbouring dissipation tests that had stabilised, the u_{0E} value was disregarded and u_0 was interpolated from the results of the neighbouring tests.

The merit of this extrapolation procedure was assessed by applying it to the results of dissipation tests in which full dissipation had been attained, i.e., u_0 was known. These series were truncated at different values of U (the remaining extent of excess pwp dissipation, Eq. 2.21) and then u_{0E} was estimated. The degree of accuracy of the extrapolation was assessed by computing the ratio u_{0E}/u_0, with $u_{0E}/u_0 \approx 1$ being an indicator of an accurate extrapolation. The ratio u_{0E}/u_0 was then compared to the ratio of the last pwp value of the truncated series (u_{0T}) to the known value of u_0.

Figure 5.7 presents the two extreme situations observed when assessing the extrapolation procedure on complete dissipation records. Figure 5.7a shows the case in which u_{0E} was very close to the recorded u_0 value ($u_{0E}/u_0 = 0.98$), and the extrapolation has provided a better estimate of u_0 than u_{0T} ($u_{0T}/u_0 = 0.86$). Conversely, Figure 5.7b shows a case in which simply adopting u_{0T} as an estimate of u_0 yields better results than adopting u_{0E}, that is, $u_{0T}/u_0 = 0.81$ is closer to 1 than $u_{0E}/u_0 = 1.30$. The previous results show that the extrapolation procedure may not always lead to an improved estimate of u_0.

Figure 5.8 summarises the results of 25 implementations of the extrapolation procedure on complete dissipation series which were truncated at different values of U. It is noted that although it

is indeed possible for u_{0T}/u_0 to be closer to 1 than u_{0E}/u_0 (Figure 5.7b), this only occurred in one instance. For the remaining 24 implementations, u_{0E} was a better estimate of u_0 than u_{0T}. This result justifies the adoption of the extrapolation procedure to refine estimates of u_0 from dissipation tests that did not stabilise. It is also noted in Figure 5.8 that in no case was it possible to perform the extrapolation when truncating the dissipation series at a U value higher than 0.35. That is, the extrapolation procedure was only possible when at least 65% of the dissipation had already taken place.

Dissipation tests conducted close to ground level occasionally exhibited a zigzag pattern (Figure 5.9) around a central value close to zero. This behaviour was interpreted as an indication that the soil was not fully saturated and accordingly, tailings above that depth were not classified with the Q-B_q chart. The association of the zigzag pattern to partial saturation was made because this pattern was only observed above the water table, where partial saturation is more likely to occur. Additionally, a few dissipation tests made at depths below the water table exhibited erratic readings (e.g. Figure 5.10). It is hypothesised that this could have been due to a malfunction of the transducers or data acquisition system. These types of results were also excluded from the estimation of the u_0 profiles. Similar erratic readings from dissipation tests in which malfunction of the equipment was also suspected were reported by Long (2007). A sample profile of u_0 from the Impala TSF is shown in Figure 5.11.

5.4 Calculation of parameters Q and B_q

Calculation of parameters Q (Eq. 2.15) and B_q (Eq. 2.16) requires knowledge of the total (σ_{v0}) and effective (σ'_{v0}) vertical stresses. The computation of σ_{v0} and σ'_{v0} was done considering the total unit weights for saturated (25 kN/m^3) and partially saturated (23 kN/m^3) tailings that were reported in Section 3.7. The total cone resistance (q_t), required to compute Q, was calculated with Eq. 2.6 adopting a = 0.8, however the difference between q_c and q_t was negligible in all cases. A B_q histogram was computed using values sampled every 100 mm along all the soundings. The sampling was done to reduce the size of the dataset and to ensure that the all depths were uniformly sampled. The B_q histogram shows that the large majority of the values were close to zero (Figure 5.12), i.e. drained penetration. The average B_q value was computed as 0.02 and will be used in the sensitivity analysis presented in Chapter 8. The low B_q values are consistent with the negligible difference between q_c and q_t.

5.5 A soil behaviour type index for the Q-B_q classification chart

Due to the absence of f_s readings from the CPTu soundings conducted at the Impala TSF, the Q-B_q chart (Figure 5.1), and not the Q_{tn}-F_r chart (Figure 2.6b), was used to infer soil behaviour type. A feature of the Q-B_q chart is that it yields a non-numerical result, i.e., although the seven zones of the chart are labelled with numbers, they could just as well be labelled with letters. Additionally, soiltype varies discretely from one zone to another. For instance, Points A and B on Figure 5.1 yield the same

classification: Zone 4, silty mixtures – clayey silt to silty clay. Unless the user looks at the chart, it is not evident that Point A is more likely a clayey silt and Point B more likely a silty clay. This reliance on visual inspection poses a challenge to incorporate the results of the chart into mathematical computations. It is therefore desirable to develop a scalar SBT index that can capture the results of the Q-B_q chart. The SBT index ($I_{Q\text{-}Bq}$) proposed for the Q-B_q chart is defined as:

$$\begin{aligned} if\ B_q \geq 0, \quad I_{Q-B_q} &= Q \cdot 10^{-1.9 \cdot B_q} \\ if\ B_q < 0, \quad I_{Q-B_q} &= Q \cdot 10^{2.8 \cdot B_q} \end{aligned} \tag{5.1}$$

The rationale behind Eq. 5.1 is that certain contours of constant $I_{Q\text{-}Bq}$ approximate the boundaries of the Q-B_q chart (Figure 5.1). This allows the user to assume that soils with similar $I_{Q\text{-}Bq}$ will exhibit similar SBT regardless of where on the chart they plot, thus allowing for the classification of soils on a continuous scale and eliminating the need to visually inspect the chart to conduct this classification. This same rationale was adopted by Jefferies and Davies (1993) when developing I_c (Eq. 2.20), except that I_c is based on a classification chart that requires f_s readings (Figure 2.6a). I_c has proven to be useful in several geotechnical applications (e.g. Jefferies and Been (2006), Robertson and Wride (1998)) and it is believed that $I_{Q\text{-}Bq}$ can also be useful when working with CPTu data that do not include f_s or where f_s is deemed unreliable. For example, Reid (2014) presented a CPT sounding in which some f_s measurements yielded negative values, thus precluding the possibility of calculating I_c. This is a situation in which $I_{Q\text{-}Bq}$ could have been used as an alternative classification index. Additionally, $I_{Q\text{-}Bq}$ may be of particular interest in the South African context in which it is quite common for historical CPT data to not include f_s readings. Even when f_s readings are available, $I_{Q\text{-}Bq}$ can provide a simple means of double checking the soil behaviour type classification made with I_c. Nonetheless, it is clearly recommendable to measure f_s in all CPT soundings as this allows for enhanced interpretations of results.

The correspondence between the zones of the Q-B_q chart and the different value ranges of $I_{Q\text{-}Bq}$ is summarized in Table 5.1. A limitation of using $I_{Q\text{-}Bq}$ is that this index on its own is unable to inform when a soil is classified in Zones 1 or 2. The index I_c proposed by Jefferies and Davies (1993) has a similar limitation, however the different applications of I_c have shown that the advantages of a quantitative SBT index outweigh this limitation. A sample profile of $I_{Q\text{-}Bq}$, which incorporates the boundaries presented in Table 5.1, is shown in Figure 5.13.

5.6 Summary

The considerations made and the equations used to process the data corresponding to the 14 CPTu soundings made at the Impala TSF have been presented. The processing of the data relied mostly on commonly used procedures with the following two exceptions being noted.

First, interpretation of incomplete dissipation tests was based on the extrapolation of the slope of the last portion of recorded data (Figure 5.6). The validity of this extrapolation procedure was

tested by implementing it on 25 complete dissipation tests. The results showed that in 24 cases, the estimation of u_0 was improved by the implementation of the method (Figure 5.8). The method has the advantage that its implementation does not require information about the state of stress or rigidity of the soil. However, it also has the disadvantage at least 65% of the dissipation must have been completed for its implementation to be feasible.

Second, a new soil behaviour type index, $I_{Q\text{-}Bq}$, was proposed. $I_{Q\text{-}Bq}$ is based on the Q-Bq classification chart proposed by Robertson (1991) and thus does not require f_s readings for its calculation. Independence from f_s was required because the CPTu soundings conducted at the Impala TSF did not include f_s. The greatest advantage of $I_{Q\text{-}Bq}$ is that it allows for quantification on a continuous scale of the results of the Q-B_q chart. This is in contrast to using one of the seven discrete and qualitative classification zones of the chart. Although it is recommended that f_s always be measured to make the most of CPT soundings, $I_{Q\text{-}Bq}$ provides a means of performing a quantitative soil behaviour type determination when f_s readings are either absent or unreliable.

The average B_q value calculated in this chapter for the Impala TSF will be used in Chapter 8 together with the SSLs of Impala tailings (Chapter 7) to assess the sensitivity of ψ to variations in λ when using Eq. 2.45 proposed by Jefferies and Been (2006). Accordingly, the experimental determination of the Impala SSLs must also be undertaken. However, before the SSLs are determined, it is imperative to understand how the SSLs of non-plastic soils are correlated to index properties. This topic will be addressed in the following chapter.

5.7 Tables and Figures

Table 5.1 Soil behaviour type from classification index $I_{Q\text{-}Bq}$.

SBT (Zone no. in Q-B_q chart)	$I_{Q\text{-}Bq}$ range
Clays - clay to silty clay (3)	< 5
Silty mixtures - clayey silt to silty clay (4)	5 to 12
Sand mixtures - silty sand to sandy silt (5)	12 to 31
Sands - clean sand to silty sand (6)	31 to 178
Gravelly sand to sand (7)	> 178

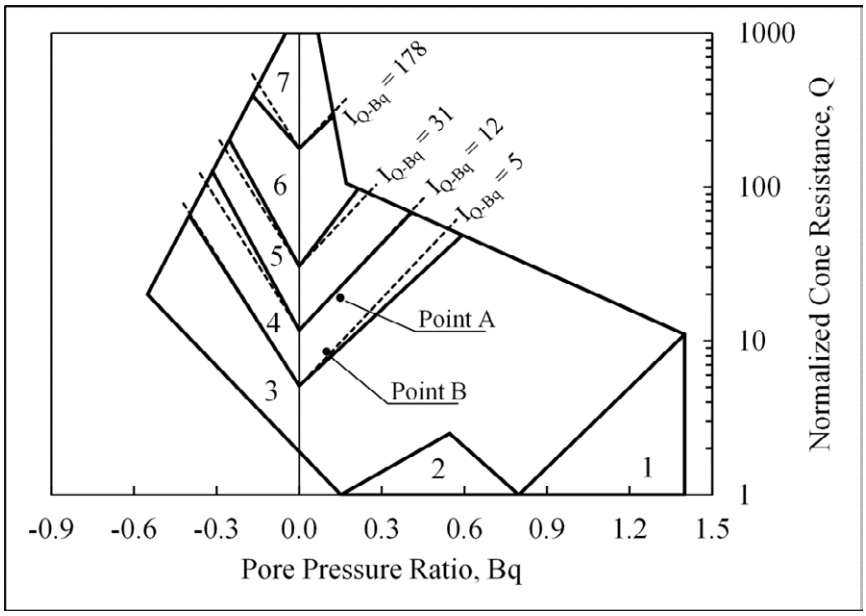


Figure 5.1 Q vs. B_q classification chart proposed by Robertson (1991) with superimposed contours of $I_{Q\text{-}Bq}$. Soiltypes: 1, sensitive, fine grained; 2, peats; 3, silty clay to clay; 4, clayey silt to silty clay; 5, silty sand to sandy silt; 6, clean sand to silty sand; 7, gravelly sand to dense sand.

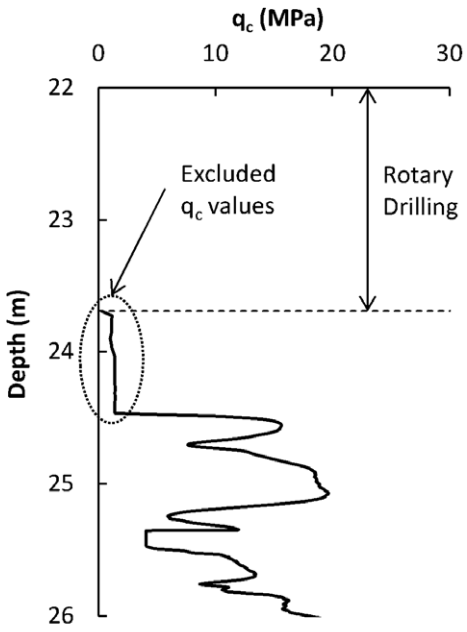


Figure 5.2 Example of the exclusion of q_c values measured immediately after rotary drilling.

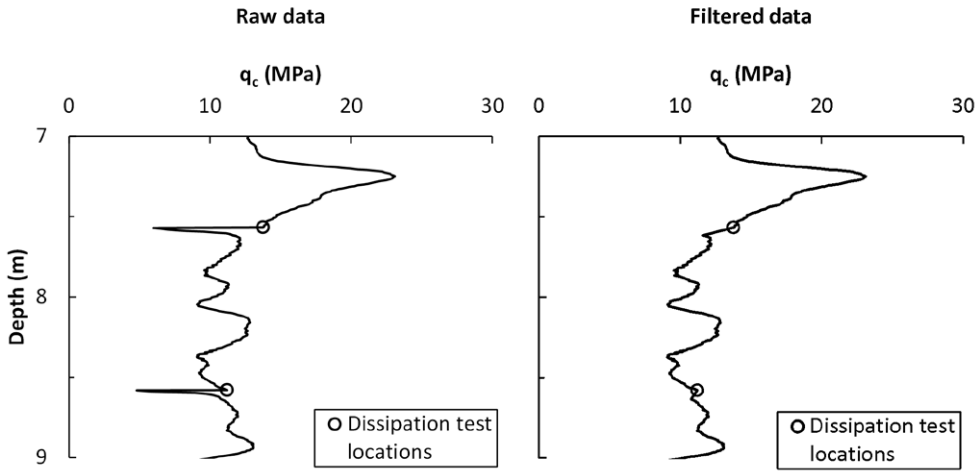


Figure 5.3 Example of the effect of pauses for dissipation tests on q_c profile.

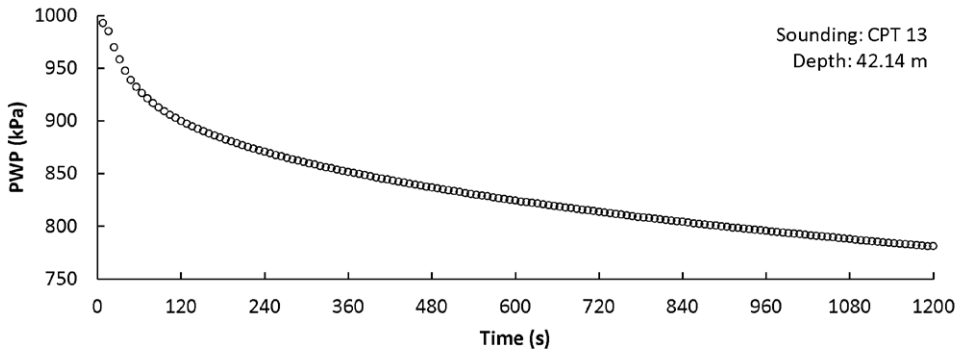


Figure 5.4 Typical results of dissipations test performed in the clay and decomposed norite that underlies the Impala tailings.

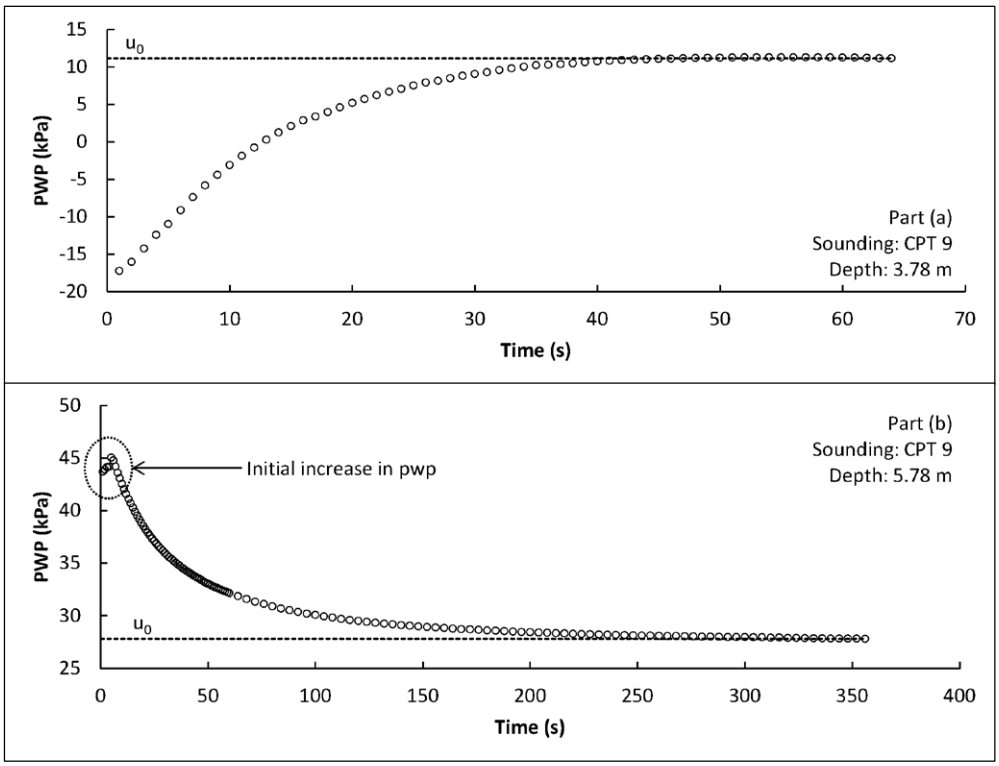


Figure 5.5 Typical results of dissipations test performed in the Impala tailings: a) PWP increases to a stable value. b) After an initial increase, PWP decreases to a stable value.

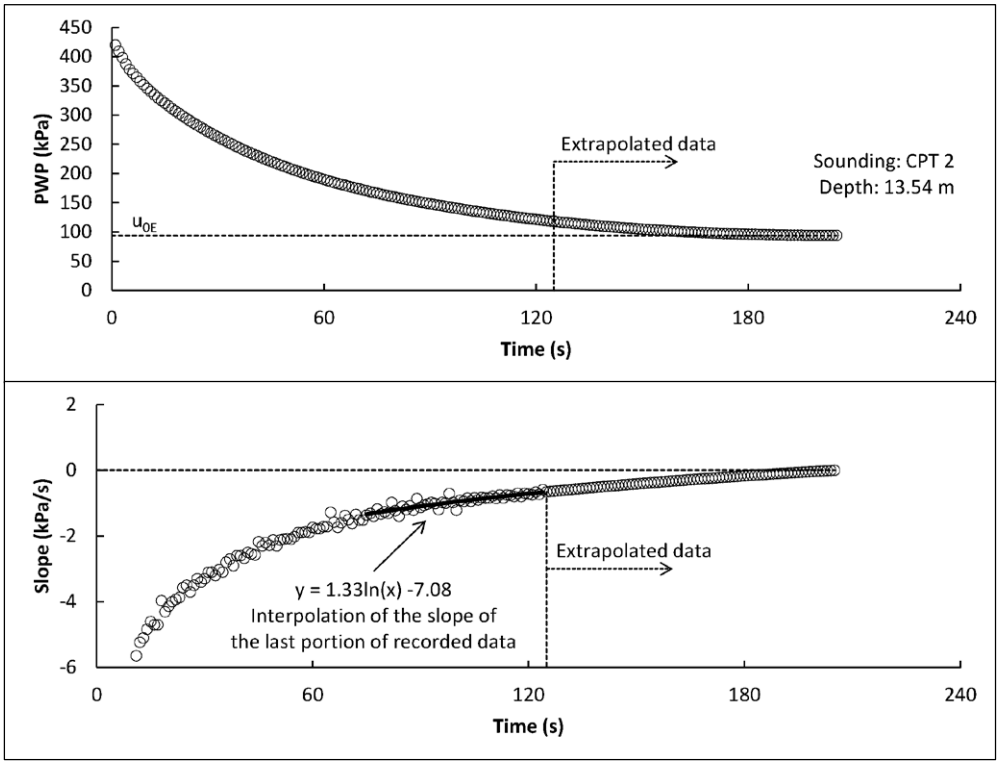


Figure 5.6 Logarithmic extrapolation used to estimate u_0 from incomplete dissipation tests.

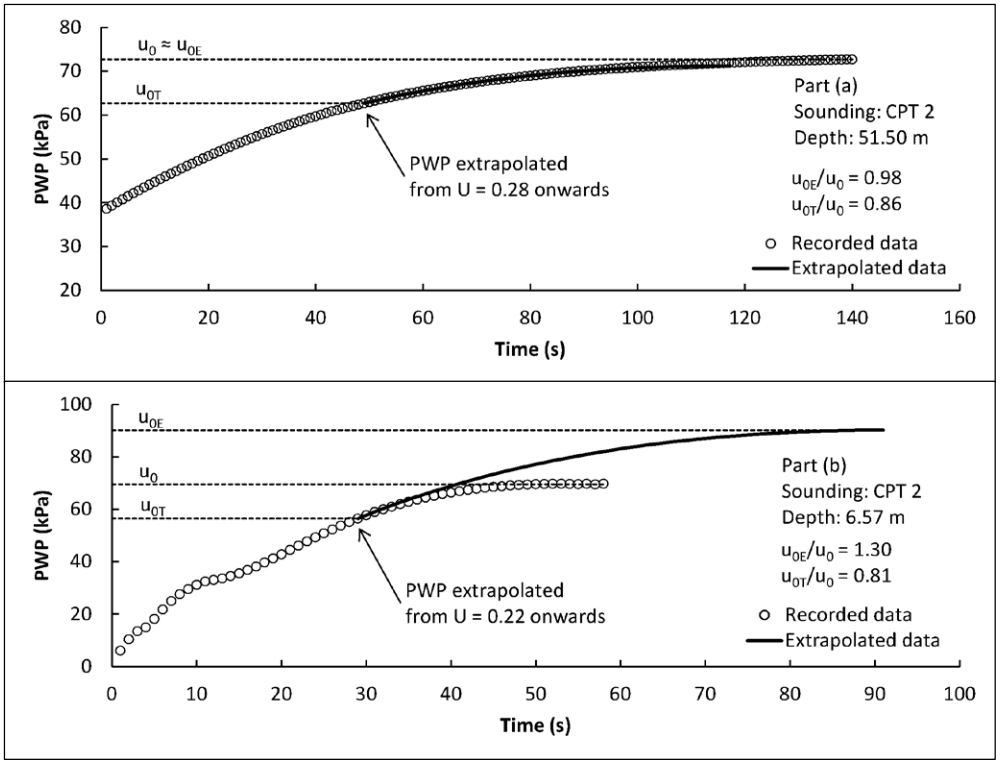


Figure 5.7 Check of the logarithmic extrapolation on dissipation records that stabilised: a) u_{0E}/u_0 is closer to 1 than u_{0T}/u_0, b) u_{0T}/u_0 is closer to 1 than u_{0E}/u_0.

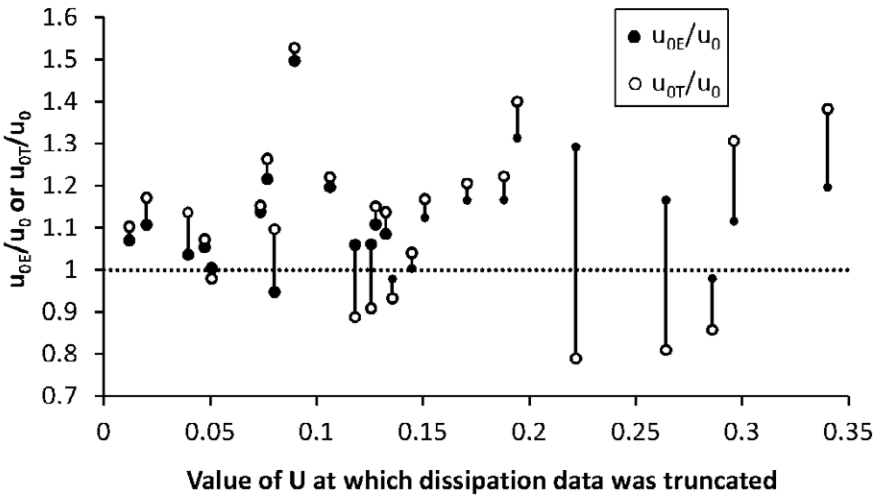


Figure 5.8 Comparison of ratios u_{0E}/u_0 and u_{0T}/u_0 to assess accuracy and merit of the extrapolation procedure.

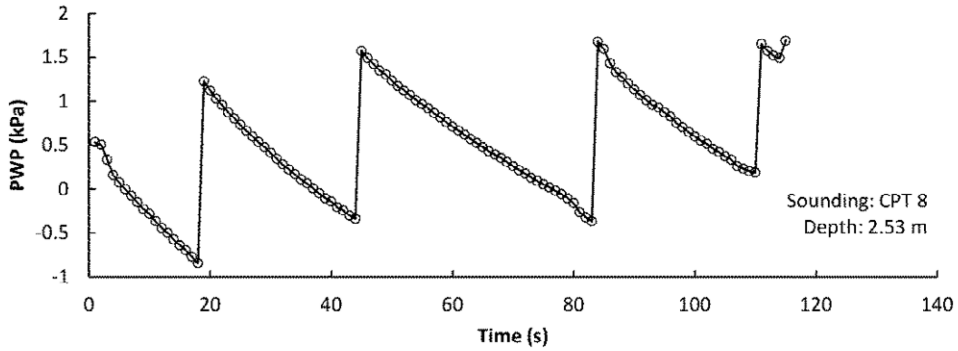


Figure 5.9 Dissipation test results exhibiting zigzag pattern and interpreted as an indication that the soil was not fully saturated.

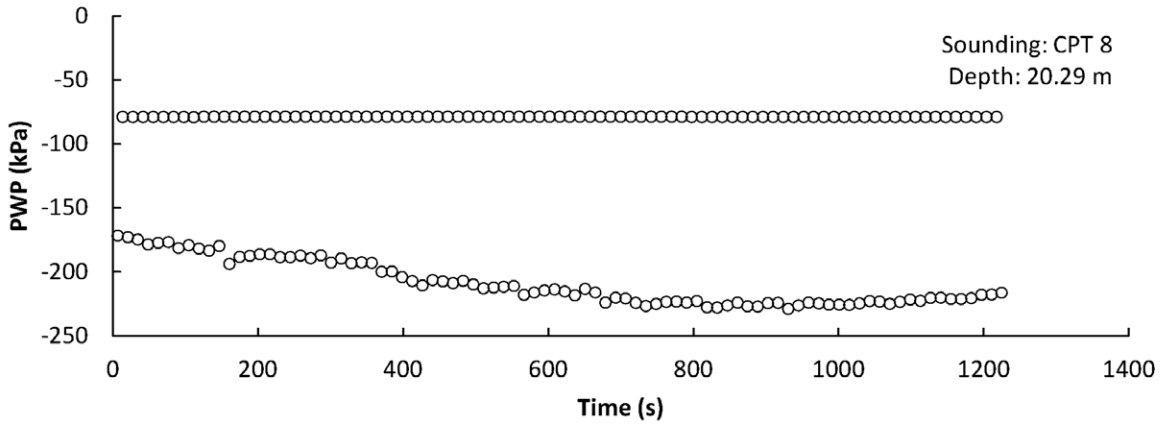


Figure 5.10 Results of a dissipation test in which transducer malfunction is suspected.

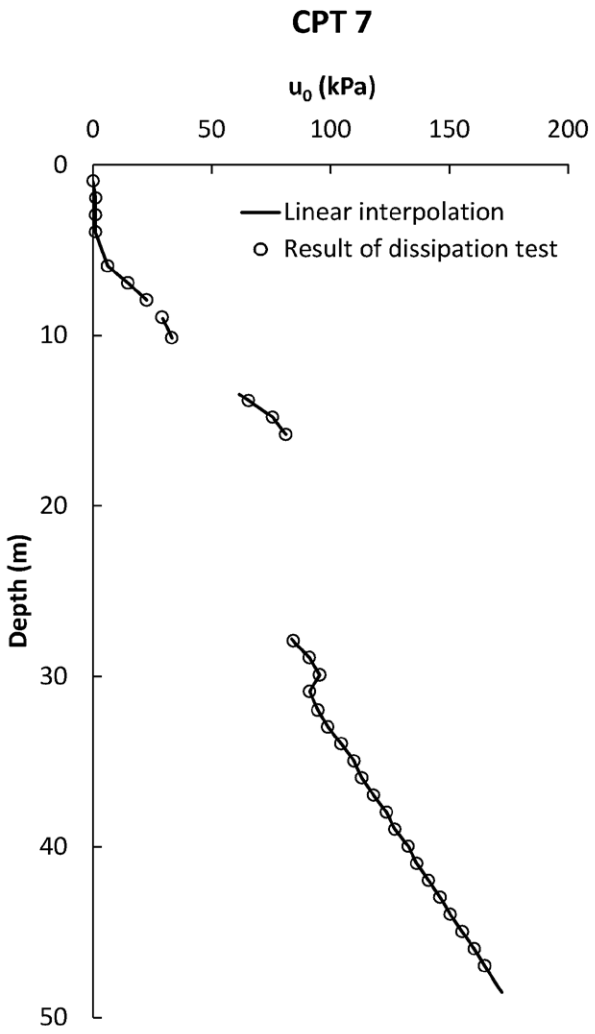


Figure 5.11 Sample profile of u_0. Note: Interruptions in the profile are due to cemented layers on which rotary drilling was used.

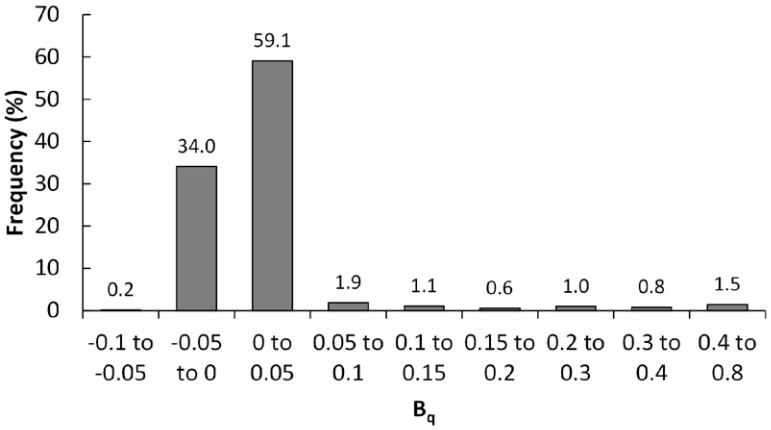


Figure 5.12 Histogram of B_q.

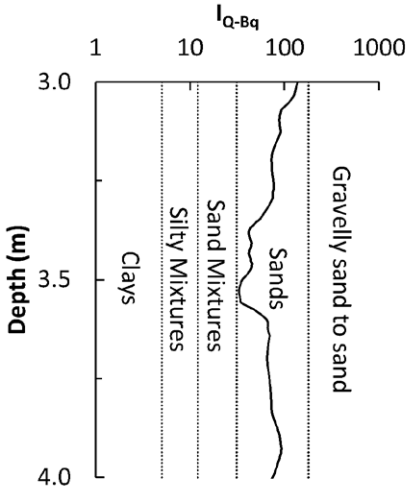


Figure 5.13 Sample profile of I_{Q-Bq}.

6 The correlation between the SSL and the minimum void ratio

6.1 Introduction

Knowledge of the steady state line (SSL) is a requirement of the methodology proposed by Jefferies and Been (2006) to infer the in situ state parameter (ψ) from CPT results. This requirement can be particularly challenging when the CPTs have been conducted in a heterogeneous soil deposit, such as a TSF, that contains a variety of soiltypes each of which may have a different SSL. In this case, the SSLs of a few representative soiltypes must be experimentally determined through a series of triaxial tests to adequately characterise the soil deposit. This approach was exemplified by Fourie and Papageorgiou (2001) who reported that FC within the Merriespruit gold TSF varied from 40% to 95%. Based on this variation, they pointed out the inadequacy of choosing a single SSL to represent the entire tailings deposit. Instead, they experimentally determined the SSLs (Figure 6.1) of four soiltypes of Merriespruit tailings with different GSD curves. Similarly, the variation of soiltypes within the Impala TSF (Figure 3.22) suggests that attempting to represent all the tailings of the impoundment with a single SSL would be inadequate. Therefore the SSLs of several representative soiltypes need to be experimentally determined for a more accurate inference of ψ.

In order to reduce the number of soiltypes whose SSLs must be experimentally determined by triaxial testing, it is necessary to understand how the SSL is affected by soil index parameters that can be easily measured. Several investigations have looked into this topic and have suggested qualitative and quantitative correlations between the SSL and different index parameters such as: FC, particle shape, shape of the grain size distribution (GSD) curve, and e_{max} and/or e_{min} (Table 6.1). However different studies have arrived at different conclusions. For instance, Been and Jefferies (1985) presented results indicating that there is a significant increase in the slope of the SSL as the FC of a soil increases (Figure 6.2). However, Thevanayagam et al. (2002) presented the SSLs of 7 soiltypes prepared by combining coarse and fine particles in different proportions. The FC of these mixtures varied from 0 to 100% but no systematic change in the slope of the SSL as a function of FC was observed (Figure 6.3). Additionally, although some authors have focused on the role of FC, Li (2013) showed that two soiltypes, one coarser than the other, with parallel GSD curves and identical in every other way, have virtually the same SSL. This result suggests that it is the shape of the entire GSD curve and not FC on its own that governs the SSL. These types of studies will be reviewed in this chapter with the aim of identifying an index parameter that can be correlated to the SSL of tailings.

The layout of the chapter is as follows. First, a review of existing correlations between the SSL and index parameters of non-plastic soils is presented. From this review it is concluded that e_{min} and e_{max} are potentially suitable index properties to correlate to SSL parameters Γ and λ (Figure 2.1). Second, a database of 151 non-plastic soils is used to assess the strength of the correlation between e_{min}, e_{max}, and the void ration range (e_{max} - e_{min}) and the different SSL parameters. Analysis of the database leads to the conclusion that e_{min} is more closely correlated than e_{max} or (e_{max} - e_{min})to Γ and λ. Third, sets of SSLs reported by individual publications are analysed to check if they are in agreement with the trends suggested by the entire database. This check was done to reduce the

scatter resulting from e_{min} being determined with different procedures, technicians, and equipment. Lastly, the chapter closes with a summary of the most salient conclusions. Throughout the chapter, the analyses are restricted to non-plastic and low plasticity soils because that is the nature of the Impala tailings, and that tends to be the nature of the majority of tailings.

6.2 A literature review of correlations between index properties and SSL parameters

6.2.1 Correlations between the SSL and FC

Been and Jefferies (1985) presented the SSLs of Kogyuk sand with four different FC (Figure 6.2). The SSLs indicated a trend of direct correlation between λ and FC. The nature of the fines that were used in the mixtures with Kogyuk sand was not reported, but given the marked effect that FC had on λ it seems likely that these were plastic fines. This is because the plasticity index of silty clays is known to be directly correlated to λ (Schofield and Wroth 1968) whereas the FC of non-plastic soils does not have a systematic effect on λ (Thevanayagam et al. 2002; Yang et al. 2006; Zlatović and Ishihara 1995). Since the present discussion focuses on non-plastic soils, the results from Been and Jefferies (1985) will not be considered any further.

Hird and Hassona (1990) presented four SSLs corresponding to clean Leighton Buzzard sand plus three mixtures of Leighton Buzzard sand and coarse mica particles. That is, all four soils had FC = 0%. The Leighton Buzzard was a uniform medium quartz sand with subrounded to subangular grains. Whereas the mica was made from compressible plate-like particles composed mostly of muscovite and about 20% of kaolinite. Their results indicated that λ was directly correlated to mica content (Figure 6.4). These results highlight that it is not necessarily FC that has an effect on λ but rather the compressibility of the grains, which in turn is governed by their shape and mineralogy. Proponents of a direct correlation between FC and λ might argue that particle size is generally correlated to particle shape and mineralogy, but as will be shown below, tailings do not necessarily exhibit changes in shape and mineralogy at the traditional fines-coarse boundary of 63 μm or 75 μm.

Bouckovalas et al. (2003) used a database of 42 sands to explore correlations between FC and SSL parameters λ, Γ_1, and M. The database was composed mostly of clean sands: 33 sands had FC between 0% to 5%, 7 sands had FC between 5% to 12%, and the remaining two sands had FC of 21% and 48%. Their results (Figure 6.5) suggest a trend of direct correlation between FC and both λ and Γ_1, whereas M was found to be largely independent of FC. The correlation of FC with λ has a reasonably high $R^2 = 0.72$ whereas the correlation of FC with Γ_1 is weaker with $R^2 = 0.52$. However, both of these correlations are significantly influenced by a single data point at FC = 48%. If the correlations are repeated without the point at FC = 48%, the R^2 values for the λ-FC and Γ_1-FC plots drop to 0.39 and 0.11 respectively (Figure 6.6). These lower values bring into question the existence of a systematic correlation of λ or Γ_1 with FC.

Jefferies and Been (2006) used a database of 59 soiltypes ranging from clean sands to silts to explore the correlation between λ and FC (Figure 6.7). They noticed that there appears to be a direct

correlation between these two parameters but that the scatter is too high for the correlation to be of practical value. They also presented the SSLs corresponding to two soiltypes with FC values of 33% and 34% and noticed that despite the similarity in FC, the two soils had significantly different SSLs. This led them to conclude that FC on its own is not a good predictor of the SSL.

Thevanayagam et al. (2002) studied how the stress-strain response of gap-graded granular mixes is affected by FC and the relative sizes of the coarse and fine particles. They determined the SSLs of 7 gap-graded soils that consisted of silica sand (foundry sand) and crushed silica fines (non-plastic) mixed in different proportions with FC varying from 0% to 100%. The resulting SSLs exhibited a marked curvature at high stress levels (p' > ≈800 kPa) in e - log(p') space. The lower stress portions of the SSLs which can be adequately represented with a straight line (Eq. 2.1) have been replotted here (Figure 6.3). Two important observations can be made regarding Figure 6.3. First, there is no trend of increase in λ as FC increases from 0% to 100%. Second, the SSLs initially shift downwards as FC increases up to 40% and then shift upwards for FC values of 60% and 100%. Both of these trends are also present in results reported by Zlatović and Ishihara (1995), Naeini and Baziar (2004), Yang et al. (2006), and Carrera et al. (2011). Thevanayagam et al. (2002) hypothesised that the observed behaviour can best be understood by considering the relative importance of coarse and fine grained material in resisting the shear stresses. Their rationale is that when a soil contains a very small amount of fines, and the fines are small enough to fit in the voids between the coarse grains, the mechanical behaviour of the soil will be determined by the mineral skeleton formed by the coarse grains alone (case i in Figure 6.8). As FC increases, fine grains begin to interact with the coarse grains and a fraction of fines now contributes to the active intergrain contacts that determine the mechanical response (cases ii and iii in Figure 6.8). Beyond a certain threshold fines content (TFC), the coarse grains start playing a secondary reinforcement role on the shear response as the coarse grains are no longer in contact with each other (case iv-2 in Figure 6.8). As FC increases beyond certain limit (FC_L) the coarse particles get located farther away from each other and they cease to provide any secondary reinforcement (case iv-1 in Figure 6.8). These ideas led Thevanayagam et al. (2002) to propose the equivalent intergranular void ratio ($(e_c)_{eq}$), and equivalent interfine void ratio ($(e_f)_{eq}$) to characterise the shear response of the soils in their study when FC < TFC and FC > TFC, respectively. They are defined as:

$$(e_c)_{eq} = \frac{e + (1-b)\cdot(FC/100)}{1-(1-b)\cdot(FC/100)} \qquad 6.1$$

$$(e_f)_{eq} = \frac{e}{\frac{FC}{100} + \frac{1-\left(\frac{FC}{100}\right)}{R_d^m}} \qquad 6.2$$

Where b denotes the fraction of the fines that contribute to the active intergrain contacts, R_d is the size ratio of the coarse grains to the fine grains, and m is a reinforcement exponent. $(e_c)_{eq}$ can be thought of as a void ratio for which the fines that do not contribute to the active intergrain contacts

are taken as voids, and $(e_f)_{eq}$ can be thought of as the void ratio of the fines only but with some consideration to the volume of coarse grains that are providing secondary reinforcement. Apparently, Thevanayagam et al. (2002) chose the D_{50} of the coarse soil and the fine soil to obtain R_d = 25. They further assumed b = 0.25 and m = 0.65 and found that the SSLs of soils with FC < TFC collapsed into a single line if $(e_c)_{eq}$ was used instead of e (Figure 6.9). Likewise, they found that the SSLs of soils with FC > TFC collapsed into a single line if $(e_f)_{eq}$ was used instead of e (Figure 6.9). These results suggest that given a parent coarse soil and a parent fine soil of similar mineralogy, the SSL of a gap-graded soil resulting from the combination of these two soils in any proportion can be determined based on the knowledge of: the SSL of any resulting soil with FC < TFC (e.g. the parent coarse soil), the SSL of any resulting soil with FC > TFC (e.g. the parent fine soil), and parameters b, m, and R_d. Such an approach would be useful to reduce the number the number of soiltypes whose SSLs have to be experimentally determined with triaxial testing to fully characterise a TSF. However, no guidelines are given for the calculation of b and m, and it is uncertain whether the method can be applied to continuously graded soils such as those found in TSFs (Figure 3.22).

Rahman and Lo (2008) used $(e_c)_{eq}$ as defined in Eq. 6.1 but developed a semi-empirical equation to calculate b as a function of TFC, FC, and R_d. They further determined m using the SSLs of Thevanayagam et al. (2002) and found this value to be applicable to other soiltypes. This allowed the prediction of the SSL for sands with FC < TFC. The main inputs of the prediction are the D_{50} of the fines, the D_{10} of the coarse material, and the SSL of the clean sand or of another sand-fines mixture with FC < TFC. An important distinction between the work of Thevanayagam et al. (2002) and Rahman and Lo (2008) is that the latter did not limit their approach to gap graded soils, but did limit it to soils with FC < TFC. Rahman and Lo (2008) and (2012) tested the proposed approach by predicting 20 SSLs. In all cases, the SSLs of sands with different FC became similar to the SSL of the clean sand when plotted in $(e_c)_{eq}$-p' space (Figure 6.10).

Despite the success of the predictions reported by Rahman and Lo (2008) and (2012), the following limitations are observed. 1) The methodology is only applicable for soils with FC < TFC. According to Rahman and Lo (2008) the TFC is generally around 40%. This significantly limits the applicability of the methodology to TSFs, where FC can easily exceed 40% (e.g. Figure 3.22 and Table 3.1). 2) The rationale behind $(e_c)_{eq}$, and in particular behind parameter b, is that the portion of the fines that does not participate in the active intergrain chain should be taken as voids. But it is known that it is not only fine particles (<75µm) which can fall out of the active intergrain chain. This was illustrated by Dodds (2003) in an experiment in which a binary disc arrangement was loaded. One type of disc had a 12.6 mm diameter and was made from relatively stiff photoelastic material, and the other type of disc had a 9.3 mm diameter and was made from rubber. The use of photoelastic material allowed the visualization of the force chains developed in the disc assembly when it was loaded. The results (Figure 6.11) show that some rubber particles fall within the voids created by the larger particles and do not participate in the force chain. This is despite the rubber particles not classifying as 'fines' in the sense that they are larger than 75µm. It is also observed that even some of the larger photoelastic discs do not participate in the force chain as they fall in the voids created by other photoelastic discs. The physical meaning of b was also questioned by Carrera et al. (2011)

who noted that Eq. 6.1 was unable to normalise the compression behaviour of Stava silty sands. More recently, Yang et al. (2015) conducted an experimental programme designed to explore the rationale behind $(e_c)_{eq}$. They found that $(e_c)_{eq}$ did not offer any advantage over the conventional void ratio as a normalising parameter of mechanical behaviour. 3) The definition of what constitutes a fine particle is entirely arbitrary, with some soil classification methods placing the coarse-fine limit at 75 μm (ASTM), while others place it at 63 μm (British Standard). Regardless of where the limit is placed, it is unrealistic to expect any drastic change in the nature of the particles across that limit, especially for non-plastic soils. For example, Vermeulen (2001) conducted a study on gold tailings which included micrographs generated with scanning electron microscopy for grains of different size categories. His results (Figure 6.12) do not reveal any drastic change in particle shape across the typically used 75 μm or 63 μm coarse-fine boundary. Furthermore, the micrographs indicate that the texture of the tailings only becomes dominated by platy, as opposed to bulky, particles when grain size is about 3 μm. Vermeulen (2001) also performed X-ray diffraction analyses to determine the chemical composition of five different size categories of gold tailings: 150 μm, 75 μm, 10 μm, 2 μm, and 1 μm. His results show that the three coarsest size categories have roughly the same composition which, in agreement with the micrographs, indicates no change in the nature of the particles over the traditional coarse-fine boundaries. The experimental results from Vermeulen (2001) indicate that there is no fundamental basis for a correlation between FC and the SSL.

6.2.2 Correlations between the SSL and particle shape

Based on the SSLs of 15 sands with subrounded, subangular, or angular grains, Poulos et al. (1985) reported that, regardless of the GSD, the slope of the SSL is affected chiefly by the shape of the grains in a given soil. Their data suggest that particle angularity is directly correlated to λ (Figure 6.13).

Using a database formed with previously published SSL parameters and particle shape information of 38 sandy soils, Cubrinovski and Ishihara (2000) presented correlations indicating that for a given void ratio range (e_{max} - e_{min}), soils with angular particles exhibit higher values of λ than soils with round grained particles. The observation was found to be independent of FC which varied from 5% to 36% (Figure 6.14). Given that quantitative particle shape information is not generally reported in the literature, Cubrinovski and Ishihara (2000) divided the 38 sandy soils into only two broad categories of particle shape: round and angular. This rough division is likely to account, at least partly, for the scatter in their correlations.

Cho et al. (2006) studied the effects of particle shape on mechanical behaviour of sands. Their study was based on two databases: One of 38 sands with quantitative particle shape information and a second one of 46 sands without quantitative particle shape information. In order to isolate the effect of particle shape, their study focused on narrow GSDs, with only 5 of the 84 sands having a coefficient of uniformity ($C_u = D_{60}/D_{10}$) > 4. Cho et al. (2006) adopted 'sphericity' and 'roundness' as defined by Krumbein and Sloss (1963) to quantify particle shape. Additionally, they used a third shape descriptor called 'regularity' as a measure of the particle's deviation from round spherical

shape. Regularity was computed as the average of sphericity and roundness. Their results (Figure 6.15) show that: a) The vertical position of the SSL as characterised by Γ_1 and Γ_{100} has a strong and inverse correlation with roundness and regularity, respectively. b) There is a weak inverse correlation between λ and regularity. c) M, or its proxy ϕ_{cs}, has a strong and inverse correlation with roundness. Despite the strength of the correlations between SSL parameters and particle shape found by Cho et al. (2006), their application to tailings is not straightforward because the correlations are based mostly on sands with $C_u < 4$, whereas tailings generally exhibit a much broader GSD (Fourie and Papageorgiou 2001; Vermeulen 2001).

Maeda et al. (2009) reported the SSLs (Figure 6.16) of three assemblies of particles modelled using the 2D discrete element method (DEM). The GSD of the three assemblies was the same, but particle shape varied from one assembly to the other. The particle shapes correspond to those shown in Figure 6.17 a, b, and d. Figure 6.16 shows that for a constant GSD, particle surface irregularity is directly correlated to Γ_1. However, there is no appreciable effect on the slope of the SSL.

Li (2013) determined the SSLs of two families of soiltypes with distinctly different particle shape: glass balls and Hostun Sand. The glass balls were commercially manufactured and therefore their particle shape was essentially spherical. The Hostun sand was a ground material with particle shape ranging from angular to subangular. Both materials were made mostly of silica (>99%) which gave the individual particles a relatively high strength. The GSD curves shown in Figure 6.18a were prepared with both glass balls and Hostun Sand, and the SSL of each soiltype (Figure 6.19 a and b) was determined through a series of triaxial tests. Li (2013) adopted Eq. 2.5 with a constant value of $\xi = 0.9$ to represent the SSLs in e-p' space. The resulting SSL parameters (e_{ref}, λ and M) of Hostun Sand and glass balls are compared in Figure 6.20. It is observed that for a given GSD and mineralogy e_{ref}, λ, and M are higher for the soil with greater particle angularity. These results are in agreement with those of Cho et al. (2006).

Sadrekarimi and Olson (2011) conducted a series of triaxial and ring shear tests on Ottawa sand, an Illinois River sand, and a Mississippi River sand. They concluded that particle shape, together with mineralogy, were the primary factors controlling the value of M. Their results also showed that the increased angularity produced by particle damage increases M.

Yang and Luo (2015) studied the correlation between particle shape and the SSL of non-plastic soils. The soiltypes they considered consisted of uniform quartz sand (Fujian sand) mixed in different proportions with either spherical glass beads or crushed angular glass particles. The GSDs of these three primary soiltypes were virtually identical. Their results show that Γ, λ, and M are inversely proportional to the overall regularity of the particles. Although Yang and Luo (2015) proposed mathematical correlations between the different SSL parameters and quantitative particle shape descriptors, these correlations cannot be extrapolated to other non-plastic soiltypes as they correspond to a specific GSD.

It is noted that the only study reviewed in this sub-section that does not report a trend of direct proportionality between λ and particle irregularity is Maeda et al. (2009). Given that the DEM model

that they used did not consider particle breakage, it appears that the mechanism that leads to a direct proportionality between λ and particle irregularity is grain crushing.

6.2.3 Correlations between the SSL and descriptors of the shape of the GSD curve

Poulos et al. (1985) observed that the vertical position of the SSL is affected by even small differences in GSD. They used C_u as a GSD descriptor and found an inverse correlation between C_u and Γ while λ appeared to be largely insensitive to C_u (Figure 6.13).

Muir-Wood and Maeda (2008) used 2D discrete element modelling (DEM) to study the effect on the SSL of gradations of varying breadth but with constant circular particle shape. Recognising that C_u is only a crude descriptor of the GSD curve, they proposed a grading state index (I_G) as a GSD curve descriptor. I_G was defined as the ratio of the area under the GSD curve of a soil in its current state, to the area under the limiting GSD curve of the soil after undergoing extensive particle crushing due to shearing and isotropic stresses. They indicate that for soils having a Gaussian GSD, I_G is proportional to $\ln(R_D)/2$, where R_D is the ratio of maximum to minimum particle size in the current GSD. Given the direct correlation between I_G and R_D, Muir-Wood and Maeda (2008) adopted R_D as a proxy for I_G. They determined SSLs of disc assemblies with four different values of R_D (Figure 6.21). The observed trend is that as R_D increases, the SSL shifts down in the e-p' plane and becomes flatter. Muir-Wood and Maeda (2008) stated that neither of these results is counter-intuitive as "*the broader the grading the more efficient the particle packing, the lower the limiting values of specific volume or void ratio (lower Γ), and the higher the stiffness (lower λ).*" It should be noted though that use of I_G for real soils is limited because its formal calculation requires knowledge of the GSD curve that the soil will attain after extensive particle crushing. In most cases this limiting GSD will not be known. R_D is also of limited applicability because it is only a suitable proxy for I_G for soils with a Gaussian GSD. However, the results of Muir-Wood and Maeda (2008) highlight the point that efficiency in particle packing has an effect on both Γ and λ.

Li (2013) explored the effects of GSD shape on the SSL. In addition to the tests on glass balls and Hostun Sand described in section 6.2.2, Li (2013) modelled triaxial tests using 3D DEM. Four different GSDs were used in the 3D DEM and all particles were spherical. Li (2013) used C_u to characterise the shape of the GSD curve and Eq. 2.5 to characterise the SSL in e-p' space. He noted that, for the three material types, C_u correlates inversely with e_{ref} and λ (Figure 6.19 and Figure 6.20). No systematic correlation between C_u and M was observed. Furthermore, the results of Li (2013) suggest that for a given particle shape distribution and mineralogy, M remains fairly constant regardless of GSD (Figure 6.20). This is in agreement with results from Huang et al. (2004) and Carrera et al. (2011). Murthy et al. (2007) did report an increase in M of Ottawa sand as the GSD was altered by increasing the silt content. However, they attributed this increase in M to the angular nature of the silt particles which was distinctly different from the rounded particles of the Ottawa sand.

C_u is similar to R_D as both parameters give an indication of the breadth of the GSD curve. Accordingly, the results of Li (2013) showing an inverse correlation between e_{ref} and C_u are consistent with the results of Muir-Wood and Maeda (2008) showing an inverse correlation between

Γ and R_D. Notwithstanding these trends, Li (2013) also referenced results indicating that C_u is not a reliable predictor of SSL because two soils with the same C_u and particle shape will not necessarily have the same SSL. This was illustrated by Li (2011) who showed that specimens of Pingtai sand with the same C_u, maximum and minimum particle size, but otherwise different GSDs, had different SSLs. Similarly, Li (2011) obtained different SSLs for specimens of Pingtai sand with the same coefficient of curvature ($C_c = D_{30}^2/(D_{10} \cdot D_{60})$), maximum and minimum particle size, but otherwise different GSDs. The results from Li (2011) highlight the difficulty of attempting to correlate the SSL to simple GSD descriptors such as C_u or C_c.

Four of the SSLs determined by Li (2013) corresponded to two pairs of Hostun Sand which were identical in every way except that their GSD curves were parallel, i.e. same size distribution but different particle sizes (Figure 6.18b). The results suggest that soils with parallel GSD curves, and similar particle shape and mineralogy will exhibit the same SSL (Figure 6.22). However, Li (2013) also noted that given that larger particles have a greater probability of containing flaws, this could induce greater particle crushing in the coarser soil and therefore changes in GSD that can have an effect on the SSL.

There is agreement in the reviewed literature that broader GSDs induce lower values of Γ. There is also agreement that changes in GSD alone, while keeping particle shape constant, have little to no effect on M. However, the effect of GSD on λ is not so clear. Poulos et al. (1985) suggest that λ is largely insensitive to GSD and rather dependent on particle shape, but the results of Muir-Wood and Maeda (2008), and Li (2013) indicate that broader GSDs lead to lower λ values. The correlation between λ and a suitable index parameter will be further explored using the database presented in section 6.3.

6.2.4 Correlations between the SSL and void ratio limits.

Cubrinovski and Ishihara (2000) noted that traditional descriptors of GSD such as FC, C_u, or D_{50}, are only able to capture one aspect of the overall grading properties. They therefore suggested the use of the range of possible void ratios at which a soil can exist (e_{max} - e_{min}) as a means to characterise the GSD of sandy soils. Their study considered correlations of (e_{max} - e_{min}) with the vertical position of the SSL and λ. They characterised the vertical position of the SSL as the parameter e_0, which is the intercept of the SSL on the void ratio axis when using a natural-scale e-p' plot. Based on a database of 52 previously published soiltypes, they showed that the relative density at e_0 (D_{r0}) is linearly and directly correlated to (e_{max} - e_{min}) and that the correlation was valid regardless of FC which varied from 5% to 36%, and of particle shape which varied from round to angular (Figure 6.23). Based on 38 soiltypes of the database for which grain shape information was available, Cubrinovski and Ishihara (2000) also concluded that λ was directly and linearly correlated to (e_{max} - e_{min}) (Figure 6.14) and that this correlation was independent of FC. However, as was mentioned in section 6.2.2, they did report a particle shape effect on the λ vs (e_{max} - e_{min}) correlation. This effect on the correlation is somewhat unexpected given that (e_{max} - e_{min}) is known to be affected by particle shape (Cubrinovski and Ishihara 2002).

As mentioned in section 6.2.2, Cho et al. (2006) reported correlations between the SSL and particle shape parameters. Cho et al. (2006) also noticed that the SSL parameters can be correlated to e_{max}, e_{min} and (e_{max} - e_{min}). Such correlations are logically sound because as shown by Cho et al. (2006) (Figure 6.24), particle shape also affects e_{max} and e_{min}. Their results (Figure 6.25) show a significant, direct and linear correlation of Γ_1 with both e_{min} and e_{max}, and a weak correlation of λ with (e_{max} - e_{min}). Both correlations appear to be independent of particle shape. Additionally, a strong, direct and linear correlation of Γ_{100} with both e_{min} and e_{max}, and a weak correlation of M with e_{max}, e_{min} and (e_{max} - e_{min}), were also reported. As noted previously, the applicability of these correlations to tailings is uncertain because they are based mostly on narrowly graded sands ($C_u < 4$).

Jefferies and Been (2006) presented a plot of Γ_1 vs e_{max} (Figure 6.26) based on a database of 59 soiltypes ranging from clean sands to silts. They noticed that the plot suggests the existence of a linear relationship between Γ_1 and e_{max}. However, given the significant scatter ($R^2 = 0.55$), they did not recommend the correlation for practical use.

The works reviewed herein indicate that the vertical location of the SSL on e-p' space exhibits a direct and linear correlation with e_{max}, e_{min}, and (e_{max} - e_{min}). The data presented by Cho et al. (2006) shows that these correlations are valid for sands with small FC and C_u. Furthermore, the data presented by Cubrinovski and Ishihara (2000) and Jefferies and Been (2006) suggest that the correlations of Γ with (e_{max} - e_{min}) and e_{max}, respectively, are also applicable to soils with up to FC ≈ 50% and with no restrictions on C_u. With regards to the correlation λ vs (e_{max} - e_{min}), Cubrinovski and Ishihara (2000) state that it is dependent on particle shape, whereas Cho et al. (2006) found it to be independent of particle shape (compare Figure 6.14 and Figure 6.25b). However, both studies agree that the correlation λ vs (e_{max} - e_{min}) is rather weak. Finally, none of the works reviewed suggests a significant correlation between M and the void ratio limits.

6.2.5 Justification to further consider e_{min} and e_{max} as predictors of Γ and λ.

The strength of the correlations between different soil index parameters and the SSL as interpreted from the previous literature review is summarised in Table 6.1. The strength of the correlations has been categorised into strong ($R^2 > 0.7$), medium ($0.4 < R^2 < 0.7$), weak ($0.1 < R^2 < 0.4$), or non-existent ($R^2 < 0.1$). When R^2 was not reported or could not be calculated from the original data, a qualitative appraisal of the correlation was made. The discussion herein will follow the structure of Table 6.1, moving from left to right and from top to bottom.

Objections to the use of FC as a predictor of SSL parameters were already raised in Section 6.2.1. Here, additional data is presented to show that e_{max} and e_{min} can also capture the trend between FC and Γ reported by Thevanayagam et al. (2002) and Rahman and Lo (2008) and (2012). In essence the trend is that Γ initially decreases as FC goes from zero to the TFC, and will then increase as FC surpasses the TFC (Figure 6.27a). This trend is very similar to that of e_{max} and e_{min} vs percentage of fines reported by Lade et al. (1998) (Figure 6.27b). Lade et al. (1998) considered several mixtures consisting of a host coarse sand (Cambria sand) and different proportions of finer Nevada sand. In this context the 'fines' make reference to the Nevada sand because it was *finer* than Cambria sand,

even though the particles of Nevada sand were not necessarily smaller than 75 μm. The similarity of the shape of the curves presented in Figure 6.27a and b suggests that the factor controlling Γ is not necessarily FC, but rather the packing characteristics which are captured by e_{max} and e_{min}. This distinction has important practical implications because variations in e_{max} and e_{min} can be measured in soils with no fines (e.g. lines labelled 80/200 and 50/80 in Figure 6.27b) and this allows estimations of the corresponding variations of Γ to be made. Whereas if FC is correlated to Γ, then variations in Γ cannot be inferred when dealing with different mixtures of clean sands because they will all have FC = 0%. As for the effect of FC on λ, it is noted that most studies suggest a weak or non-existent correlation between these two parameters.

Particle shape has been found to have a strong effect on Γ (or its proxies e_0 and e_{ref}). However, any correlation between these two parameters is strongly dependent on GSD. This is illustrated by the results of Li (2013) (Figure 6.20) in which the e_{ref} of Hostun Sand is seen to increase systematically from 0.61 to 0.77 as C_u decreases from 20 to 1.1. Hence, the effect of the GSD precludes the possibility of a correlation between particle shape and Γ applicable to non-plastic soils of all gradings.

The reviewed literature, except for Maeda et al. (2009), is conclusive in that particle shape has at least a weak effect on λ. However, it is not clear whether this particle shape effect can be captured by e_{max}, e_{min} or (e_{max} - e_{min}). The results from Cubrinovski and Ishihara (2000) (Figure 6.14) suggest that it cannot, but the results from Cho et al. (2006) suggest that it can (Figure 6.25b). Given that Cho et al. (2006) used quantitative particle shape data, whereas Cubrinovski and Ishihara (2000) worked with qualitative particle shape data, it seems reasonable to lend greater credence to the results of Cho et al. (2006). Additionally, void ratio limits are known to be dependent on particle shape (Biarez and Hicher 1994; Cho et al. 2006), accordingly capturing particle shape effects through e_{max} and e_{min} seems plausible.

Particle shape emerges as the only index parameter that is correlated with M. Namely, as particle regularity increases, M decreases (Figure 6.15a). Furthermore, the results from Huang et al. (2004), Carrera et al. (2011), and Li (2013), suggest that for a given particle shape distribution and mineralogy, the value of M is independent from GSD.

GSD has been found to have a strong effect on Γ. However, two challenges arise when considering this correlation. 1) There is no simple way of describing the GSD curve because the typically used scalar descriptors (e.g. FC, C_u, C_c) describe only isolated aspects of the curve (Cubrinovski and Ishihara 2000). 2) Even if a scalar (or vector) quantity could be devised to accurately describe the GSD, its use would be limited because Γ is also affected by particle shape. This is clearly demonstrated by the results of Li (2013) which show that soils with identical GSD and mineralogy but different particle shape yield different values of e_{ref}, which is a proxy for Γ (Figure 6.20). Similarly, any correlation between λ and GSD would also be dependent on particle shape. Again, the approach adopted in this study will be to rely on e_{max} and e_{min} to capture the effects of changes in GSD. This approach is supported by the results of Li (2013) (Figure 6.28) and Lade et al. (1998) (Figure 6.27b) which show that e_{max} and e_{min} are sensitive to changes in GSD.

e_{max} and e_{min} are the parameters of choice to correlate to Γ and λ because they can capture the combined effect that particle shape and GSD have on packing efficiency. This confers e_{max} and e_{min} applicability across a wide variety of soiltypes. Such broad applicability is highly desirable even if it means sacrificing somewhat the strength of the correlation. That is, notice that correlations between e_{max} and e_{min} with Γ have been classified as medium, not strong (Table 6.1).

It is not clear from the literature review whether either e_{max} or e_{min} should be expected to correlate more strongly to Γ. The results of Cho et al. (2006) (Figure 6.25a) suggest that Γ is more strongly correlated to e_{max} (R^2 = 0.60) than to e_{min} (R^2 = 0.54). However, the database used by Jefferies and Been (2006) to explore the correlation between Γ_1 and e_{max} (R^2 = 0.55) was independently processed in this study to explore the correlation between Γ_1 and e_{min} and a stronger correlation (R^2 = 0.64) was found (Figure 6.26). So while Cho et al. (2006) suggest that Γ_1 is more strongly correlated to e_{max}, the data from Jefferies and Been (2006) suggests that Γ_1 is more strongly correlated to e_{min}. As for λ, none of the works reviewed has reported a correlation between this parameter and e_{min} or e_{max}, and only a weak correlation was reported by Cho et al. (2006) between M and e_{min} or e_{max}.

Lastly, it is acknowledged that since the range (e_{max} - e_{min}) is also dependent on particle shape and GSD, there is a fundamental basis to correlate it to the SSL. However, the use of e_{max} and e_{min} alone seems preferable for the following two reasons: 1) Cubrinovski and Ishihara (2002) showed that there is a strong correlation between e_{max} and e_{min} for a wide variety of soiltypes ranging from gravels to silty soils with up to 20% by weight of clay-sized particles (Figure 6.29). In their analysis they used different equations to model the e_{max} vs e_{min} correlation of the different soiltypes. However, Figure 6.29 suggests that the use of a single equation to represent the e_{max} vs e_{min} correlation for all soiltypes is also reasonable. A functional correlation between e_{max} and e_{min} implies that both parameters contain essentially the same information. And that therefore the range (e_{max} - e_{min}) can also be expressed in terms of only e_{max} or only e_{min}. 2) Cubrinovski and Ishihara (2000) showed that there is a strong correlation between e_0 (as represented by D_{r0}) and (e_{max} - e_{min}) (Figure 6.23). However, the same database reveals that a direct correlation between e_0 and e_{min} is also significant and even slightly stronger (Figure 6.30). This result suggests that e_{min} alone can capture the correlations found when using (e_{max} - e_{min}). It is noted, however, that the correlation between e_0 and e_{max} is considerably weaker. On the basis of these two observations it is concluded that there is no fundamental reason to prefer the use of (e_{max} - e_{min}) over e_{max} or e_{min} alone, and simplicity seems best served by the latter alternative. However, considering that correlations between SSL parameters and (e_{max} - e_{min}) have been considered in previous works (Cho et al. 2006; Cubrinovski and Ishihara 2000), such correlations will also be explored in the following section.

6.3 A database to assess the correlation of SSL parameters with void ratio limits

To assess the correlation of Γ and λ with e_{min} or e_{max}, a database of 151 soiltypes for which the SSL and e_{min}, e_{max}, or both had been reported in the literature was compiled. It was established in Section 6.2 that no correlations should be expected between M and e_{min}, e_{max} or (e_{max} - e_{min}). So as a

way of confirmation, the values of M against the void ratio limits were also plotted. Table 6.2 contains the index properties and references of the 151 soiltypes, and Table 6.3 contains the corresponding SSL parameters. To ensure the relevance of the analysis to non-plastic soils, no soiltypes were included in the database for which the plasticity index (PI) of the fines was reported as being greater than 12, or which were known to be predominantly of clay mineralogy. For several soiltypes no PI value was reported in the references, however most of these soiltypes had FC < 5%. Accordingly, it was assumed that any possible plasticity of the fines would have a limited effect on mechanical behaviour. Perhaps the most significant exception to the above condition are the Ardebil sand-silt mixes reported by Naeini and Baziar (2006). These soiltypes (represented with symbol ARM in Table 6.2) have important amounts of fines whose PI is not known. Regardless, they were included in the database because the fact that Naeini and Baziar (2006) made no comments about the plasticity of the silt, led the current author to believe that PI was probably low.

Soils with platy particles (e.g. mica grains) were not included in the database. This was done because platy particles are known to behave distinctly differently from bulky particles and the applicability of the SSL concept to soils with platy particles has been questioned (Clayton et al. 2009). No other limitations were imposed on the database, and the variety of soils included is quite wide: natural sands, laboratory sands, tailings, glass balls and 2D DEM soils.

Several of the soiltypes in the database had SSLs that exhibited a marked curvature in e-p' space that cannot be modelled with Eq. 2.1. Two alternatives for modelling these SSLs were considered: 1) adopting a higher order representation of the SSL (such as Eq. 2.5), or 2) modelling the SSL only over the p' domain in which there is no marked curvature. Adopting a higher order equation would have implied introducing additional SSL parameters. So with the purpose of focusing the analysis only on Γ and λ, the second alternative was adopted. Table 6.3 shows the p' domain over which the SSLs were modelled using the reported values of Γ and λ. As will be explained below, this p' domain is an important input into the analysis of the correlation between λ and e_{min}. Consequently, soiltypes were only included in the database if the p' domain of their SSL was known.

For 82 of the 151 soiltypes, values of Γ_{50} and λ were calculated from (p', e) data points. For some of these soiltypes, q coordinates or stress paths were also available which allowed the calculation of M. The (p', e, q) coordinates used for these calculations, and the methods used to estimate M when q values were not available, are presented in Appendix C. For the remaining 69 soiltypes for which (p', e, q) coordinates could not be obtained, the SSL parameters were adopted as reported in the relevant references.

Two types of trends were searched for in the database. Firstly, the trends indicated by the entire database were considered. The trends identified in this manner have the advantage of being representative of a wide variety of soiltypes. However, the disadvantage is that by mixing experimental data from different references and obtained through different procedures, the scatter in the data can reduce the strength of any existing correlations. To overcome this disadvantage, eleven subsets of the database coming from a single reference were individually analysed. This allowed an assessment of the strength of the correlations identified in the entire database but without the scatter due to combining data obtained through different experimental procedures.

6.4 Correlations between void ratio limits and SSL parameters

6.4.1 Trends identified in the entire database

Figure 6.31 shows plots of Γ_{50}, λ, and M vs e_{min}. A strong linear correlation ($R^2 = 0.74$) is observed between Γ_{50} and e_{min}, with the best fit line being described by:

$$\Gamma_{50} = 1.24 \cdot e_{min} + 0.11 \qquad 6.3$$

Figure 6.31b seems to reveal a weak trend of direct correlation between λ and e_{min}, however the plot exhibits too much scatter to be conclusive. It is significant that the seven soiltypes with the highest values of λ correspond to the Ardebil sand-silt mixtures reported by Naeini and Baziar (2004) for which the plasticity index is unknown. Upon first inspection of Figure 6.31b, these atypically high λ values seem to be indicative of a plastic soil. However, if the fines in the Ardebil sand-silt mixtures were plastic, there should be a direct correlation between FC and λ, which is not the case (Table 6.3). Accordingly, although the atypical magnitude of these λ values is noted, the Ardebil sand-silt mixtures were not excluded from the following analyses.

As expected, Figure 6.31c shows no significant correlation between e_{min} and M. Figure 6.32 shows plots of Γ_{50}, λ, and M vs e_{max}. No significant correlations are observed with any of the SSL parameters. However, it is noteworthy that in the Γ_{50} vs e_{max} plot, virtually the entire data set falls within the boundaries defined by $\Gamma_{50} = 1.1 \cdot e_{max}$ and $\Gamma_{50} = 0.38 \cdot e_{max}$. Figure 6.33 shows plots of (e_{max} - e_{min}) vs Γ_{50}, λ, and M. No significant correlations are observed in any of the plots.

Since the effect of FC on the SSL has received considerable attention by other researchers, it is deemed appropriate to investigate herein if FC has an effect on the correlation between Γ_{50} and e_{min}. To do this, Figure 6.31a was disaggregated into four different FC ranges and the resulting plots are shown in Figure 6.34. Also shown in each of these four plots is the best fit line of the entire database (Eq. 6.3). It is observed that: 1) There is no systematic change in the location of the data points with respect to the global best fit line as the range of FC is modified. 2) Parts a to c of Figure 6.34 indicate that the global best fit line is in agreement with the trend of the data points regardless of the FC range. 3) Figure 6.34d on its own indicates that soils with FC > 50 tend to plot below the global best fit line. However this tendency is obscured by the scatter and is not supported by Figure 6.34 a to c. In accordance with the previous observations it seems justified to conclude that FC does not have an effect on the Γ_{50} vs e_{min} correlation.

The effect of particle shape on the Γ_{50} vs e_{min} correlation was also investigated. For this purpose, the database was split into two groups. One group was composed of soils with angular grains and included the soiltypes whose particle shape classification (Table 6.2) was angular (A), sub-angular (SA), or angular to sub-angular (A-SA). The other group was composed of soils with rounded grains and included the soiltypes whose particle shape classification was rounded (R), sub-rounded (SR), or rounded to sub-rounded (R-SR). In order to focus only on soils with particle shapes that were

unambiguously angular or rounded, soiltypes with particle shape sub-angular to sub-rounded (SA-SR) were not considered. Figure 6.35 shows that both data groups adjust well to the best fit line of the entire database. It is therefore concluded that the Γ_{50} vs e_{min} correlation is independent of particle shape. The independence of the Γ_{50} vs e_{min} correlation from FC and particle shape is in agreement with the observations made in section 6.2 that e_{min} captures the effect of changes in FC (moreover, changes in GSD in general) and particle shape.

Correlations between e_{min} and values of Γ associated with higher stress levels were also investigated. Namely, Γ_{90}, Γ_{150}, Γ_{250}, Γ_{450}, and Γ_{800} were plotted against e_{min} (Γ_n is defined in section 2.1). The stress levels associated with Γ were chosen so that they were approximately uniformly distributed in a $\log_{10}(p')$ scale. Soiltypes were only included in a correlation of e_{min} with Γ_n if n fell within or was close to the p' domain of their SSL. For instance, the SSL domain for *HKS sand and CHB silt mix (0)* extends from 15 kPa to 335 kPa (Table 6.3). Therefore, this soiltype was only considered when investigating correlations between e_{min} and Γ_{90}, Γ_{150}, and Γ_{250}. This was done to prevent excessive extrapolation of the SSLs from obscuring the correlations. The plot of Γ_{50} vs e_{min} was repeated using the same approach, i.e., including only soiltypes with a p' domain that either included or was close to 50 kPa. Table D.1 in the appendix indicates the Γ_n vs e_{min} correlations in which each soiltype was included.

The resulting plots of the different Γ_n vs. e_{min} are shown in Figure 6.36. The plots indicate that significant correlations ($R^2 > 0.6$) exist for all *n* values. If one accepts that these correlations have a fundamental basis (and the existence of such a basis will be addressed in the discussion), the implication is that e_{min} can be used to estimate the entire SSL in e-p' space up to p' = 800 kPa, and not only its vertical location (Γ). To make this prediction Γ_n is calculated by evaluating e_{min} in the corresponding correlation shown in Figure 6.36, thus a total of six (p', e) points of the SSL can be calculated.

Figure 6.37 shows the predicted SSLs for different e_{min} values and the best fit lines of the form $e = \Gamma - \lambda \cdot log_{10}(p')$. A consistent trend of direct correlation between λ and e_{min} is observed. This trend is summarised in Figure 6.38 and can be represented with the following equation:

$$\lambda = 0.13 \cdot e_{min} + 0.01 \qquad 6.4$$

The $R^2 = 1$ value shown in Figure 6.38 is a consequence of the SSLs in Figure 6.37 being generated from a fixed set of equations (the equations shown in Figure 6.36), and should not be interpreted as meaning that λ can be explained entirely by e_{min}. Figure 6.39 compares the λ-e_{min} correlation from Figure 6.38 (Eq. 6.4) to the λ-e_{min} data points from Figure 6.31b. Naturally, the correlation is in general good agreement with the data from which it originated, with a slight tendency of the correlation to overestimate λ for a given value of e_{min}.

Given that Cubrinovski and Ishihara (2000) indicated that the correlation between λ and void ratio limits was dependent on particle shape (Figure 6.14), and having noted that the database suggests a correlation between λ and e_{min} (Figure 6.38 and Eq. 6.4), the effect of particle shape on this correlation was also explored. This was done by splitting Figure 6.31b into the same two particle

shape groups that were used in Figure 6.35. The resulting plots (Figure 6.40) do not reveal any significant differences between rounded and angular soiltypes in λ-e_{min} space.

6.4.2 Trends identified in sub-sets of the database obtained from a single reference

Figure 6.41a to Figure 6.41k contain the plots of Γ_{50} vs e_{min} and λ vs e_{min} obtained from eleven subsets of the database, each obtained from a single reference. A linear trendline and the corresponding R^2 value have been added to the plots that indicate a significant correlation. With regards to the plots of Γ_{50} vs e_{min}, seven of the eleven datasets indicate a linear correlation with $R^2 \geq 0.65$. Furthermore, in six of these seven plots the linear correlation is quite strong with $R^2 \geq 0.88$. It is also noted that the data in Figure 6.41j seem to suggest a direct correlation between Γ_{50} and e_{min}, however the correlation is non-linear. The data from Zlatović and Ishihara (1995) (Figure 6.41k) is also interesting in that four of the six data points suggest a strong linear correlation between Γ_{50} and e_{min}, but the remaining two points plot away from this trend. It is not clear what could be the reason for this behaviour.

As for the plots of λ vs e_{min}, only two datasets reveal a direct and linear correlation between these two parameters (Figure 6.41 c and f). Additionally, the trend is vaguely present in the data from Papadopoulou and Tika (2008) (Figure 6.41 b).

All the data points in Figure 6.41 are labelled with the FC expressed as a percentage. The labels indicate that in the plots in which there is a correlation, this correlation is independent of the FC. Additionally, and in agreement with Figure 6.34, inspection of the labels also reveals that neither Γ_{50} nor λ are correlated to FC.

6.5 Discussion

The issue of whether there is a fundamental basis for e_{min} to be correlated to the entire projection of the SSL in e-p' space, i.e. Γ and λ, is now addressed. For this purpose it is convenient to recall the observation made by Muir-Wood and Maeda (2008) (section 6.2.3). Namely, changes in GSD have an effect on both Γ and λ because both parameters are affected by the packing efficiency of the soil, and packing efficiency is influenced by GSD. That is, Γ and λ are fundamentally linked through packing efficiency. Since Muir-Wood and Maeda (2008) used only circular particle shapes in their experiments, they effectively removed the effect of particle shape and were able to characterise packing efficiency by considering only the GSD curve (parameter R_D). However, this is not possible when considering soils with differences in particle shape because packing efficiency is affected by these differences and is no longer a function of GSD alone. The advantage of correlating e_{min} to the SSL is that e_{min} is a direct indicator of packing efficiency that reflects the combined effect of particle shape and GSD. This leads to the conclusion that there is a fundamental basis for both Γ and λ to be correlated to e_{min}. This is further reflected in the similarity between Figure 6.21 and Figure 6.37: In both figures Γ and λ are directly proportional to packing efficiency ($1/e_{min}$ or R_D). This

means that the global trends observed in the database of non-plastic soils (Figure 6.37) are in general agreement with the DEM experiments of Muir-Wood and Maeda (2008).

There are also important reasons that limit the extent to which the e_{min} values reported in Table 6.2 can be correlated to the SSL and these are now discussed. First of all it is recognised that the e_{min} calculated from any given standard method is most likely not the densest state, i.e. the true e_{min}, at which that soil can exist. Rather, it is the void ratio reached when following that standard method. For example, the true e_{min} of an array of cubes all of the same size is zero (attained by packing the cubes flush against each other). However, it is unlikely that the cubes would reach this true e_{min} by any amount of shaking on a vibrating table (ASTM D4253) or by subjecting them to the standard or modified Proctor compaction procedures (ASTM D698, ASTM D1557). Thus it seems reasonable to assume that the true e_{min} of a soil is actually unknown and that the e_{min} values measured with any given procedure are only estimates.

There is also the issue of the scatter due to comparing e_{min} values obtained through different procedures, performed by different technicians, and employing different equipment, such as in Table 6.2. Tavenas and Rochelle (1972) reported that in such cases the scatter in maximum index dry density values is of ±64 kg/m^3. Assuming typical values for the maximum index dry density and G_s of 1760 kg/m^3 and 2.7 respectively, the corresponding uncertainty in e_{min} is ±0.055. Given that the slopes of the linear correlations in Figure 6.36 are close to 1, the resulting uncertainty in Γ_n would also be about ±0.055. Jefferies and Been (2006) suggest that Γ_n should be determined with a precision of about ±0.01. Clearly this criterion cannot be met by using the correlations in Figure 6.36 and therefore these correlations are inadequate to try to estimate the SSL of a soil based only on its e_{min}.

Furthermore, the e_{min} values obtained from a single standardised procedure have uncertainties that are not negligible. For example, ASTM D4253 (2006) states that the acceptable range of the maximum index dry density obtained by two laboratories is ±22 kg/m^3. Assuming again a maximum index dry density of 1760 kg/m^3 and a G_s of 2.7, the corresponding uncertainty in e_{min} and Γ_n is ±0.02. Although there is a sensible reduction in the uncertainty of Γ_n, the ±0.01 criterion suggested by Jefferies and Been (2006) is still not met. These are considerations to be kept in mind if the SSL of a soil is to be estimated based only on its e_{min}.

Another limitation to correlating e_{min} with the SSL is that e_{min} is not always affected by particle crushing. For instance several methods of determining e_{min} have been specifically designed to minimise particle crushing e.g. (Germaine and Germaine 2009; Lade et al. 1998). Conversely, there are at least two ways in which particle crushing can affect the SSL. First, several authors e.g. (Been et al. 1991; Konrad 1997) have indicated that the curvature exhibited by the SSL in e-log(p') space at p' $\geq\approx$ 800 kPa is an effect of particle crushing. And second, the works reviewed in section 6.2.2 suggest that particle crushing of angular grains can have an effect on λ even at relatively low p' values. It must then be concluded that e_{min} in general cannot adequately capture the effects of particle crushing on the SSL.

Not all the datasets obtained from a single reference follow the global trends of Γ vs e_{min} and λ vs e_{min} indicated by the entire database (Figure 6.41). This is despite the fact that the scatter in e_{min}

values is lower when using information from a single source. However, six of the eleven datasets do corroborate the trend of Γ vs e_{min} with values of R^2 greater than 0.88. The experimental support for a direct linear correlation between λ and e_{min} was much weaker, with only two of the eleven datasets exhibiting a strong correlation ($R^2 > 0.7$). Overall, the datasets suggest that at least Γ can be strongly correlated to e_{min} values obtained from a single procedure but that it is less common for λ to be strongly correlated to e_{min}.

Both the analysis of the entire database and of subsets from individual references lent greater support to a direct linear correlation of e_{min} with Γ than with λ. The reason for this might be partly due to the way in which Γ and λ are affected by errors in void ratio measurements. For instance, Figure 6.42 shows an SSL with average values of Γ_1 and λ of 0.9 and 0.07 respectively, defined between 50 kPa < p' < 1000 kPa. The shaded area around the average SSL indicates the zone in which the true SSL can exist if the error in void ratio measurements is assumed to be ±0.01. The two dashed lines represent the steepest and shallowest SSLs that can exist within the shaded area. The shallowest SSL has parameters Γ_1 = 0.864, and λ = 0.055, whereas the steepest SSL has parameters Γ_1 = 0.936, and λ = 0.085. That is, the average SSL has a potential uncertainty on Γ and λ of ± 0.036 and ±0.015, respectively. In terms of percentage these uncertainties correspond to ±4.0% for Γ and ±22% for λ. Figure 6.31a and b show that the values of Γ and λ chosen for this example are fairly typical of non-plastic soils. On that basis it can be generalised that for a given error on void ratio measurements, the potential relative error of λ is much greater than that of Γ_1.

More fundamentally, the effects that particle crushing may have on λ are also likely to weaken the correlation with e_{min} since, as noted earlier, these particle crushing effects are not generally captured by e_{min}. The weak correlation between e_{min} and λ could also be the result of particle shape effects. That is, the reviewed literature shows that particle shape has an effect on λ (Table 6.1). It was hypothesised in this work that since e_{min} is also affected by particle shape, any correlation between e_{min} and λ would implicitly account for particle shape effects. The reviewed database seems to support this hypothesis (Figure 6.40) but additional experimental data is needed in this regard.

6.6 Concluding remarks

A critical review of published correlations between index parameters and the SSL was performed. From the review it was established that there are fundamental reasons to expect e_{min}, e_{max}, and (e_{max}-e_{min}) to be correlated to both Γ and λ. As for M, the experimental data indicates that it is strongly correlated to particle shape and largely independent of other soil properties such as GSD and the void ratio limits. Through the analysis of a database of 151 non-plastic soils with a wide variety of GSDs and bulky particle shapes, it was established that Γ is strongly correlated to e_{min}, but no significant correlations were found between Γ and e_{max} or (e_{max}-e_{min}). The Γ_{50} vs e_{min} correlation was found to be independent of FC and particle shape. Such independence is reasonable given that e_{min} already captures the effect of variations in GSD and particle shape. The correlations of e_{min} with Γ_n at different stress values further revealed a correlation between e_{min} and λ implying that, in

principle, the whole e-p' projection of the SSL is correlated to e_{min}. The results indicated that the λ-e_{min} correlation is independent of particle shape.

The discussion has drawn attention to the fact that the uncertainty arising from mixing e_{min} values obtained through different procedures, technicians and equipment in Table 6.2, implies that the SSLs of Figure 6.37 cannot be relied upon to make reliable SSL predictions based only on e_{min}. However, analyses of datasets of SSLs and e_{min} values obtained from a single reference indicate that within a single triaxial testing programme e_{min} can be a reliable predictor of Γ.

The correlations between e_{min}, Γ, and λ identified in this chapter will now be used to plan and execute a triaxial testing programme aimed at determining the variability of SSL parameters at the Impala TSF. The details of this testing programme are the subject of the next chapter.

6.7 Tables and figures

Table 6.1 Correlations between soil index parameters and the SSL.

	Γ, Γ_{100}, e_0	**λ**	**M, ϕ_{cs}**
FC	**Strong:** Thevanayagam et al. (2002), Rahman and Lo (2008) **Weak:** Bouckovalas et al. (2003)	**Weak:** Thevanayagam et al. (2002), Jefferies and Been (2006), Rahman and Lo (2008), Bouckovalas et al. (2003) **None:** Cubrinovski and Ishihara (2000)	**None:** Bouckovalas et al. (2003)
Particle shape	**Strong:** Cho et al. (2006), Maeda et al. (2009), Li (2013), Yang and Luo (2015)	**Strong:** Poulos et al. (1985), Yang and Luo (2015), Hird and Hassona (1990) **Medium:** Cubrinovski and Ishihara (2000) **Weak:** Cho et al. (2006), Li (2013) **None:** Maeda et al. (2009)	**Strong:** Cho et al. (2006), Li (2013), Sadrekarimi and Olson (2011), Yang and Luo (2015)
GSD	**Strong:** Poulos et al. (1985), Muir-Wood and Maeda (2008), Li (2013)	**Medium:** Muir-Wood and Maeda (2008) **None:** Poulos et al. (1985), Li (2013)	**None:** Li (2013)
e_{max}	**Medium:** Jefferies and Been (2006), Cho et al. (2006)		**Weak:** Cho et al. (2006)
e_{min}	**Medium:** Cho et al. (2006)		**Weak:** Cho et al. (2006)
e_{max} - e_{min}	**Medium:** Cubrinovski and Ishihara (2000)	**Weak:** Cubrinovski and Ishihara (2000), Cho et al. (2006)	**Weak:** Cho et al. (2006)

Table 6.2 Index properties of soils in the database.

Soiltype (FC %)	Sym.	PI of fines	G_s	D_{50} (μm)	C_u	Grain shape[j]	e_{min}		e_{max}		References
							Value	Method	Value	Method	
Ardebil sand-silt mix (0)	ARM	n/a[k]	2.67	190	1.6	SR	0.746	n/k	1.09	n/k	Naeini and Baziar (2004)
Ardebil sand-silt mix (10)		n/k[l]	2.69	180	1.9	SR	0.625		1.16		
Ardebil sand-silt mix (20)		n/k	2.71	140	2.4	SR	0.594		1.24		
Ardebil sand-silt mix (30)		n/k	2.73	100	3.1	SR	0.592		1.33		
Ardebil sand-silt mix (35)		n/k	2.73	80	3.6	SR	0.615		1.40		
Ardebil sand-silt mix (50)		n/k	2.75	75	3.7	n/k	0.630		1.64		
Ardebil sand-silt mix (100)		n/k	2.78	25	2.3	n/k	0.765		1.72		
Assyros sand-silt mix (0)	ASM	n/a	2.649	330	1.3	R-SR	0.582	ASTM D4253 (2A) & ASTM D698	0.841	ASTM D4254 (C) & Dry pluviation	Papadopoulou and Tika (2008)
Assyros sand-silt mix (5)		np[m]	2.650	330	1.9	R-SR	0.543		0.761		
Assyros sand-silt mix (10)		np	2.650	330	3.3	R-SR	0.487		0.788		
Assyros sand-silt mix (15)		np	2.651	330	10	R-SR	0.377		0.747		
Assyros sand-silt mix (25)		np	2.653	300	18	R-SR	0.346		0.684		
Assyros sand-silt mix (35)		np	2.654	260	28	R-SR	0.341		0.776		
Assyros sand-silt mix (40)		np	2.655	230	32	R-SR	0.379		0.804		
Assyros sand-silt mix (60)		np	2.657	60	11	R-SR	0.468		0.948		
Assyros sand-silt mix (100)		np	2.663	24	7.5	R-SR	0.658		1.663		
DEM discs 1 (0)	CP	n/a	n/k	71[a]	2[b]	R	0.210	Control of interparticle friction and porosity in DEM	0.277	Control of interparticle friction and porosity in DEM	Muir-Wood and Maeda (2008)
DEM discs 2 (0)		n/a	n/k	44[a]	5[b]	R	0.195		0.254		
DEM discs 3 (0)		n/a	n/k	31[a]	10[b]	R	0.176		0.231		
DEM discs 4 (0)		n/a	n/k	23[a]	20[b]	R	0.158		0.207		
Duzce-1 (13)	DUZ	np	2.732	380	9.7	n/k	0.366	*Same as ASM*	0.724	*Same as ASM*	*Same as ASM*
Glass balls 1 (0)	GB	n/a	2.6	920	1.1	R	0.497	ASTM D4253 - 96	0.790	ASTM D4254 - 96	Li (2013)

Table 6.2 Index properties of soils in the database. *(Continued…)*

Soiltype (FC %)	Sym.	PI of fines	G_s	D_{50} (µm)	C_u	Grain shape[j]	e_{min}		e_{max}		Reference
							Value	Method	Value	Method	
Glass balls 2 (0)	GB	n/a	2.6	920	1.4	R	0.467	ASTM D4253-96	0.760	ASTM D4254-96 (B)	Li (2013)
Glass balls 3 (0)		n/a	2.6	920	2.5	R	0.330		0.686		
Glass balls 4 (0)		n/a	2.6	920	5	R	0.260		0.576		
Glass balls 5 (0)		n/a	2.6	920	10	R	0.218		0.511		
Glass balls 6 (10)		np	2.6	920	20	R	0.160		0.432		
HKS sand & CHB silt mix (0)	HCM	n/a	2.712	446	2.4	A	0.572	n/k	0.949	n/k	Yang et al. (2006)
HKS sand & CHB silt mix (5)		np	2.713	431	3.4	A	0.540		0.865		
HKS sand & CHB silt mix (10)		np	2.715	418	6.6	A	0.509		0.782		
HKS sand & CHB silt mix (15)		np	2.718	399	11	A	0.450		0.752		
HKS sand & CHB silt mix (20)		np	2.719	379	13	A	0.390		0.728		
HKS sand & CHB silt mix (30)		np	2.721	328	14	A	0.394		0.717		
HKS sand & CHB silt mix (50)		np	2.726	72	8.9	A	0.452		0.874		
HKS sand & CHB silt mix (70)		np	2.732	45	2.2	A	0.631		1.121		
HKS sand & CHB silt mix (94)		np	2.739	34	2.0	A	0.731		1.413		
Hostun sand 1 (0)	HOS	n/a	2.6	920	1.1	A	0.583	ASTM D4253-96	0.901	ASTM D4254-96 (B)	Li (2013)
Hostun sand 2 (0)		np	2.6	920	1.4	A	0.577		0.881		
Hostun sand 3 (0)		np	2.6	920	2.5	A	0.473		0.863		
Hostun sand 4 (0)		np	2.6	920	5	A	0.444		0.834		
Hostun sand 5 (0)		np	2.6	920	10	A	0.376		0.782		
Hostun sand 6 (10)		np	2.6	920	20	A	0.348		0.752		
Hostun sand 7 (0)		np	2.6	350	1.1	A	0.592		0.918		
Hostun sand 8 (0)		np	2.6	750	1.4	A	0.575		0.878		

Table 6.2 Index properties of soils in the database. *(Continued…)*

Soiltype (FC %)	Sym.	PI of fines	G_s	D_{50} (µm)	C_u	Grain shape[j]	e_{min}		e_{max}		Reference
							Value	Method	Value	Method	
Leighton Buzzard 1 (0)	LBS	n/a	n/k	860	1.2	SA-SR	0.58	ASTM D2049-69	0.750	ASTM D2049-69	Sladen et al. (1985)
Leighton Buzzard 2 (0)		n/a	n/k	500	n/a	SA-SR	0.515	Vibrating hammer	0.790	ASTM D2049	Hird & Hassona (1990)
Mai Liao sand-silt mix (0)	MLM	n/a	2.69	125	1.7	A	0.646	ASTM D4253 (1A)	1.125	ASTM D4254 (C)	Huang et al. (2004)
Mai Liao sand-silt mix (15)		< 8	2.69	115	2.1	A	0.589		1.058		
Mai Liao sand-silt mix (30)		< 8	2.70	100	3.2	SA	0.593		1.213		
Mai Liao sand-silt mix (50)		< 8	2.70	75	3.3	SA	0.564		1.308		
Merriespruit tailings (0)	MER	n/a	≈2.7	130	1.9	A-SA	0.738	ASTM D2049-83	1.221	ASTM D2049-83	Fourie and Papageorgiou (2001), Papageorgiou (2004), Tshabalala (2003)
Merriespruit tailings (20)		1-8	≈2.7	120	4.7	A-SA	0.696		1.326		
Merriespruit tailings (30)		1-8	≈2.7	100	30	A-SA	0.577		1.331		
Merriespruit tailings (60)		1-8	≈2.7	60	25	A-SA	0.655		1.827		
Mizpah dam tailings (72)	MIZ	7	2.73	32	28	A-SA	0.481	BS 1377	1.8	Slurry sediment.[c]	Vermeulen (2001)
Ottawa sand-silt mix (0)	OTM	n/a	2.65	390	1.4	R	0.48	ASTM D4253-04	0.78	ASTM D4254-04	Murthy et al. (2007)
Ottawa sand-silt mix (5)		np	2.65	375	2.1	R	0.42		0.70		
Ottawa sand-silt mix (10)		np	2.65	365	4.4	SR	0.36		0.65		
Ottawa sand-silt mix (15)		np	2.65	349	11	SR	0.32		0.63		
Pay dam tailings (77)	PAY	7	2.74	25	22	A-SA	0.64	I.C. to 400 kPa[d]	2.1	Slurry sediment.[c]	Vermeulen (2001)
Rimnio (37)	RIM	np	2.667	100	5.3	n/k	0.419	*Same as ASM*	1.059	*Same as ASM*	*Same as ASM*
Silica sand-silt mix (0)	SIM	n/a	n/k	250	1.7	A-SA	0.608	ASTM D1557	0.800	ASTM D4254	Thevanayagam et al. (2002)
Silica sand-silt mix (7)		np	n/k	235	2.1	A-SA	0.524		0.777		
Silica sand-silt mix (15)		np	n/k	230	14	A-SA	0.428		0.750		
Silica sand-silt mix (25)		np	n/k	215	28	A-SA	0.309		0.860		
Silica sand-silt mix (40)		np	n/k	190	47	A-SA	0.330		1.070		

Table 6.2 Index properties of soils in the database. *(Continued…)*

Soiltype (FC %)	Sym.	PI of fines	G_s	D_{50} (µm)	C_u	Grain shape[j]	e_{min}		e_{max}		Reference
							Value	Method	Value	Method	
Silica sand-silt mix (60)	SIM	np	n/k	30	26	A-SA	0.413	ASTM D1557	1.350	ASTM D4254	Thevanayagam et al. (2002)
Silica sand-silt mix (100)		np	n/k	10	10	A-SA	0.627		2.100		
Stava tailings (0)	STA	n/a	2.721	190	2.4	SA-SR	0.770	Densest odometer specimen	1.079	Loosest odometer specimen	Carrera et al. (2011)
Stava tailings (30)		<9.4	2.753	130	9.7	SA-SR	0.692		0.852		
Stava tailings (50)		<9.4	2.775	75	10	SA-SR	0.481		0.759		
Stava tailings (100)		<9.4	2.828	25	7.8	SA-SR	0.751		0.928		
Toyoura sand-silt mix (5)	TOM	np	2.65	168	1.7	A-SA	0.563	Japanese Geotechnical Society Standard	1.002	Japanese Geotechnical Society Standard	Zlatović and Ishihara (1995), Ishihara (1993)
Toyoura sand-silt mix (10)		np	2.65	160	4.3	A-SA	0.528		1.041		
Toyoura sand-silt mix (15)		np	2.65	155	11	A-SA	0.496		1.079		
Toyoura sand-silt mix (30)		np	2.65	140	31	A-SA	0.519		1.204		
Toyoura sand-silt mix (100)		np	2.65	10	6.9	A-SA	0.618		1.749		
7U7-crushed sand (4.4)	CDS 1[e]	n/k	n/k	300	3.2	SA	n/k	ASTM D1557	0.790	ASTM D4254 (A)	Cho et al. (2006)[i]
8M8 crushed sand (1.6)		n/k	n/k	380	3.3	SA	n/k		0.970		
9C1 crushed sand (0.7)		n/k	n/k	520	2.3	SA	n/k		0.910		
ASTM 20/30 sand (0)		n/a	n/k	600	1.4	R	n/k		0.690		
ASTM graded sand (0)		n/a	2.65	350	1.7	SR	0.500		0.820		
Blasting sand (0)		n/a	2.65	710	1.9	A	0.698		1.025		
Glass beads (0)		n/a	2.46	320	1.4	R	0.542		0.720		
Granite powder (44)		n/k	2.75	90	6.2	A	0.482		1.296		
Jekyll Island sand (0)		n/a	n/k	170	1.7	SA-SR	n/k		1.040		
Margaret River sand (0)		n/a	n/k	490	1.9	SR	n/k		0.870		

Table 6.2 Index properties of soils in the database. *(Continued…)*

Soiltype (FC %)	Sym.	PI of fines	G_s	D_{50} (μm)	C_u	Grain shape[j]	e_{min}		e_{max}		Reference
							Value	Method	Value	Method	
Nevada sand (2.2)	CDS 1[e]	n/k	n/k	150	1.8	SR	0.570	ASTM D1557	0.850	ASTM D4254 (A)	Cho et al. (2006)[i]
Ottawa #20/30 sand (0)		n/a	2.65	720	1.2	SR	0.502		0.742		
Ottawa F-110 sand (6)		n/k	2.65	120	1.7	SR	0.535		0.848		
Ponte Vedra sand (0.3)		n/a	n/k	180	1.8	SA-SR	n/k		1.070		
Sandboil (4)		n/k	2.62	360	2.4	SA-SR	0.510		0.790		
Ticino sand (0)		n/a	2.68	580	1.5	A	0.574		0.990		
Banding sand 1 (0)	CDS 2[e]	n/a	n/k	180	1.5	n/k	0.54	ASTM D2049-69	0.82	ASTM D2049-69	Cho et al. (2006)[i]
Banding sand 5 (0)		n/a	n/k	110	1.4	n/k	0.55		0.87		
Banding sand 6 (0)		n/a	n/k	160	1.7	n/k	0.52		0.82		
Banding sand 9 (0)		n/a	n/k	140	1.6	n/k	0.53		0.80		
Brenda sand (0)		n/a	2.7	100	1.9	n/k	0.688	n/k	1.060	n/k	
Chonan silty sand (18)		n/k	n/k	150	4.1	n/k	0.69	n/k	1.310	n/k	
Dune sand (6)		np	n/k	210	2.1	A-SA	0.540	ASTM D2049	0.910	ASTM D2049	
Fort Peck sand (2)		n/k	n/k	n/a	n/a	n/k	n/k	n/k	1.010	n/k	
Fraser River sand (0)		n/a	2.75	250	1.7	n/k	0.6	ASTM D2049	1.000	ASTM D2049	
Hostun RF sand (0)		n/a	n/k	320	1.8	n/k	0.655	n/k	1.000	n/k	
Kogyuk 350 (0)		n/a	n/k	350	1.7	SA-SR	0.523	n/k	0.783	n/k	
Lagunillas (70)		4	2.68	50	3	n/k	0.766	JSSMFE[f] method	1.389	JSSMFE[f] method	
Likan (0)		n/a	n/k	240	2.9	n/k	0.756	n/k	1.239	n/k	
Lornex (0)		n/a	n/k	300	2.0	A	0.68	n/k	1.080	n/k	
Mailiao (5)		n/k	n/k	250	2.9	n/k	0.739	n/k	1.279	n/k	
Mailiao (10)		n/k	n/k	220	3.5	n/k	0.595	n/k	1.151	n/k	

Table 6.2 Index properties of soils in the database. *(Continued…)*

Soiltype (FC %)	Sym.	PI of fines	G_s	D_{50} (μm)	C_u	Grain shape[j]	e_{min}		e_{max}		Reference
							Value	Method	Value	Method	
Mailiao (15)	CDS 2[e]	n/k	n/k	210	4.2	n/k	0.44	n/k	1.031	n/k	Cho et al. (2006)[i]
Massey tunnel (3)		n/k	2.68	250	1.5	n/k	0.71	ASTM D4253	1.102	ASTM D4254	
Monterey #0 (0)		n/a	2.65	380	1.6	SR	0.53	M.J.M.[g]	0.860	Dry pluviation	
Monterey #16 (0)		n/a	2.65	1300	1.3	SA-SR	0.49		0.710	Wet pluviation	
Nerlerk (2)		n/k	n/k	280	2.0	SA-SR	0.62	ASTM D2049-69	0.940	ASTM D2049-69	
Nevada fine (5)		n/k	n/k	120	1.8	n/k	0.57	n/k	0.870	n/k	
Ottawa C109 (0)		n/a	2.67	350	1.7	R-SR	0.50	ASTM D4254	0.820	ASTM D4253	
S (12)		n/k	n/k	800	3.0	n/k	0.596	n/k	1.133	n/k	
S (20)		n/k	n/k	700	3.8	n/k	0.547	n/k	1.111	n/k	
Sacramento (0)		n/a	2.68	300	1.7	SR	0.53	M.J.M.[g]	0.870	Dry pluviation	
Sydney (0)		n/a	n/k	300	1.5	n/k	0.565	n/k	0.855	n/k	
Syncrude (12)		np	2.62	170	2.4	SA	0.520	ASTM D4254	0.960	ASTM D4253	
Tar Island Dyke (5)		n/k	n/k	n/k	n/k	n/k	n/k	n/k	1.005	n/k	
Tia Juana Silty (12)		np	2.68	160	2.7	n/k	0.62	JSSMFE[f] method	1.099	JSSMFE[f] method	
Toyoura 1 (0)		n/a	2.65	170	1.7	SA	0.597	JSSMFE[f] method	0.977	JSSMFE[f] method	
Unimin 2010 (0)		n/a	2.665	870	2.0	A	0.646	ASTM D4253-93 (1A)	1.027	ASTM D4254-91 (A)	
Castro Sand B (0)	JB1[h]	n/a	n/k	150	n/k	n/k	0.500	n/k	0.840	n/k	Jefferies and Been (2006)[i]
Castro Sand C (0)		n/a	n/k	280	n/k	n/k	0.660	n/k	0.990	n/k	
Hokksund (0)		n/a	n/k	390	n/k	n/k	0.550	n/k	0.910	n/k	
Monterey (0)		n/a	n/k	370	n/k	n/k	0.540	n/k	0.820	n/k	
Ottawa (0)		n/a	n/k	530	n/k	n/k	0.490	n/k	0.790	n/k	
Reid Bedford (0)		n/a	n/k	240	n/k	n/k	0.550	n/k	0.870	n/k	

Table 6.2 Index properties of soils in the database. *(Continued…)*

Soiltype (FC %)	Sym.	PI of fines	G_s	D_{50} (μm)	C_u	Grain shape[j]	e_{min}		e_{max}		Reference
							Value	Method	Value	Method	
Ticino-4 (0)	JB1[h]	n/a	2.67	530	n/k	n/k	0.600	n/k	0.890	n/k	Jefferies and Been (2006)[i]
Toyoura 2 (0)		n/a	2.65	160	n/k	SA	0.608	n/k	0.981	n/k	
Toyoura 3 (0)		n/a	n/k	210	n/k	SA	0.656	n/k	0.873	n/k	
Alaskan Beaufort (5)	JB2[h]	n/k	2.7	140	n/k	n/k	0.565	n/k	0.856	n/k	
Alaskan Beaufort (10)		n/k	2.7	140	n/k	n/k	0.530	n/k	0.837	n/k	
Chek Lap Kok (0.5)		n/a	2.65	1000	n/k	n/k	0.411	n/k	0.682	n/k	
Duncan Dam (6.5)		np	2.77	200	n/k	n/k	0.760	n/k	1.150	n/k	
Erksak (0.7)		n/a	2.66	330	n/k	SR	0.521	n/k	0.747	n/k	
Erksak (1)		n/k	2.67	320	n/k	SR	0.614	n/k	0.808	n/k	
Erksak (3)		n/k	2.67	355	n/k	SR	0.525	n/k	0.963	n/k	
Fraser River (Massey) (<5)		np	2.68	200	1.6	SR	0.700	"ASTM standards"	1.100	"ASTM standards"	
Isserk (2)		n/k	2.67	210	n/k	n/k	0.520	n/k	0.760	n/k	
Isserk (5)		n/k	n/k	210	n/k	n/k	0.550	n/k	0.830	n/k	
Isserk (10)		n/k	n/k	210	n/k	n/k	0.440	n/k	0.860	n/k	
Nerlerk (1.9)		n/k	2.66	270	n/k	SA-SR	0.536	n/k	0.812	n/k	
Nerlerk (12)		n/k	n/k	280	n/k	SA-SR	0.430	ASTM D2049-69	0.960	Kolbuszewski (1948)	
Highland Valley Copper (8)	JB3[h]	np	2.66	200	2.8	A	0.544	"ASTM standards"	1.055	"ASTM standards"	
Hilton Mines (2.5)		n/k	n/k	200	n/k	n/k	0.620	n/k	1.050	n/k	
Syncrude (Mildred Lake) (10)		n/k	2.66	160	2.2	SA-SR	0.522	"ASTM standards"	0.958	"ASTM standards"	
Syncrude Oil Tailings (3.5)		n/k	2.64	207	n/k	n/k	0.544	n/k	0.898	n/k	

a) D_{50} expressed in mm; b) Value of R_D = (max particle size/min. particle size); c) highest void ratio attainable when preparing a triaxial specimen by slurry sedimentation; d) Void ratio of triaxial specimen after being isotropically consolidated to 400 kPa; e) CDS1 and CDS2 refers to soiltypes with and without particle shape information, respectively, reported by Cho et al. (2006) ; f) Japanese Society of Soil Mechanics and Foundation Engineering; g) Modified Japanese Method; h) JB1, JB2, and JB3, refer to laboratory, natural, and tailings sands, respectively, reported in Table 2.1 of Jefferies & Been (2006) and its companion website; i) Secondary reference. When possible, the primary references were used to collect the relevant information; j) Particle shape symbols: A = angular, R = rounded, and S = sub-; k) n/a = not applicable; l) n/k = not known; m) np = non-plastic.

Table 6.3 SSL parameters of the different soiltypes.

Soiltype (FC %)	p' domain (kPa)	Γ_{50}	λ	M	Soiltype (FC %)	p' domain (kPa)	Γ_{50}	λ	M
Ardebil sand-silt mix (0)	105 - 290	1.126	0.242	1.57	Glass balls 2 (0)	120 - 1260	0.649	0.022	0.89
Ardebil sand-silt mix (10)	90 - 265	1.104	0.269	1.46	Glass balls 3 (0)	140 - 840	0.602	0.035	0.87
Ardebil sand-silt mix (20)	80 - 245	0.968	0.205	1.36	Glass balls 4 (0)	130 - 550	0.485	0.032	0.84
Ardebil sand-silt mix (30)	65 - 265	0.935	0.227	1.12	Glass balls 5 (0)	140 - 570	0.436	0.042	0.81
Ardebil sand-silt mix (35)	65 - 255	0.897	0.261	1.00	Glass balls 6 (10)	75 - 580	0.350	0.042	0.82
Ardebil sand-silt mix (50)	70 - 270	0.916	0.239	1.01	HKS sand & CHB silt mix (0)	15 - 335	0.840	0.035	1.64
Ardebil sand-silt mix (100)	90 - 240	1.002	0.214	1.49	HKS sand & CHB silt mix (5)	10 - 310	0.777	0.022	n/a
Assyros sand-silt mix (0)	75 - 1410	0.791	0.108	1.36	HKS sand & CHB silt mix (10)	50 - 500	0.704	0.043	n/a
Assyros sand-silt mix (5)	250 - 1040	0.759	0.069	1.41	HKS sand & CHB silt mix (15)	10 - 310	0.641	0.046	n/a
Assyros sand-silt mix (10)	40 - 1800	0.693	0.099	1.45	HKS sand & CHB silt mix (20)	1 - 515	0.568	0.056	n/a
Assyros sand-silt mix (15)	40 - 875	0.603	0.046	1.54	HKS sand & CHB silt mix (30)	1 - 530	0.522	0.032	1.73
Assyros sand-silt mix (25)	20 - 1700	0.489	0.061	1.41	HKS sand & CHB silt mix (50)	1 - 260	0.641	0.038	1.66
Assyros sand-silt mix (35)	5 - 1420	0.427	0.035	1.44	HKS sand & CHB silt mix (70)	1 - 250	0.846	0.041	n/a
Assyros sand-silt mix (40)	5 - 780	0.428	0.019	1.44	HKS sand & CHB silt mix (94)	1 - 240	1.088	0.051	1.52
Assyros sand-silt mix (60)	10 - 1220	0.524	0.048	1.44	Hostun sand 1 (0)	25 - 640	0.763	0.056	1.13
Assyros sand-silt mix (100)	160 - 900	0.817	0.125	1.51	Hostun sand 2 (0)	10 - 630	0.750	0.051	1.08
DEM discs 1 (0)	70 - 2820	0.247	0.025	0.61	Hostun sand 3 (0)	10 - 640	0.739	0.054	1.10
DEM discs 2 (0)	70 - 2860	0.238	0.024	0.61	Hostun sand 4 (0)	160 - 645	0.720	0.053	1.12
DEM discs 3 (0)	70 - 2860	0.219	0.022	0.61	Hostun sand 5 (0)	165 - 650	0.627	0.020	1.16
DEM discs 4 (0)	80 - 2930	0.196	0.020	0.61	Hostun sand 6 (0)	165 - 645	0.616	0.027	1.15
Duzce-1 (13)	35 - 930	0.561	0.085	1.50	Hostun sand 7 (0)	160 - 630	0.755	0.055	1.11
Glass balls 1 (0)	140 - 1360	0.682	0.026	0.90	Hostun sand 8 (10)	165 - 630	0.745	0.043	1.08

Table 6.3 SSL parameters of the different soiltypes. *(Continued...)*

Soiltype (FC %)	**p' domain (kPa)**	**Γ_{50}**	**λ**	**M**	**Soiltype (FC %)**	**p' domain (kPa)**	**Γ_{50}**	**λ**	**M**
Leighton Buzzard 1 (0)	90 - 900	0.864	0.080	1.19	Silica sand-silt mix (60)	5 - 185	0.519	0.022	1.30
Leighton Buzzard 2 (0)	6 - 400	0.622	0.040	n/a	Silica sand-silt mix (100)	10 - 315	0.830	0.059	1.60
Mai Liao sand-silt mix (0)	70 - 465	0.921	0.148	1.24	Stava tailings (0)	63 - 1080	0.995	0.180	1.44
Mai Liao sand-silt mix (15)	20 - 265	0.734	0.100	1.24	Stava tailings (30)	44 - 1350	0.675	0.138	1.45
Mai Liao sand-silt mix (30)	16 - 260	0.625	0.114	1.24	Stava tailings (50)	13 - 770	0.601	0.061	1.44
Mai Liao sand-silt mix (50)	35 - 300	0.579	0.070	1.21	Stava tailings (100)	16 - 1220	0.737	0.081	1.38
Merriespruit tailings (0)	2 - 192	1.129	0.061	1.24	Toyoura sand-silt mix (5)	32 - 660	0.880	0.047	1.30
Merriespruit tailings (20)	7 - 80	1.143	0.157	1.17	Toyoura sand-silt mix (10)	11 - 590	0.811	0.042	1.30
Merriespruit tailings (30)	2 - 130	0.920	0.073	1.12	Toyoura sand-silt mix (15)	49 - 305	0.739	0.059	1.30
Merriespruit tailings (60)	11 - 125	0.769	0.024	1.19	Toyoura sand-silt mix (30)	33 - 730	0.502	0.034	1.30
Mizpah dam tailings (72)	22 - 240	0.773	0.136	1.47	Toyoura sand-silt mix (100)	30 - 500	0.695	0.040	n/a
Ottawa sand-silt mix (0)	24 - 1400	0.711	0.044	1.21	7U7-crushed sand (4.4)	20 - 100[a]	0.951	0.064	1.51
Ottawa sand-silt mix (5)	20 - 1130	0.700	0.055	1.23	8M8 crushed sand (1.6)	20 - 100[a]	0.926	0.138	1.64
Ottawa sand-silt mix (10)	35 - 700	0.619	0.038	1.28	9C1 crushed sand (0.7)	20 - 100[a]	0.946	0.067	1.59
Ottawa sand-silt mix (15)	30 - 1230	0.567	0.061	1.39	ASTM 20/30 sand (0)	20 - 100[a]	0.650	0.053	1.29
Pay dam tailings (77)	30 - 200	0.752	0.176	1.40	ASTM graded sand (0)	20 - 100[a]	0.733	0.080	1.20
Rimnio (37)	53 - 1120	0.776	0.105	1.39	Blasting sand (0)	16 - 520	0.954	0.051	1.33
Silica sand-silt mix (0)	5 - 470	0.764	0.042	1.40	Glass beads (0)	20 - 100[a]	0.741	0.039	0.81
Silica sand-silt mix (7)	5 - 435	0.689	0.047	1.50	Granite powder (44)	20 - 100[a]	1.005	0.070	1.37
Silica sand-silt mix (15)	17 - 310	0.579	0.057	1.60	Jekyll Island sand (0)	20 - 100[a]	0.890	0.053	1.64
Silica sand-silt mix (25)	11 - 790	0.432	0.058	n/a	Margaret River sand (0)	20 - 100[a]	0.753	0.051	1.33
Silica sand-silt mix (40)	4 - 265	0.383	0.022	1.30	Nevada sand (2.2)	20 - 100[a]	0.919	0.071	1.24

Table 6.3 SSL parameters of the different soiltypes. *(Continued...)*

Soiltype (FC %)	p' domain (kPa)	Γ_{50}	λ	M	Soiltype (FC %)	p' domain (kPa)	Γ_{50}	λ	M
Ottawa #20/30 sand (0)	10 - 630	0.701	0.031	1.09	Massey tunnel (3)	100 - 400	1.061	0.040	1.61
Ottawa F-110 sand (6)	20 - 100[a]	0.806	0.077	1.24	Monterey #0 (0)	1 - 200	0.839	0.039	1.33
Ponte Vedra sand (0.3)	20 - 100[a]	0.906	0.061	1.59	Monterey #16 (0)	1 - 1000	0.691	0.023	1.33
Sandboil (4)	73 - 690	0.692	0.062	1.33	Nerlerk (2)	60 - 600	0.812	0.040	1.20
Ticino sand (0)	20 - 100[a]	0.960	0.053	1.51	Nevada fine (5)	2 - 26	0.736	0.067	1.16
Banding sand 1 (0)	10 - 400[b]	0.816	0.020	1.29	Ottawa C109 (0)	10 - 800	0.800	0.074	1.20
Banding sand 5 (0)	10 - 400[b]	0.844	0.045	1.20	S (12)	10 - 400[b]	0.914	0.046	1.59
Banding sand 6 (0)	10 - 400[b]	0.782	0.040	1.14	S (20)	20 - 400[b]	0.917	0.056	1.55
Banding sand 9 (0)	10 - 400[b]	0.799	0.030	1.06	Sacramento (0)	1 - 600	0.839	0.039	1.34
Brenda sand (0)	0 - 200	0.942	0.100	1.46	Sydney (0)	10 - 400[b]	0.845	0.073	1.24
Chonan silty sand (18)	20 - 100	0.991	0.090	1.37	Syncrude (12)	7 - 800	0.845	0.062	1.20
Dune sand (6)	40 - 700	0.869	0.159	1.29	Tar Island Dyke (5)	10 - 400[b]	0.788	0.057	n/a
Fort Peck sand (2)	20 - 400	0.731	0.087	1.29	Tia Juana Silty (12)	8 - 656	0.899	0.076	1.35
Fraser River sand (0)	10 - 800	0.996	0.067	1.40	Toyoura 1 (0)	70 - 720	0.936	0.065	1.24
Hostun RF sand (0)	10 - 400[b]	0.852	0.069	1.40	Unimin 2010 (0)	20 - 450	0.957	0.091	1.33
Kogyuk 350 (0)	25 - 1000	0.760	0.014	1.24	Castro Sand B (0)	10 - 700	0.729	0.035	1.21
Lagunillas (70)	15 - 275	0.873	0.086	n/a	Castro Sand C (0)	10 - 80	0.923	0.038	1.37
Likan (0)	10 - 700	1.113	0.148	1.40	Hokksund (0)	11 - 750	0.842	0.054	1.29
Lornex (0)	10 - 400[b]	1.015	0.050	1.42	Monterey (0)	9 - 700	0.829	0.029	1.29
Mailiao (5)	10 - 400[b]	0.908	0.071	n/a	Ottawa (0)	4 - 800	0.706	0.028	1.13
Mailiao (10)	10 - 400[b]	0.829	0.086	n/a	Reid Bedford (0)	6 - 1050	0.904	0.065	1.29
Mailiao (15)	10 - 400[b]	0.714	0.068	n/a	Ticino-4 (0)	11 - 800	0.891	0.056	1.24

Table 6.3 SSL parameters of the different soiltypes. *(Continued...)*

Soiltype (FC %)	p' domain (kPa)	Γ_{50}	λ	M	Soiltype (FC %)	p' domain (kPa)	Γ_{50}	λ	M
Toyoura 2 (0)	30 - 500	0.919	0.039	n/a	Isserk (2)	7 - 990	0.760	0.043	1.22
Toyoura 3 (0)	8 - 1050	0.934	0.039	1.24	Isserk (5)	6 - 700	0.728	0.089	1.24
Alaskan Beaufort (5)	7 - 160	0.847	0.037	1.22	Isserk (10)	17 - 400	0.724	0.123	1.24
Alaskan Beaufort (10)	5 - 150	0.830	0.053	1.20	Nerlerk (1.9)	7 - 300	0.766	0.049	1.29
Chek Lap Kok (0.5)	2 - 900	0.684	0.130	n/a	Nerlerk (12)	9 - 400	0.681	0.070	1.24
Duncan Dam (6.5)	1 - 220	1.025	0.085	n/a	Highland Valley Copper (8)	1 - 220	0.864	0.068	n/a
Erksak (0.7)	6 - 500	0.762	0.022	1.27	Hilton Mines (2.5)	50 - 985	1.026	0.170	1.42
Erksak (1)	10 - 720	0.803	0.086	1.19	Syncrude (Mildred Lake) (10)	1 - 370	0.860	0.035	n/a
Erksak (3)	8 - 1100	0.756	0.054	1.18	Syncrude Oil Tailings (3.5)	10 - 620	0.750	0.065	1.33
Fraser River (Massey) (<5)	1 - 250	1.006	0.038	n/a	--	--	--	--	--

a) SSL determined using the simplified procedure proposed by Santamarina & Cho (2001) which is applicable up to p'≈100 kPa; b) Approximate domain reported by Cho et al. (2006).

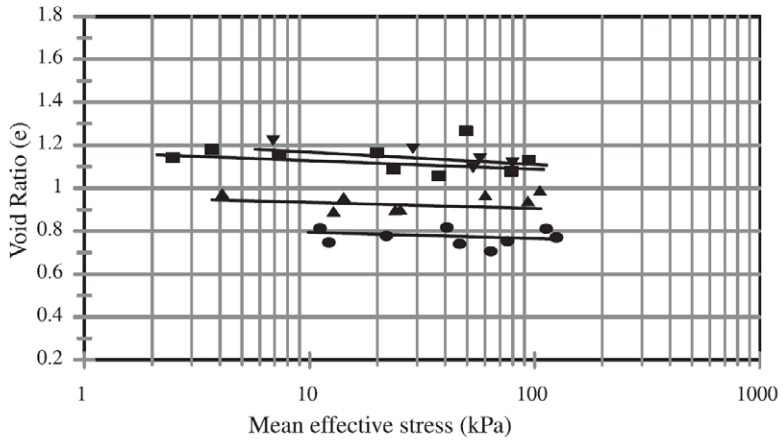


Figure 6.1 SSLs corresponding to four different GSDs of gold tailings from the Merriespruit TSF (Fourie and Papageorgiou 2001).

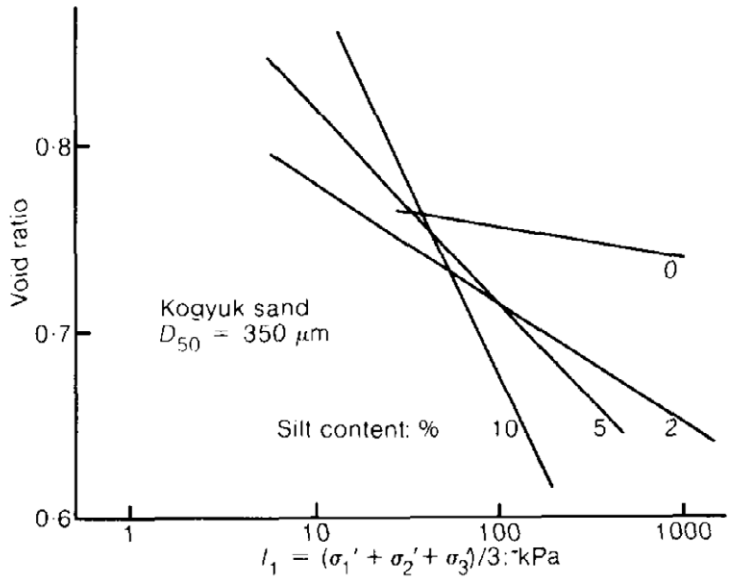


Figure 6.2 SSLs for Kogyuk 350 sand with different silt contents (Been and Jefferies 1985).

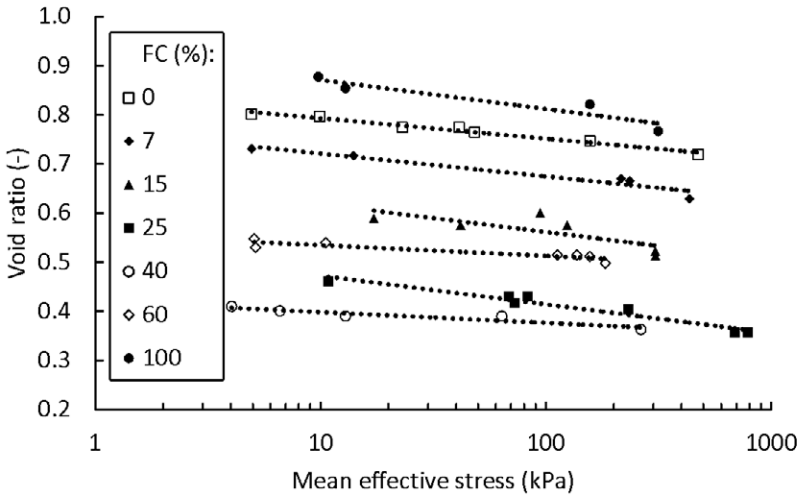


Figure 6.3 Lower stress portions of SSLs of non-plastic soils. Data from Thevanayagam et al. (2002).

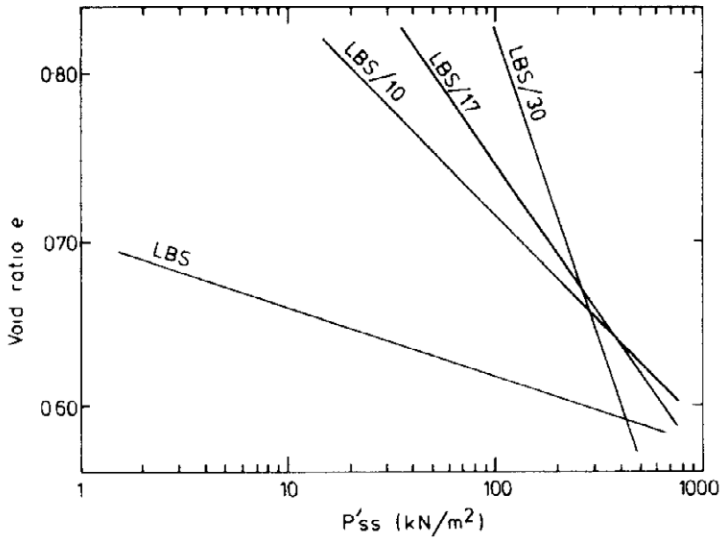


Figure 6.4 SSLs for micaceous sands (Hird and Hassona 1990). Notes: 1) LBS = Leighton Buzzard Sand. 2) Number after slash indicates percentage of mica.

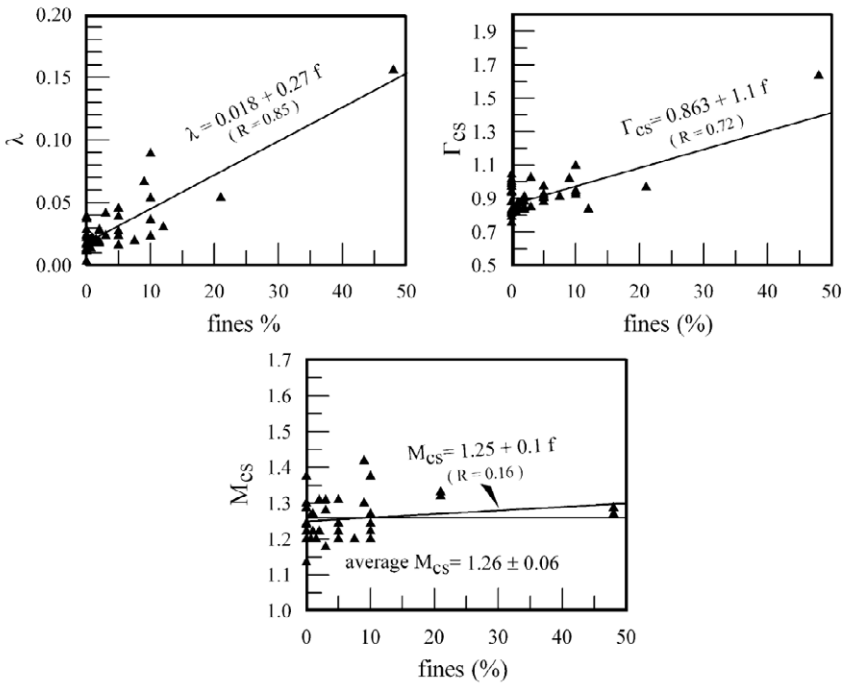


Figure 6.5 Correlations between FC and λ, Γ_1 (= Γ_{cs}), and M (= M_{cs}) (Bouckovalas et al. 2003).

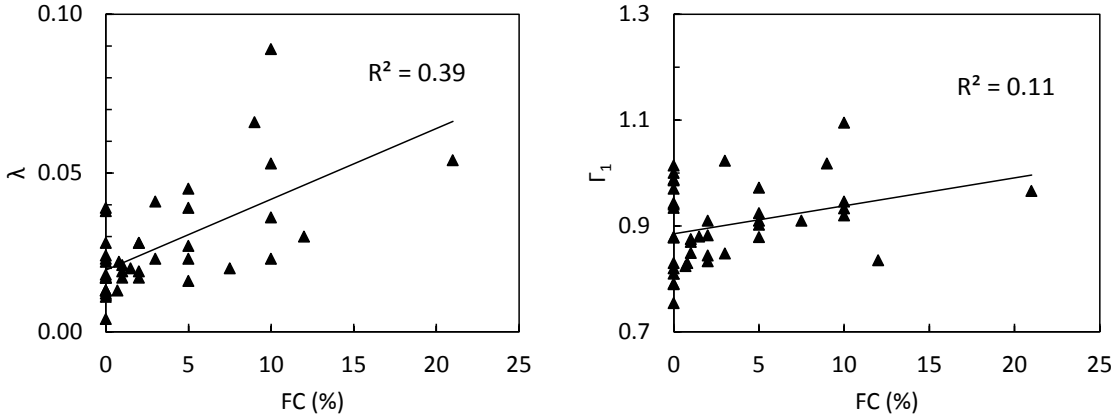


Figure 6.6 Correlations λ vs FC and Γ_1 vs FC shown in Figure 6.5 but excluding the data point at FC = 48%. Data from Bouckovalas et al. (2003).

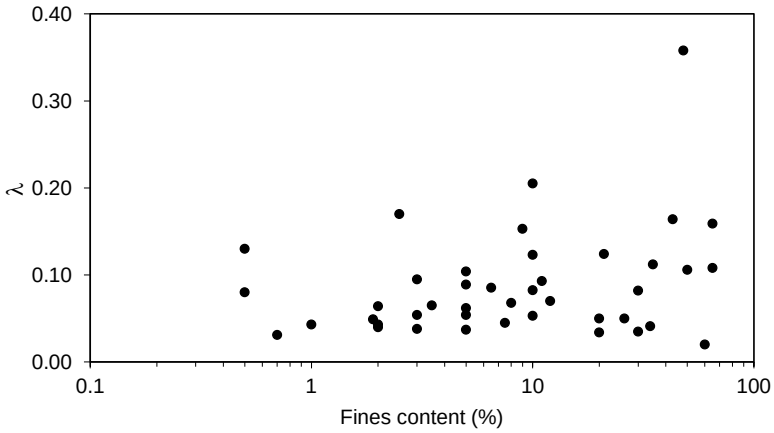
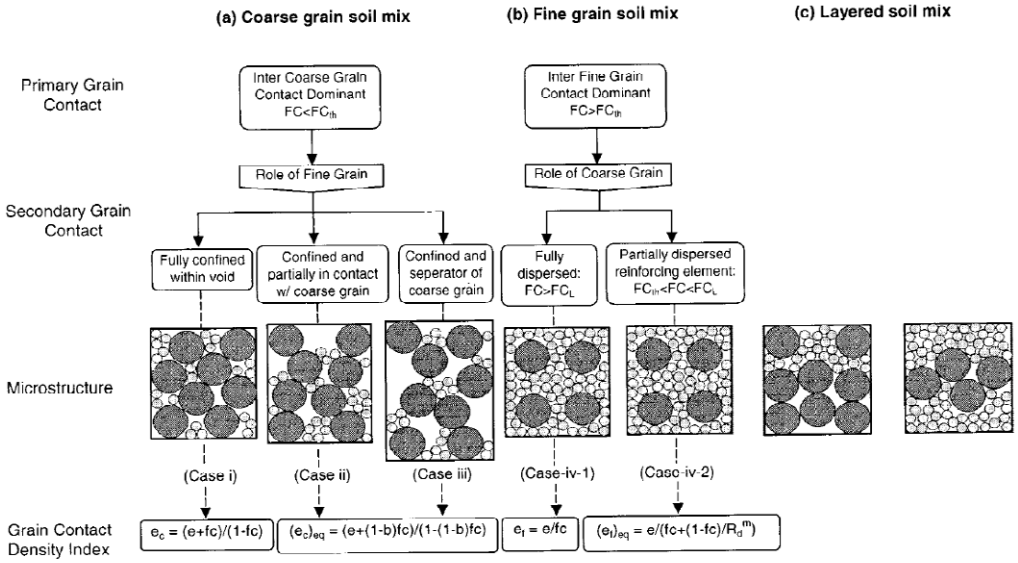


Figure 6.7 Correlation between λ and FC (Jefferies and Been 2006).



b=portion of the fine grains that contribute to the active intergrain contacts; e=global void ratio; FC=fine grains content; FC_{th}=threshhold fine grains content; FC_L=limit fines content; m: reinforcement factor; R_d=D/d=particle size disparity ratio

Figure 6.8 Rationale adopted by Thevanayagam et al. (2002).

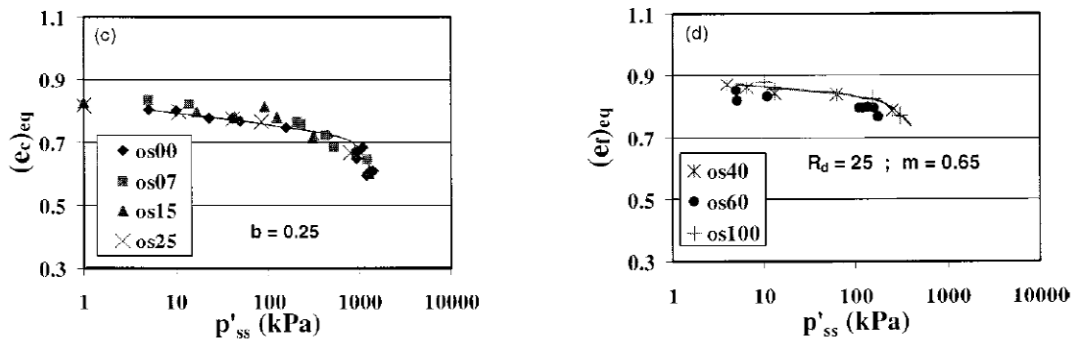


Figure 6.9 SSLs in terms of $(e_c)_{eq}$ and $(e_f)_{eq}$ Thevanayagam et al. (2002).

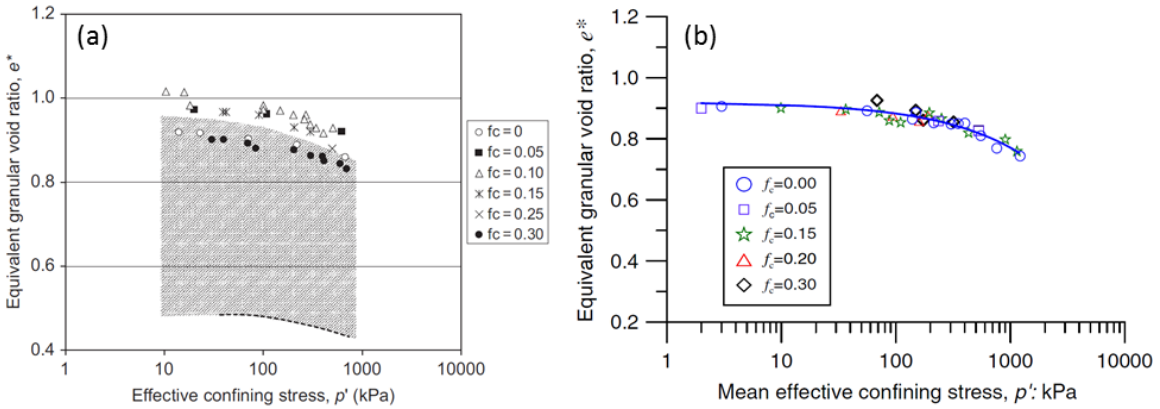


Figure 6.10 Unification of SSLs in $(e_c)_{eq}$ vs p' space for soils with FC < TFC. (a) Rahman and Lo (2008), (b) Rahman and Lo (2012). Note: $e^* = (e_c)_{eq}$.

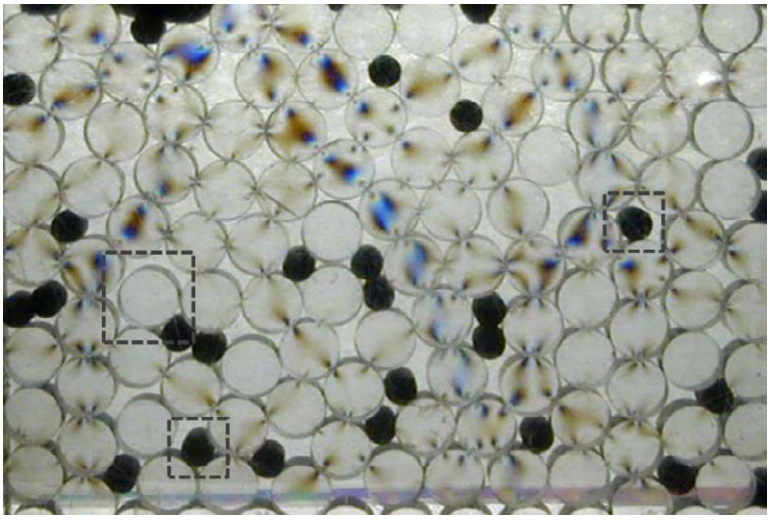


Figure 6.11 Assembly of photoelastic and rubber discs. Note: Dashed squares enclose particles that do not contribute to the force chains (Original photograph from Dodds (2003))

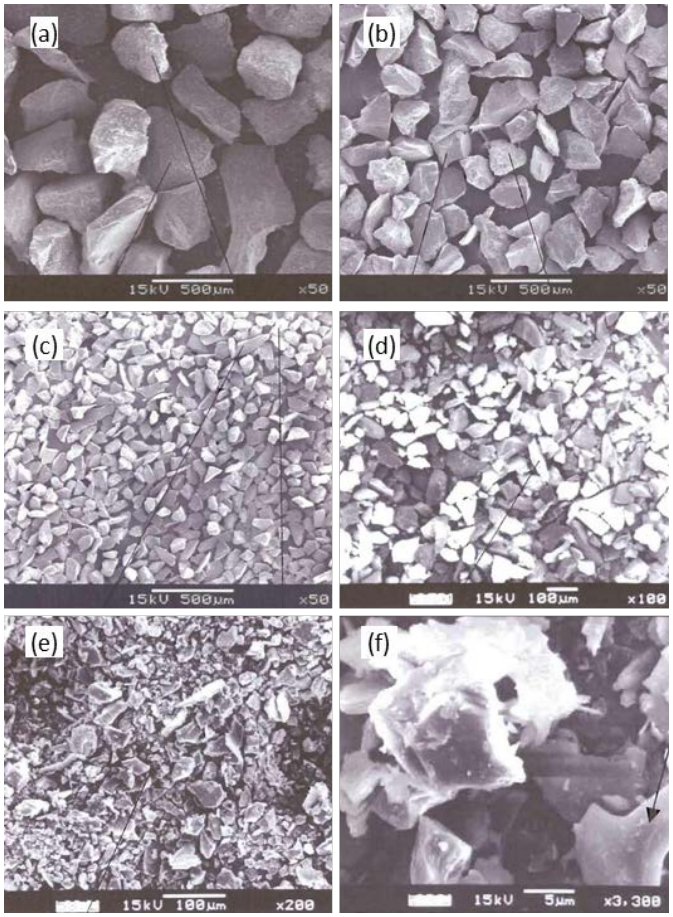


Figure 6.12 Gold tailings retained on sieve aperture: (a) 300 µm, (b) 150 µm, (c) 63 µm; and settled in water after: (d) 4 minutes or >20 µm, (e) 30 minutes or >8 µm, (f) 4 hours or >3µm. (Original micrographs from Vermeulen (2001)).

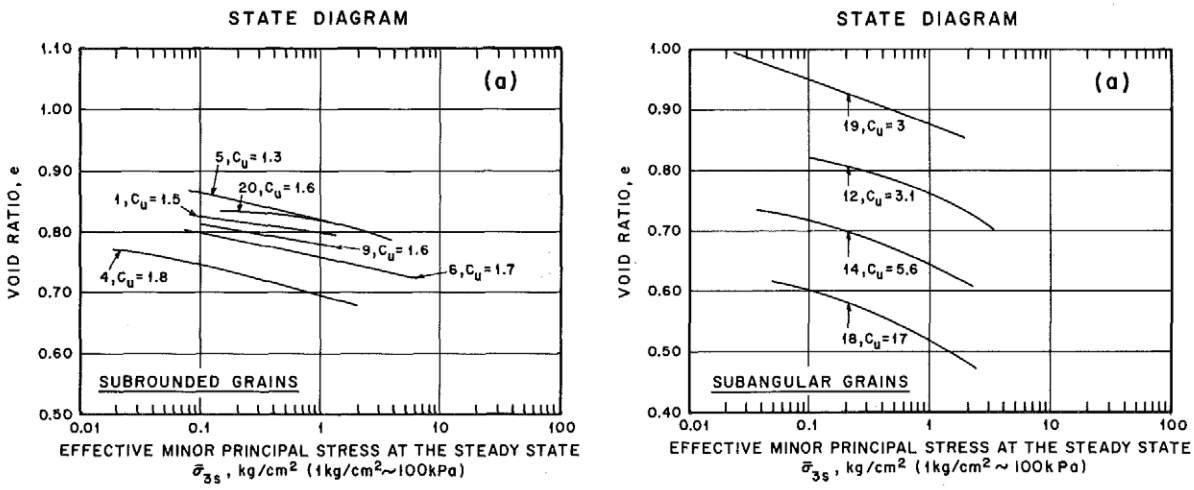


Figure 6.13 Influence of particle shape and GSD on the slope and vertical position of the SSL, respectively (Poulos et al. 1985).

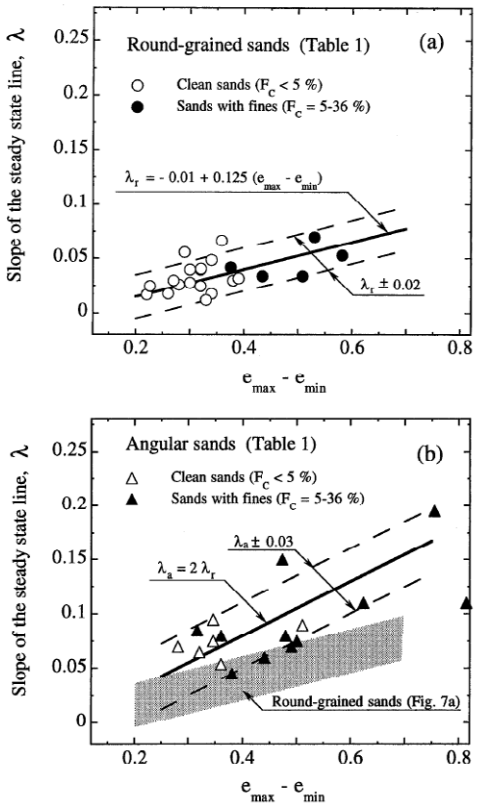


Figure 6.14 Effect on λ of void ratio range and particle shape (Cubrinovski and Ishihara 2000).

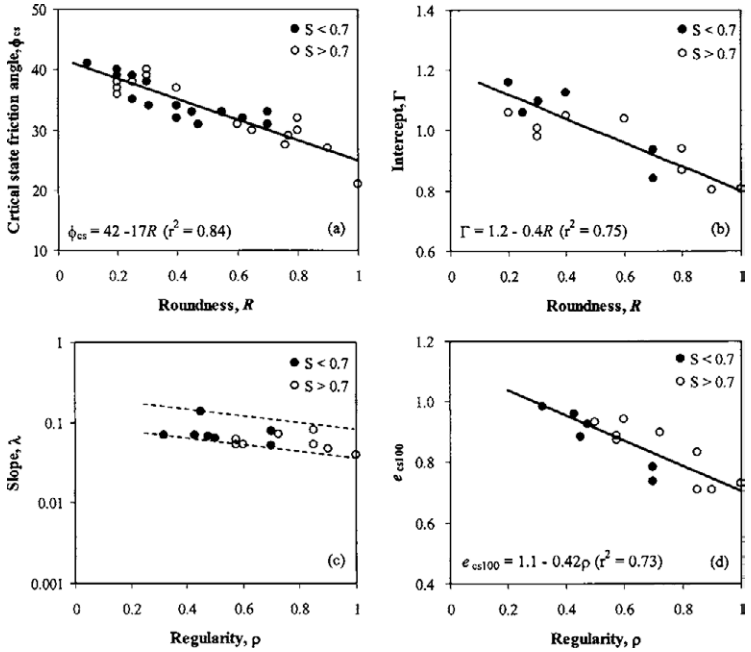


Figure 6.15 Correlations between SSL and particle shape (Cho et al. 2006). *Note:* $e_{cs100} = \Gamma_{100}$

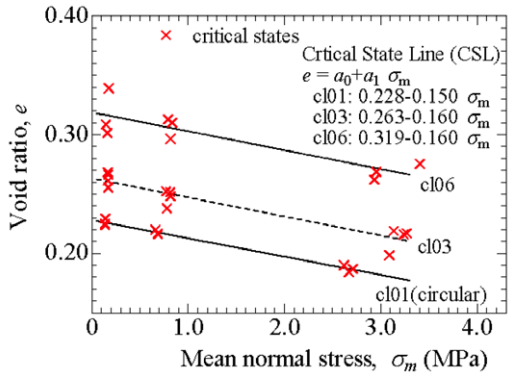


Figure 6.16 SSLs obtained from a 2D-DEM of assemblies with identical GSD but different particle shape (Maeda et al. 2009).

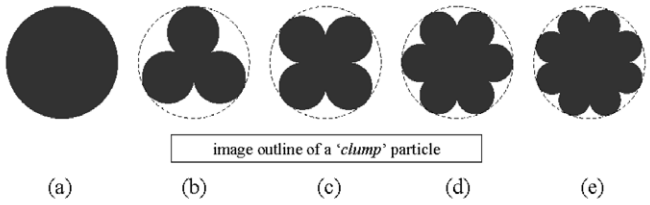


Figure 6.17 Particle shapes of the assemblies whose SSLs are shown in Figure 6.16. Note: a) cl01, b) cl03, and d) cl06 (Maeda et al. 2009).

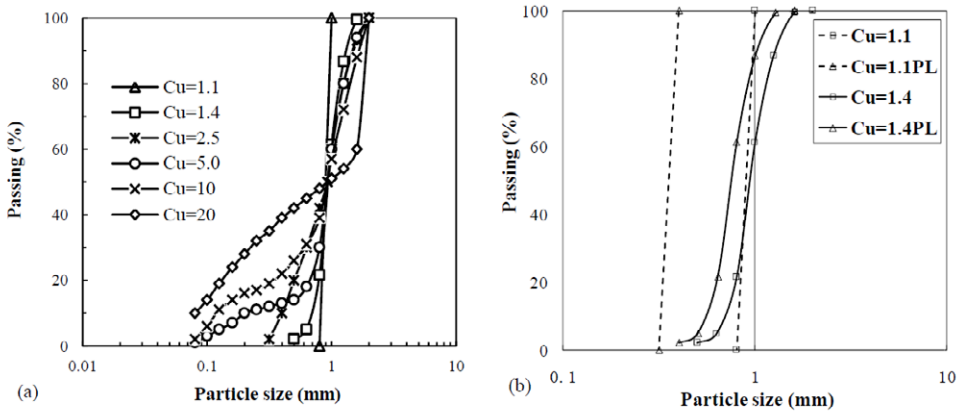


Figure 6.18 a) GSD curves used with Hostun Sand and glass balls. b) Parallel GSD curves of Hostun Sand (Li 2013).

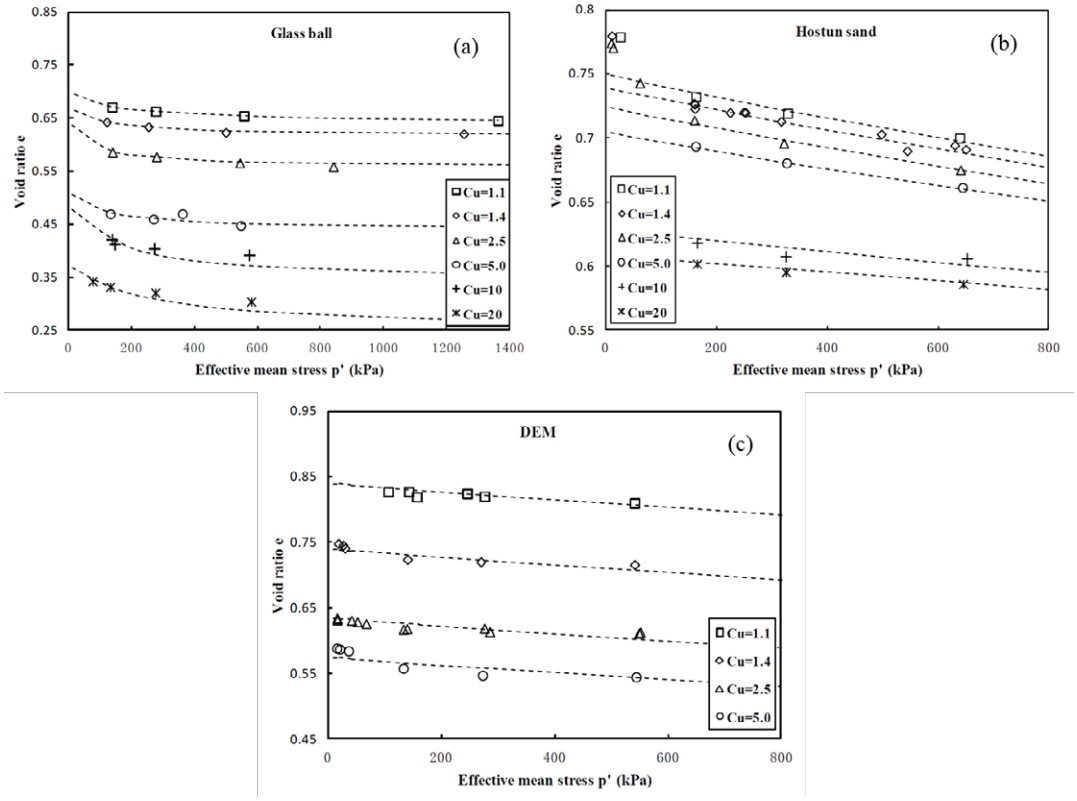


Figure 6.19 Effect of particle shape and GSD on the SSL (Li 2013).

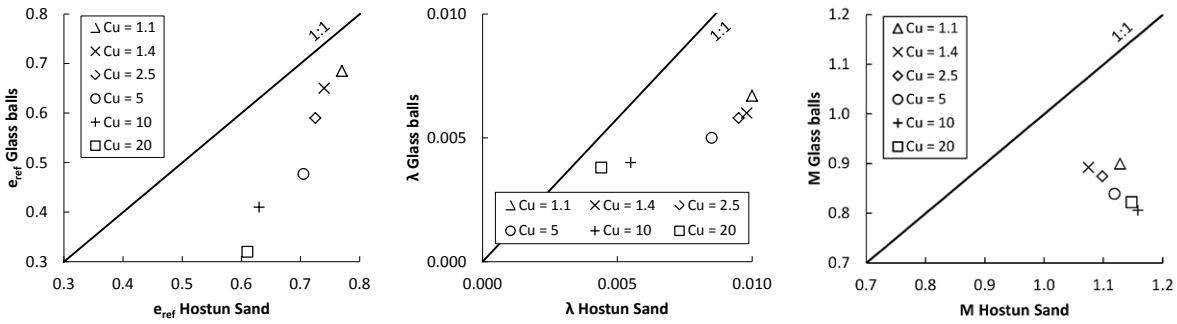


Figure 6.20 Comparison of SSL parameters of soils with identical mineralogy and GSD but different particle shape. Data from Li (2013).

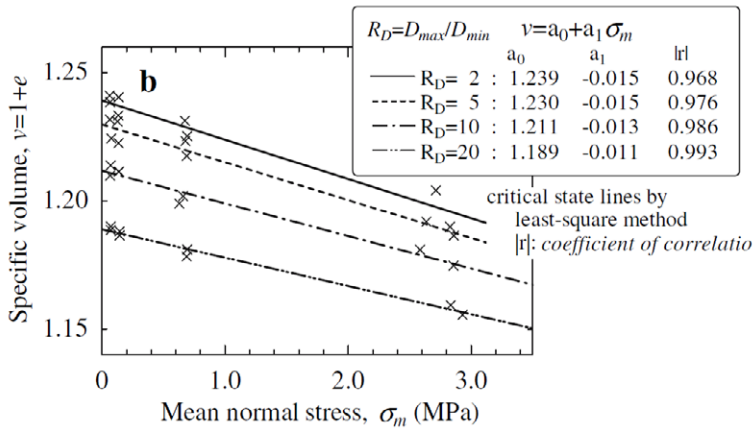


Figure 6.21 SSLs of 2D DEM disc assemblies with different GSDs (Muir-Wood and Maeda 2008).

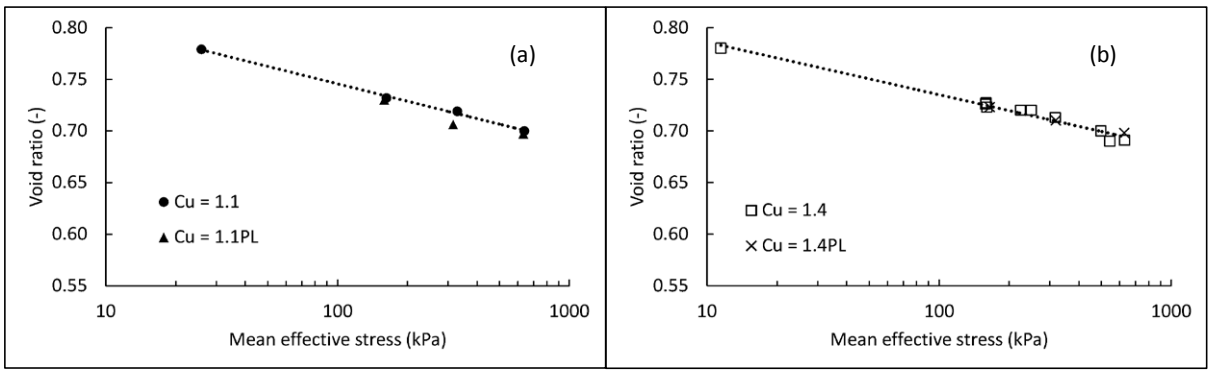


Figure 6.22 SSLs of Hostun sand with parallel GSDs. a) C_u = 1.1 and b) C_u = 1.4. Data from Li (2013).

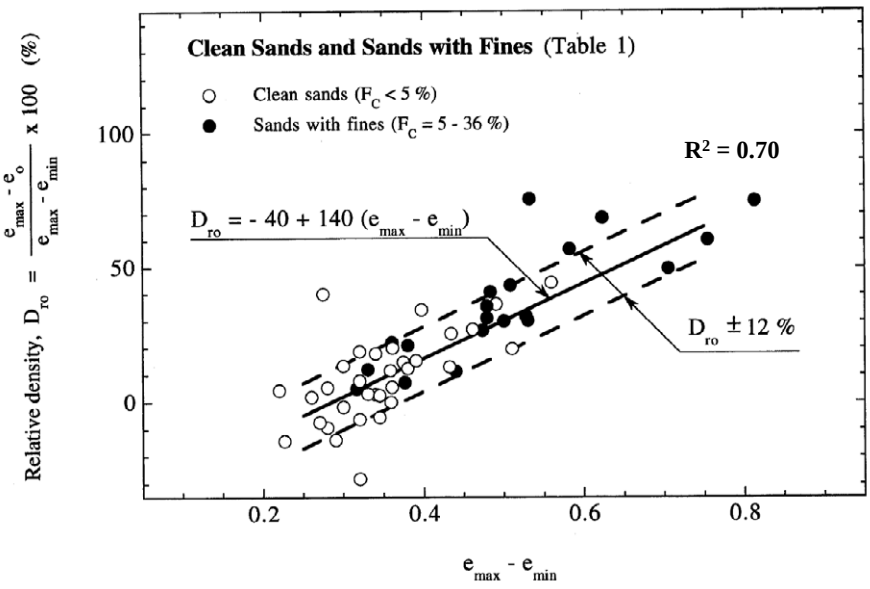


Figure 6.23 Correlation between D_{r0} and (e_{max} - e_{min}). R^2 value calculated in present work (Cubrinovski and Ishihara 2000).

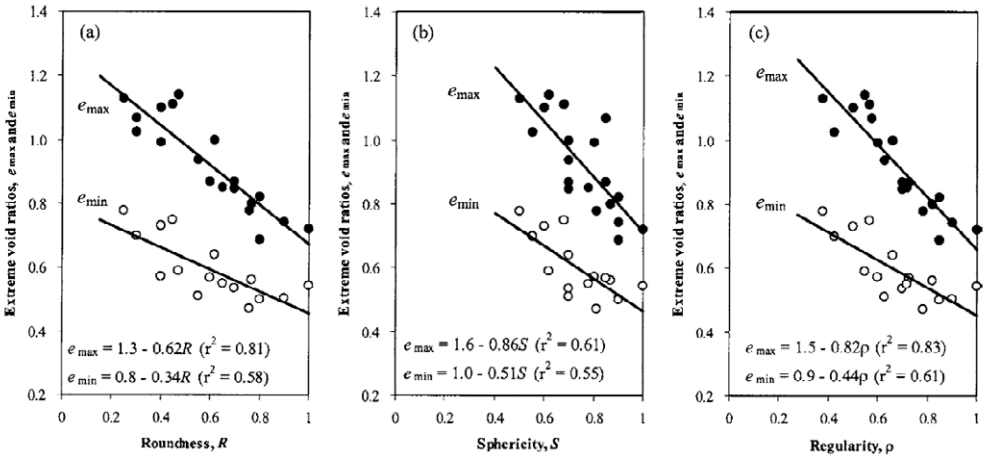


Figure 6.24 Effect of particle shape on void ratio limits (Cho et al. 2006).

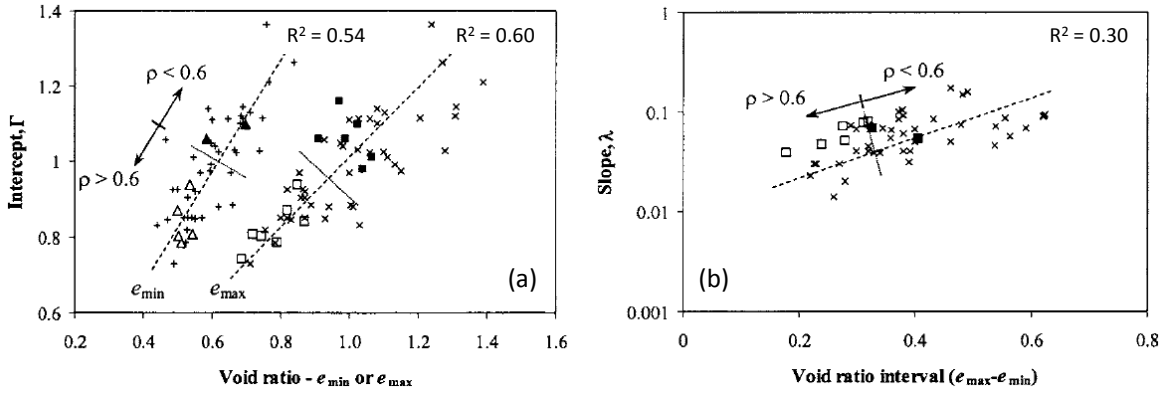


Figure 6.25 Correlations of Γ_1 (=Γ) and λ with limiting void ratios. Filled symbols represent regularity (ρ) < 0.6, empty symbols represent regularity > 0.6, and line symbols represent soils with no particle shape information. R^2 values were calculated in the current work (Cho et al. 2006).

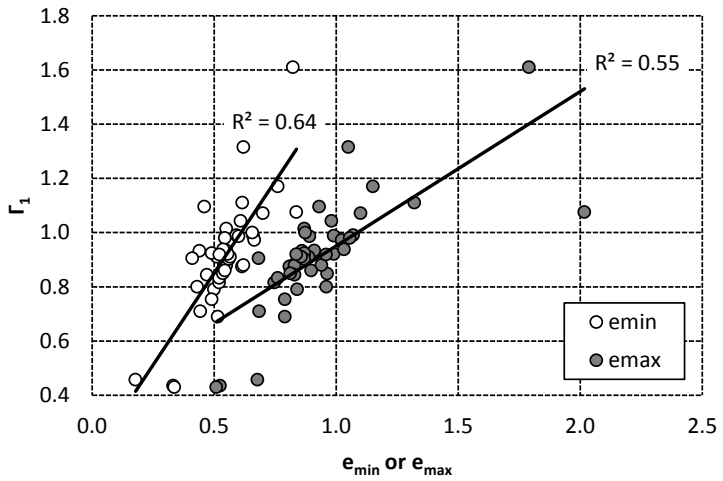


Figure 6.26 Correlations of e_{min} and e_{max} with Γ_1. Data from Table 2.1 of Jefferies and Been (2006).

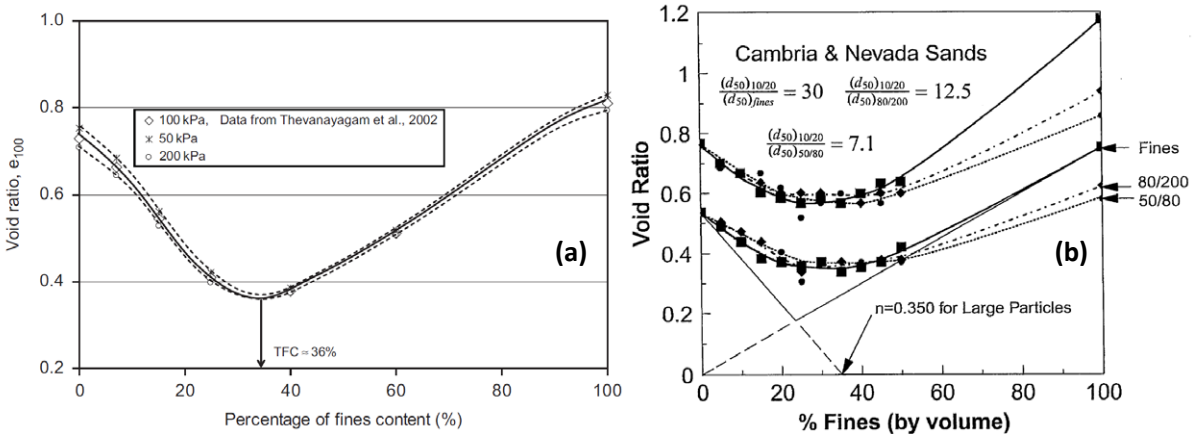


Figure 6.27 Effect of FC on: a) Γ_{100} (= e_{100}) (Rahman and Lo 2008), and b) e_{max} and e_{min} (Lade et al. 1998).

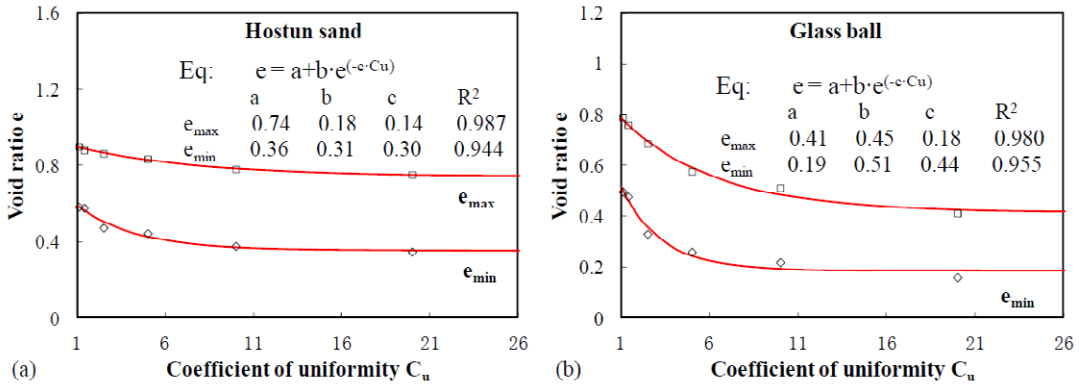


Figure 6.28 Effect of GSD (C_u) on e_{max} and e_{min} (Li 2013).

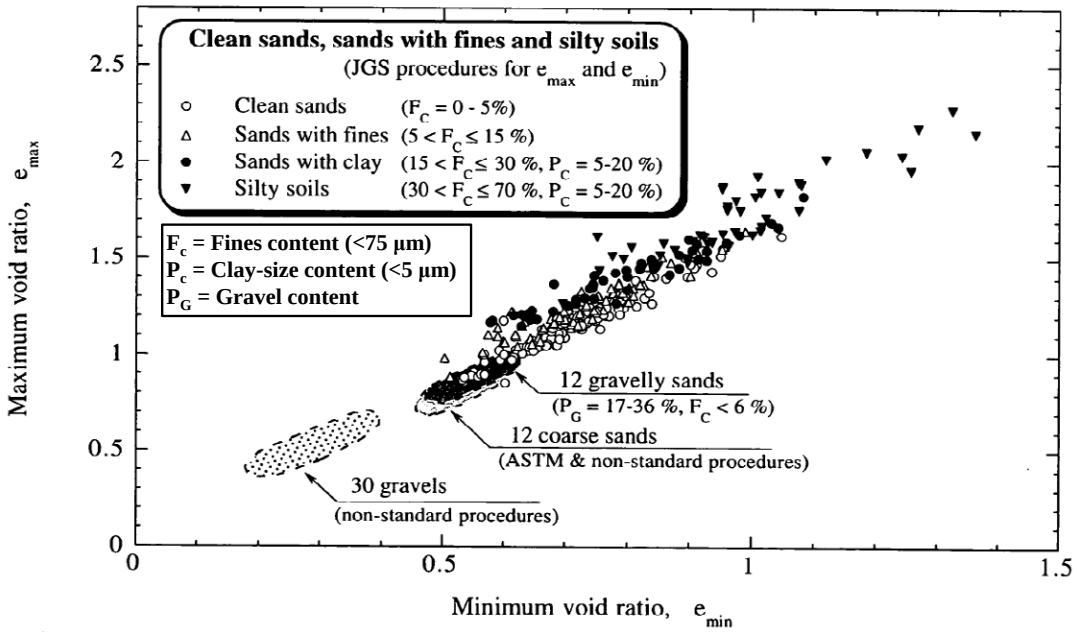


Figure 6.29 Correlation between emax and emin of different natural soiltypes (Cubrinovski and Ishihara 2002).

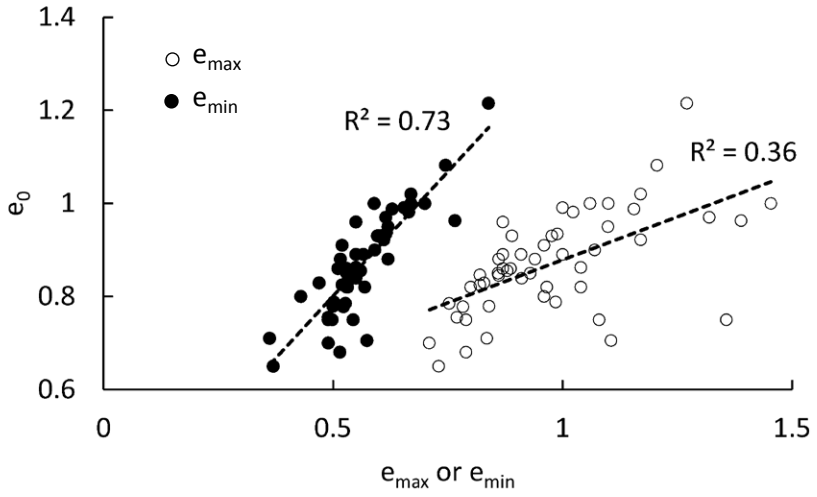


Figure 6.30 Correlations of e_0 with e_{max} and e_{min}. Data from Cubrinovski and Ishihara (2000).

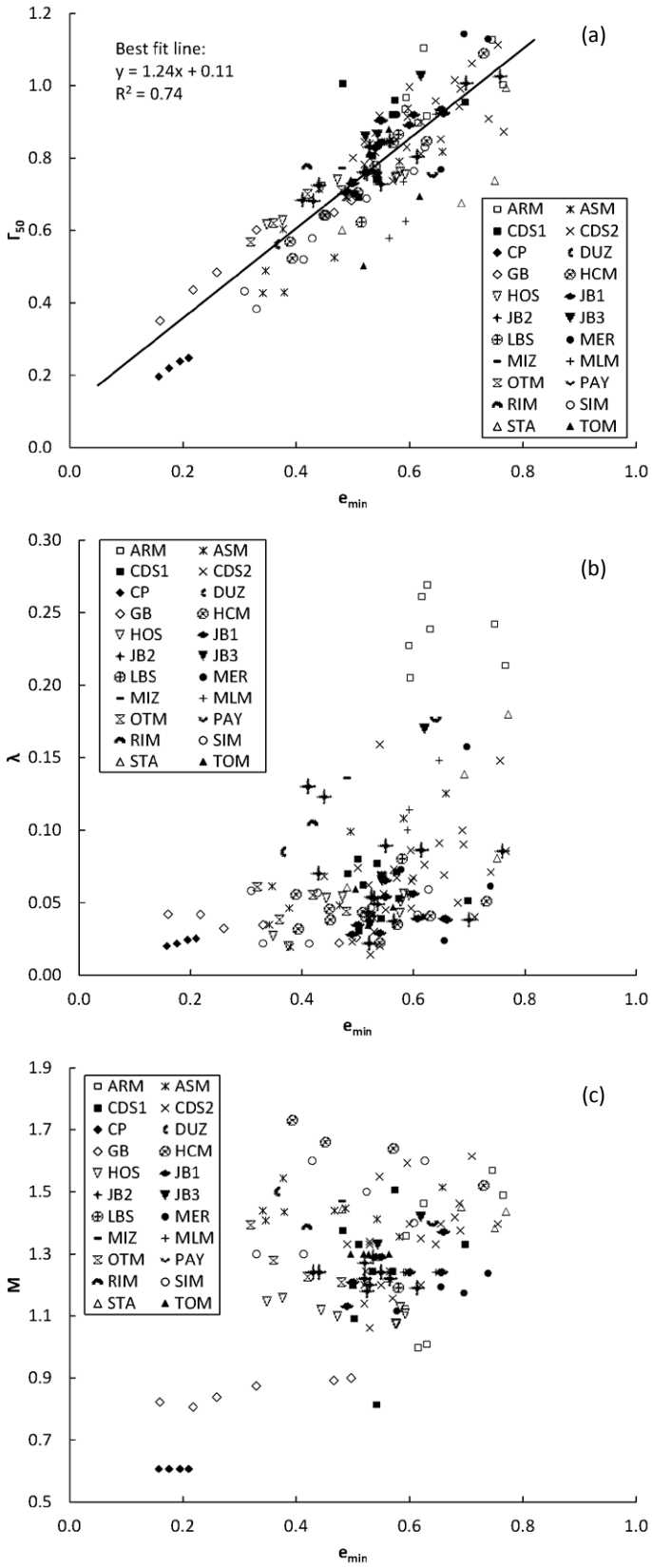


Figure 6.31 Plots of Γ_{50}, λ, and M vs e_{min}.

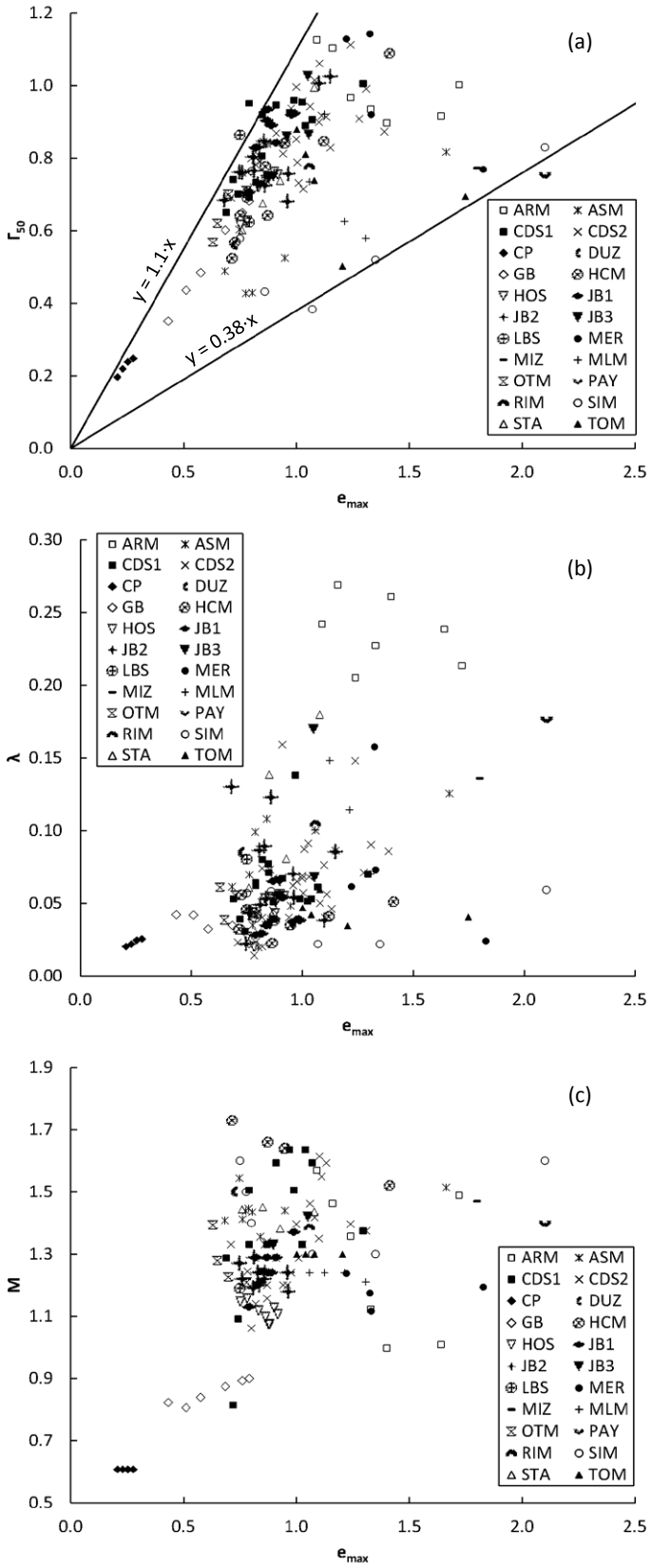


Figure 6.32 Plots of Γ_{50}, λ, and M vs e_{max}.

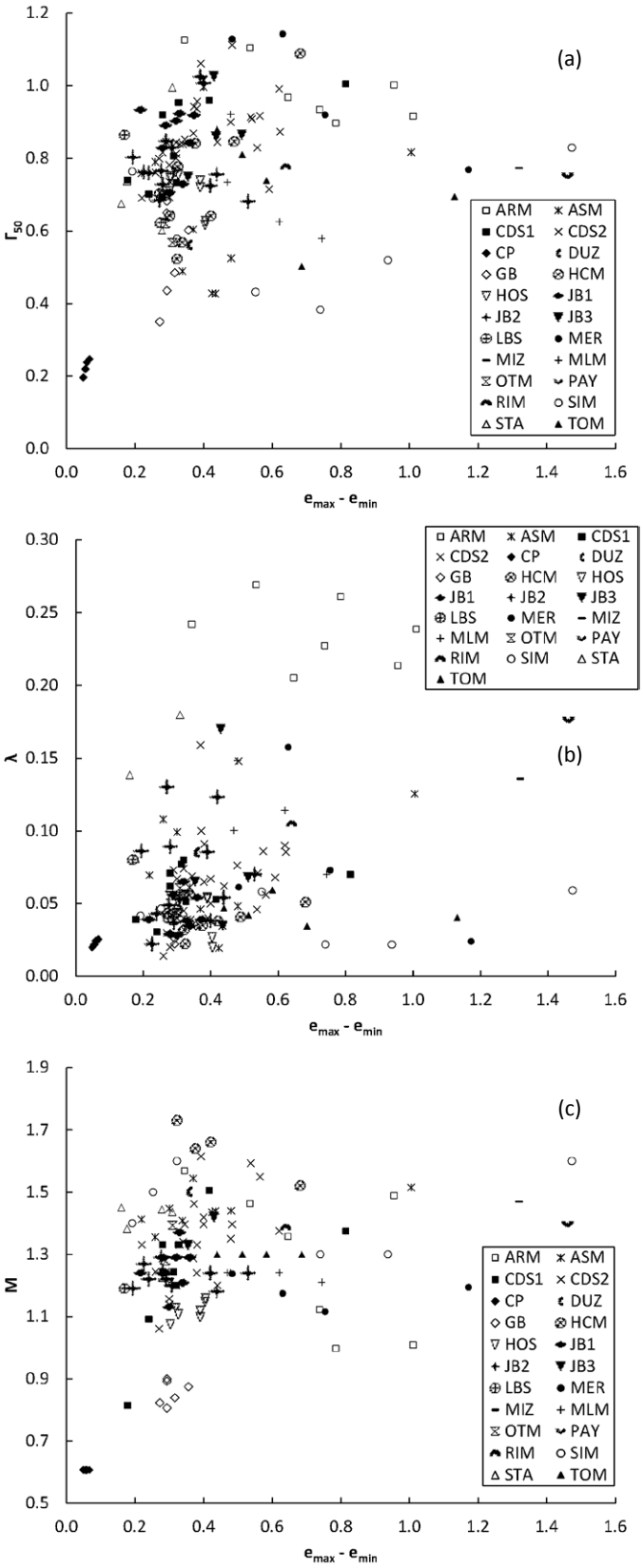


Figure 6.33 Plots of Γ_{50}, λ, and M vs (e_{max} - e_{min}).

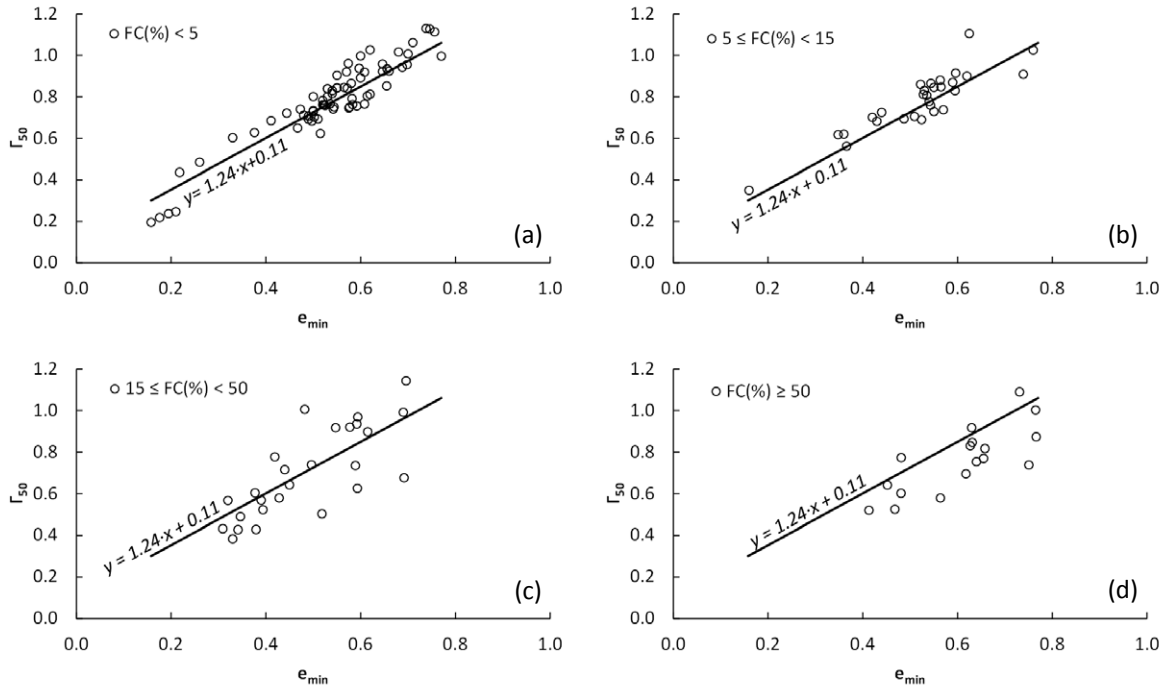


Figure 6.34 Plots of Γ_{50} vs e_{min} grouped by FC. The line in each plot is the best fit line for the entire database (Figure 6.31a).

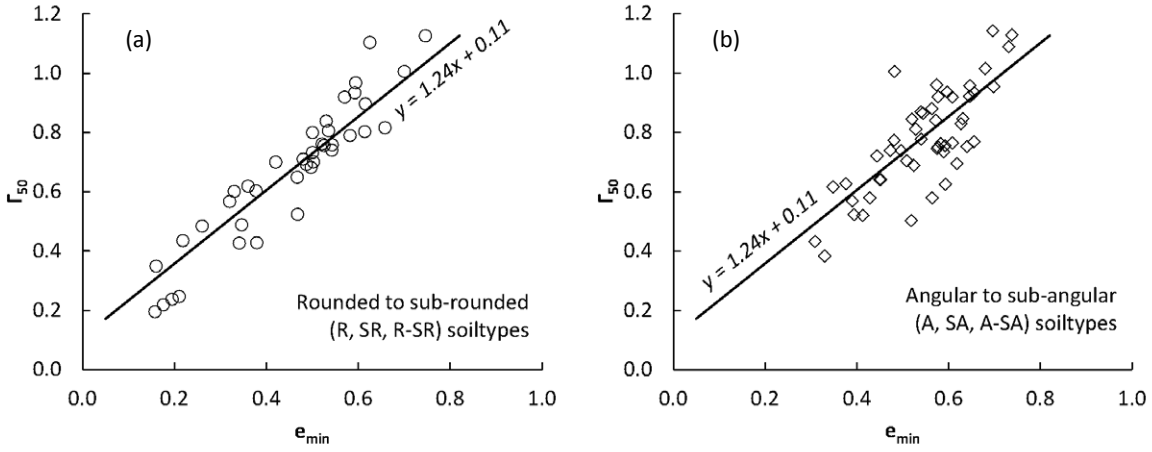


Figure 6.35 Γ_{50} vs e_{min} for a) rounded to sub-rounded soiltypes and b) angular to sub-angular soiltypes. The solid line is the best fit line for the entire database (Figure 6.31a).

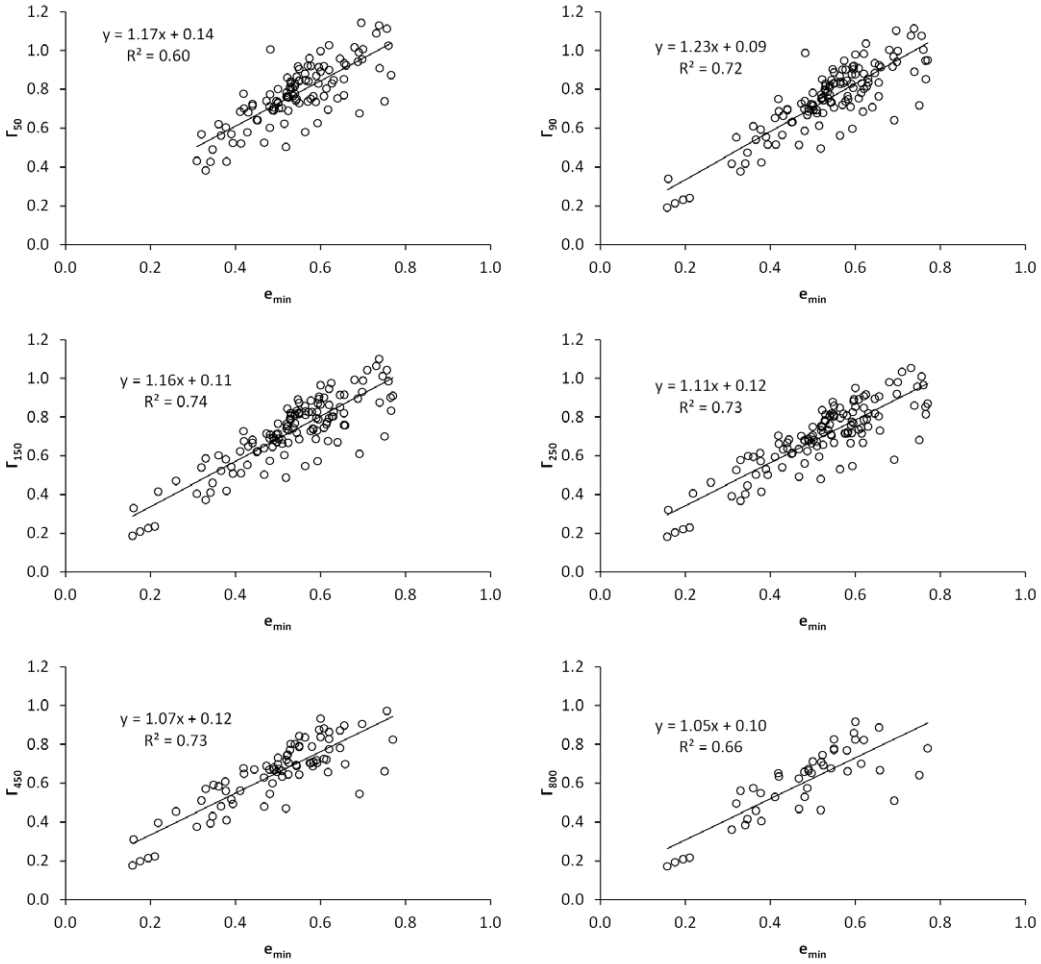


Figure 6.36 Correlations between e_{min} and Γ_n for n = 50, 90, 150, 250, 450, and 800 kPa. Note: Appendix D indicates which soiltypes were included in each correlation.

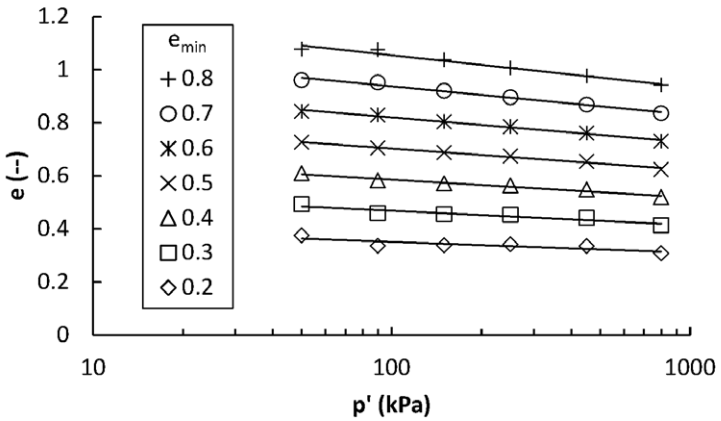


Figure 6.37 SSLs predicted as a function of e_{min} using the correlations in Figure 6.36.

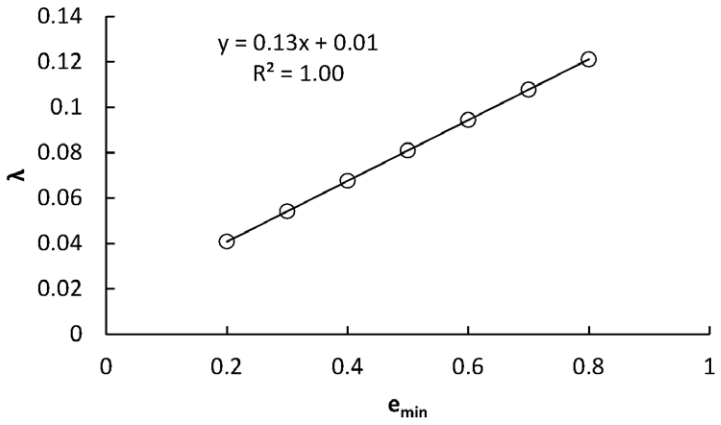


Figure 6.38 Relationship between e_{min} and λ as inferred from the SSLs in Figure 6.37 (Eq. 6.4).

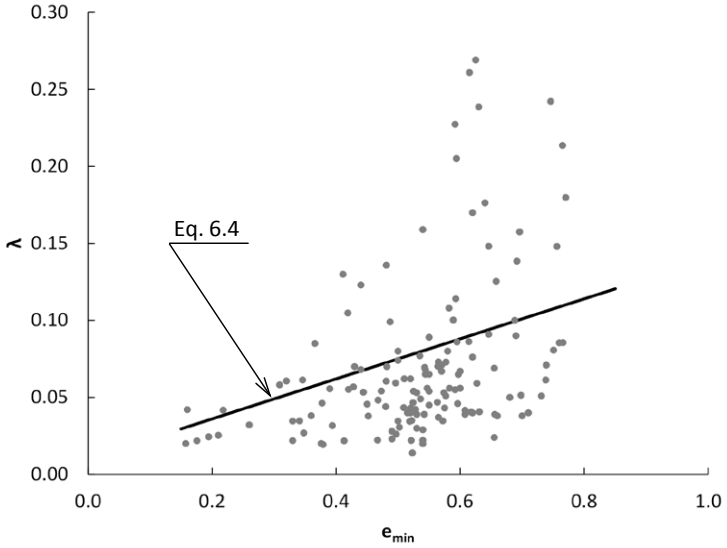


Figure 6.39 Comparison between Equation 6.4 (Figure 6.38) and the datapoints in Figure 6.31b.

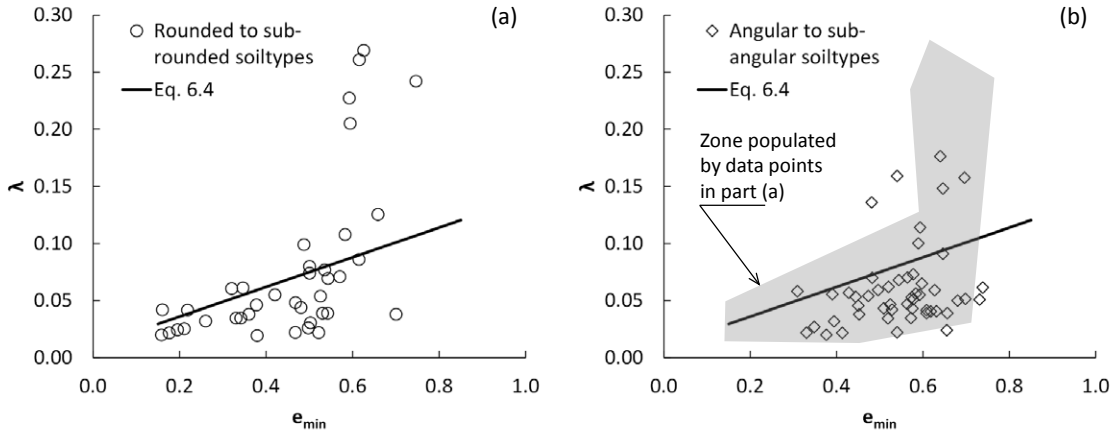


Figure 6.40 λ vs e_{min} for a) rounded to sub-rounded soiltypes and b) angular to sub-angular soiltypes.

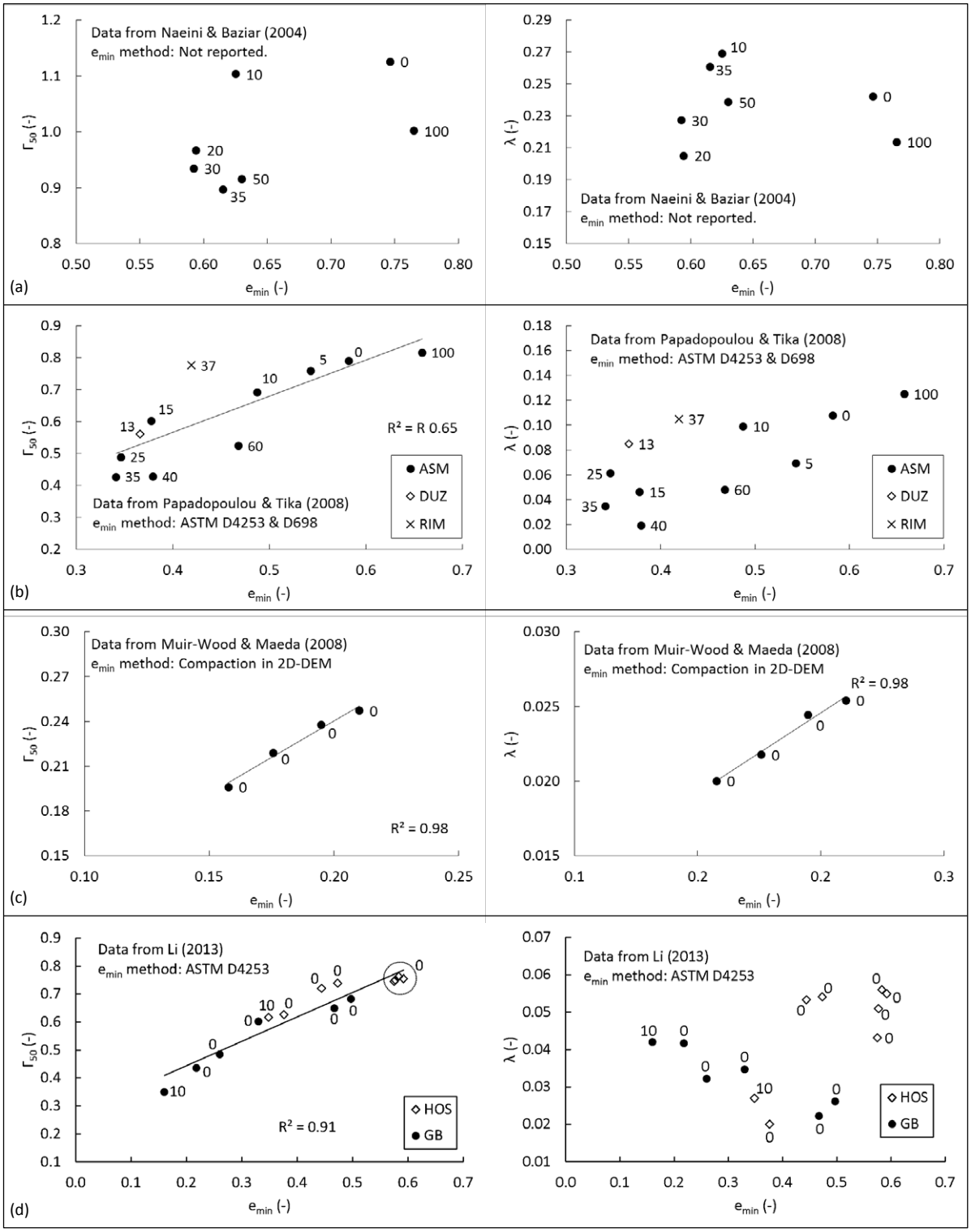


Figure 6.41 Plots of SSL parameters vs e_{min} using data from a single reference. Labels next to each data point indicate FC(%). Figure continues below.

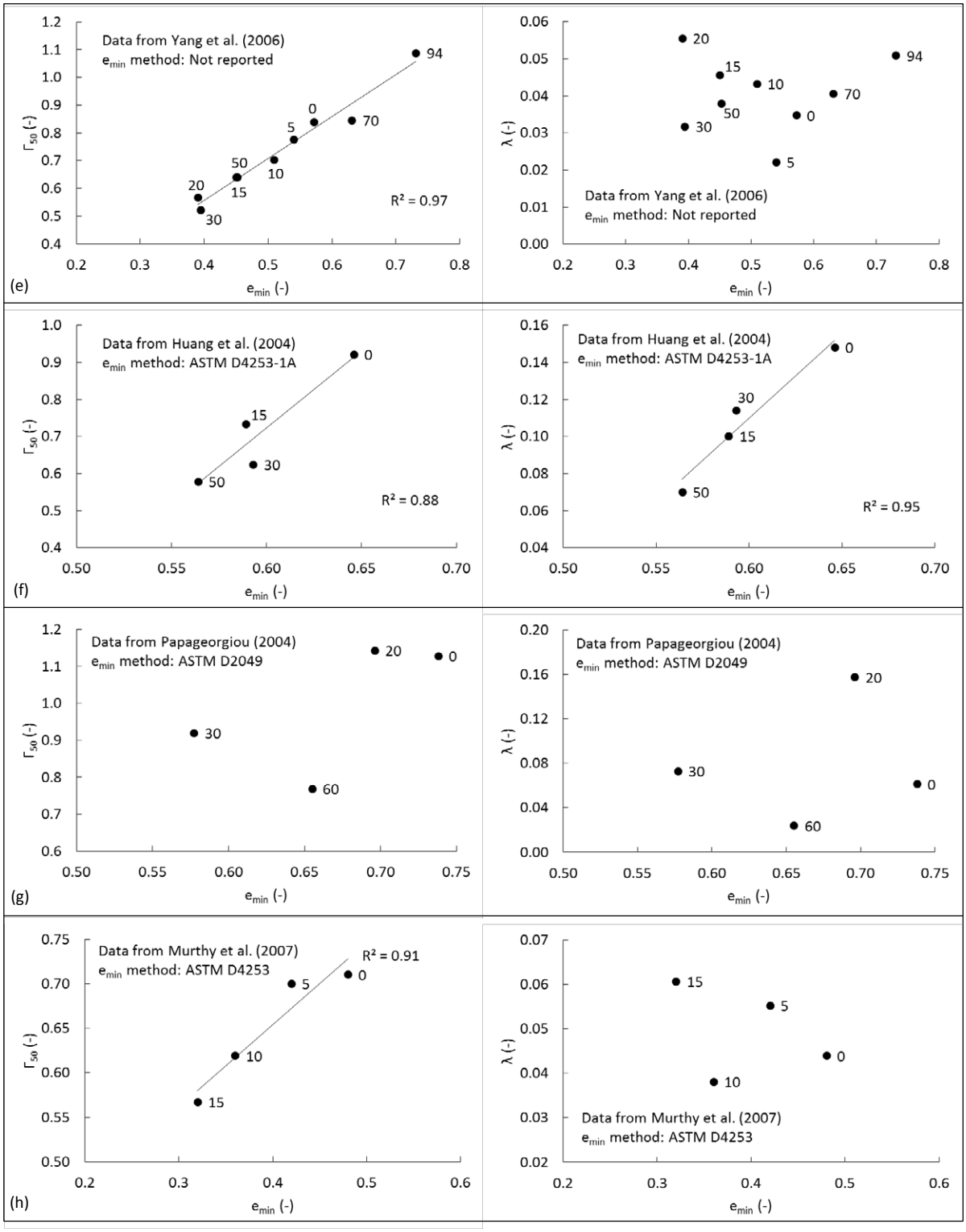


Figure 6.41 continued. Figure continues below.

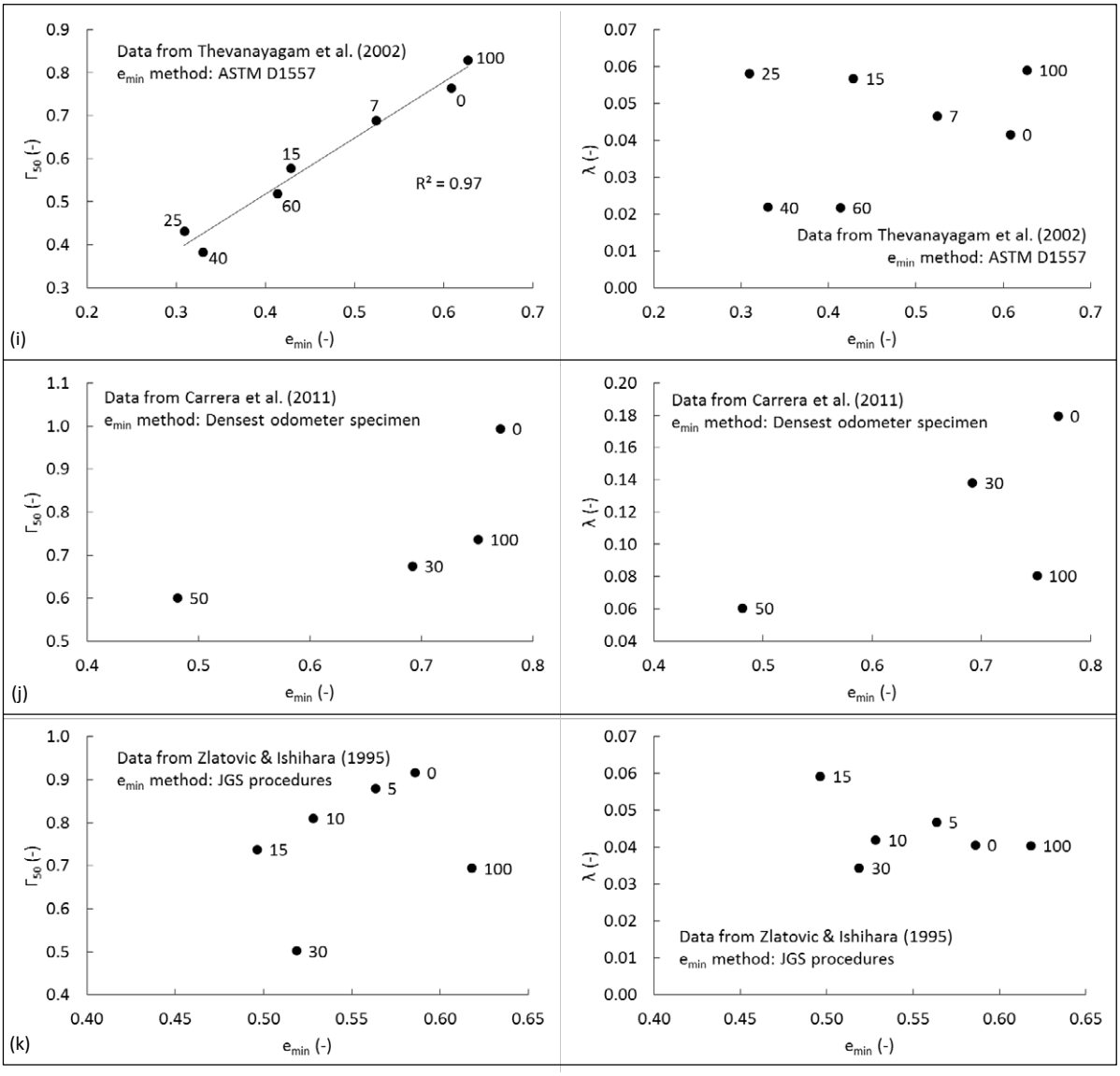


Figure 6.41 continued.

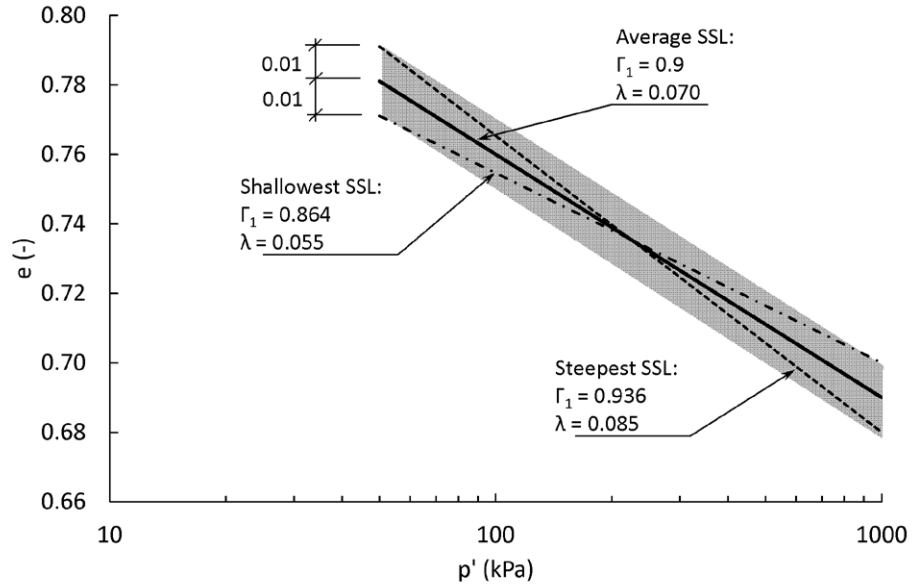


Figure 6.42 Potential effect on SSL parameters of error in void ratio measurements.

7 Experimental determination of the SSLs of Impala platinum tailings

7.1 Introduction

The present chapter describes the experimental work conducted to determine steady state lines (SSLs) used to characterise the tailings at the Impala TSF. Fourie and Papageorgiou (2001) noted that given the presence of multiple soiltypes at the Merriespruit TSF, it was inadequate to define a single SSL to characterise the entire deposit. The variety of grain size distribution (GSD) curves in Figure 3.22 show that in this regard the Impala TSF is no different from the Merriespruit TSF and that therefore several SSLs must be experimentally determined to account for the different soiltypes in the deposit. Since it is not practical to determine the SSL for every soiltype, it is important to ensure that the SSLs that are experimentally determined, give an accurate representation of the range of SSLs that can be found in the TSF. Therefore, it is essential to understand which are the soil index parameters that have the greatest influence on the SSL so as to use them to choose an appropriate range of soiltypes for which to determine their SSLs.

The analysis presented in Chapter 6 indicated that the vertical location of the e-p' projection of the SSL (Γ) is strongly correlated to e_{min} (Figure 6.31a). Additionally, Chapter 6 also indicated that e_{min} might also have an effect on the slope (λ) of the e-p' projection of the SSL (Figure 6.38), although the correlation between e_{min} and λ was found to be much weaker than between e_{min} and Γ (compare Figure 6.31a and Figure 6.31b). The results of Hird and Hassona (1990) (Figure 6.4) indicate that the presence of platy particles can also have a marked effect on λ. This observation may be of importance when analysing tailings because it is known that although most tailings particles are bulky, the very fine particles (≈< 10μm) can have flaky or platy shapes (Vermeulen et al. 2002; Vermeulen 2001). The fact that platy particles increase λ, and that very fine tailings can be platy, implies that FC could potentially also increase λ. Accordingly, the approach adopted in this chapter consisted in testing soiltypes that covered a wide range in both e_{min} and FC values to understand the variation in Γ and λ in the Impala TSF. The hypothetical direct FC-λ correlation was taken into account when selecting representative soiltypes even though the analysis presented in Chapter 6 did not identify a single study on non-plastic soils in which a direct FC-λ correlation was observed (Figure 6.41).

Regarding the q-p' projection of the SSL, which is characterised by its slope (M) (Eq. 2.2), the references reviewed in Chapter 6 indicate that it is strongly dependent on particle shape and mineralogy while largely independent of GSD (Cho et al. 2006; Sadrekarimi and Olson 2011). Given that all the tailings at the Impala TSF come from the same two ore bodies it seems reasonable to hypothesise that there are no significant changes in mineralogy throughout the TSF. Therefore it is expected that the different soiltypes at the Impala TSF will only exhibit significantly different values of M if particle shape distribution changes from one soiltype to another.

7.2 Soiltypes used to characterise the tailings from the Impala TSF

A critical question to address at the onset of the testing programme is: How many soiltypes from the Impala TSF should have their SSLs experimentally determined? Naturally, the answer depends on the degree of heterogeneity in the soil deposit, but for reference, it is useful to consider what has been done in previous studies. Fourie and Papageorgiou (2001) determined the SSL of four soiltypes from the Merriespruit Gold TSF, however two of their SSLs were indistinguishable from each other (Figure 6.1), suggesting that the study of three soiltypes could have been sufficient. Vermeulen (2001) determined the SSLs of two soiltypes to characterise the Pay Dam TSF. Jefferies and Been (2006) recommend that for important projects, "*two (or even three) CSLs that span the range of gradations*" in the deposit should be experimentally determined. Shuttle and Cunning (2007) used a single SSL to characterise a uniform deposit of silt sized tailings. Similarly Been et al. (2012), studied two tailings deposits and used a single SSL to characterise each deposit. These references suggest that one to three SSLs are generally sufficient to characterise a TSF.

The next point to address is the variability of soiltypes in the Impala TSF. Figure 3.22 shows that from an FC point of view the variability is significant, with FC ranging from 33% to 95%. However, in accordance with the arguments presented in the introduction to this chapter, variability in e_{min} must also be determined. To do this, six mixes of Impala tailings that covered a wide range of FC values were prepared. The FC values of these mixes were: 10%, 30%, 47%, 64%, 81%, and 98%. The mixes with FC between 30% and 98% were prepared because they cover the range in FC that is representative of the Impala TSF (Figure 3.22). The mix with FC = 10% was deliberately given a narrow GSD so that it would exhibit a high e_{min} value, thus expanding the e_{min} range covered by the soiltypes available for testing. The codes used to distinguish the different mixes consisted of the FC expressed as a percentage followed by the e_{min} multiplied by 100. For example, the mix with FC = 10% and e_{min} = 0.70 was given the code 10/70 (Table 7.1). The methods used to determine e_{min} are addressed below.

As discussed in Chapter 6, FC is only one feature of the GSD, and for a given particle shape and mineralogy, it is the entire shape of the GSD, and not FC alone, that determines soil properties. Consequently, an effort was made to control the coarse fraction (> 75μm) of the mixes so that their GSD was similar to that of the coarse fraction of the GSD curves in Figure 3.22 that had a similar FC. A match of the fine portion of the GSD curve is also desirable; however the author had no means of controlling the shape of this part of the GSD curve.

In order to have some degree of control over the coarse fraction of the GSD curve, the bulk tailings collected from the Impala TSF were initially sieved into three size categories: Coarse (between 600 μm and 150 μm), medium (between 150 μm and 75 μm), and fine (smaller than 75 μm). Considering the amount of each mix that would be needed for the experimental programme, it was found that it was not practical to use the conventional 200 mm diameter laboratory sieves. Instead, two nests of sieves with a 450 mm diameter were built for this task. Given the larger diameter of these sieves (Figure 7.1), it was not possible to use a standard sieve shaker and instead a concrete vibrating table was used. The mesh used for the 450 mm diameter sieves was of

commercial quality, as opposed to laboratory quality. The difference between these two quality designations is that the laboratory quality mesh is manufactured with a tighter control of its apertures. Given the nonstandard mesh and shaker used, once the tailings had been sieved into the three initial size categories, the GSD of each category was confirmed by means of a standard sieve (ASTM D6913) and hydrometer analysis (ASTM D422). Figure 7.2 shows the GSD curves corresponding to each category.

The coarse, medium, and fine categories were then combined in proportions such that the resulting mix had the desired FC and a GSD curve whose coarse fraction resembled the GSD curves in Figure 3.22 with a similar FC value. It should be noted that since there are no in situ GSD curves that exhibit an FC as low as 10%, no attempt was made to match the GSD of the mix 10/70 to any in situ GSD curves. Instead, the criterion used for the mix 10/70 was, in principle, to create a GSD that was as narrow as possible in order to produce a soiltype with a high e_{min}. This criterion alone would have led to the adoption of the tailings in the medium category as an ideal "mix" (see Figure 7.2). However, it was deemed desirable to incorporate some tailings from the fine category to give the resulting mix a greater representability of the tailings present in the Impala TSF. No tailings from the coarse category were included in the mix 10/70.

The resulting GSD curves of the laboratory mixes are shown in Figure 7.3. As was sought, the GSD curve of the mix 10/70 is the narrowest of all six curves. Additionally, the coarse fractions of the mixes with FC from 30% to 81% are in good agreement with the in situ GSD curves. However, the match is not as good on the fine portion of the GSD curves, with finer particles being generally underrepresented in the laboratory mixes with FC between 30% and 98%. That is, the GSD curves of these laboratory mixes tend to plot below the in situ GSD curves. It is also noted that there is a significant discrepancy between the GSD of the mix 98/65 and the in situ GSD with FC = 95% (Figure 7.3f). The lack of control over the GSD of the fines meant that it was not possible to alleviate the underrepresentation of the finer particles, nor to improve the agreement between the lab mix with FC = 98% and the in situ curve with FC = 95%. Despite the above mentioned limitations, the laboratory mixes with FC varying from 30% to 81% exhibit the same overall shape as their in situ counterparts and were therefore deemed adequate to study the mechanical behaviour of the tailings.

Values of e_{min} were determined using the modified Proctor compaction test (ASTM D1557) and a nonstandard method. The modified Proctor test is discussed first. The resulting compaction curves of the mixes with FC between 30% to 98% are shown in Figure 7.4. These curves indicate the maximum dry density (ρ_{dry}) attained at an optimum water content (w = mass of water/mass of solids). It is noteworthy that the compaction curve of the 30/53 mix exhibits a double peak and the curve of the 47/52 peak may also be indicating the presence of a second peak at low water contents. These types of curves, which deviate from the typical single-peak compaction curve, are known to be common of sandy soil specimens with liquid limits smaller than 30% (Lee and Suedkamp 1972).

Calculation of e_{min} from the peak value of ρ_{dry} requires the determination of the particle density (ρ_s) of each soiltype. ASTM D854 was used for all ρ_s determinations. Figure 7.5 shows a clear trend of direct correlation between ρ_s and FC for the mixes with FC between 30% and 98%. The fact that the

mix 10/70 does not follow the same trend is explained by the absence of coarse tailings in this mix. The ρ_s of the coarse and medium size categories into which the tailings were initially sieved are also reported in Figure 7.5. The ρ_s of the tailings sieved into the fine category is the same as the ρ_s of the mix 98/65 as this "mix" consisted entirely of the tailings that had been sieved into the fine category.

The e_{min} values inferred from the ρ_s and the peak ρ_{dry} are shown in Figure 7.6. Their e_{max} values determined using ASTM D4254 is also included for reference. Given that the modified Proctor compaction procedure has the potential to alter the GSD of the soils by particle crushing, all the compacted tailings were discarded. This situation, coupled with limitations on the amount of tailings available for testing meant that it was not possible to use the modified Proctor compaction test to determine e_{min} of the mix 10/70. A nonstandard method was therefore adopted which consisted in depositing dry tailings into a cylindrical steel mould that had a height of 103.4 mm, internal diameter of 80.0 mm, and a mass of 8.1 kg (Figure 7.7). The mould was fitted with an extension sleeve that had a length of 185 mm and a mass of 4.4 kg. With the extension sleeve in place, the tailings were deposited in 40 layers of approximately equal mass, and each layer was compacted by hitting the mould 8 times with a rubber mallet, two impacts on opposite sides. During the filling and compaction procedure, the mould was placed unrestrained on a smooth and horizontal surface and the impacts from the mallet made the mould slide a few centimetres each time. The total mass deposited in the mould extended into the sleeve by one or two centimetres. After the last layer was deposited, a cylindrical overburden weight of 7.1 kg was slid into the extension sleeve, placed on top of the specimen, and the mould was hit with the mallet 8 more times, again two impacts on opposite sides. The mass of 7.1 kg was chosen to generate an average compressive stress of 13.8 kPa (2 psi) which is the overburden stress used in ASTM D4253 (vibratory table method). However, the use of the overburden stress did not significantly change the degree of compaction that had already been attained using only the mallet. After compaction under the overburden load, the 7.1 kg mass and the extension sleeve were removed and the compacted specimen was trimmed level with the top of the mould by scraping with a straightedge. Any particles lying on the outer part of the mould were removed and the mould was weighed to determine the mass of dry soil which, combined with the volume of the mould and ρ_s (Figure 7.5), was used to calculate e_{min}. In order to maximise the repeatability of the procedure, all implementations were made by the same technician using the same equipment. The procedure was implemented on all the laboratory mixes in order to check that the trends in results were the same as those obtained using ASTM D1557. To check the repeatability of the results, the test was made three times on the mixes 10/70, 30/53, 64/59, and 81/63.

The nonstandard e_{min} values exhibited the same trend as those obtained from ASTM D1557 (Figure 7.6). This match in trends is interpreted as a validation of the nonstandard procedure. It is also apparent that the nonstandard method consistently yields lower e_{min} values than ASTM D1557. This mismatch is expected as different e_{min} determination procedures are known to yield different values (Tavenas and Rochelle 1972). With regard to the repeatability of the nonstandard procedure, the results of multiple repetitions are plotted in Figure 7.8 with an expanded vertical scale. The results from three repetitions on the same mix of tailings fall within ±0.01 of the average value. This range is smaller than the range of ±0.02 set by ASTM D4253 for tests done by two different

laboratories (the range ±0.02 assumes G_s = 2.7 and maximum index dry density of 1760 kg/m^3). Based on the agreement of trends with ASTM D1557 and its good repeatability, the e_{min} nonstandard procedure was considered reliable. The correlation between the e_{min} values obtained using the nonstandard procedure and using ASTM D1557 (Figure 7.9) was used to estimate the e_{min} value that would be obtained for mix 10/70 if it were subjected to the ASTM D1557 procedure. The e_{min} values included in the codes assigned to each mix (Table 7.1) correspond to the nonstandard procedure.

The nonstandard e_{min} values (Figure 7.6 and Figure 7.8) show that, as was sought, the e_{min} of the mix 10/70 is distinctly higher than the rest. It is also noted that the range of nonstandard e_{min} values covered by the mixes is 0.18 (from 0.52 to 0.70). For context, it is useful to compare this range to the e_{min} range suggested by Figure 6.31 as being applicable to non-plastic soils in general. By excluding the circular plates (CP) and the glass balls (GB) (which are not real soils), this e_{min} range can be estimated as 0.5 (from 0.3 to 0.8). That is, the e_{min} range covered by the six mixes of Impala tailings is about 36% of the e_{min} range possible in non-plastic soils in general.

In order to characterise the SSLs of the Impala tailings, three mixes were chosen to cover a wide range of e_{min} and FC values. The selected mixes were 10/70, 30/53 and 81/63. Mix 10/70 was chosen because it has the highest e_{min} and the lowest FC. Mix 30/53 was chosen because, within experimental scatter, its e_{min} is the lowest and has an intermediate value of FC. Finally, mix 81/63 was chosen because it represents a case of very high FC and has an intermediate value of e_{min}. Choosing mix 98/65 instead of 81/63 would also seem as a reasonable option given that it has an even higher FC and very similar e_{min}. However, mix 81/63 was preferred given its greater similarity with the in situ GSDs (Figure 7.3).

7.3 Triaxial testing programme

7.3.1 Rationale

The main objective of the triaxial tests was to shear isotropically consolidated specimens by monotonic axial compression until they reached steady state, i.e. constant values of mean effective stress (p'), deviatoric stress (q), and void ratio (e). The values of p', q, and e attained by each specimen at steady state defines one point of the SSL. The general approach adopted to obtain points that are adequately distributed along the SSL was the one suggested by Jefferies and Been (2006). In this approach only contractive specimens are used and drained and undrained tests are combined to define the SSL. Consolidated undrained (CU) triaxial tests are used to define the lower stress (≈< 200 kPa) portion of the SSL, and consolidated drained (CD) triaxial tests are used to define the higher stress (≈> 200 kPa) portion. Jefferies and Been (2006) argue in favour of using only contractive (loose) specimens because, unlike dilatant specimens, contractive specimens maintain a uniform void ratio distribution during shearing. Since it is the global void ratio of the specimen that is measured in the laboratory, it is essential that the steady state condition of triaxial specimens is not controlled by a localised void ratio which could potentially develop, for example, along a shear band. Distinction between dilatant and contractive specimens sheared under drained conditions is

straightforward because the former will reduce their void ratio when sheared, while the latter will increase it. For specimens sheared under undrained conditions, Verdugo and Ishihara (1996) noted that a dilatant response is characterised by a deviator stress that increases monotonically until the specimen deforms continuously under a constant shear stress (Figure 7.10a); whereas the contractive response is characterised by the development of a minimum strength followed by a dilative behaviour where the strength is regained and it eventually reached an ultimate value at large strains (see curves labelled "σ'_0 = 2.0 MPa" and "σ'_0 = 3.0 MPa" in Figure 7.10b).

The distribution of void ratios in triaxial tests was studied by Desrues et al. (1996). They conducted a series of drained triaxial tests on Hostun RF sand consolidated by an isotropic stress of 60 kPa and used computer tomography to measure local and global void ratios at different levels of shearing. They found that the zones of localised strain that develop in dilatant specimens have void ratios that are significantly higher than the global void ratio of the specimen (Figure 7.11). The discrepancy (≈ 0.07) between local and global void ratios was observed even when shearing the specimens with lubricated and enlarged end platens in order to achieve a more uniform strain distribution. Furthermore, they stated that such discrepancy rendered the global void ratio a meaningless parameter. Conversely, for contractive specimens, Desrues et al. (1996) found that the local and global void ratios were indistinguishable from each other even when lubricated and enlarged end platens were not used. These results suggest that drained triaxial tests on dilatant specimens are not adequate for SSL determination.

A similar conclusion is arrived at when considering the results obtained by Verdugo and Ishihara (1996) from an extensive triaxial testing programme on Toyoura sand. When considering e-p' space, the steady state points of drained dilatant specimens tend to plot below the SSL defined by undrained tests and contractive drained tests (Figure 7.12). This result is in general agreement with the observations made by Desrues et al. (1996), although the mismatch in void ratio of the drained dilatant specimens tested by Verdugo and Ishihara (1996) is about 0.02, which is smaller than the discrepancy of 0.07 observed by Desrues et al. (1996). In light of this potential mismatch, drained tests on dilatant specimens were not conducted to define the SSL of Impala tailings.

Verdugo and Ishihara (1996) also tested undrained dilatant specimens and compared the SSL defined by these tests with the SSL defined by undrained contractive specimens. Their results (Figure 7.13) show that both types of test define the same SSL. However, dilatant specimens do have the disadvantage of requiring higher shear strains to reach steady state (Jefferies and Been 2006; Verdugo and Ishihara 1996). Despite the attempt made in this study to use only contractive specimens for both drained and undrained tests, dilatant behaviour could not be completely avoided in the undrained tests. This occurred because triaxial testing for each soiltype began with undrained tests and at this stage the location of the SSL was unknown. This implied that there was uncertainty of the void ratio at which the specimens should be prepared to result in contractive behaviour.

7.3.2 Triaxial testing procedure

The moist tamping method of specimen preparation was adopted as it allows good control over the formation void ratio of the specimen. This method has also been reported as the most adequate to prepare loose specimens which exhibit contractive behaviour (Ishihara 1993). Specimens were tamped in six layers of equal mass of solids. Prior to tamping, each layer was mixed with water to achieve water contents of 7% for mixes 10/70 and 30/53, and 11% for mix 81/63. The higher water content for mix 81/63 was due to its greater FC, which meant that a greater amount of water was necessary to wet the surface of all the particles. After mixing with water, the containers holding each layer were sealed with cling wrap and the soil was allowed to cure for at least 4 hours.

After curing, each layer was scooped into a split mould with an internal diameter of 70 mm and a height of 141 mm. A tamper was used to densify each layer to one sixth of the height of the mould. To ensure that each layer had the same height, the tamper had an adjustable cross bar which could be moved along the stem of the tamper (Figure 7.14). Grooves on the stem of the tamper and a spring mechanism on the cross bar facilitated the location of the cross bar to the correct position. The cross bar was released and locked into position by adjusting a cap screw. In order to tamp the last layer, an extension sleeve was adapted to the mould. The internal wall of the extension sleeve was flush with the internal wall of the split mould. Although the extension sleeve was only necessary to tamp the last layer, it was kept in position (Figure 7.14b) for the tamping of all the layers. The tamped surface of each layer, except the last one, was scarified to enhance the adherence between layers. After tamping all layers, the extension sleeve was removed and filter paper and a porous stone were placed on one end of the specimen (still in the split mould). Next, the specimen was placed on the pedestal of the triaxial cell with the end covered by the porous stone touching the pedestal. The split mould was then removed carefully to minimise any disturbance of the specimen. All specimens stood upright after the removal of the split mould. Another piece of filter paper and porous stone were then placed on top of the specimen (Figure 7.15a) and a membrane stretcher was used to place the membrane. Once the membrane was in place, its bottom end was slid upwards just enough to disclose the sides of the pedestal and allow the removal of any particles that could compromise a proper seal. After cleaning the sides of the pedestal the membrane was slid down again. At this point the top cap was put in position and two O-rings were used to seal the membrane against the pedestal and against the top cap (Figure 7.15b). The top cap had a central coned seating in its upper surface to accommodate the loading ram (Figure 7.15b). In turn, the loading ram had a rounded tip that fitted in the coned seating. This type of connection between top cap and loading ram ensures central application of the load and automatically corrects any lack of axial alignment in the early stages of loading. However, this aligning action may lead to an uncertain start to the stress-strain curve under small loads (Bishop and Henkel 1957).

If considered necessary to ensure stability, the specimen would at this stage be subjected to a suction between 30 to 40 kPa. The perspex cover of the triaxial cell was then fixed into position and the cell was filled with water and pressurised to between 30 kPa to 40 kPa. If the specimen had been

subjected to suction, it was released at this stage. Care was taken to ensure that the specimen was not overconsolidated by the suction pressure or the initial cell pressure.

In order to reduce the time and back pressures required for saturation, the specimens were flushed with an upward flow of carbon dioxide (CO_2) for at least one hour. The flow rate of CO_2 was adjusted so that the flow could barely be felt when holding the outlet pipe against the palm of the hand. This was done to ensure that the flow of CO_2 would not disturb the internal fabric of the specimen. During flushing, the open end of the outlet pipe was kept under water and the resulting bubbles served as an indicator that the flow of CO_2 remained steady. After completion of the CO_2 treatment, the specimens were flushed with an upward flow of one litre of deaired water under a 15 kPa pressure head. This process generally lasted between two to three hours. Once flushing was complete, the saturation process continued by applying a back pressure of 220 kPa over a period of at least 24 hours. The specimen was considered to be saturated when a B value greater than 0.96 was obtained. B value measurements were done over a period of one hour to check that the readings did not drop below 0.96 and did not exceed 1, as B > 1 typically indicates a leak between the specimen and the cell. B > 0.96 was typically attained after the first 24 hours of backpressure. For the few cases in which this was not the case, the backpressure was increased by 100 kPa and allowed to act on the specimen for another 24 hour period before measuring B again.

Once saturation was achieved, the specimen was consolidated by closing the specimen drainage valve and increasing the cell pressure until the difference between the cell pressure and backpressure was equal to the desired consolidation stress. During this process the backpressure was kept equal to at least the value at which saturation had been achieved. The drainage valve was then opened while the pwp and the volume of water squeezed out of the specimen were recorded. For the three mixes tested, the excess of pwp induced by consolidation fully dissipated after approximately 30 minutes. This dissipation indicated the end of primary consolidation. Nonetheless all specimens were allowed to consolidate for at least an additional two days to allow secondary consolidation, which is associated with creep effects (Lambe and Whitman 1979), to continue. Allowing consolidation to continue after the end of primary consolidation was done in agreement with ASTM D4767 which requires "*consolidation to continue for at least one log cycle of time or one overnight period after 100% primary consolidation has been achieved*". At the end of consolidation the lower tip of the loading rod of the triaxial cell was brought into imminent contact with the upper cap and the length of rod outside of the cell was used to infer the consolidated height of the specimen (H_c).

All specimens were sheared monotonically by axial compression under displacement controlled conditions and constant cell pressure. Two different triaxial testing setups were used. Setup 1 consisted of an automated triaxial testing system which included automated pressure controllers (Figure 7.16), and setup 2 consisted of a Wykeham Farrance 5 ton compression frame operated in conjunction with an air compressor system (Figure 7.17). Setup 1 comes with built-in transducers and data logging capabilities, whereas for setup 2 the transducers and a data logging system were adapted. Thus, all data acquisition for both setups was fully automated. The pressure, load, and

volume change transducers of both setups were calibrated to ensure that they yielded equivalent readings. Table 7.3 provides further detail on the transducers used in both setups.

All tests were made in a temperature controlled environment. The temperature control for setup 1 was done by means of an inverter air conditioner that had heating and cooling capabilities to keep a constant air temperature in the room. For setup 2 the temperature control was done by installing a small booth around the triaxial frame. The booth was made with material used to insulate roofs (Figure 7.17). A fan heater which was connected to a temperature controller and a solid state relay, ensured that the temperature inside the booth remained constant (Figure 7.18). The importance of an adequate temperature control system is illustrated in Figure 7.19. These readings correspond to a trial undrained specimen of the mix 30/53 which had been consolidated to 400 kPa using setup 1 without any temperature control. The readings were made over three days in which the room temperature fluctuated between 14°C and 17°C. The PWP is seen to accompany this fluctuation with values ranging from 260 kPa (initial backpressure) to 285 kPa. No axial load was applied to the specimen during the period over which these readings were made.

The use of enlarged and lubricated end platens is sometimes adopted when shearing to large values in order to promote the development of uniform radial strain along the height of the specimen (Been et al. 1991; Rees 2010; Verdugo and Ishihara 1996). These types of platens were not adopted in this testing programme for two reasons. Firstly, it is known that although lubricated platens may help reduce non-uniformities in radial strain, such provision is not always entirely effective. For instance, Rees (2010) reported barrelling and caving of specimens despite the use of lubricated platens (Figure 7.20). Second, several investigators have determined SSLs without using lubricated platens and have obtained consistent and repeatable results (Fourie and Papageorgiou 2001; Li 2013).

All specimens were sheared at a rate of 4.4% axial strain per hour. Comparison of this shearing rate to the rate that has been adopted in previous works with non-plastic soils with comparable FC (Table 7.2) suggests that 4.4%/hr was likely a conservative rate. Nonetheless, it was preferred to shear too slowly rather than too quickly.

At the end of each test the void ratio of the specimen was determined using a variation of the method proposed by Verdugo and Ishihara (1996). In the original method, when removing the specimen from the triaxial cell, the entire specimen is transferred into a drying bowl to determine the remaining water content (w_r) and the mass of solids of the specimen. Verdugo and Ishihara (1996) recommended the use of a spatula to ensure that all the soil attached to the membrane and end platens is transferred to the drying bowl. However, in trial tests, the author found that even when using a spatula, it was time consuming to collect all the soil attached to the membrane. The delay introduced by the requirement of having to clean the membrane with the spatula had the potential to compromise the measurements of w_r. This is because while the membrane is cleaned, water starts evaporating from the drying bowl and from the membrane itself, and this evaporated water would not be accounted for when calculating w_r. Therefore, the following approach was adopted. The original method proposed by Verdugo and Ishihara (1996) was followed up to the point when the triaxial cell is disassembled. At that point most of the specimen was transferred to

the drying bowl although some soil was still attached to the membrane. The wet weight of the portion of the specimen in the drying bowl was then measured and this value combined with the oven dried mass of the specimen was used to determine w_r and the first portion of the mass of solids (M_{s1}). Then the soil that had remained stuck to the membrane was washed into a second drying bowl from which the second portion of the mass of solids was determined (M_{s2}). Typically M_{s2} was about 1% to 4% of M_{s1}. Besides limiting the extent of unaccounted evaporation, the adopted procedure also has the advantage of making it easier to collect all the particles from the membrane, as this is done with water, as opposed to with only a spatula. The total mass of solids was determined from the sum of M_{s1} and M_{s2}. The post-shearing void ratio (e_f) was then calculated as:

$$e_f = \frac{\Delta Vol + w_r(M_{s1} + M_{s2})}{M_{s1} + M_{s2}}\rho_s \qquad 7.1$$

Where *ΔVol* is the volume of water squeezed out of the specimen before removing it from the triaxial cell as indicated by Verdugo and Ishihara (1996) and ρ_s is the density of the solids. Strictly, equation 7.1 is not dimensionally consistent because a volume and mass are being added in the numerator. However, it is noted that the mass of water is numerically equal to its volume, i.e., Verdugo and Ishihara (1996) implied that for all practical purposes it can be assumed that the density of water is equal to 1 g/cm^3.

The cross sectional area of the specimen at the end of consolidation (A_c) was computed as:

$$A_c = \frac{V_{wf} + V_s}{H_c} \qquad 7.2$$

Where V_{wf} is the volume of water after consolidation. In the case of undrained tests, V_{wf} was equal to the numerator of Eq. 7.1. For drained tests, V_{wf} was equal to the numerator of Eq. 7.1 plus the volume of water squeezed out of the specimen during shearing (ΔVol_{TOT}). V_s is the volume of solids calculated as:

$$V_s = \frac{M_{s1} + M_{s2}}{\rho_s} \qquad 7.3$$

Axial strain (ε_a) for a given applied axial load was calculated as:

$$\varepsilon_a = \frac{\Delta H}{H_c} \qquad 7.4$$

Where ΔH is the change in height of the specimen during loading. The deviator stress (σ_d) was calculated as:

$$\sigma_d = \frac{P}{A} \quad 7.5$$

Where P is the axial load corrected for uplift and piston friction, and A is the cross sectional area of the deformed specimen. Two different equations were considered to compute A:

$$A = A_c \frac{1 - \varepsilon_v}{1 - \varepsilon_a} \quad 7.6$$

$$A = \frac{V_c - \Delta V_i}{H_c - \Delta H} \cdot \left(1 + \frac{\Delta H}{2 \cdot H_c}\right) \quad 7.7$$

Where ε_v is the volumetric strain of the specimen induced by shearing (compression taken as positive), V_c is the post-consolidation volume of the specimen, and ΔV_i is the specimen volume change during loading. Equation 7.6 is more widely used (e.g. Bishop and Henkel (1957), ASTM D4767) and is based on the assumption that the specimen deforms as a right circular cylinder. Equation 7.7 yields larger values of A as it accounts for the barrelled geometry of the triaxial test specimen and is used in the French Standard NF P 94-074. Equations 7.6 and 7.7 are not applicable when significant sliding occurs along a preferential rupture plane, e.g. when shear bands develop.

The minor total stress (σ_3) was calculated as:

$$\sigma_3 = CP - BP \quad 7.8$$

Where CP is the cell pressure and BP is the backpressure. The major total stress (σ_1) was calculated as:

$$\sigma_1 = \sigma_3 + \sigma_d \quad 7.9$$

The minor and major effective stresses, σ'_1 and σ'_3 respectively, were calculated as:

$$\sigma'_3 = \sigma_3 - \Delta u \quad 7.10$$

$$\sigma'_1 = \sigma_1 - \Delta u \quad 7.11$$

Where Δu is the shear-induced change in pore water pressure. For drained tests, the void ratio (e_i) at any point in the test was calculated as:

$$e_i = e_f + \frac{\Delta Vol_{TOT} - \Delta Vol_i}{V_s} \quad 7.12$$

Where e_f is the final void ratio (Eq. 7.1), ΔVol_i is the volume of water that had been squeezed out of the specimen up to that stage of shearing, and V_s is the volume of solids (Eq. 7.3). The mean total stress (p), the mean effective stress (p'), and the triaxial deviator stress (q) were calculated as:

$$p = (\sigma_1 + \sigma_2 + \sigma_3)/3 \quad 7.13$$

$$p' = p - \Delta u \quad 7.14$$

$$q = \sigma_d = \sigma_1 - \sigma_3 \quad 7.15$$

Corrections for membrane stiffness as suggested by ASTM D4767 were found to be negligible and were therefore not performed. Similarly, corrections for membrane penetration as suggested by Jefferies and Been (2006) were also found to be negligible considering the D_{50} of the soils and were not performed.

Several authors (Carrera et al. 2011; Jefferies and Been 2006; Li 2013; Verdugo and Ishihara 1996) have reported triaxial test results in which a specimen does not reach steady state even after being sheared to significantly large strains. For such cases Carrera et al. (2011) proposed an extrapolation scheme to allow the estimation of the most probable steady state values of p' and q. This extrapolation scheme was adopted in this study and is illustrated in Figure 7.21: M is inferred by plotting q/p' against the rate of change of pore water pressure to change in shear strain ($\delta(\Delta u)/\delta\varepsilon_s$) and then extrapolating the q/p' plot to $\delta(\Delta u)/\delta\varepsilon_s = 0$ (i.e., steady state). For the example shown in Figure 7.21b, at the end of the test the specimen was still dilating at about 4 kPa/% and the extrapolation suggests M ≈ 1.45. Figure 7.21c shows how the inferred value of M can then be used to estimate the steady state values of q and p'. Carrera et al. (2011) noted that the steady state points calculated with this method were in good agreement with tests that had reached the steady state. Carrera et al. (2011) also used this extrapolation scheme to account for the development of shear bands (Figure 7.22). In such cases, the data collected prior to the appearance of the shear band was extrapolated, while the data collected after the shear band had developed was discarded. The same approach was also adopted in the present work.

Analogous extrapolations were implemented in this study for the drained tests, except that instead of using $\delta(\Delta u)/\delta\varepsilon_s$ to assess proximity to the steady state, it was necessary to use the rate of change of volumetric strain to change in shear strain ($\delta\varepsilon_v/\delta\varepsilon_s$), i.e. dilation. For the drained tests that did not reach steady state, plots of e vs $\delta\varepsilon_v/\delta\varepsilon_s$, and q/p' vs $\delta\varepsilon_v/\delta\varepsilon_s$ were used to estimate the steady state values of p', q, and e. The way in which these plots were used is illustrated in Section 7.3.3. Given that radial strains were not measured in the current study, axial strain (ε_a) was used as a proxy for shear strain (ε_s). The same approach was adopted by Carrera et al. (2011). The adopted sign convention for $\delta(\Delta u)/\delta\varepsilon_a$ and $\delta\varepsilon_v/\delta\varepsilon_s$ was that negative indicated dilation (i.e. reduction in pwp or increase of volume) and positive indicated contraction (i.e. increase in pwp or reduction of volume).

7.3.3 Results of the triaxial tests

The stress vs strain curves of most triaxial tests exhibited an atypical behaviour at axial strains smaller than approximately 1% (e.g. Figure 7.23). This is attributed to the connection between the top cap and the loading ram described in Section 7.3.3 and which leads to an uncertain start of the stress-strain curve. However, such uncertainty only affects the deformation characteristics at small strains (Bishop and Henkel 1957) and is of no consequence to the interpretation of steady states.

The values of q varied appreciably depending on whether Eq. 7.6 or Eq. 7.7 was used to calculate the cross sectional area. Figure 7.23a shows a typical result: Both equations yield virtually the same values of q at low strain levels (ε_a < 5%) when the area correction is small. But as ε_a increases, the value of q calculated with Eq. 7.7 becomes lower than the value calculated with Eq. 7.6. The adoption of Eq. 7.6 or Eq. 7.7 also affected the estimation of M, with lower values being estimated when using Eq. 7.7 to compute the deviator stress (Figure 7.23b). Equation 7.7 was preferred to process the data because its underlying assumption of a barrel-like deformed geometry was in good agreement with the deformed geometry of most specimens (Figure 7.24). Detailed measurements of stress, strain, and void ratio of all the tests are reported in a companion spreadsheet. The σ_1 values reported in this spreadsheet were calculated using Eq. 7.7.

Figure 7.25 and Figure 7.26 show examples of CU and CD tests, respectively, in which the steady state was reached as indicated by the stability of the readings towards the end of the test. In the case of Figure 7.25 (CU test), q is still decreasing slightly when the test was ended. However, the stability of the PWP readings suggests that steady state had been reached. Jefferies and Been (2006) indicated that these variations in q readings may be due to errors introduced by the area corrections used in the calculation of q (Eqs. 7.6 and 7.7). Since the potential errors due to area corrections increase with ε_a, the steady state values of q and p' extracted from results such as those shown in Figure 7.25 corresponded to the smallest ε_a value at which steady state was reached, i.e., the smallest ε_a value at which PWP readings had stabilised. In the case of Figure 7.25 this stabilisation occurred at ε_a = 25%.

Figure 7.27 shows the results of a CU test on mix 81/63 in which the steady state was not reached, as indicated by the changes in readings taking place at the end of the test. Figure 7.28 illustrates the implementation of the extrapolation scheme proposed by Carrera et al. (2011) for these cases. The plot of $\delta(\Delta u)/\delta\varepsilon_a$ vs ε_a is shown in Figure 7.28a. In order to reduce the noise in the data, the values of $\delta(\Delta u)/\delta\varepsilon_a$ were calculated over every 1% axial strain, instead of over every two consecutively logged data points. The figure shows that at the end of shearing the PWP was still reducing at a rate of 4 kPa/%. Figure 7.28b shows the plot of q/p' vs $\delta(\Delta u)/\delta\varepsilon_a$. The values of q/p' in this plot have also been averaged over 1% to avoid plotting an instantaneous quantity against an averaged one. If this plot is projected to the steady state condition (i.e. $\delta(\Delta u)/\delta\varepsilon_a = 0$), the value of M can be estimated as 1.25. This value is marginally smaller than the value of q/p' = 1.29 that corresponds to the end-of-test condition. The stress path (Figure 7.28c) can then be extended to intersect the line q/p' = M. Figure 7.28d is a magnified version of Figure 7.28c and illustrates how the point of intersection between the stress path and q/p' = M is used to estimate the steady state

values of p' and q. This extrapolation procedure was only implemented on CU tests that had absolute values of $\delta(\Delta u)/\delta\varepsilon_a$ greater than 1 kPa/% at the end of shearing. It was found that below this value, the extrapolation had negligible effects on the estimation of steady state values. As indicated in Table 7.4, extrapolation was only performed on a minority of undrained tests and the extrapolated results were in good agreement with those of tests that were not extrapolated.

Figure 7.29 shows the results of a CD test made on mix 30/53 that did not reach steady state. Additionally, a sudden change in q readings is observed at $\varepsilon_a \approx 19\%$. Although less noticeable, this change is also reflected in the e and p' readings. It is hypothesised that this change is due to the development of a shear band (Figure 7.30). In these cases, the recommendation of Carrera et al. (2011) (Figure 7.22) was followed and the data collected after the change in trend was discarded. Figure 7.31 illustrates the implementation of the extrapolation procedure for such cases. A plot of $\delta\varepsilon_v/\delta\varepsilon_a$ vs ε_a up to $\varepsilon_a = 19\%$ is presented in Figure 7.31a. To reduce the noise in the data, the values of $\delta\varepsilon_v/\delta\varepsilon_a$ were averaged over every 1% of axial strain. The plot shows that the specimen was contracting at a rate of 0.03 before the data was affected by the shear band. Extrapolation of the void ratio to steady state was done by plotting e vs $\delta\varepsilon_v/\delta\varepsilon_a$ and projecting the data to $\delta\varepsilon_v/\delta\varepsilon_a = 0$ (Figure 7.31b). The plot suggests that the steady state value of e is 0.773, which is similar to value of e = 0.776 which had already been attained at $\varepsilon_a = 19\%$. Figure 7.31c shows a plot of q/p' vs $\delta\varepsilon_v/\delta\varepsilon_a$ used to attempt to infer an M value by projecting the plot to $\delta\varepsilon_v/\delta\varepsilon_a = 0$. However, in this case it is not very clear what the projected value of M should be. In these cases it was deemed preferable to use the average M value obtained from other triaxial tests, CU and CD, conducted on the same soiltype (mix 30/53 in this case). This approach is justified because for a given loading condition (in this case triaxial compression) M is a constant independent of drainage conditions (Jefferies and Been 2006; Verdugo and Ishihara 1996). Figure 7.31d illustrates how the average M value from other triaxial tests on mix 30/53 and the stress path of the triaxial test under consideration were used to infer the steady state values of p' and q. The close similarity between the extrapolated values of e (Figure 7.31b), p', and q (Figure 7.31d), with the recorded values at $\varepsilon_a = 19\%$ (Figure 7.29) suggest that the specimen was very close to steady state before the shear band developed. Lastly, it is noted that in Figure 7.31b and Figure 7.31c the values of e and q/p', respectively, have been averaged over 1% to avoid plotting an instantaneous quantity against an averaged one.

A total of 20 triaxial tests were conducted to define the SSLs of the three mixes of Impala tailings. The main features of each test are presented in Table 7.4. In four of the 20 triaxial tests, M was adopted as the average value calculated from other triaxial tests on the same soiltype. As sought, the large majority of the specimens exhibited contractive behaviour with the only exceptions being Tests 7 and 8 which were made on mix 30/53.

The e-p' and the q-p' projections of the SSLs for the three soiltypes tested are shown in Figure 7.32, Figure 7.33, and Figure 7.34. The corresponding state and stress paths are also included. For a given soiltype, drained and undrained tests define the same SSL, which is in agreement with previous works such as Been et al. (1991), Verdugo and Ishihara (1996), and Li et al. (2013). The e-p' and the q-p' projections of the SSL have been fitted with Eqs. 2.1 and 2.2, respectively. When fitting the e-p' projection of the SSL of mix 30/53, the data point with the highest p' value (540 kPa) was

not considered. The location of this point may be indicating a curvature in the SSL, and although it could be fitted with a higher order equation such as Eq. 2.5, the use of Eq. 2.1 was preferred to enable a comparison of the SSLs with the trends identified in Chapter 6.

The e-p' projections of the three Impala SSLs are plotted together in Figure 7.35 and the Γ_{50} and λ values are reported in Table 7.1. The q-p' projections of the three Impala SSLs are plotted in Figure 7.36. M varies from 1.25 to 1.29 with no systematic variation with e_{min} or FC. As indicated by Figure 7.36d, an average value of M = 1.27 can adequately be fitted to all three soiltypes. The observed lack of dependence of M on the GSD of the soiltype is in agreement with the results reported by others such as Carrera et al. (2011) and Li et al. (2013). The M values are also reported in Table 7.1.

7.4 Discussion and concluding remarks

Figure 7.37 shows the correlation between e_{min} and Γ_{50} of the three Impala SSLs. The three data points suggest a linear correlation regardless of the e_{min} method considered. Figure 7.38 shows the three Γ_{50} vs e_{min} data points corresponding to the Impala SSLs compared to the database of Chapter 6. Regardless of the method used to determine e_{min}, the data from the Impala tailings is in good agreement with the global trend of the database. It is also important to note that Figure 7.38 highlights the limited predictive power of Eq. 6.3 which describes the overall Γ_{50} vs e_{min} trend of the database of Chapter 6. The vertical offset between the Impala data points and the best fit line (Eq. 6.3) shown in Figure 7.38 varies between 0.02 and 0.09. These errors are considerably higher than the precision with which the e-p' projection of the SSL can be experimentally determined (Figure 7.35). So although Eq. 6.3 is useful in predicting the qualitative behaviour of Γ as a function of e_{min}, clearly it is not an adequate substitute for triaxial testing. The reasons for the limited predictive power of Eq. 6.3 were discussed in Section 6.5.

Figure 7.39 compares all the tailings soiltypes to the remainder of the database presented in Chapter 6 in Γ_{50}-e_{min} space. In general, good agreement is observed between tailings and the trend established by other non-plastic soils. There are only two noticeable deviations (encircled in the figure) which correspond to two SSLs of Stava tailings reported by Carrera et al. (2011). In assessing the significance of this deviation, it must be noted that the e_{min} value of the Stava tailings was not formally determined but rather approximated to the void ratio of the densest odometer specimen tested by Carrera et al. (2011) (Table 6.2). It is likely that a formal determination of e_{min} would yield lower void ratio values therefore shifting the Stava data points to the left and closer to the global trend of non-plastic soils. Accordingly, it is concluded that there are no significant differences between the trends of Γ_{50} vs e_{min} followed by tailings and non-plastic soils in general. This agreement with the global trend lends credibility to the concept that e_{min} is a suitable index parameter to characterise the variability of Γ in a deposit of non-plastic tailings.

It is also apparent in Figure 7.39 that tailings soiltypes plot on the upper half of the e_{min} domain. This is likely caused by the characteristic angular shape of tailings (e.g. Figure 6.12) which is in turn caused by the rock grinding process from which they originate. Previous research shows that for a

given GSD, soils with angular particles will exhibit higher e_{min} values than soils with rounded particles (Biarez and Hicher 1994; Cho et al. 2006; Li 2013).

Figure 7.40 shows a plot of λ vs e_{min} for the Impala SSLs. Regardless of the e_{min} determination method, a direct correlation is observed. This is in agreement with the trends identified in Section 6.4 and the findings of Muir-Wood and Maeda (2008). Conversely, although it was noted in the introduction of this chapter that a high FC may increase the value of λ due to the presence of platy particles, Figure 7.40 shows that this was not the case for Impala tailings. Interestingly, the mix with the highest λ (mix 10/70) is also the mix with the lowest FC. This absence of a correlation between λ and FC was also observed for Merriespruit tailings (Figure 6.41g) and Stava tailings (Figure 6.41j). However, it is also noted that neither Merriespruit nor Stava tailings exhibited a correlation between λ and e_{min}.

Figure 7.41 shows the e_{min} vs λ data points corresponding to Impala tailings compared to the database of Chapter 6. The Impala tailings are observed to exhibit λ values typical of non-plastic soils. Figure 7.42 further illustrates how the λ vs e_{min} data points corresponding to tailings compare to the remainder of the database. Although no particular trend is evident, it is noteworthy that in λ-e_{min} space tailings are indistinguishable from other non-plastic soils.

The fact that the three Impala SSLs can be well represented by a single M value (Figure 7.36d) agrees with the results of Carrera et al. (2011) for Stava tailings. The results from Chapter 6 imply that this similarity in M values suggests that there are no significant changes in mineralogy or grain shape between the tested mixes of Impala tailings. The results also showed that the area correction adopted to calculate the deviator stress (Eqs. 7.6 or 7.7) has a small yet systematic effect on the calculations of M. Namely, assumption of a barrel-shape deformed geometry (Eq. 7.7) yields lower values of M. Accepting that the barrel-like deformed geometry of the triaxial specimens (Figure 7.24) implies that Eq. 7.7 yields more realistic results, then the use of Eq. 7.6 leads to slightly unconservative estimates of M.

The experimental determination of the SSL of three mixes of Impala tailings has served to support the suitability of using e_{min} as an index parameter to characterise the variability in Γ values within a tailings deposit. The Impala SSLs also exhibited a direct correlation between λ and e_{min}, however the absence of this correlation in most of the non-plastic soils included in Figure 6.41, and in particular in the Merriespruit and Stava tailings, suggests that additional testing is required to further understand the correlation between λ and e_{min}.

The λ values that have been experimentally determined for Impala tailings will be used in the following chapter to determine how the variability in λ affects the uncertainty of ψ values inferred using Eq. 2.45 proposed by Jefferies and Been (2006). The following chapter will also propose a tentative approach to estimate SSL parameters from CPT and laboratory data. The estimation of SSL parameters, specifically λ, can assist in the reduction of the uncertainty of ψ when calculated from Eq. 2.45.

7.5 Tables and Figures

Table 7.1 Index properties and SSL parameters of the laboratory mixes of Impala tailings.

Code	FC (%)	ρ_s (g/cm^3)	e_{min} [a]	e_{min} [b]	e_{max}	GSD in Figure 7.3	SSL parameters		
							Γ_{50}	λ	M
10/70	10	3.505	0.70	0.72[c]	n/a	(a)	1.05	0.076	1.25
30/53	30	3.426	0.53	0.59	0.90	(b)	0.82	0.042	1.29
47/52	47	3.480	0.52	0.58	0.93	(c)	n/a[d]	n/a	n/a
64/59	64	3.538	0.59	0.61	0.93	(d)	n/a	n/a	n/a
81/63	81	3.587	0.63	0.66	1.12	(e)	1.07	0.069	1.25
98/65	98	3.607	0.65	0.68	1.18	(f)	n/a	n/a	n/a

Notes: a) e_{min} determined using the nonstandard procedure described in Section 7.2; b) e_{min} determined using ASTM D1557; c) Value estimated with the correlation shown in Figure 7.9; d) n/a = not available.

Table 7.2 Shearing rates in axial strain per hour adopted in investigations with non-plastic soils.

Reference	Rate (%/hr)	Range of FC tested
This work	4.4	10% to 81%
Rees (2010)	18	0% to 30%
Papadopoulou and Tika (2008)	3	0% to 100%
Naeini and Baziar (2004)	60	0% to 100%
Thevanayagam et al. (2002)	36	0% to 100%
Zlatović and Ishihara (1995)	18	5% to 100%

Table 7.3 Transducers used in triaxial testing setups 1 and 2.

Measured parameter	Transducer specification	
	Setup 1: Automated system	Setup 2: Wykeham Farrance frame + air compressor
Cell pressure	25 bar - 250 cm^3 APC[a] (VJT2260)[b]	10 bar pressure transducer (Gems CVD sensors 2200 series)
Back pressure	25 bar - 250 cm^3 APC (VJT2260)	n/a[c] - monitored with dial gauge
PWP	10 bar pressure transducer (VJT0250)	10 bar pressure transducer (Gems CVD sensors 2200 series)
Specimen volume changes	25 bar - 250 cm^3 APC (VJT2260)	80 cm^3 volume change transducer (EL27-1641)
Displacement	50 mm LVDT (VJT0272)	50 mm LVDT (DCTH 1000A)
Load	10 kN internal load cell (VJT0352B)	10 kN S-type external load cell (RLT1000)

Notes: a) APC = Automated pressure controller, b) Codes in parenthesis indicate manufacturer's reference, c) n/a = not available.

Table 7.4 Summary of the triaxial testing programme

Mix	Test ID no.	Test type (CD or CU)	Behaviour (Con or Dil)[a]	p'_c[b] (kPa)	e_c[c]	Steady state parameters				End of test condition	Extrapolated to steady state
						e	p' (kPa)	q (kPa)	M		
10/70	1	CU	Con	400	1.020	1.020	177	216	1.22	Reached steady state	No
	2	CU	Con	400	1.040	1.040	145	174	1.20	Reached steady state	No
	3	CD	Con	205	1.057	1.018	328	384	1.17	$\delta\varepsilon_v/\delta\varepsilon_a$ = -0.03	Yes
	4	CU	Con	400	1.040	1.040	105	131	1.25	$\delta(\Delta u)/\delta\varepsilon_a$ = -0.6 kPa/%	No
	5	CD	Con	270	1.077	0.992	469	612	1.30	Reached steady state	No
	6	CU	Con	400	1.056	1.056	95	117	1.23[d]	$\delta(\Delta u)/\delta\varepsilon_a$ = -2.5 kPa/%	Yes
30/53	7	CU	Dil	160	0.755	0.755	540	701	1.30	Reached steady state	No
	8	CU	Dil	105	0.813	0.813	90	118	1.31	$\delta(\Delta u)/\delta\varepsilon_a$ = -0.8 kPa/%	No
	9	CU	Con	195	0.806	0.806	138	178	1.29	Reached steady state	No
	10	CU	Con	400	0.812	0.812	144	187	1.29	$\delta(\Delta u)/\delta\varepsilon_a$ = 1 kPa/%	No
	11	CU	Con	295	0.808	0.808	77	101	1.30	$\delta(\Delta u)/\delta\varepsilon_a$ = -0.8 kPa/%	No
	12	CD	Con	165	0.834	0.802	285	368	1.29[d]	$\delta\varepsilon_v/\delta\varepsilon_a$ = 0.02	Yes
	13	CD	Con	290	0.829	0.773	502	648	1.29[d]	$\delta\varepsilon_v/\delta\varepsilon_a$ = 0.03	Yes
81/63	14	CU	Con	400	0.885	0.885	326	408	1.25	$\delta(\Delta u)/\delta\varepsilon_a$ = -4 kPa/%	Yes
	15	CU	Con	400	0.889	0.889	335	419	1.25[d]	$\delta(\Delta u)/\delta\varepsilon_a$ = -5 kPa/%	Yes
	16	CU	Con	400	0.891	0.891	335	415	1.24	$\delta(\Delta u)/\delta\varepsilon_a$ = -5 kPa/%	Yes
	17	CU	Con	400	0.916	0.916	119	146	1.23	Reached steady state	No
	18	CD	Con	260	0.920	0.879	448	568	1.27	$\delta\varepsilon_v/\delta\varepsilon_a$ = -0.03	No
	19	CU	Con	400	0.914	0.914	175	215	1.23	$\delta(\Delta u)/\delta\varepsilon_a$ = -3 kPa/%	Yes
	20	CD	Con	140	0.947	0.892	239	303	1.27	$\delta\varepsilon_v/\delta\varepsilon_a$ = -0.01	No

Notes: a) Con = contractive, Dil = dilatant; b) p'_c = consolidation stress; c) e_c = post-consolidation void ratio; d) M estimated as the average M value of the other tests done on the same mix.



Figure 7.1 Nonstandard (450 mm diameter) and standard (200 mm diameter) sieves.

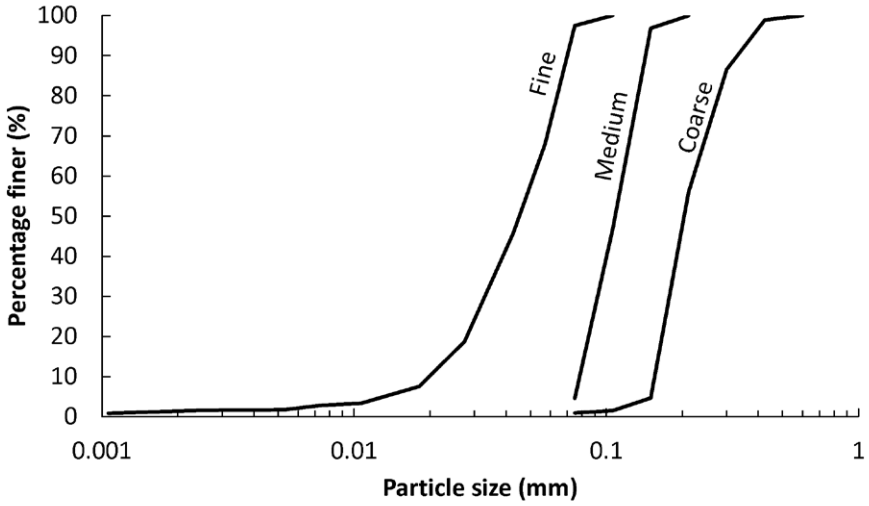


Figure 7.2 GSD curves of the fine, medium, and coarse categories into which the Impala tailings were initially separated.

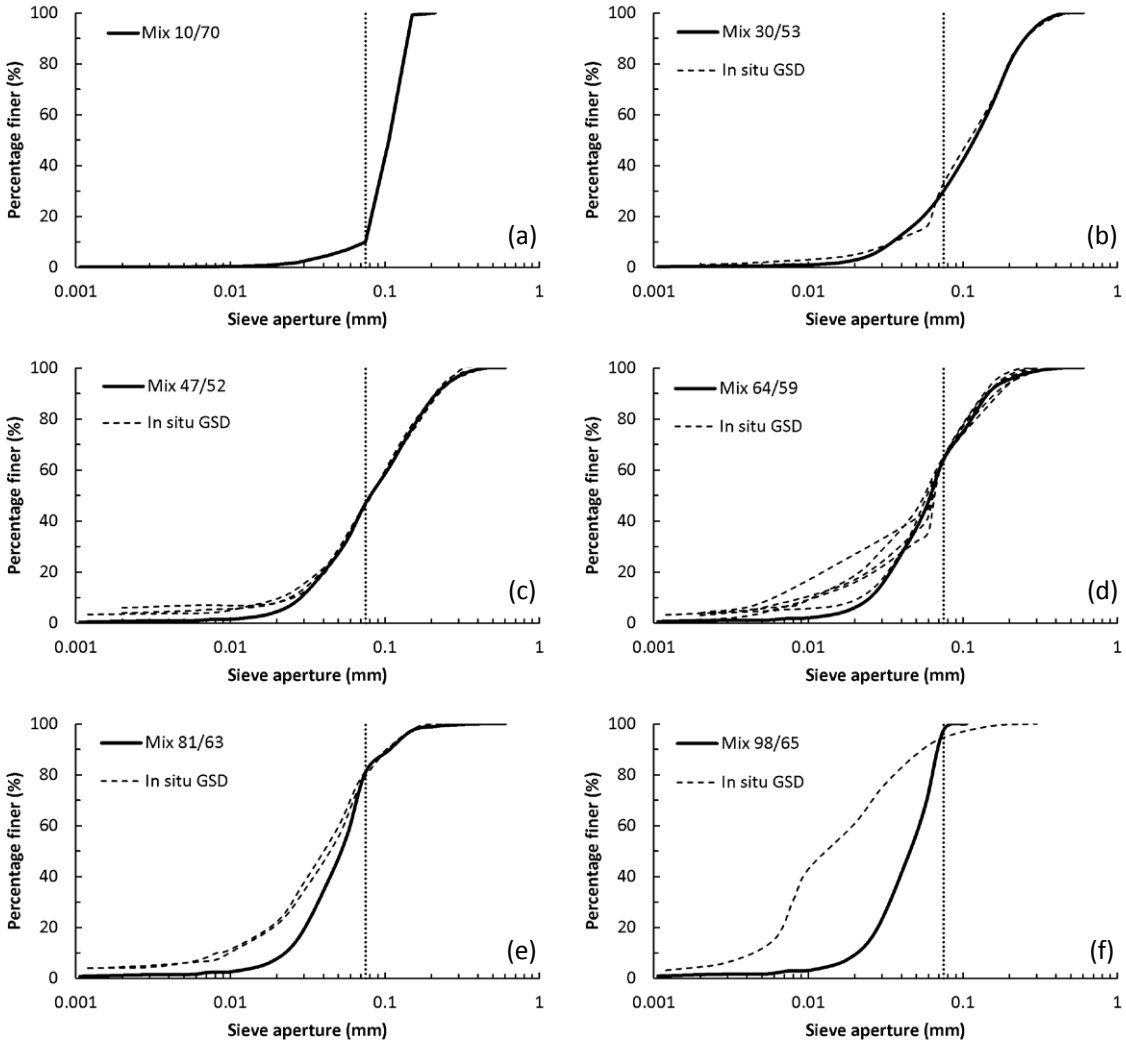


Figure 7.3 GSDs of laboratory mixes and in situ samples of Impala tailings. Note: Vertical dotted line indicates sieve aperture = 75 µm. In situ GSD curves were extracted from Figure 3.22.

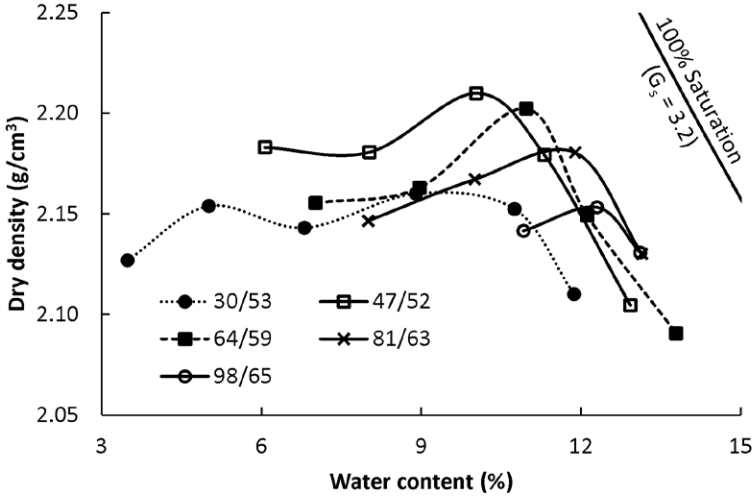


Figure 7.4 Compaction curves from the modified Proctor procedure - ASTM D1557.

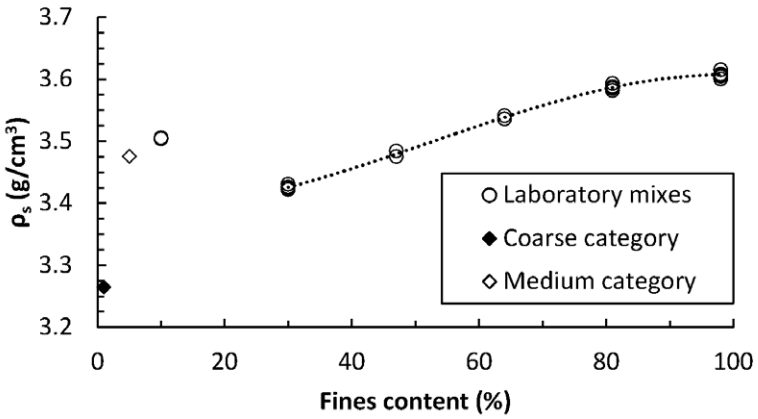


Figure 7.5 Particle density (ρ_s) of the different soiltypes used in the experimental programme.

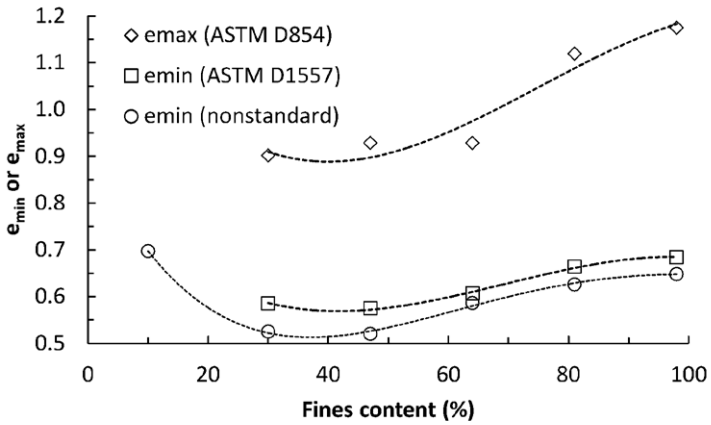


Figure 7.6 Void ratio limits of Impala tailings.



Figure 7.7 Equipment used to conduct nonstandard e_{min} determinations: a) compaction mould, b) extension sleeve, c) overburden weight, and d) rubber mallet.

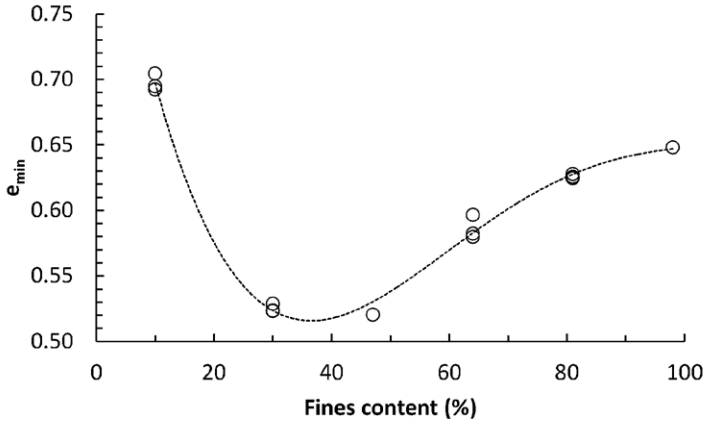


Figure 7.8 Repeatability of the nonstandard procedure to determine e_{min}.

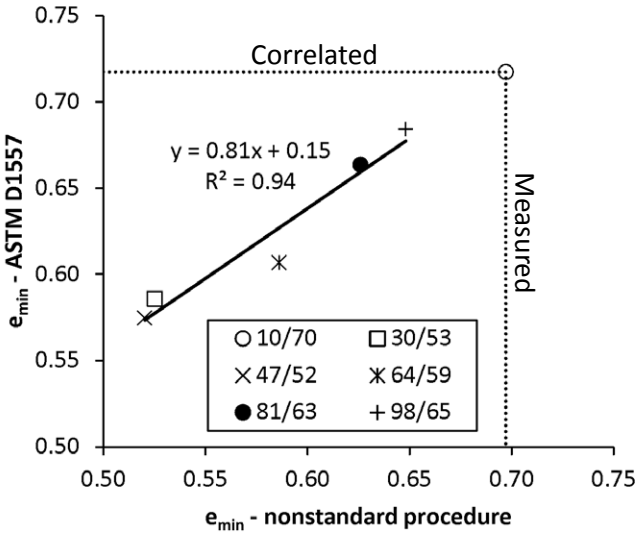


Figure 7.9 Correlation between e_{min} values obtained using the nonstandard procedure and using ASTM D1557.

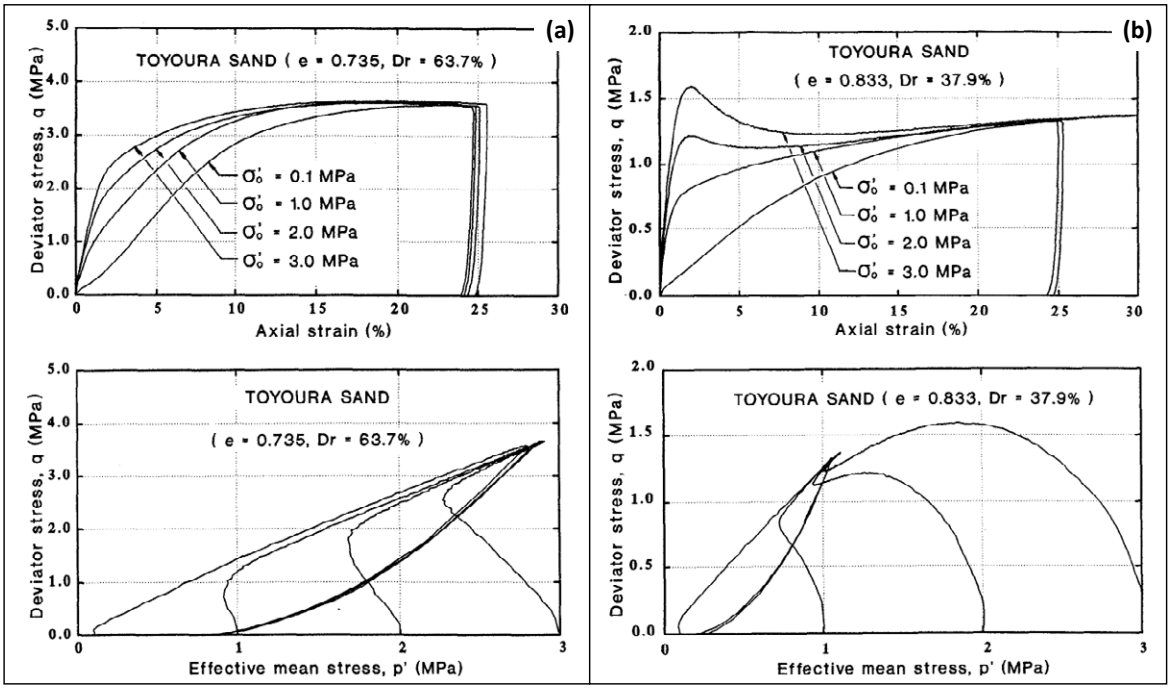


Figure 7.10 Mechanical responses reported by Verdugo and Ishihara (1996) for undrained triaxial tests. a) Dilatant response, b) contractive response in curves labelled σ'_o = 3.0 MPa and σ'_o = 2.0 MPa.

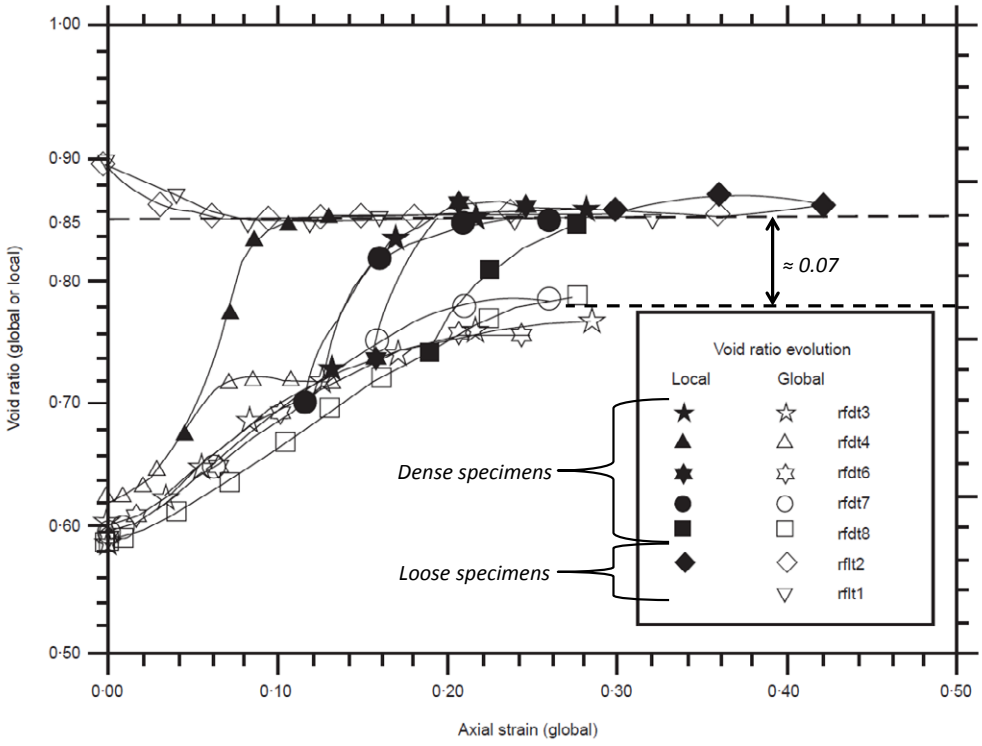


Figure 7.11 Comparison between local and global void ratios measured using computer tomography (Desrues et al. 1996). Note: Annotations in italic were added in the current work.

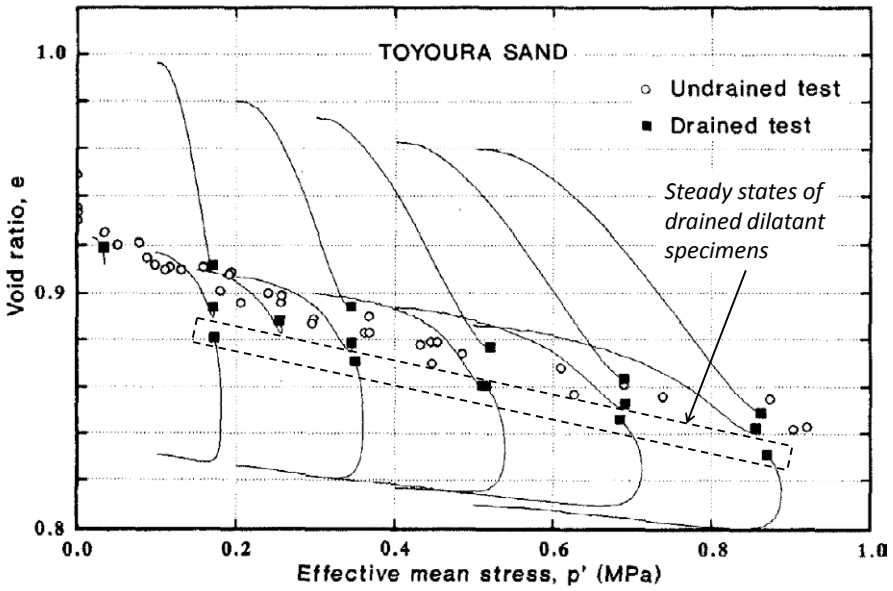


Figure 7.12 The SSL of Toyoura sand defined by drained and undrained triaxial tests. Note: Annotation in italic was added in the current work.

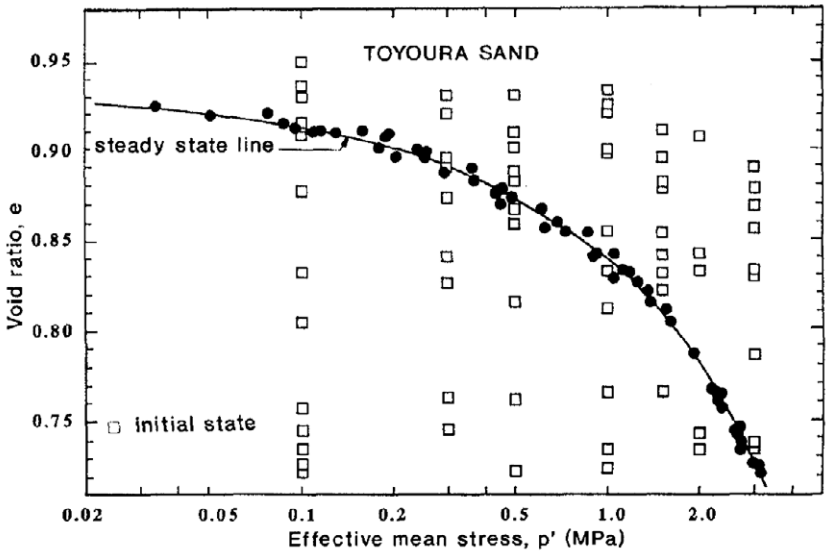


Figure 7.13 Steady state line defined from contractive and dilatant specimens tested under undrained conditions (Verdugo and Ishihara 1996).

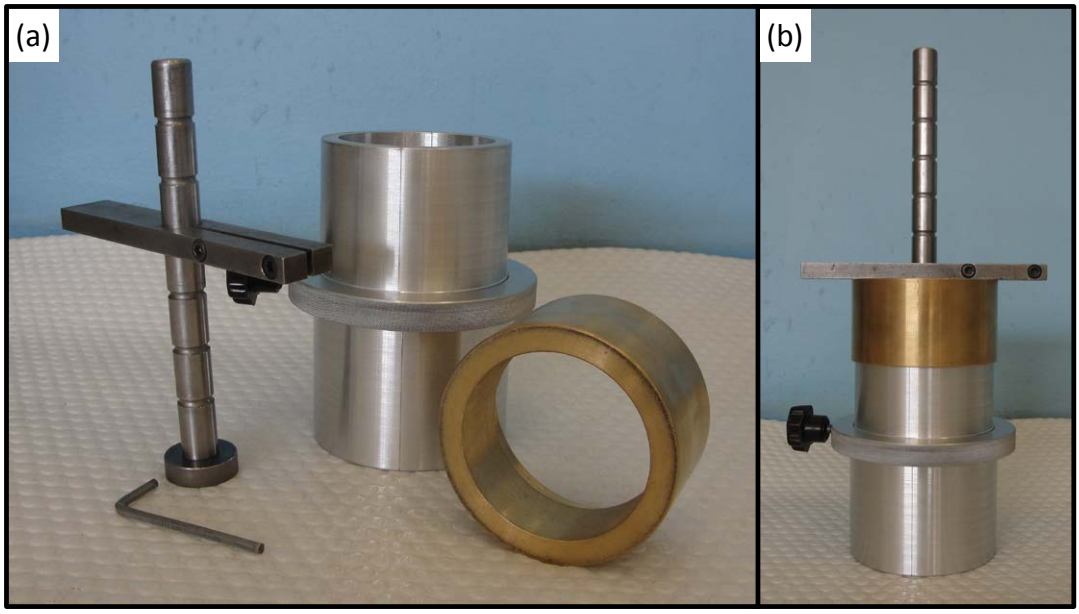


Figure 7.14 a) Instruments used to tamp the triaxial test specimens. b) Setup adopted when tamping.

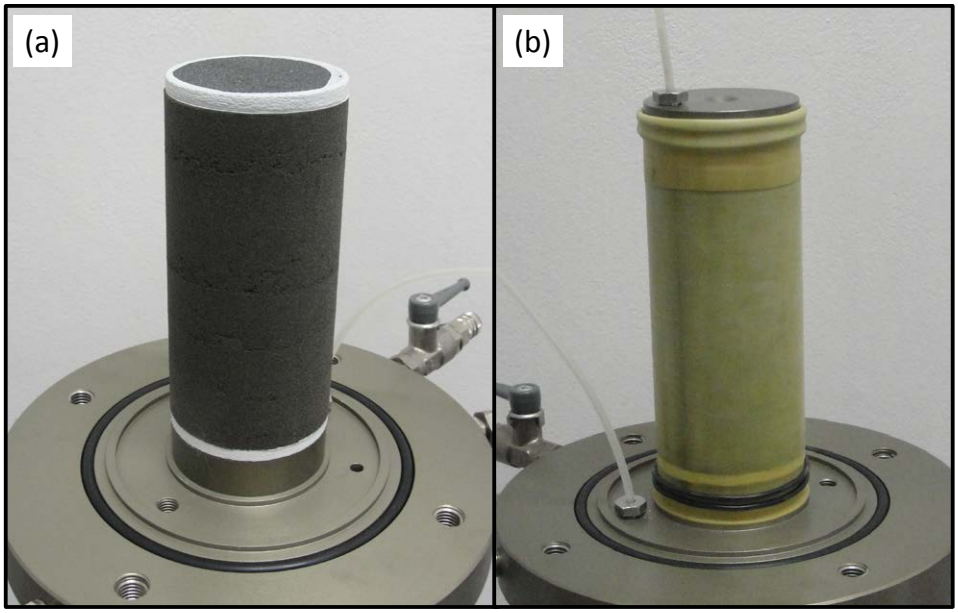


Figure 7.15 Specimen on the base of the triaxial cell.



Figure 7.16 Triaxial testing Setup 1: automated system.

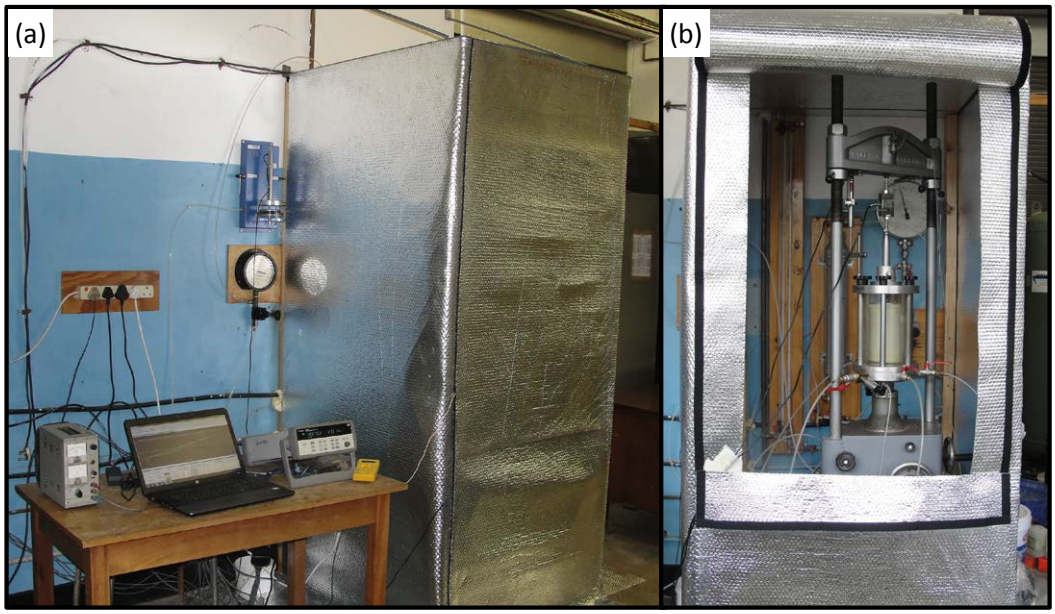


Figure 7.17 Triaxial testing Setup 2. a) Temperature control booth closed and on table: power supply for transducers, laptop computer, and data logger. b) Temperature control booth open with triaxial cell inside.

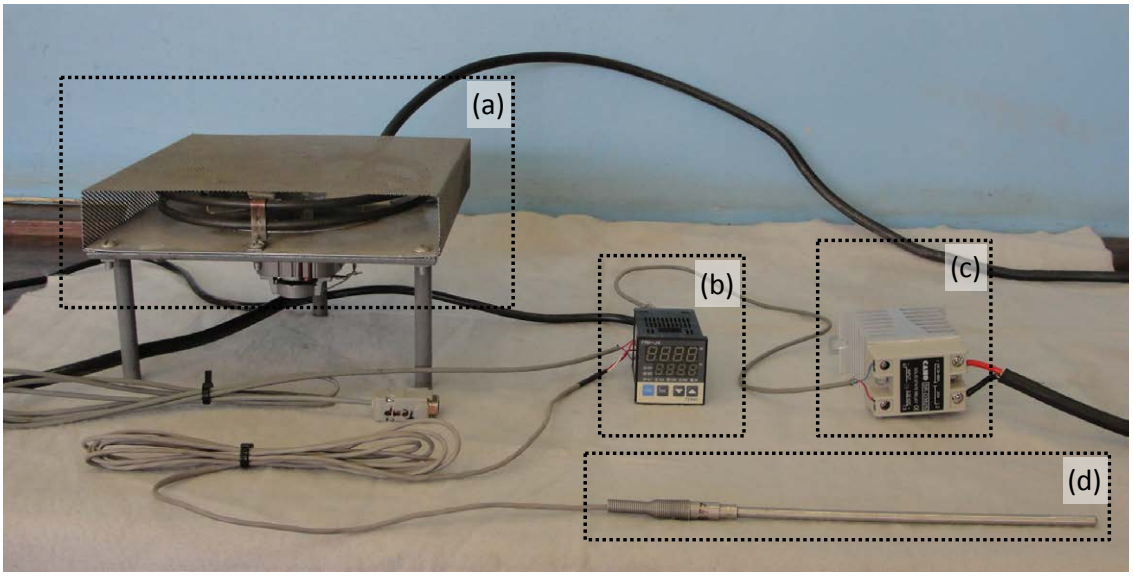


Figure 7.18 Components of the temperature control system used in setup 2: a) fan heater, b) temperature controller, c) Solid state relay, d) thermocouple.

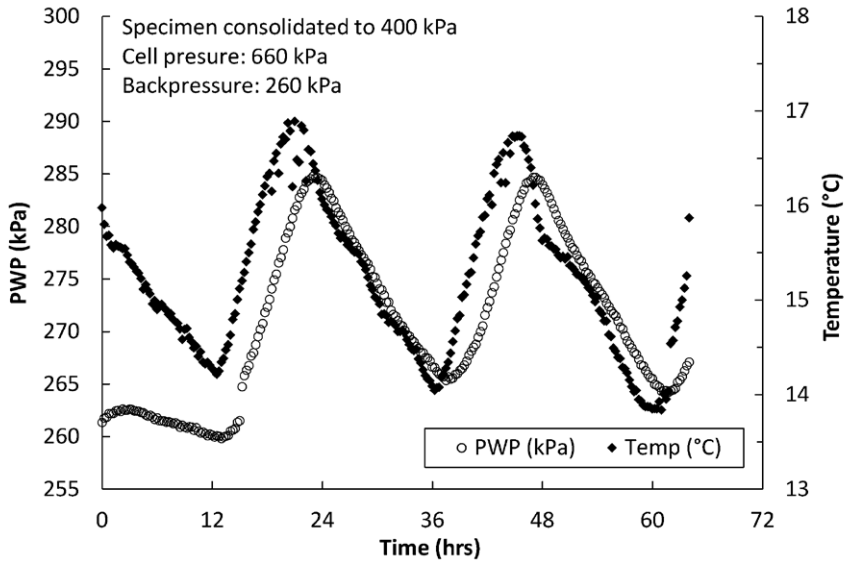


Figure 7.19 Temperature effects on PWP readings under undrained conditions.

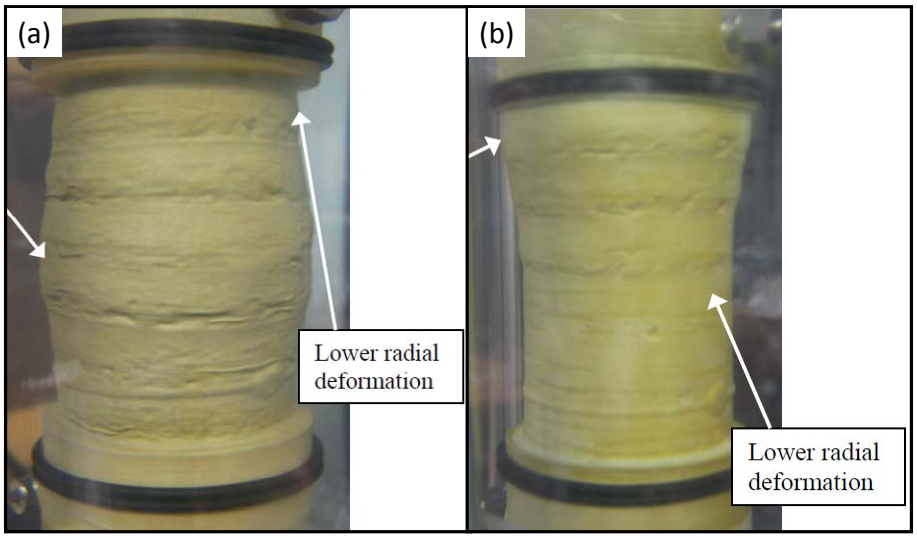


Figure 7.20 Non-uniform radial strains in specimens tested with enlarged and lubricated end platens. Original pictures from Rees (2010).

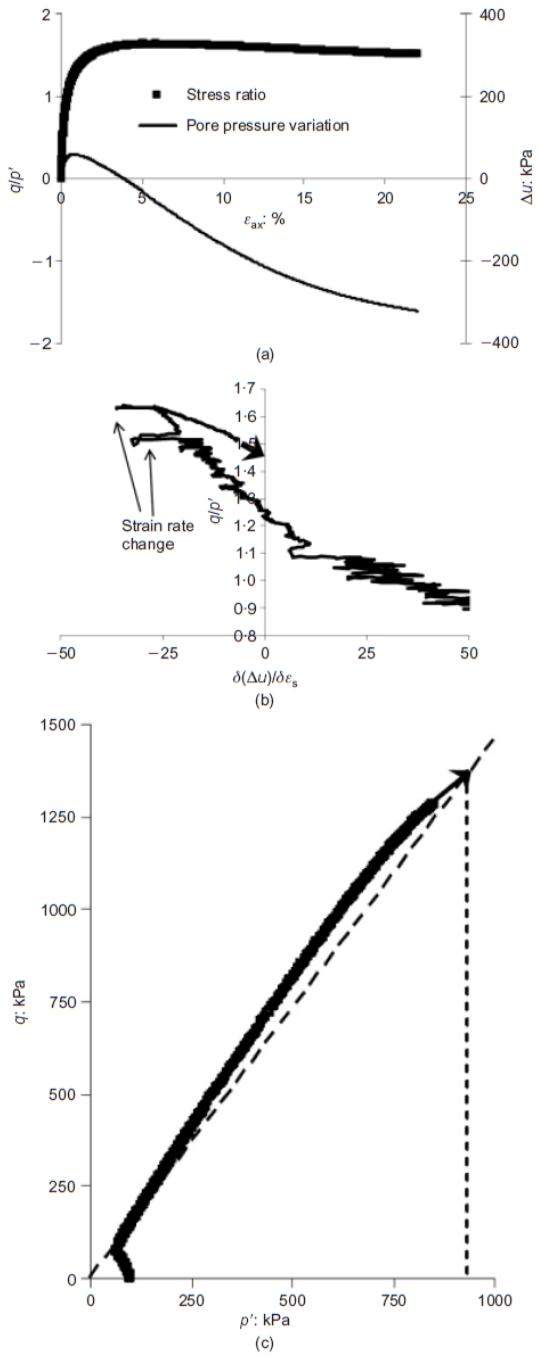


Figure 7.21 Extrapolation scheme to infer the steady state values of p' and q (Carrera et al. 2011).

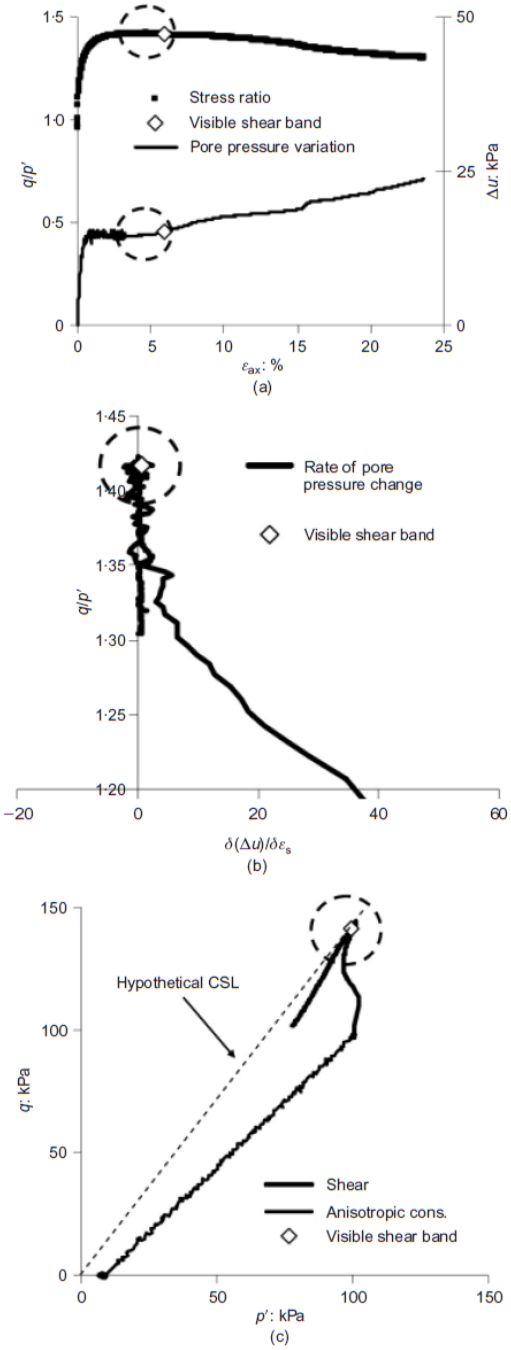


Figure 7.22 Accounting for shear bands in the estimation of steady state values of p' and q (Carrera et al. 2011).

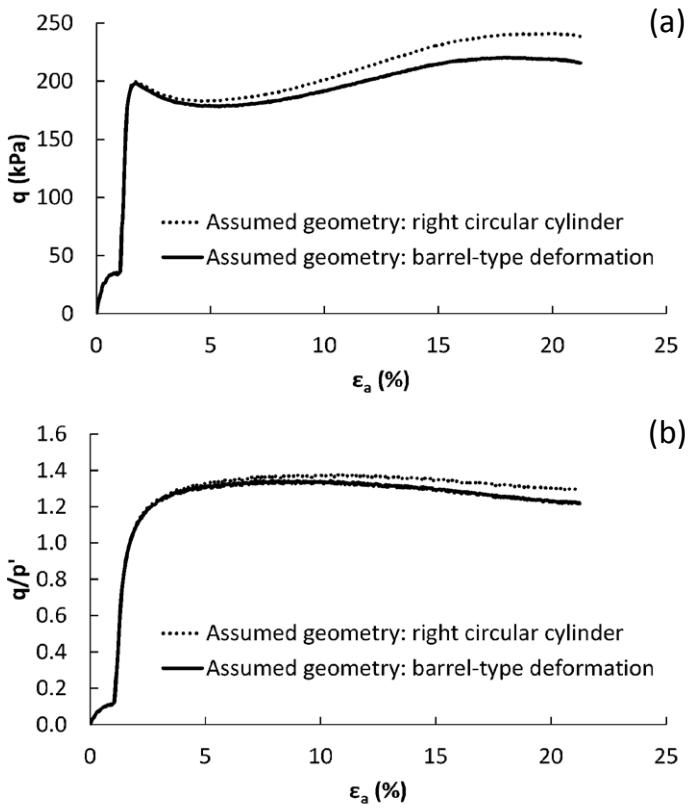


Figure 7.23 Deviator stress and q/p' values calculated with Eq. 7.6 (right circular cylinder) and with Eq. 7.7 (barrel-type deformation). Results correspond to Test 1.



Figure 7.24 Typical barrel-like geometry of sheared specimens.

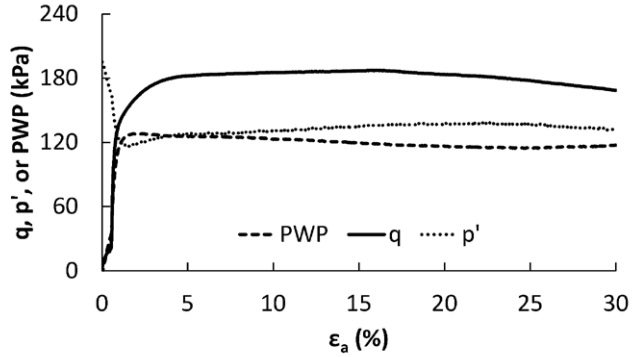


Figure 7.25 Results of a CU triaxial test on mix 30/53 (Test 9) in which the steady state was reached.

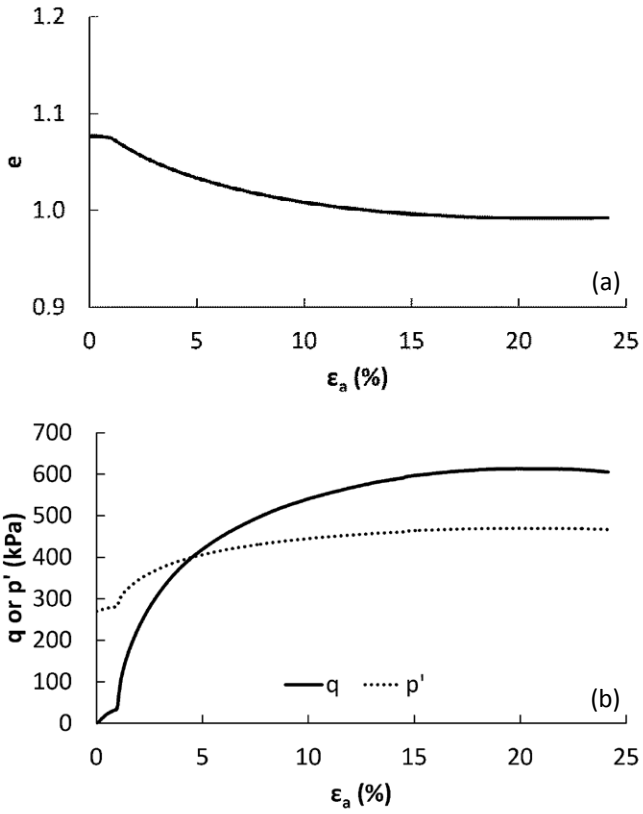


Figure 7.26 Results of a CD triaxial test on mix 10/70 (Test 5) in which the steady state was reached.

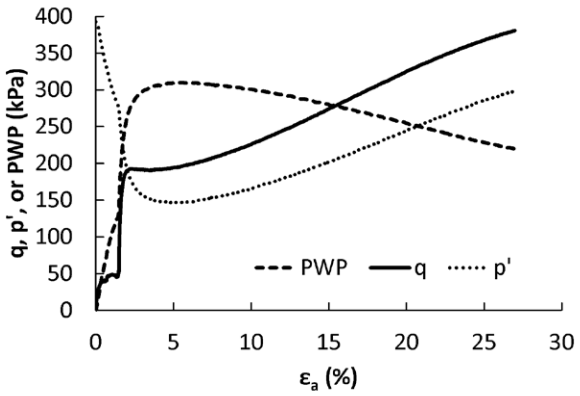


Figure 7.27 Results of a CU test on mix 81/63 (Test 14) in which the steady state was not reached.

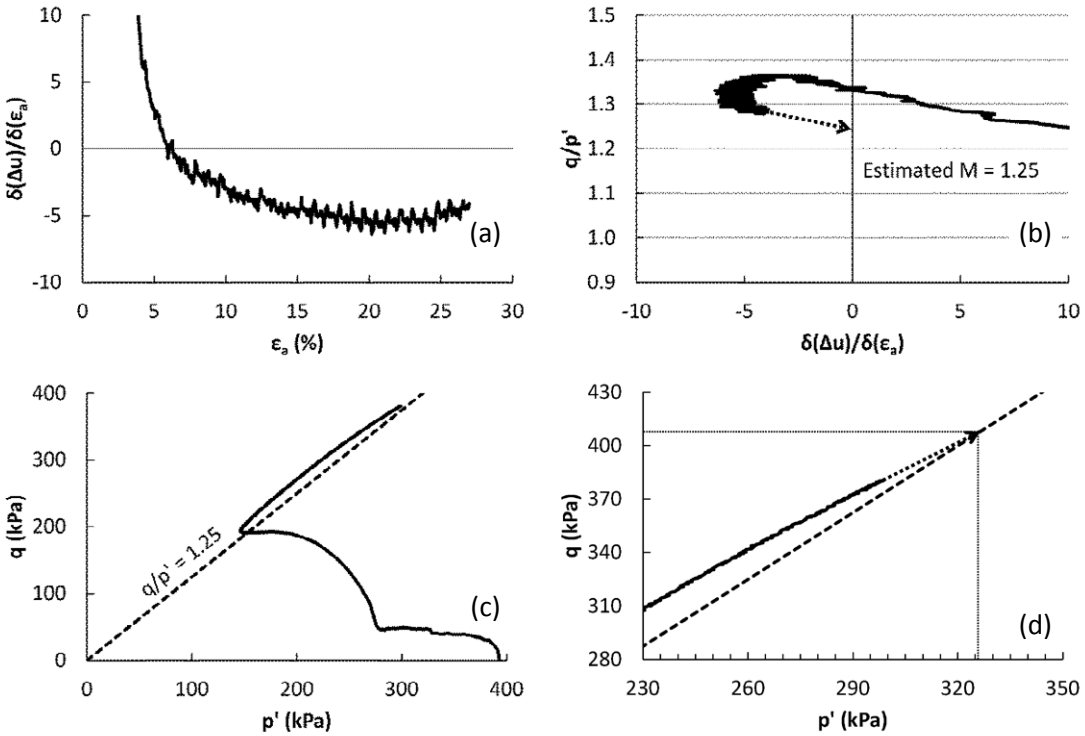


Figure 7.28 Implementation of the extrapolation method suggested by Carrera et al. (2011) on a CU test on mix 81/63 (Test 14).

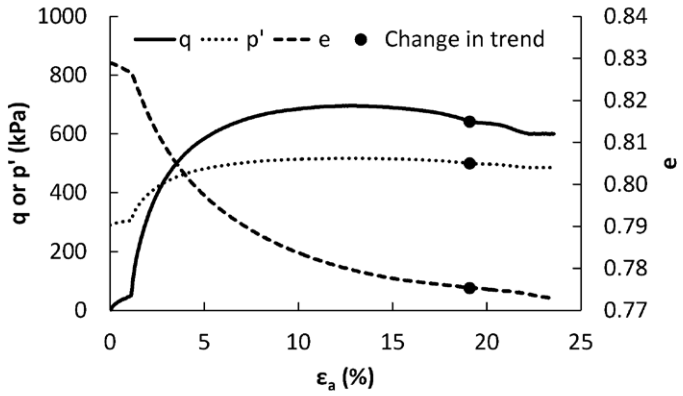


Figure 7.29 Results of CD test on mix 30/53 (Test 13) in which a shear band developed.



Figure 7.30 Development of a shear band during Test 13.

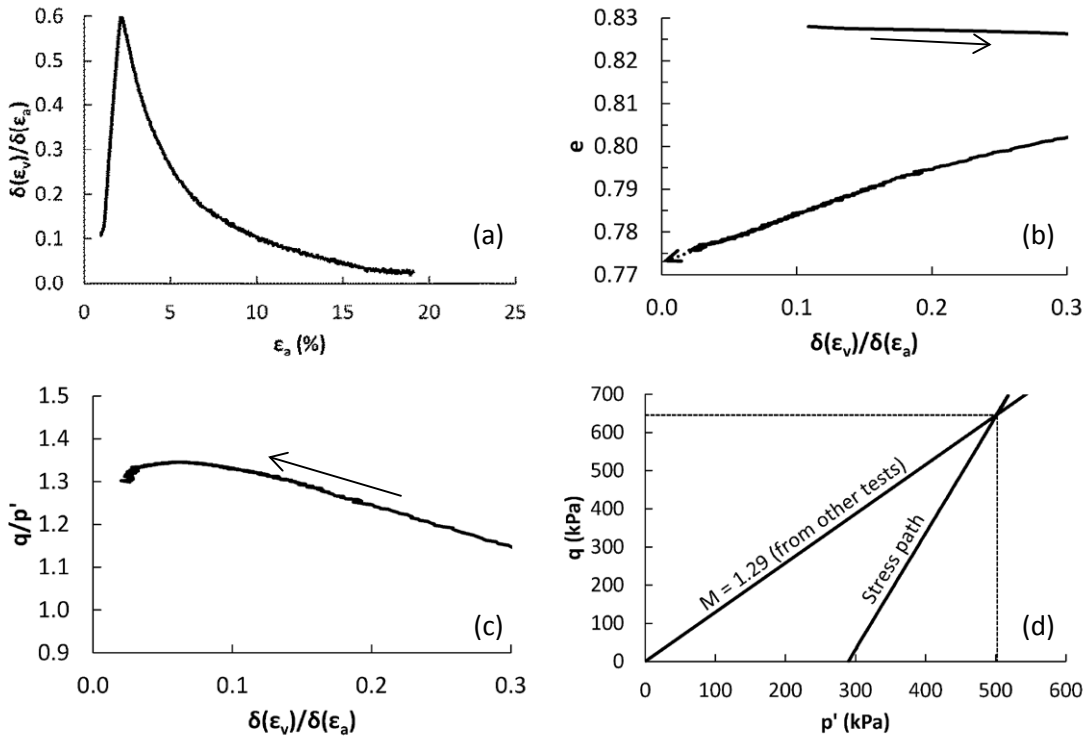


Figure 7.31 Implementation of extrapolation procedure on a CD test of mix 30/53 (Test 13). Notes: Arrows in parts (b) and (c) indicate direction of shear. M value indicated in part (d) was measured in triaxial tests on the same soiltype.

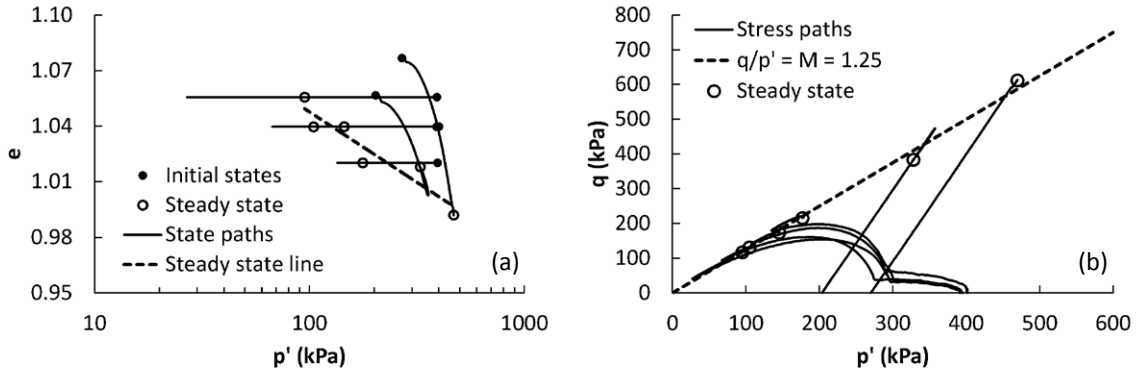


Figure 7.32 State and stress paths of the triaxial tests on mix 10/70.

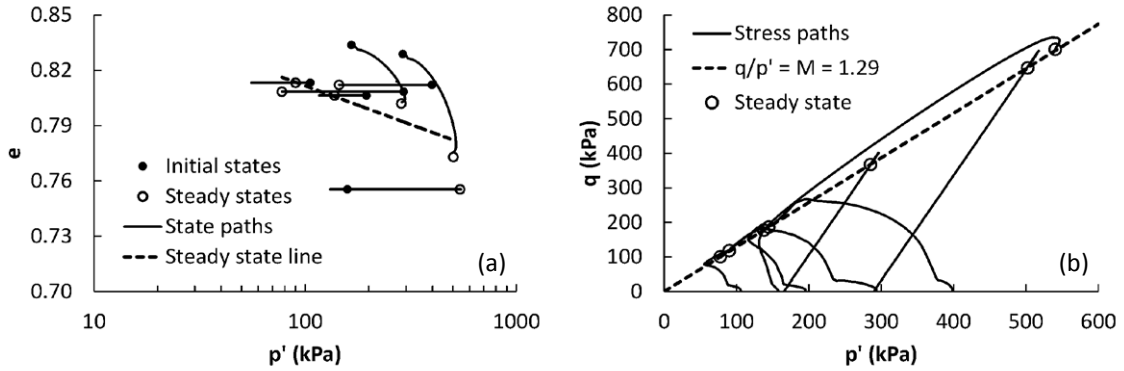


Figure 7.33 State and stress paths of the triaxial tests on mix 30/53.

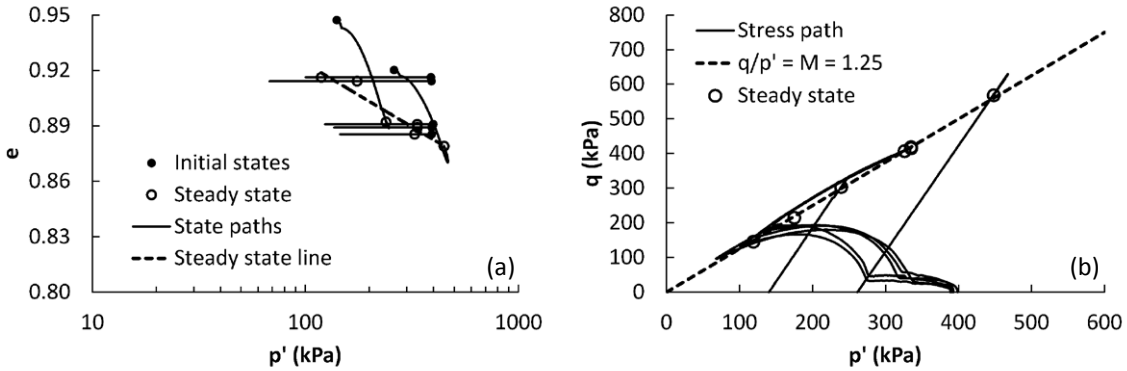


Figure 7.34 State and stress paths of the triaxial tests on mix 81/63.

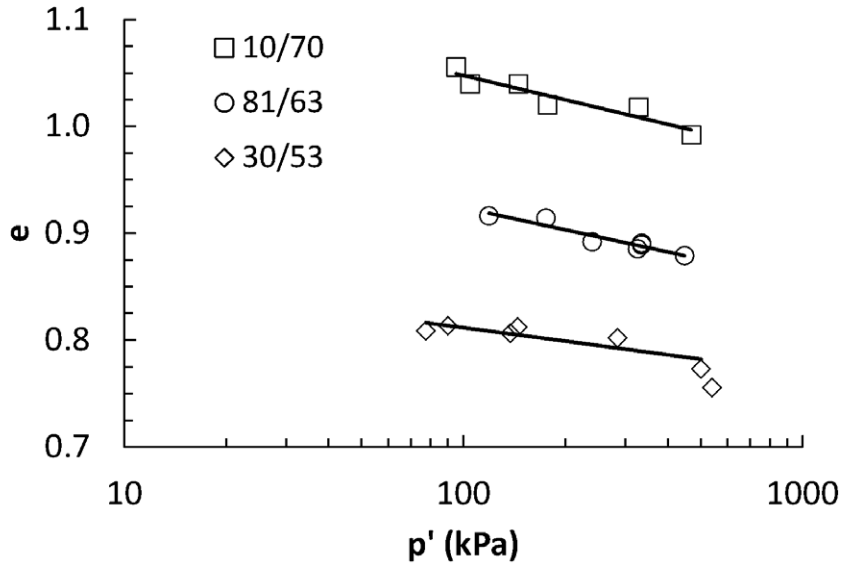


Figure 7.35 SSLs of Impala tailings in e-p' space with best fits of the form of Eq. 2.1.

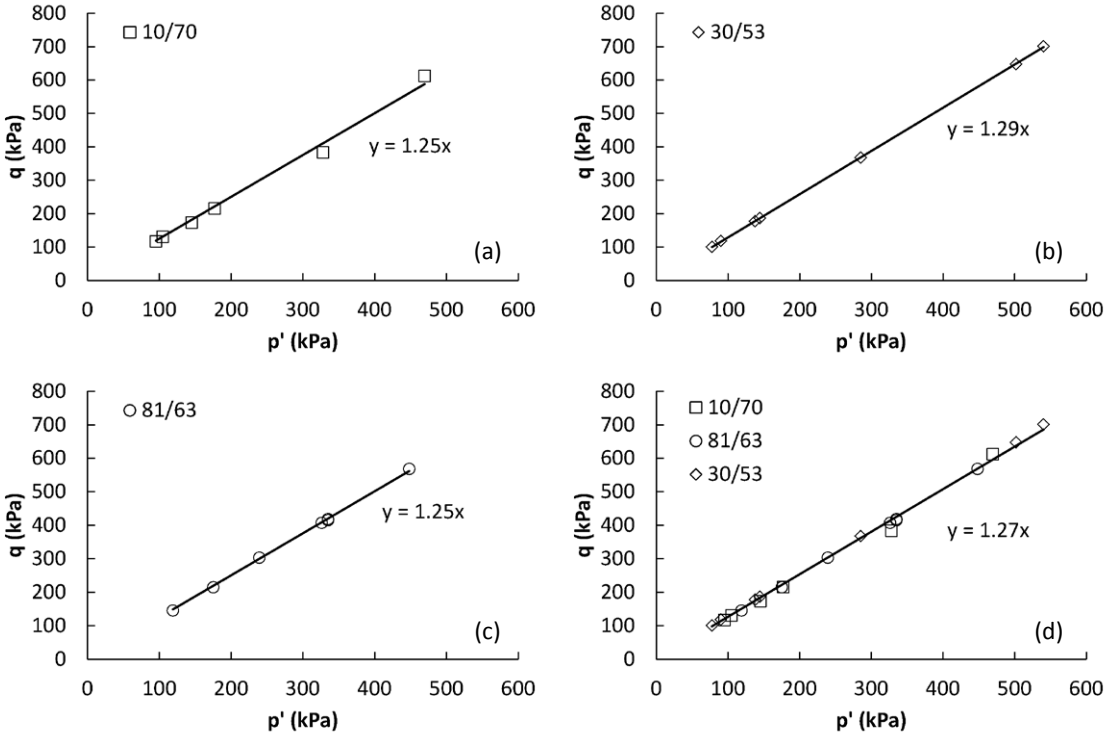


Figure 7.36 SSLs in q-p' space of Impala platinum tailings.

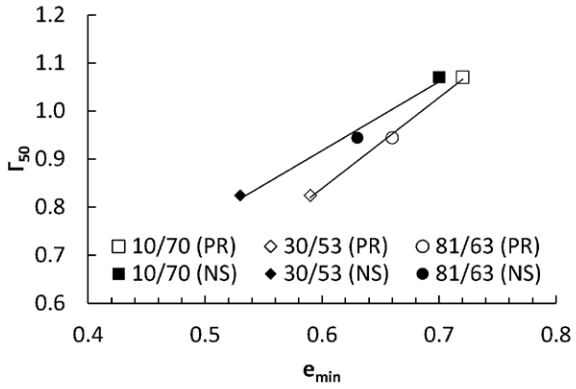


Figure 7.37 Γ_{50} vs e_{min} plot of Impala platinum tailings. Note: The code in parenthesis indicates e_{min} method. PR = Modified Proctor (ASTM D1557), and NS = Nonstandard method (Section 7.2).

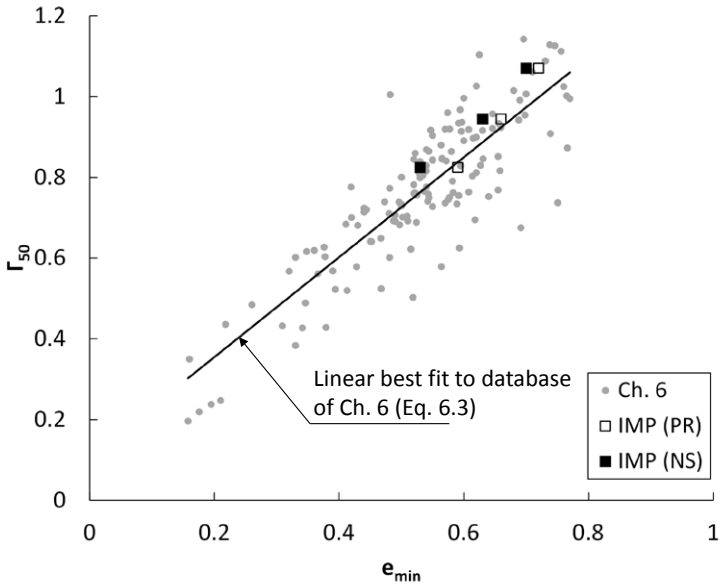


Figure 7.38 Γ_{50} vs e_{min} data points of Impala platinum tailings compared with the database of non-plastic soils from Chapter 6. Note: IMP stands for Impala tailings.

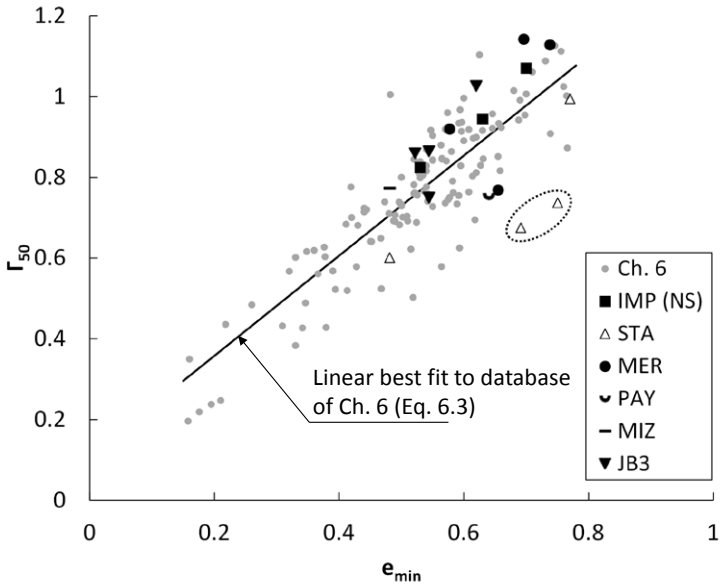


Figure 7.39 Γ_{50} vs e_{min} data of tailings compared with the database of non-plastic soils from Chapter 6. Note: Soiltypes in the legend are abbreviated as per Table 6.2.

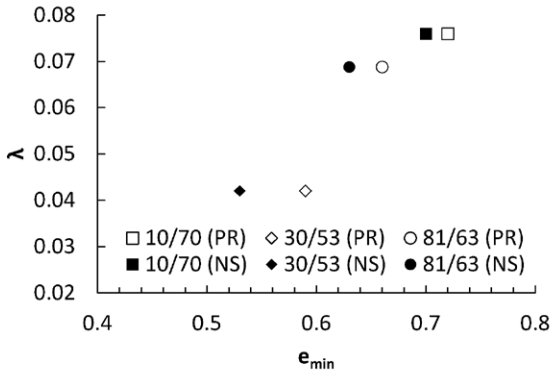


Figure 7.40 λ vs e_{min} plot of Impala platinum tailings.

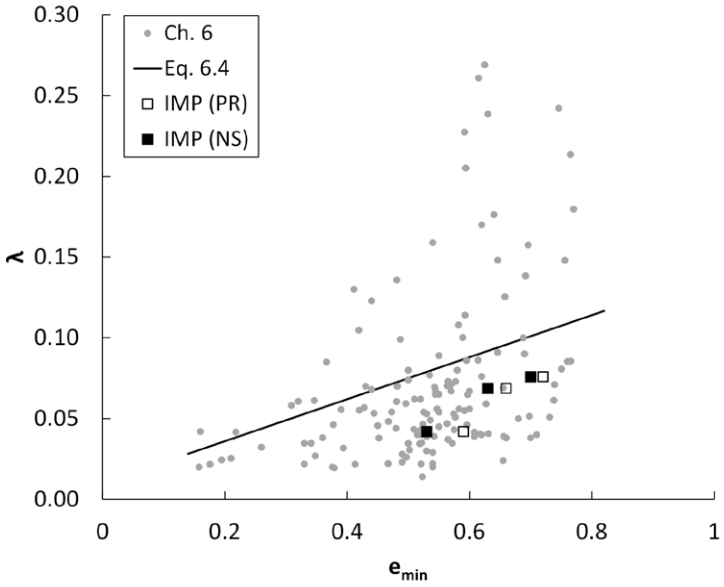


Figure 7.41 λ vs e_{min} data points of Impala platinum tailings compared with the database of non-plastic soils from Chapter 6.

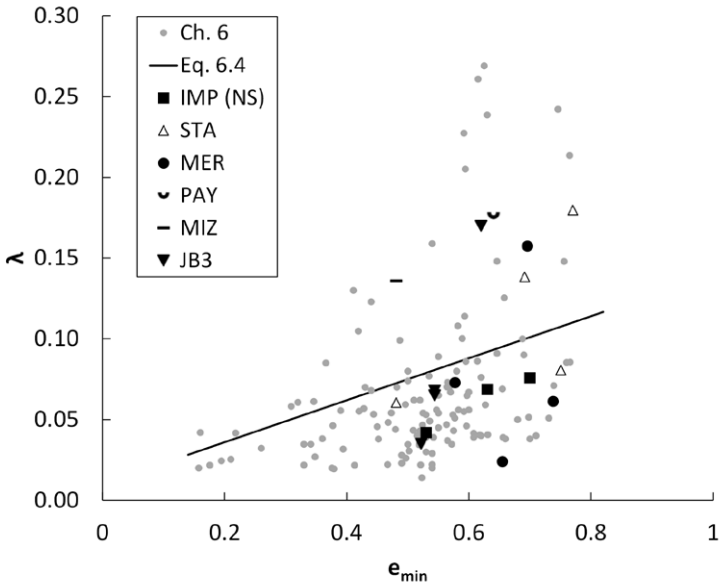


Figure 7.42 λ vs e_{min} data of tailings compared with the database of non-plastic soils from Chapter 6.

8 Sensitivity of the state parameter to uncertainty on λ

8.1 Introduction

In order to gain the greatest advantage from the predictive power of the state parameter ψ, it is necessary to determine ψ in-situ. Jefferies and Been (2006) described an approximate method to estimate ψ in-situ from CPTu data measured under both drained and undrained conditions. Equations 2.45 to 2.47 summarise the main calculations of the method. Two SSL parameters are required for its implementation: the slope of the SSL in q-p' space (M) and the slope of the SSL in e-$\log_{10}$(p') space (λ). Accordingly, a difficulty arises when implementing this simplified method in a heterogeneous soil deposit such as a TSF because, in principle, both M and λ may vary throughout the deposit. As will be shown in this chapter, the variability of M typically observed in TSFs has a negligible effect on the accuracy with which ψ can be estimated. However, the variability of λ has an important effect on the outcome of Equations 2.45 to 2.47. The current chapter will explore the uncertainty in estimated values of ψ due to this variability in λ.

Several attempts have been made to correlate λ directly to CPT readings (e.g. Figure 2.14 and Figure 2.15). Nonetheless, it is known that the uncertainty introduced by estimating λ from these correlations can be significant. This was shown by Reid (2014) who analysed a database of 31 soiltypes, including natural soils and tailings, for which CPT results and λ measurements were available. The data was reduced to plots of λ vs F_r and λ vs I_c, where F_r is the sleeve friction ratio (Eq. 2.12) and I_c is the soil behaviour type index defined as either Eq. 2.11 or 2.20 (Reid used both definitions). Reid noted that although the data agreed well with previously proposed correlations, the amount of scatter implied that it was not feasible to make reliable estimations of λ based on CPT results alone (Figure 8.1 and Figure 8.2). Furthermore, Reid (2014) pointed out that some of the most noticeable outliers to the general trend of the database were mine tailings.

Reid's observations highlight the need of using SSLs determined in the laboratory to achieve reliable estimations of λ from CPT readings in TSFs. However, the correlation between the λ values obtained in the laboratory and the CPT readings made in the field is not straightforward. This is because, as discussed in Chapters 6 and 7, variations in λ of non-plastic soils can be correlated to: particle shape (Figure 6.15), grain size distribution (Figure 6.20), or limiting void ratios (Figure 7.40) which reflect the combined effect of particle shape and size. But in the literature reviewed for this thesis, no correlations were found between any of those parameters and CPT readings. Notwithstanding the absence of these correlations, the experimentally determined SSLs are useful because they provide a range within which λ is likely to vary throughout the TSF. And as will be shown in this Chapter, there are circumstances in which this range of λ is sufficiently small that the implementation of Equation 2.45 with a single average λ value does not significantly compromise the accuracy of ψ. Conversely, there are also circumstances in which the range of λ is sufficiently large that the use of a single average λ value will significantly compromise the accuracy of ψ. Clearly, it is desirable to establish with certainty how the variability of λ within a TSF will affect the accuracy of ψ estimations based on Equation 2.45 and the current literature does not offer a quick way of

achieving this. Accordingly, the main objective of this chapter is to quantify the sensitivity of ψ to the variability of λ under conditions typical of non-plastic tailings impoundments. Estimations of ψ are known to also be sensitive to variations in the effective horizontal stress (σ'_h) as it is required to calculate Q_p (Eq. 2.17). The importance of these variations in (σ'_h) has been previously reported elsewhere (Jefferies et al. 1987) and will not be discussed herein.

The remainder of the chapter will be divided into two main sections. The first section (8.2) will present the sensitivity of ψ, as estimated from Equation 2.45, to variations in λ. Additionally, SSL and CPT data corresponding to five TSFs will be used to illustrate how the implications of the variability of λ can be significantly different from one case to the other. The second section (8.3) will present observations regarding the GSD curves of samples collected at the Impala and Merriespruit TSFs which indicate a correlation between FC and the overall shape of the GSD curve. On the basis of this observation, it is proposed that it might be possible to develop site-specific correlations between e_{min} and CPT results which, together with SSLs measured in the laboratory, allow improved estimates of the variation of λ and therefore a reduced uncertainty in ψ. This improved estimation of λ can be necessary when the range over which λ varies throughout the entire TSF is too wide to allow the use of a single average λ to estimate ψ.

8.2 The sensitivity of ψ to variations in λ

8.2.1 Description of the procedure

In order to study the sensitivity of ψ to variations in λ it is convenient to rearrange Equation 2.45 so as to make ψ the subject and replace k' and m' using the expressions in Eqs. 2.46 and 2.47:

$$\psi = \frac{-1}{11.9 - 13.3\lambda} \ln\left[\frac{Q_p}{(3 + 0.85/\lambda)M\left(1 - B_q\right)}\right] \qquad 8.1$$

The uncertainty on ψ due only to variations in λ will be referred to as $\Delta\psi_\lambda$. If the uncertainty on λ (Δλ) is small compared to the values of λ, then $\Delta\psi_\lambda$ can be calculated as (Taylor 1997):

$$\Delta\psi_\lambda = \frac{\partial\psi}{\partial\lambda}\Delta\lambda = \left[\frac{17}{20\lambda^2(13.3\lambda - 11.9)(0.85\lambda + 3)} - \frac{133ln(A/(3 + 0.85/\lambda))}{10(13.3\lambda - 11.9)^2}\right]\Delta\lambda \qquad 8.2$$

where $A = Q_p/[M(1\text{-}B_q)]$. Careful inspection of Eq. 8.2 provides useful insights into the sensitivity analysis by anticipating that $\Delta\psi_\lambda$ is inversely correlated to Q_p and λ. However, Eq. 8.2 was not used in the subsequent sensitivity analysis because the values of Δλ considered herein were not always small when compared to λ and in some cases the situation Δλ > λ was considered.

Having ruled out the possibility of using Eq. 8.2, the sensitivity analysis was done as follows. A central value of λ, termed λ_c, and an uncertainty range Δλ were first chosen. Then, using Eq. 8.1, ψ was calculated for $\lambda_{min} = \lambda_c - \Delta\lambda/2$ and $\lambda_{max} = \lambda_c + \Delta\lambda/2$. The values of ψ corresponding to λ_{min} and λ_{max}

were termed $\psi_{\lambda min}$ and $\psi_{\lambda max}$, respectively. $\Delta\psi_\lambda$ was then computed as $\psi_{\lambda min}$ - $\psi_{\lambda max}$ and was always positive since, as will be shown below, for fixed values of Q_p, B_q and M there is an inverse correlation between ψ and λ. For any given value of λ_c, $\Delta\psi_\lambda$ was calculated for increasing values of Δλ until $\Delta\psi_\lambda$ reached 0.1. This upper bound for $\Delta\psi_\lambda$ was adopted because it is equal to the intrinsic uncertainty of Eq. 2.45, estimated as follows. Jefferies and Been (2006) reported an error of ±0.05 at 90% confidence when inferring ψ from Eq. 2.42. They did not report the uncertainty associated with Eq. 2.45, but considering the common framework of Eqs. 2.42 and 2.45, it was assumed herein that the ψ values estimated from Eq. 2.45 also have an intrinsic uncertainty of ±0.05, which is equivalent to a ψ range of 0.1.

The value of $\Delta\psi_\lambda$ depends on Q_p, B_q, λ, and M (Eq. 8.2). It is thus necessary to estimate magnitudes of these values that can be expected in non-plastic TSFs to ensure that the sensitivity analysis is realistic. The soil behaviour type classification chart proposed by Robertson (1991) (Figure 2.6b) suggests that Q can vary from 1 to 1000 and that this range covers virtually the entire spectrum of soil types. Due to the similarity in the definitions of Q and Q_p (Eqs. 2.15 and 2.17), it is reasonable to expect that Q_p will also vary over a similarly wide range. Not all of this range may be typical of TSFs, however, a Q_p from 1 to 1000 varying in increments of half $\log_{10}$ cycles was chosen herein to adequately illustrate the dependence of the sensitivity analysis on Q_p. Regarding B_q, a credible range for non-plastic tailings is 0 to 0.2 (Table 8.1), so the analysis was conducted for both of these extreme values. The range of λ_c can be estimated as 0.02 to 0.2 (Figure 7.42 and Table 8.1) and the entire range was considered in increments of 0.02. Finally, the range for M can be estimated as 1.2 to 1.5 (Table 8.1) and the analysis was performed for a single average value of 1.35. The adoption of a single average M value is justified below.

The general trend of Eq. 8.1 is that for given values of Q_p, B_q and M, there is an inverse correlation between ψ and λ. This trend is consistent with the natural expectation that if two soils with different compressibility exhibit the same M, and mobilise the same effective penetration resistance $Q_p/(1-B_q)$, then the softer soil must exist at a lower ψ to compensate for its greater compressibility (i.e. higher λ). Nonetheless a deviation from this expected trend occurs at low values of Q_p and relatively high values of λ. This is illustrated in Figure 8.3 in which, for Q_p = 1, Eq. 8.1 yields ψ values that initially decrease as λ increases from zero, but then increase slightly when λ exceeds approximately 0.23. It is noted that although this slight increase in ψ is inconsistent with real soil behaviour, it occurs at λ values greater than 0.2 which are atypical of tailings (Figure 7.42). Furthermore, Figure 6.31b shows that the only non-plastic soils for which λ > 0.2 has been measured are the Ardebil sand-silt mixes which were reported by Naeini and Baziar (2004) and, as noted in Section 6.4.1, these are unusually high values. Accordingly, the slight increase in ψ with increasing λ observed in Figure 8.3 does not seem to affect the type of soils (non-plastic) for which the state parameter concept, and thus Eq. 8.1, was developed. Notwithstanding, for completeness of the sensitivity analysis presented herein, λ > 0.2 had to be considered in some cases and accordingly, Eq. 8.1 was modified to avoid an unrealistic increase in ψ at large values of λ. In the modified version of Eq. 8.1, ψ was prevented from increasing at large values of λ, and instead was made equal to the

minimum value of ψ (Figure 8.3). It is noted in Figure 8.3 that the slight increase in ψ is not observed for medium and high values of Q_p (e.g. Q_p >≈ 10).

8.2.2 Resulting values of $\Delta\psi_\lambda$

Figure 8.4 and Figure 8.5 show the results of the sensitivity analysis for values of B_q = 0 and B_q = 0.2, respectively. The following numerical example further clarifies how the data was generated: Adopting Q_p = 10, B_q = 0, M = 1.35, λ_c = 0.1, and $\Delta\lambda$ = 0.05; thus λ_{min} = 0.1 - 0.05/2 = 0.075 and λ_{max} = 0.1 + 0.05/2 = 0.125; and Eq. 8.1 yields $\psi_{\lambda min}$ = 0.061, and $\psi_{\lambda max}$ = 0.027. This result is reflected in Figure 8.4c as follows. Entering Figure 8.4c on the horizontal axis at $\Delta\lambda$ = 0.05, the intersection with the line for λ_c = 0.1 (labelled ψ = 0.04) gives a vertical axis value of of $\Delta\psi_\lambda$ = 0.061 - 0.027 = 0.034.

The differences between Figure 8.4 and Figure 8.5 are relatively small, so the linear interpolation of $\Delta\psi_\lambda$ for intermediate values of B_q results only in insignificant errors. Similarly, if the results of either chart are compared to the $\Delta\psi_\lambda$ values obtained when the calculations are done with M = 1.2 or M = 1.5, a maximum absolute difference of 0.006 is observed, with the average difference being a much lower 8 x 10^{-4}. Accordingly, although both figures were computed with M = 1.35, they can be used for any M value between 1.2 and 1.5 with negligible loss in accuracy. As shown in part (a) of Figure 8.4 and Figure 8.5, each line of the plots corresponds to a constant value of λ_c. Since Q_p, B_q, and M are constant for each line, then there is also a unique value of ψ that can be associated with each line through Eq. 8.1. This ψ value, which falls between $\psi_{\lambda min}$ and $\psi_{\lambda max}$, is indicated in Figure 8.4 and Figure 8.5.

In agreement with Eq. 8.2, Figure 8.4 and Figure 8.5 show that, regardless of Q_p, for any given $\Delta\psi_\lambda$ a larger λ_c allows for a greater uncertainty $\Delta\lambda$. This is reasonable as there is a decrease of the relative importance of $\Delta\lambda$ as λ_c increases. This trend is hardly noticeable for values of $Q_p \geq 320$ and $\lambda_c \geq 0.16$. In these cases the value of $\Delta\psi_\lambda$ that corresponds to a given value of $\Delta\lambda$ is largely independent of λ_c. This is reflected in parts (f) and (g) of the figures, as the “indistinguishable” lines. It is also noted that, again In agreement with Eq. 8.2, for fixed values of $\Delta\lambda$ and λ_c there is a direct correlation between Q_p and $\Delta\psi_\lambda$. From a practical point of view this is a positive feature, as it means that for a fixed $\Delta\lambda$, the weaker soils (lower Q_p) can be assessed with a greater accuracy than the stronger soils (higher Q_p). Finally, it is observed that as Q_p increases, the correlation between $\Delta\psi_\lambda$ and $\Delta\lambda$ becomes more linear. This increase in linearity is particularly noticeable for the higher values of λ_c.

Five TSFs for which at least two SSLs were experimentally determined were found in the literature and are listed in Table 8.1. For four of these five TSFs values of B_q were also available. $\Delta\psi_\lambda$ at different Q_p levels was determined for these five TSFs to assess the significance of the variability of λ throughout the deposit. However, it must be noted that the $\Delta\lambda$ reported for each TSF in Table 8.1 does not necessarily correspond to the actual in-situ range. For example, in the case of the Merriespruit TSF, Fourie and Papageorgiou (2001) explicitly stated reasons for not calculating the SSLs representative of the entire range of gradations known to be present in the TSF. Furthermore, their experimental programme included two gradations that were known not to be representative of the in-situ gradations. This is analogous to the use of soiltype 10/70 in Chapter 7 of this thesis.

Similarly, for the Australian Gold Tailings and the Molybdenum Tailings, it is unknown whether the range of λ reported by Reid (2014) covers the entire range of in-situ values. Accordingly, the values of Δλ reported in Table 8.1 may be an over or underestimation of the true values. Despite these uncertainties, it will be assumed herein that although these Δλ may not be real, they are at least realistic, hence justifying their use.

Figure 8.6 illustrates $\Delta\psi_\lambda$ for the five TSFs of Table 8.1. For reference, shaded areas representing the intrinsic uncertainty of Eq. 8.1 (±0.05) have also been included. In agreement with the trends observed in Figure 8.4 and Figure 8.5, the values of $\Delta\psi_\lambda$ vary with Q_p. Values of $\Delta\psi_\lambda$ at Q_p = 10 and Q_p = 320 are annotated in Figure 8.6. Average values of $\Delta\psi_\lambda$ vary widely throughout the five TSFs, from a minimum of 0.025 for the Molybdenum tailings (Figure 8.6e) to a maximum of 0.161 for the Merriespruit TSF (Figure 8.6c). That is, depending on the TSF-specific parameters, $\Delta\psi_\lambda$ can be lower or higher than the intrinsic uncertainty of 0.1. The combined total uncertainty $\Delta\psi_T$ due to both the intrinsic uncertainty and the average $\Delta\psi_\lambda$ of each TSF can then be estimated by adding these two values in quadrature (Taylor 1997):

$$\Delta\psi_T = \sqrt{0.1^2 + \Delta\psi_\lambda^2} \qquad 8.3$$

The resulting values of $\Delta\psi_T$ (Figure 8.7) indicate that in the case of the Molybdenum tailings and the Impala TSF, $\Delta\psi_\lambda$ has only a very small effect on $\Delta\psi_T$. For the other three TSFs the effects are more noticeable, with the $\Delta\psi_T$ of the Merriespruit dam being almost twice as large as the intrinsic uncertainty.

The results of the sensitivity analysis can also be used to assess the significance of the scatter reported by Reid (2014) when assessing the λ-F_r and λ-I_c correlations (Figure 8.1 and Figure 8.2). Adopting λ = 0.1 as a value representative of tailings (Table 8.1), the corresponding value of F_r suggested by the trendline in Figure 8.1 is 1%. The scatter in the data indicates that F_r = 1% can correspond to λ values ranging approximately from 0.03 to 0.22, that is, Δλ = 0.19. Figure 8.4 and Figure 8.5 show that for λ = 0.1, the uncertainty $\Delta\psi_\lambda$ due to Δλ = 0.19 is greater than 0.1 (the intrinsic uncertainty of Eq. 2.45) and therefore not within the graphs' range regardless of Q_p. Accordingly, $\Delta\psi_\lambda$ has to be estimated from the direct implementation of Eq. 8.1 with λ = 0.03 and λ = 0.22. Performing the calculations with Q_p = 32, M = 1.35, and B_q = 0, yields $\Delta\psi_\lambda$ = 0.02 - (-0.14) = 0.16. This value is similar to the value obtained for the Merriespruit TSF, and as noted above, Figure 8.7 indicates that $\Delta\psi_\lambda$ = 0.16 implies that $\Delta\psi_T$ will be almost double the intrinsic uncertainty of Eq. 8.1. Similarly, for λ = 0.1, the trendline (Eq. 2.49) in Figure 8.2 indicates I_c = 2.4. In turn, the scatter in the data indicates that I_c = 2.4 can correspond to 1/λ values ranging approximately from 3.4 to 18, i.e., λ ranging from 0.3 to 0.06, which implies Δλ = 0.24. This will result in a greater $\Delta\psi_\lambda$ than was obtained when considering Figure 8.1 and consequently a greater $\Delta\psi_T$. These results are in agreement with Jefferies and Been (2006) and Reid (2014) in that they emphasise the importance of experimentally determining the range of SSLs for high risk projects.

The exact value of $\Delta\psi_T$ that is acceptable will depend on the specific conditions under which Eq. 8.1 is being applied. However, it seems reasonable to expect that in most cases a $\Delta\psi_T$ that is twice the intrinsic error will be considered excessive. In such cases, where $\Delta\lambda$ is sufficiently large to significantly compromise the estimations of ψ if a single λ_c is used, it is necessary to estimate how λ varies along the CPT sounding. The following section highlights features of the tailings at the Impala and Merriespruit TSFS which may be useful in developing a method to make the required λ estimations.

8.3 A tentative path from CPT results to λ in TSFs

Chapters 6 and 7 presented general and case-specific experimental results which suggest a direct correlation between λ and e_{min} (Figure 6.38 and Figure 7.41). Although it was observed in Chapter 6 that the correlation λ-e_{min} was not as strong as the correlation Γ-e_{min}, the experimental results of the Impala Tailings suggest that at least in some cases a TSF-specific λ-e_{min} correlation can be established (Figure 8.8a)[1]. But even if one accepts the hypothesis that a λ-e_{min} correlation can be established for all non-plastic TSFs, there is still the challenge that the correlation is not useful to estimate λ in-situ unless e_{min} can be estimated from CPT results. And there appears to be no published method of using CPT results to estimate e_{min}.

Conversely, several authors (e.g. Cetin and Ozan (2009), Robertson and Wride (1998)) have proposed correlations to estimate fines content (FC) from CPT results and these correlations have been usefully implemented for a variety of purposes. For example, Yi (2014) presented results of a site exploration programme on a non-plastic soil in which three CPT soundings were paired with boreholes from which soil samples were extracted and had their FC determined. The distance between the CPT sounding and its corresponding borehole was approximately 2.5 m. The tip resistance (q_c) and the sleeve friction (f_s) were used to calculate FC profiles using general correlations proposed in the literature (e.g. Figure 2.5). The results of Yi (2014) (Figure 8.9) show that the predicted FC tends to underestimate the measured FC. Nonetheless, the results also show that although the correlations were not calibrated with site-specific data, the estimated FC profiles follow the same trends as the measured values. This is particularly evident for the soundings CPT-2 and CPT-3.

A similar example was reported by Boone and Freitas (2010) who developed a site-specific correlation between I_c (Eq. 2.11) and FC based on data obtained from 19 pairs of CPTu sounding and boreholes that were typically 1.5 m apart. The correlation was established by pairing the percentiles of FC and I_c, and then performing a regression on the resulting data points. As noted by Boone and Freitas (2010), despite significant over- and underestimation at certain locations, the estimated and measured FC values are generally in reasonable agreement (Figure 8.10). Similarly, Torres-Cruz (2015) also suggested a correlation between $I_{Q\text{-}Bq}$ (Eq. 5.1) and FC that involved the pairing of

[1] The λ-e_{min} correlation appears to exhibit some curvature, but considering that the data reviewed in Chapter 6 (Figure 6.31b) did not reveal any particular functional correlation between λ and e_{min}, the suggested linear fit seems adequate.

percentiles. It is noted that the validity of the approach of pairing percentiles that was adopted by Boone and Freitas (2010) and Torres-Cruz (2015) depends on the existence of an underlying correlation between the variables. Widely used CPT-based soil behaviour type charts (e.g. Figure 2.6a and Figure 5.1) suggest that such a correlation exists between FC and the relevant soil behaviour type index (I_c or $I_{Q\text{-}Bq}$). However, neither Boone and Freitas (2010) nor Torres-Cruz (2015) presented experimental data to demonstrate the existence of this correlation. It is important to note that the pairing of percentiles of any two variables can lead to an apparent correlation even in the absence of an underlying link between the two variables. In such a case the pairing of percentiles would lead to meaningless results.

In general, the results from Yi (2014), and Boone and Freitas (2010) suggest that it is feasible to estimate FC from CPT results. If that is indeed the case, the next question to address would be whether there exists a correlation between FC and e_{min}. In addressing this question it must first be recognised that e_{min} depends on both the overall shape of the GSD curve and particle shape (Biarez and Hicher 1994, Li 2013). However FC is, in principle, independent from both of these soil characteristics. This implies that a general FC-e_{min} correlation applicable over a wide variety of non-plastic soiltypes is not possible. Consequently, if an FC-e_{min} correlation is to be identified it will have to be TSF-specific.

Dependence of e_{min} on particle shape is unlikely to be of major consequence in a TSF because, given the rock crushing process from which tailings originate and their common mineralogy, two samples with similar GSD, are likely to also exhibit a similar particle shape distribution. The key issue to address then is whether FC can be correlated to the shape of the GSD curve. For this purpose, a subset of the 49 GSDs of Impala samples that were presented in Figure 3.22 were grouped according to their FC and replotted in Figure 8.11. The range of variation in FC within each group of GSDs was limited to 2%. The plots show that samples with similar FC also have a similar overall GSD. It is significant to note that the agreement between the GSD curves is better for the coarse particles (> 75μm), than for the fines. Given that the GSD of the coarse and fine fractions were determined by sieve and hydrometer analysis, respectively, the lesser agreement between the fine fractions of the GSD curves may be associated with the repeatability of hydrometer testing. It is also significant that samples within the same FC group were generally collected from very different locations of the TSF. For example, considering the four samples whose GSD curves with FC ≈ 75% are shown in Figure 8.11: one sample was collected at a distance from the outer wall of 300 m along alignment 1; two samples were collected at distances from the outer wall of 200 m and 350 m along alignment 2; and one sample was collected at a distance from the outer wall of 300 m along alignment 3 (see alignments in Figure 3.21). Thus, the correlation between FC and GSD appears to be valid regardless of the locations from which the samples were collected.

In order to explore whether this correspondence between FC and GSD is a distinctive feature of the Impala TSF or is also present in other hydraulically deposited TSFs, GSDs of samples recovered from the Merriespruit TSF (Section 3.6) were also grouped by FC. The observed trend (Figure 8.12) again leads to the tentative conclusion that GSD curves with a similar FC tend to have similar shapes. This similarity is probably because tailings originating from a single ore body are generally subjected

to the same mineral extraction processes. Consequently, any two samples within a TSF are likely to have similar values of maximum and minimum particle size (e.g. Figure 3.22). The further imposed condition of comparing GSDs with similar FC thus secures a third point of similarity between the GSD curves. Additionally, since all tailings within a single TSF are typically deposited using the same method, they are all acted upon by the same size sorting mechanisms, which may also contribute to the similarity of GSD curves with a given FC. Details of size sorting mechanisms during hydraulic deposition are discussed by Blight (2010). It is suitable to recall here that the results of Chapters 6 and 7 indicated that FC is not a good predictor of SSL parameters. Accordingly, the attention given in this section to FC estimations from the CPT is not due to the relevance of FC in and of itself, but rather on the observation that samples of Impala and Merriespruit tailings with similar FC also tend to have a similar overall GSD curve.

In an attempt to quantify the correlation between FC and shape of the GSD curve of the 49 Impala samples, the commonly used GSD descriptors, coefficient of uniformity ($C_u = D_{60}/D_{10}$) and coefficient of curvature ($C_c = D_{30}^2/(D_{60}\times D_{10})$), were plotted against FC (Figure 8.13). It is clear that neither of these parameters exhibits a correlation with FC. This lack of correlation is unsurprising when one considers that parameters such as C_u and C_c are only first-order descriptors of GSD and that neither of them is able to capture the entire shape of the GSD curve (Cubrinovski and Ishihara 2000; Muir-Wood and Maeda 2008).

Despite the lack of correlation between FC and either C_u or C_c, the qualitative observations based on Figure 8.11 and Figure 8.12 indicate that within a TSF, FC can be correlated to the overall shape of the GSD curve. Given the additional similarity in the particle shape distribution, it follows that two samples with the same FC will also have the same e_{min} and on this basis, it is possible to propose a site-specific e_{min}-FC correlation. Formal demonstration of the existence of this correlation requires the e_{min} values of the samples whose GSDs were included in Figure 8.11 and Figure 8.12. But unfortunately these e_{min} measurements are not available. Nonetheless, the arguments presented herein suggest that there is a rationale to expect the existence of a FC-e_{min} correlation and, in the opinion of the author, this hypothesis warrants further investigation.

The e_{min}-FC data points corresponding to the six laboratory mixes of Impala tailings described in Chapter 7 is shown in Figure 8.14. A correlation has been proposed using the five data points whose FC values are representative of in situ conditions (Figure 3.22). Accepting that the laboratory mixes are respresentative of the in situ soiltypes, this correlation can be used to convert an FC profile obtained from CPT results into an e_{min} profile. In turn, the e_{min} profile can be used together with the site-specific λ-e_{min} correlation derived from laboratory testing (e.g. Figure 8.8a) to obtain a profile of λ that can aid in reducing the uncertainty incurred when estimating ψ from Eq. 8.1 or from any other method that uses λ as an input. Figure 8.15 summarises the proposed procedure to estimate λ profiles.

Lastly, it is noted that if a reliable e_{min} profile can indeed be estimated from a CPT sounding, then it is also possible to use the laboratory data (e.g. Figure 8.8b) to establish a corresponding Γ profile. It is acknowledged that Γ is not required to estimate ψ from Eqs. 2.42 or 2.45, however, as noted in

Section 2.5.2, Γ can be useful in checking the values of ψ estimated from these two equations as exemplified by Shuttle and Cunning (2007).

8.4 Concluding remarks

A sensitivity analysis was conducted from which a set of charts for typical TSF conditions has been produced to allow a quick assessment of the effect that the uncertainty of λ has on the uncertainty of ψ. A method proposed by Jefferies and Been (2006) (Eq. 8.1) was used as the means to calculate ψ. It was identified that ψ is less sensitive to uncertainty in λ in weak soils (low Q_p) than in strong soils (high Q_p). From a practical point of view, this is a favourable feature as the weaker soils are likely to be the main focus of a site investigation. The charts agree with previous observations made by Reid (2014) indicating that λ-F_r and λ-I_c correlations cannot be used when reliable estimates of λ are needed and that in such cases experimental determination of the SSLs is necessary.

Data corresponding to five TSFs were also used to determine how the uncertainty on ψ due to variability in λ varies amongst TSFs. The relative importance of this uncertainty was assessed by computing its contribution to the total uncertainty on ψ which also includes the intrinsic uncertainty of Eq. 8.1. It was found that this contribution can be virtually negligible in some TSFs, but very significant in others (Figure 8.7). These results indicate that there are cases in which it is not enough to implement Eq. 8.1 with a single average λ, making it necessary to estimate how λ varies along the CPT sounding.

A tentative approach to estimate how λ varies along the CPT sounding has been proposed. The approach is summarised in Figure 8.15 and relies on the following correlations. First, a site-specific correlation between CPT readings and FC. Results previously reported in the literature (Figure 8.9 and Figure 8.10) suggest that development of such a correlation is feasible. Second, a site-specific correlation between FC and e_{min}. The existence of an FC-e_{min} correlation is based on two premises: i) samples obtained from the same TSF that exhibit the same GSD will also have a similar particle shape distribution, and ii) samples obtained from the same TSF that exhibit the same FC will also exhibit a similar overall GSD. The first premise seems a logical consequence of the common mineralogy and rock crushing origin of the tailings, and the second premise is supported by data from two hydraulically deposited TSFs (Figure 8.11 and Figure 8.12). Lastly, a site-specific correlation between λ and e_{min}. Development of this correlation requires a series of triaxial tests to formally determine SSLs (e.g. Figure 8.8a). Although data that suggests the feasibility of the proposed approach has been presented in this chapter, experimental validation of the proposed approach is still lacking in this sense.

8.5 Tables and Figures

Table 8.1 Soil behaviour type from classification index $I_{Q\text{-}Bq}$ and FC from site-specific calibration.

TSF	λ_{min}	λ_{max}	$\Delta\lambda$	λ_c	M[a]	B_q[a]	FC range[b] (%)	PI[c]
Impala[d]	0.042	0.069	0.027	0.056	1.27	0.02	30 - 81	NP[i]
Merriespruit[e]	0.024	0.157	0.133	0.091	1.18	0.15	0 - 60	1 - 8
Stava[e]	0.061	0.180	0.119	0.121	1.43	0[g]	0 - 100	< 9.4
Australian Gold Tailings (AGT)[f]	0.058	0.131	0.073	0.095	1.30	0.03	32 - 100	NP
Molybdenum Tailings (MT)[f]	0.086	0.115	0.029	0.101	1.45	0	22-51	NP

Notes: a) Average values; b) refers to FC in soils tested, not to range of FC in TSF; c) PI = plasticity index; d) Data from Chapter 7; e) References indicated in Table 6.2; f) Data from Reid (2014); g) Assumed value; i) NP = non-plastic.

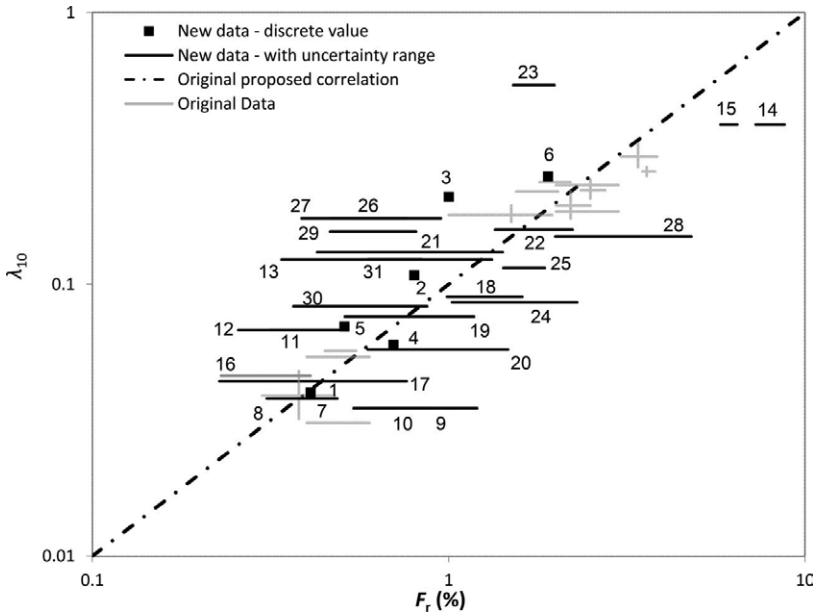


Figure 8.1 λ_{10} vs F_r (Reid 2014). Note: $\lambda_{10} = \lambda$ (Eq. 2.1).

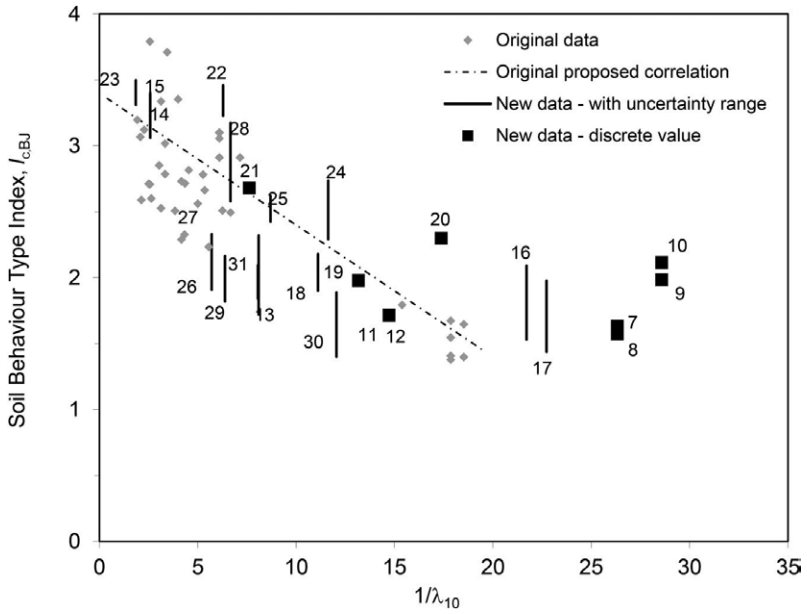


Figure 8.2 $I_{c,BJ}$ vs $1/\lambda_{10}$ (Reid 2014). Note: $I_{c,BJ} = I_c$ (Eq. 2.20); and $\lambda_{10} = \lambda$ (Eq. 2.1).

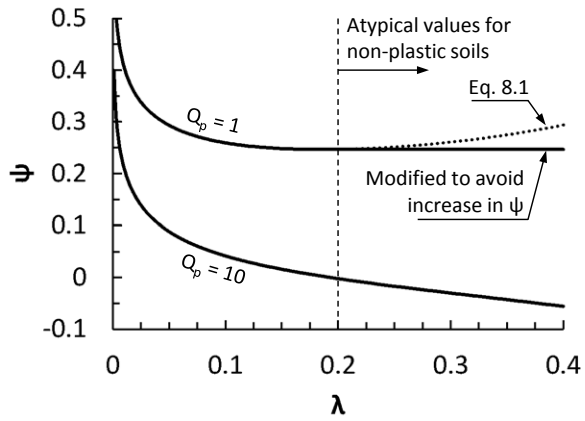
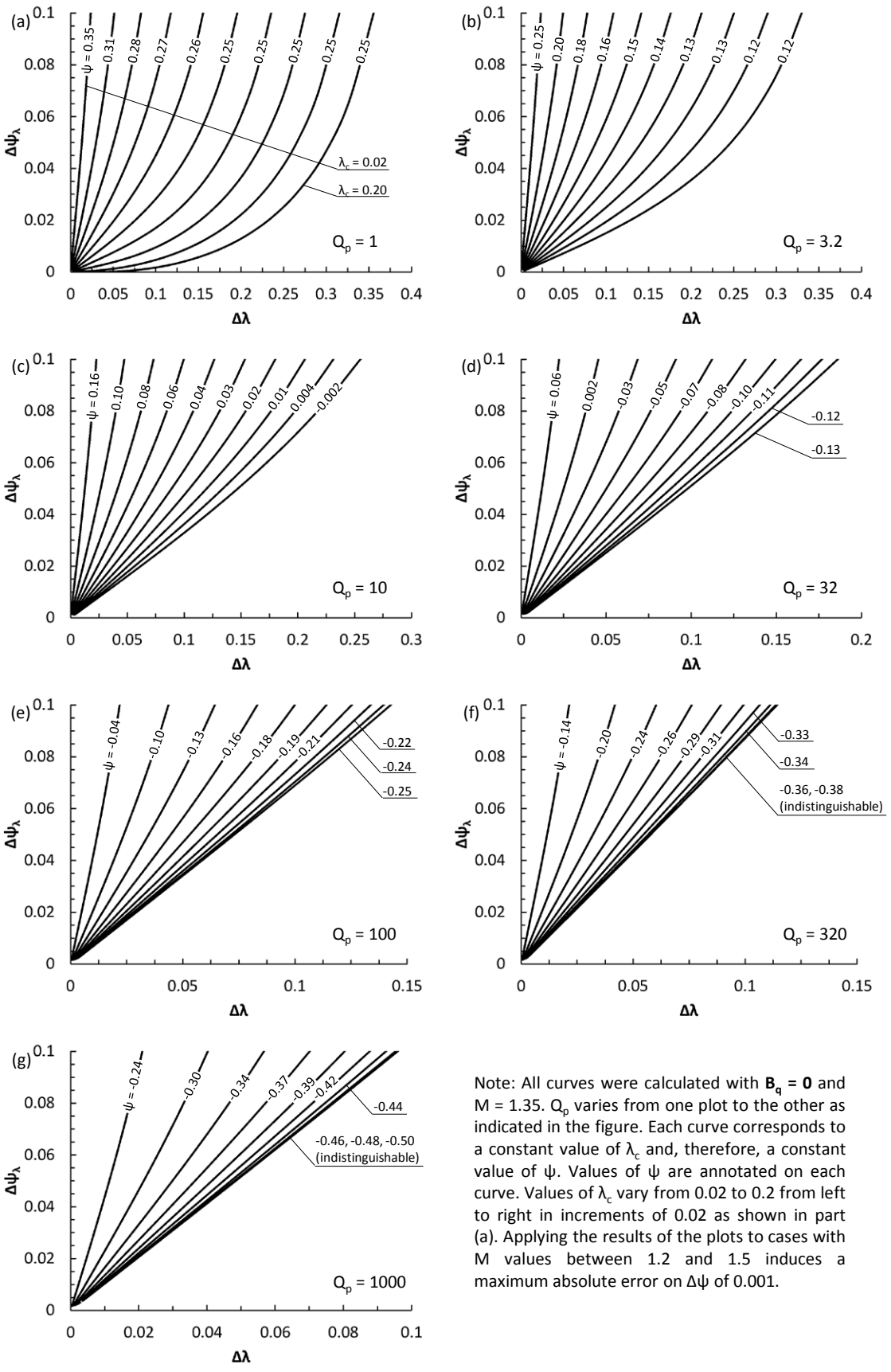
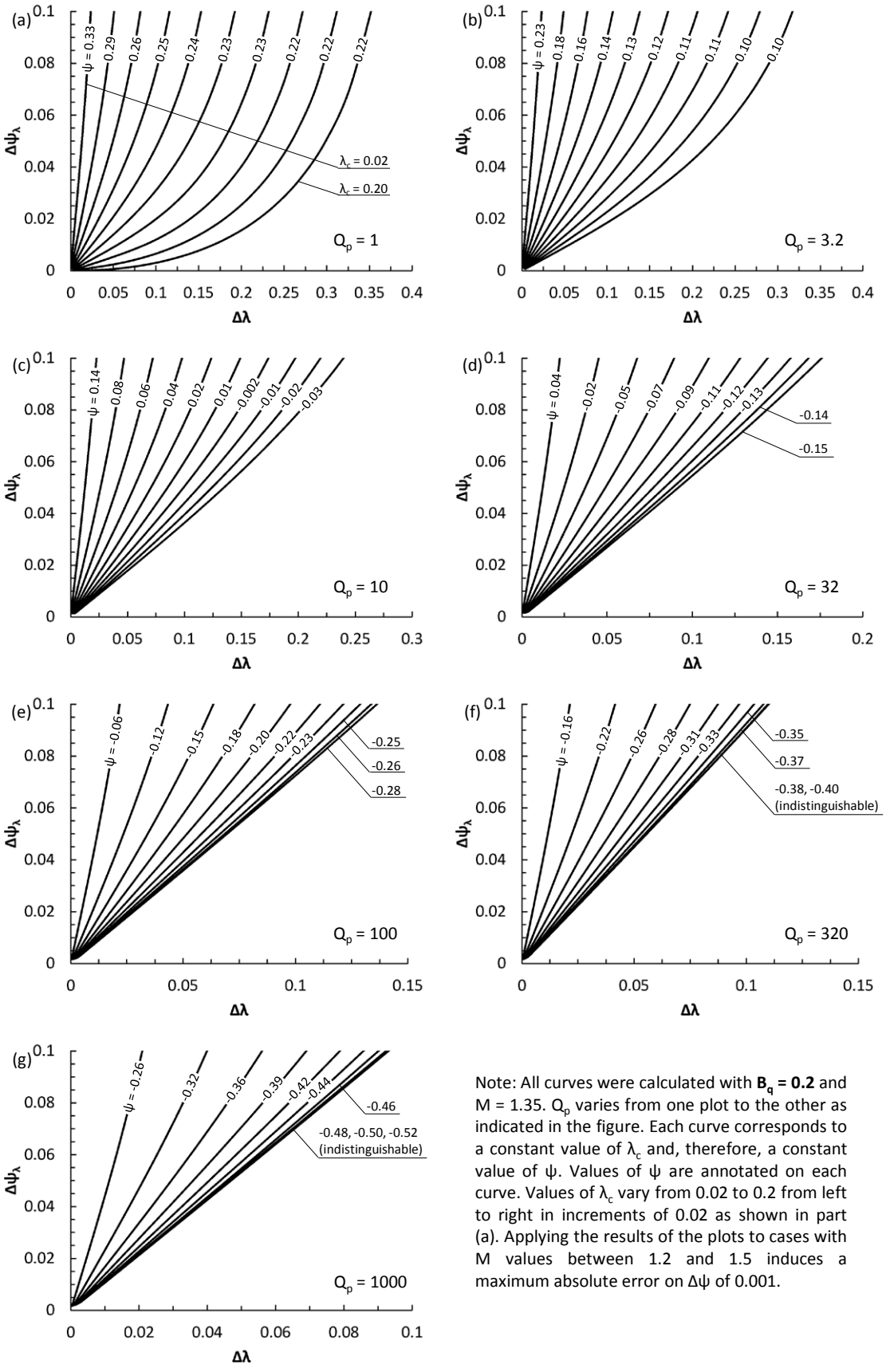


Figure 8.3 Increase of ψ with increase of λ at low Q_p and large λ. Note: Eq. 8.1 was computed with M = 1.35 and $B_q = 0$.



Note: All curves were calculated with $\mathbf{B_q = 0}$ and M = 1.35. Q_p varies from one plot to the other as indicated in the figure. Each curve corresponds to a constant value of λ_c and, therefore, a constant value of ψ. Values of ψ are annotated on each curve. Values of λ_c vary from 0.02 to 0.2 from left to right in increments of 0.02 as shown in part (a). Applying the results of the plots to cases with M values between 1.2 and 1.5 induces a maximum absolute error on Δψ of 0.001.

Figure 8.4 Dependence of $\Delta\psi_\lambda$ on $\Delta\lambda$ for $B_q = 0$.



Note: All curves were calculated with **B_q = 0.2** and M = 1.35. Q_p varies from one plot to the other as indicated in the figure. Each curve corresponds to a constant value of λ_c and, therefore, a constant value of ψ. Values of ψ are annotated on each curve. Values of λ_c vary from 0.02 to 0.2 from left to right in increments of 0.02 as shown in part (a). Applying the results of the plots to cases with M values between 1.2 and 1.5 induces a maximum absolute error on Δψ of 0.001.

Figure 8.5 Dependence of $\Delta\psi_\lambda$ on $\Delta\lambda$ for B_q = 0.2.

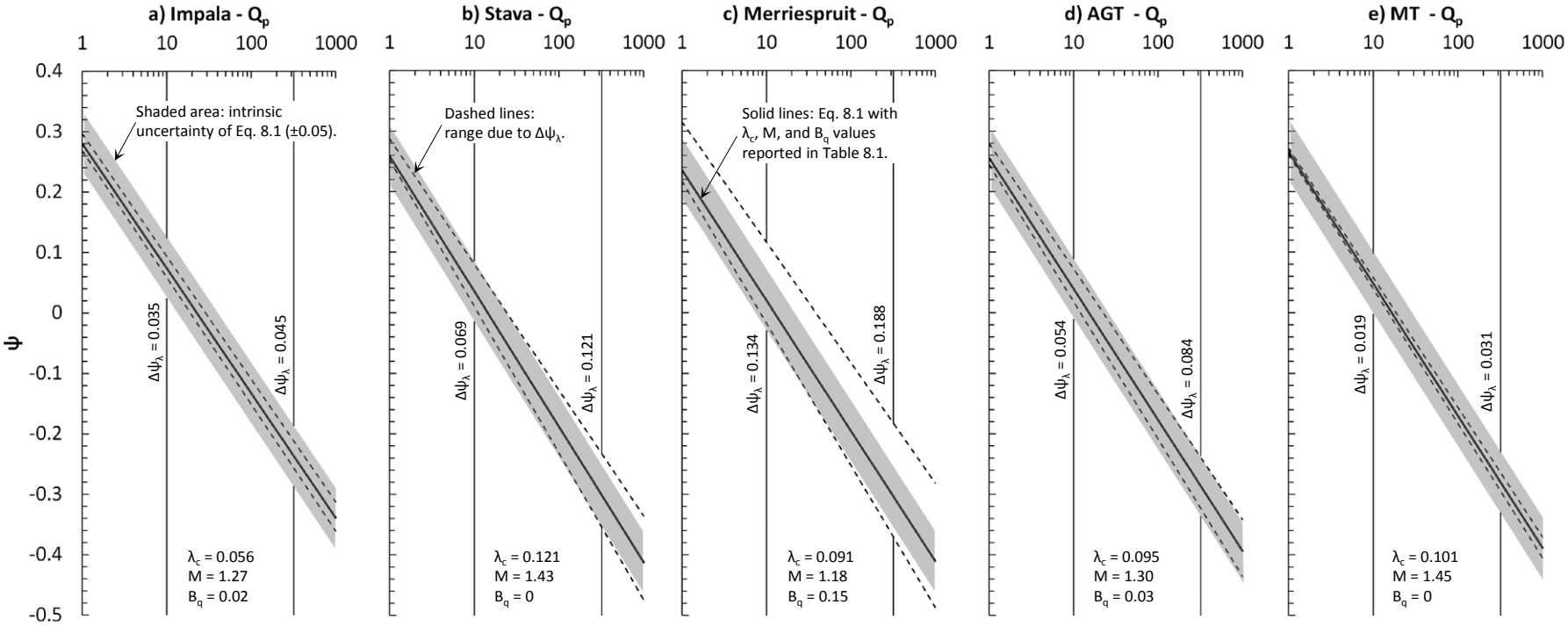


Figure 8.6 Variation of $\Delta\psi_\lambda$ with Q_p for the five TSFs in Table 8.1. Note: $\Delta\psi_\lambda$ is annotated at Q_p = 10 and Q_p = 320.

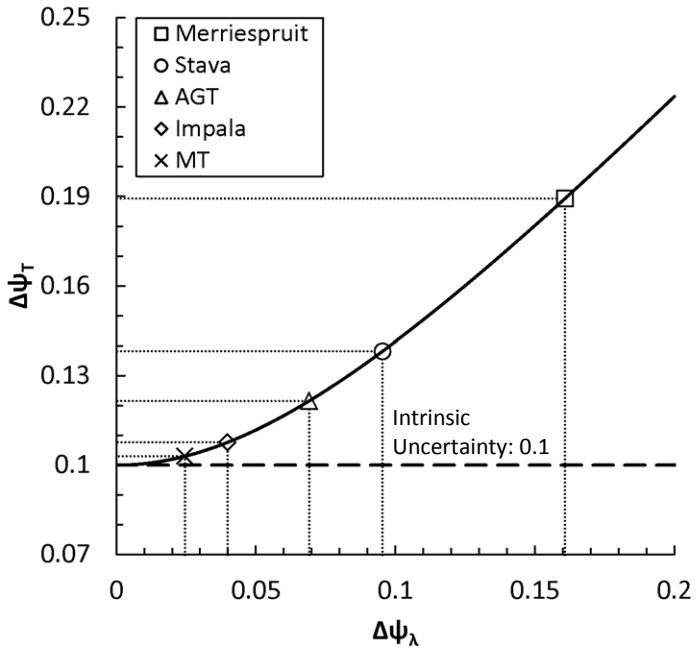


Figure 8.7 Uncertainty on ψ estimated from Eq. 8.1 due to Δλ and the intrinsic uncertainty.

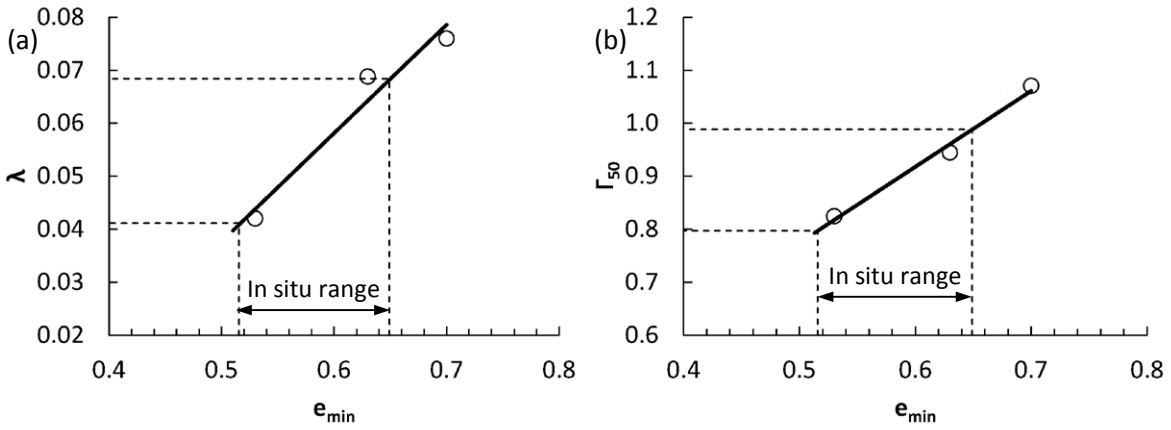


Figure 8.8 Site-specific λ-e_{min} and Γ_{50}-e_{min} correlations for the Impala TSF. Note: e_{min} determined using the non-standard method described in Section 7.2.

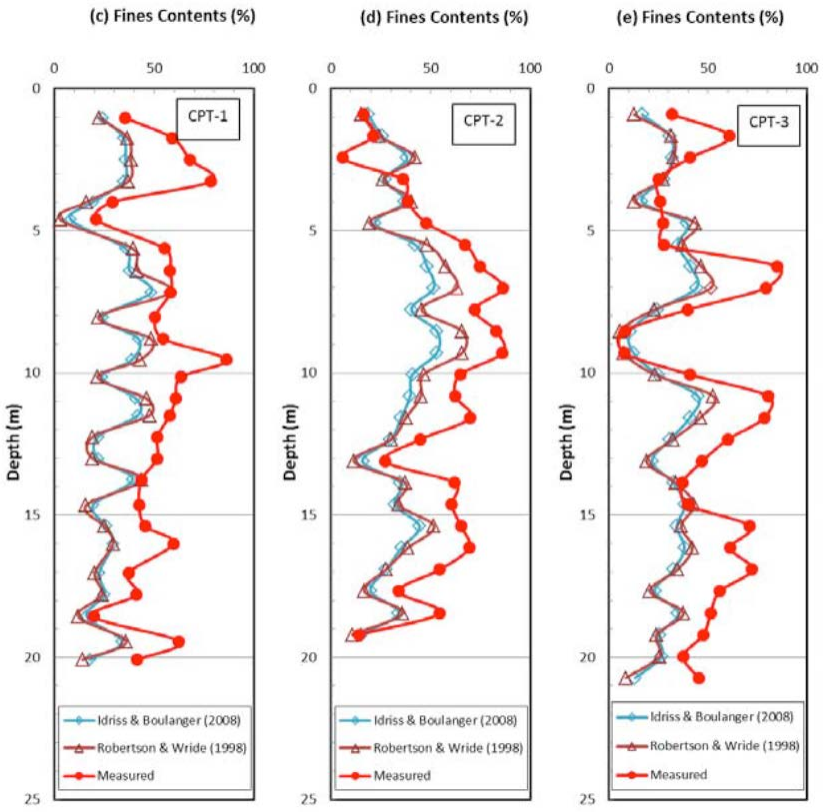


Figure 8.9 Profiles of estimated and measured FC (Yi 2014).

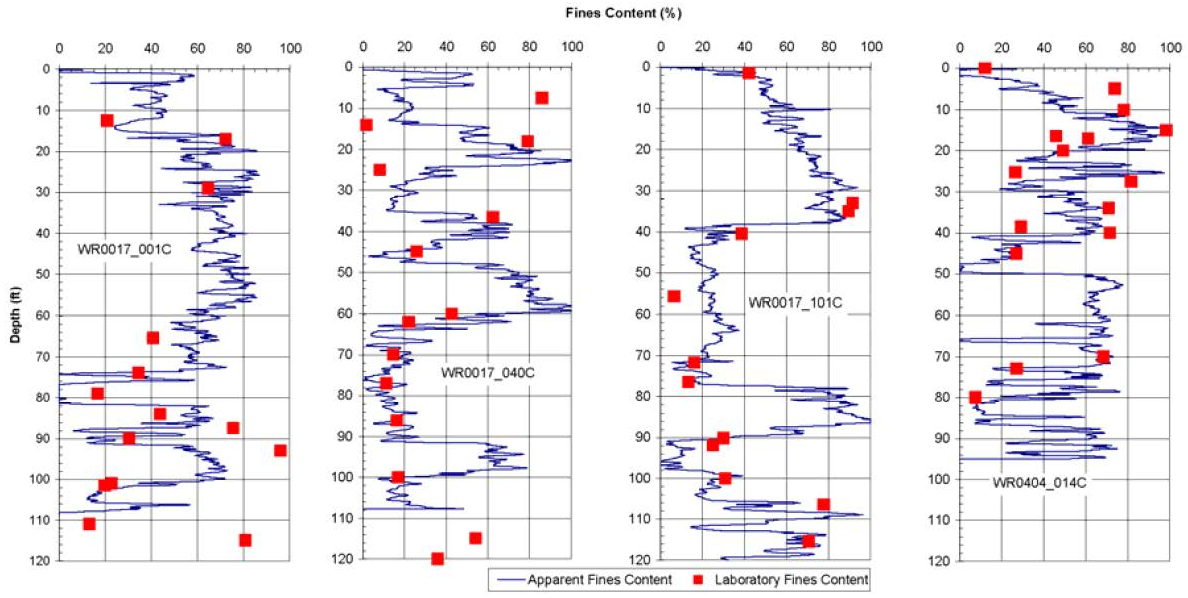


Figure 8.10 Profiles of estimated and measured FC (Boone and Freitas 2010).

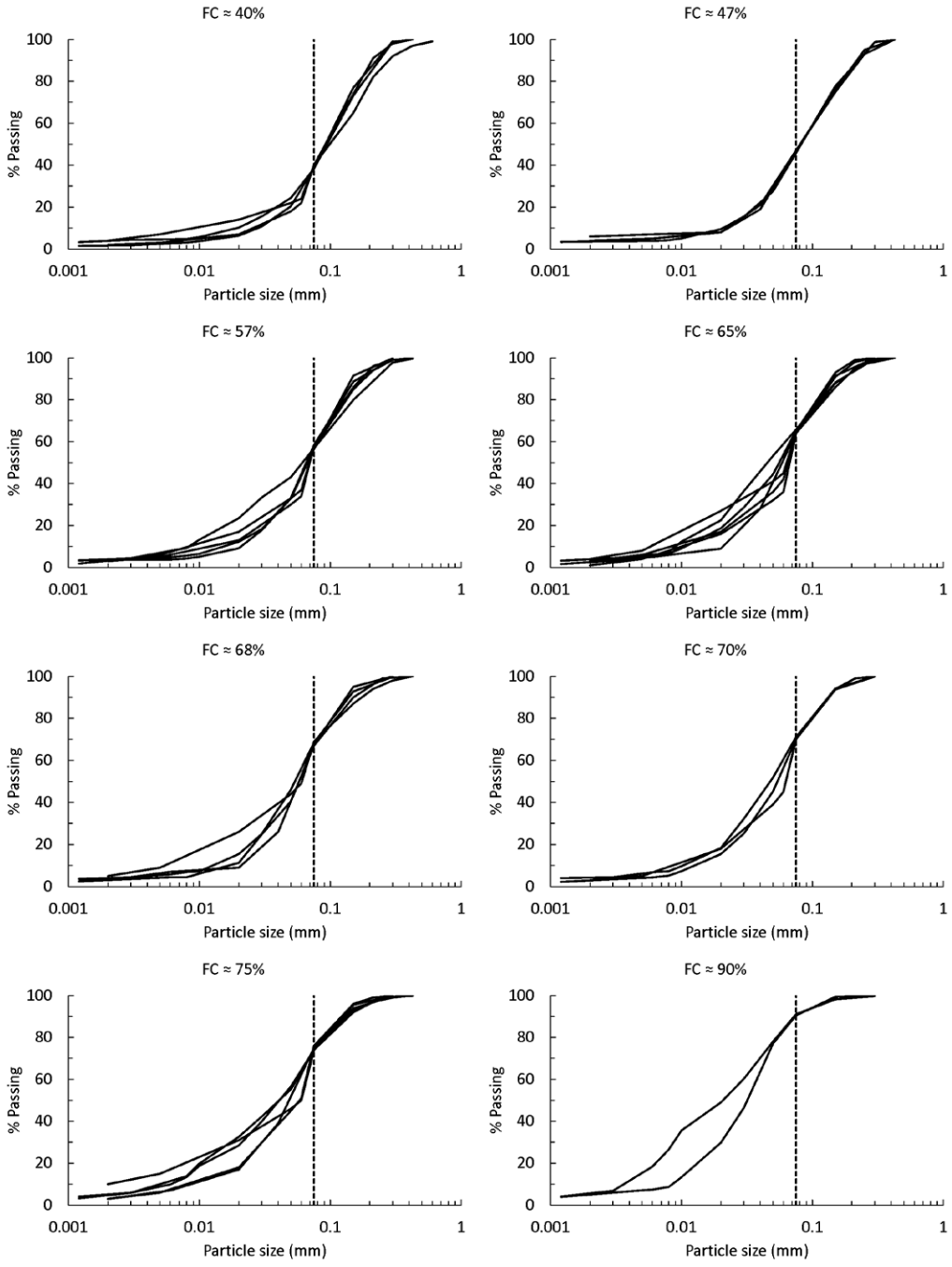


Figure 8.11 GSD curves of samples from the Impala TSF grouped by FC.

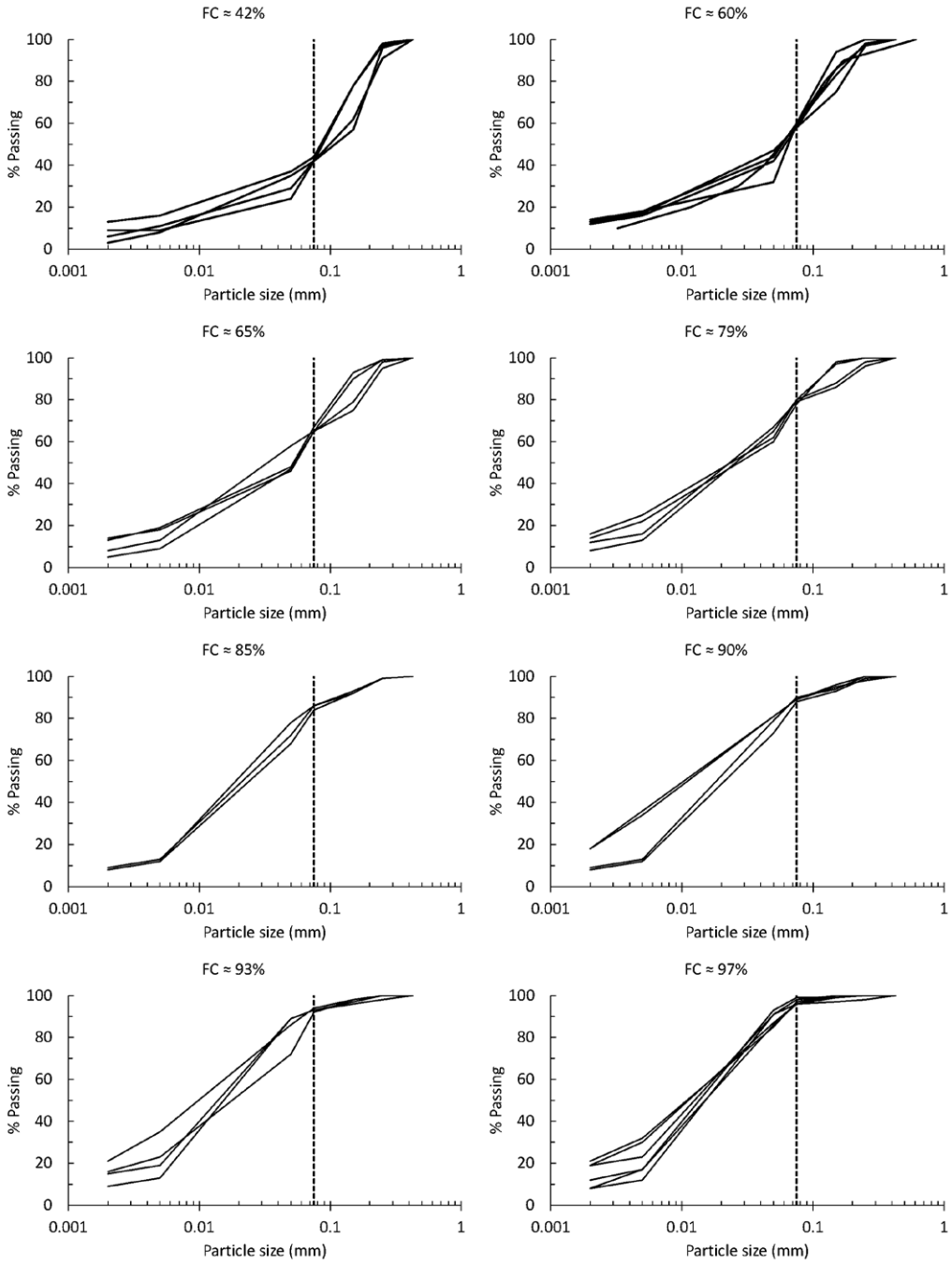


Figure 8.12 GSD curves of samples from the Merriespruit TSF grouped by FC. Data from Williams and Strydom (1994).

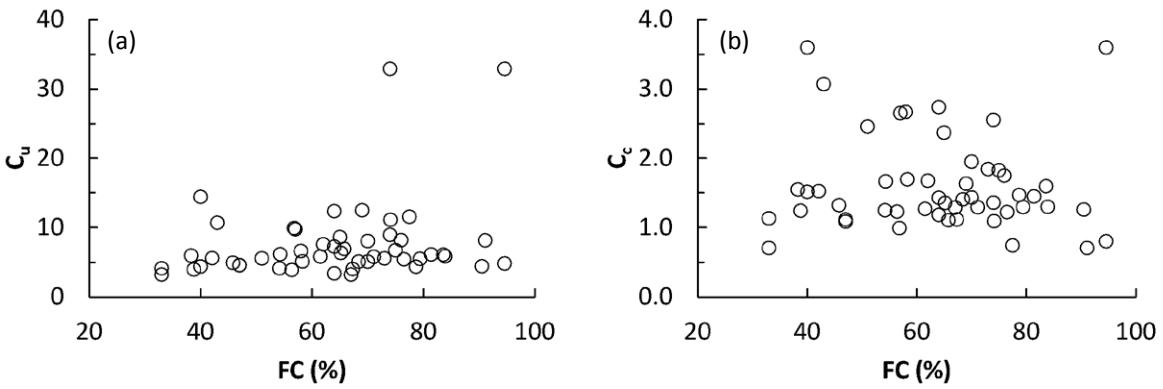


Figure 8.13 Poor correlation between C_u and C_c, and FC for samples from the Impala TSF.

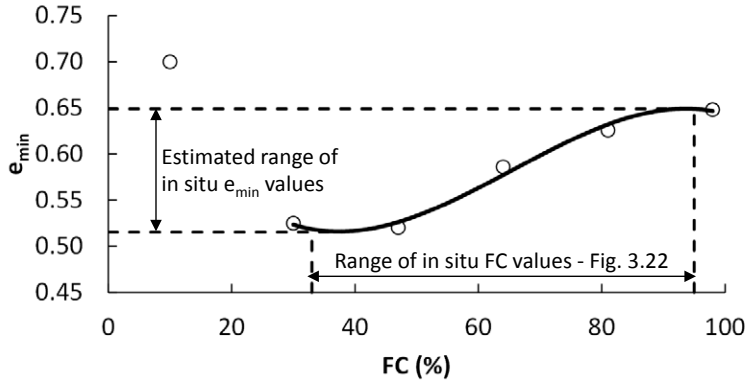


Figure 8.14 Hypothetical e_{min}-FC correlation for the Impala TSF. Note: e_{min} determined using the non-standard method described in Section 7.2.

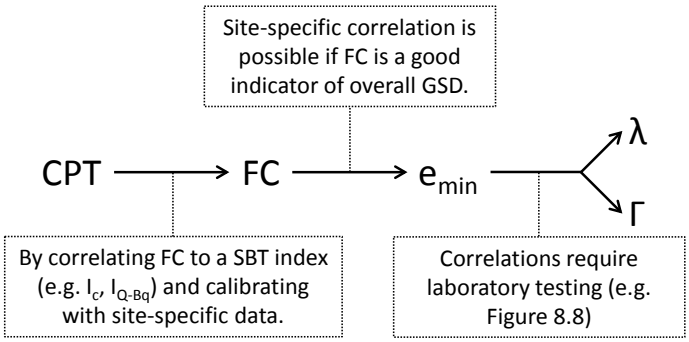


Figure 8.15 Tentative approach to estimate λ and Γ in situ using CPT results and laboratory data.

9 Conclusions and recommendations

The failure case histories presented in Chapter 3 highlight the importance of continuing to develop liquefaction assessment methods for TSFs. This thesis has focused on CPT-based methods because the difficulties associated with undisturbed sampling in tailings imply that in situ testing must be relied on to assess mechanical behaviour. This closing chapter summarises the main findings of the study and presents recommendations for future work.

9.1 Summary of main findings

1. Equation Eq. 2.22 proposed as a liquefaction susceptibility boundary by Olson and Stark (2003) was initially proposed by Fear and Robertson (1995) (in terms of SPT) as being applicable to clean Ottawa sand under lateral stress conditions of $K_0 = 0.5$. However, Olson and Stark (2003) do not mention any restrictions regarding the nature of soiltypes on which Eq. 2.22 is applicable. Comparison of Eq. 2.22 with the contractive-dilative boundary for Alaska sand tailings (Figure 2.7) suggests that Eq. 2.22 is too conservative for generalised use in tailings.
2. The work presented by Olson and Stark (2002) and (2003) highlights the difficulties of relying solely on trends based on the back-analyses of case histories to perform liquefaction potential assessments. Some of the difficulties inherent in this approach are limitations in the available data and the scatter introduced by the unavoidable uncertainties involved when back-analysing case histories. For instance, it was noted that Eq. 2.23, proposed by Olson and Stark (2003) to estimate S_u(yield) from CPT readings, is based on eight case histories of which only two had CPT data available. For the remaining six case histories, values of q_{c1} were inferred from SPT results, relative density, or were otherwise estimated. Such correlations between q_{c1} and other geotechnical parameters introduce uncertainty which may partly account for the weak correlation ($R^2 = 0.15$) in the eight YSR vs q_{c1} data points that support Eq. 2.23 (Figure 2.8a).
3. Similar observations are also applicable to Eq. 2.24, proposed by Olson and Stark (2002) to estimate S_u(LIQ) from CPT readings in the post-triggering analysis. Eq. 2.24 is based on 21 case histories of which only seven had CPT data available. For the remaining 14 case histories, values of q_{c1} were inferred from SPT results, relative density, or were otherwise estimated. As noted above, this reliance on correlations to infer q_{c1} is an important source of uncertainty that may partly account for the weak correlation ($R^2 = 0.21$) in the 21 YSR vs q_{c1} data points that support Eq. 2.24 (Figure 2.8b).
4. The susceptibility analysis proposed by Robertson (2010) is based on the premise that $Q_{tn,cs}$ is a proxy for the state parameter (ψ). However, the current work has pointed out important aspects which may limit the extent to which $Q_{tn,cs}$ can be relied on as an effective screening criterion to detect contractive soils. Firstly, $Q_{tn,cs}$ is a function of the stress exponent 'n' which is defined by Eq. 2.10 but for which no supporting data was found in the literature. Similarly, $Q_{tn,cs}$ is also a function of parameter K_c which is defined by Eq. 2.14 but for which no supporting data was found in the literature either. Additionally, it was noted that $Q_{tn,cs}$ and K_c are directly

correlated (Eq. 2.13). K_c in turn is directly correlated to I_c which is expected to increase with fines content (FC) (Figure 2.5). The implication is that soils with higher FC will yield higher values of K_c and $Q_{tn,cs}$, making them less likely to be classified as contractive. However, the validity of this implication, at least for non-plastic soils, is not supported by the analyses presented in Chapters 6 and 7 which indicate that for a large variety of soiltypes the SSL, and therefore ψ, is independent of FC.

5. The value of I_c also plays a central role in the triggering analysis proposed by Robertson (2009b), with soils being treated differently depending on whether their I_c value is greater or smaller than 2.6. Again, this approach suggests that I_c, and therefore FC (Figure 2.5), has a dominant role on the mechanical behaviour of the soil. But as noted above, this is not supported by the analyses presented in Chapters 6 and 7 for non-plastic soils.
6. Similarly, the correlation between λ and I_c (Figure 2.15) used in the screening method to infer ψ described by Jefferies and Been (2006) does not seem to be applicable to non-plastic soils. This was also highlighted by the results of Reid (2014) which illustrate the large uncertainties involved in attempting to infer the SSL parameters of tailings deposits from CPT results alone.
7. The susceptibility, triggering, and post-triggering analyses proposed by Olson and Stark (2002) and (2003), and the susceptibility analysis proposed by Robertson (2010) were implemented on the seven TSF case histories presented in Chapter 3 in which an undrained response was suspected to have occurred. Additionally, the triggering analysis of the Robertson-based method was implemented only on the case histories that involved seismic loading. Table 4.1 summarises the success of the methods in predicting the performance of the different case histories. The Olson and Stark method yielded incorrect predictions in only 3 out of 21 instances, whereas the Robertson-based method yielded incorrect predictions in only 1 out of 12 instances. Nonetheless, these rates of success must be tempered by the objections made to the formulations of both methods (Sections 2.3 and 2.4), as these objections indicated important limitations that may compromise the applicability of the methods to TSFs.
8. A new CPT-based soil behaviour type index ($I_{Q\text{-}Bq}$) that does not depend on sleeve friction readings was proposed (Eq. 5.1 and Figure 5.1). $I_{Q\text{-}Bq}$ is based on the Q-B_q chart of Robertson (1991) and assigns a numerical value to the classification made with the chart. This eliminates the need to visually inspect the chart to interpret its results and allows for a mathematical treatment of these results.
9. Analysis of a database of 151 non-plastic or low plasticity soiltypes showed that e_{min} and Γ_{50} are strongly correlated (R^2 = 0.74) (Figure 6.31a) and that this correlation is independent of FC (Figure 6.34) and particle shape (Figure 6.35). Although no significant correlation was found in the λ vs e_{min} plot (Figure 6.31b) further analysis of the database showed Γ_n and e_{min} were significantly correlated for n values that ranged from 50 kPa to 800 kPa (Figure 6.36). The implication of these correlations is that e_{min} also has an effect on λ (Figure 6.38) and evidence from the literature was presented which indicated that there is a rationale for a λ-e_{min} correlation. The annotated FC values on the λ vs e_{min} plots in Figure 6.41 show that there is no correlation between λ and FC.

10. The correlations between Γ_n and e_{min} presented in Figure 6.36 were developed from soiltypes whose e_{min} values were measured using a wide variety of methods (Table 6.2). This introduces a significant degree of scatter in the correlations which limits their predictive power. So although the correlations presented in Figure 6.31a and Figure 6.38 may be useful in qualitatively understanding how Γ and λ, respectively, are affected by changes in e_{min}, they are no substitute for experimental determination of the SSL.
11. The Γ_{50} and λ of three SSLs of Impala tailings were found to be directly correlated to e_{min} and these correlations agreed well with the trends observed in the database of non-plastic soils analysed in Chapter 6 (Figure 7.38 and Figure 7.41). Moreover, tailings in general agreed well with the Γ_{50} vs e_{min} trend identified for other non-plastic soils (Figure 7.39). Similarly, the λ vs e_{min} data points corresponding to tailings were indistinguishable from other non-plastic soils. Conversely, no correlations were found between either Γ or λ and FC. As for the M value, no significant differences were found between the three Impala SSLs (Figure 7.36d). The results of the triaxial testing programme confirmed that e_{min} can be a useful indicator of the variability of Γ and λ within a TSF. It is also important to note that the triaxial testing programme confirmed the significant errors that can be incurred in if Γ_n is estimated from e_{min} alone. In the case of the Impala tailings, errors as large as 0.09 would have occurred if Γ_{50} had been estimated from Eq. 6.3.
12. Charts that allow the quick assessment of the uncertainty of ψ, as estimated with Eq. 2.45 proposed by Jefferies and Been (2006), were developed for conditions typical of TSFs (Figure 8.4 and Figure 8.5). For a given uncertainty in λ the uncertainty in ψ was found to be lower in weak soils (low Q_p) than in strong soils (high Q_p). From a practical point of view, this is a favourable feature as the weaker soils are likely to be the main focus of a site investigation. Additionally, data from five TSFs showed that in some cases it is feasible to ignore the variability of λ within a TSF and implement Eq. 2.45 with a single average λ without significantly compromising the accuracy of the ψ estimations. However, the data also showed that there might be cases in which it is necessary to estimate how λ is varying along the depth of the CPT sounding.
13. A tentative approach was presented to make estimations of how λ varies along the depth of a CPT sounding (Figure 8.15). The approach is based on essentially on three correlations: i) A correlation between CPT results and FC; ii) A correlation between FC and e_{min}; and iii) A correlation between e_{min} and λ. Experimental data supporting the first and third correlations were presented (Figure 8.8 to Figure 8.10). However, the method is tentative because experimental evidence in support of the second correlation was not presented. Nonetheless, characteristics of GSDs from two hydraulically deposited TSFs (Figure 8.11 and Figure 8.12) suggest that for a given TSF, FC might be a good predictor of e_{min}.

9.2 Recommendations for future research

1. The correlation with e_{min} of the SSL parameters Γ_{50} and λ has been highlighted in the current thesis. However, in compiling the database of non-plastic soils presented in Chapter 6, it became evident that the void ratio limits are often overlooked as potential indicators of mechanical behaviour. This seems to be particularly true when the soiltype being studied contains a significant amount of fines. However, Figure 6.34 suggests that the Γ_{50} - e_{min} correlation does not change systematically with FC. It is thus recommended that e_{min}, and the method used to estimate it, is always reported. Even for soils with a significant amount of non-plastic fines.
2. Additional testing on a variety of soiltypes is required to arrive at a better understanding of the correlation between λ and void ratio limits. The results from Cubrinovski and Ishihara (2000), Cho et al. (2006), and this thesis indicate a direct correlation between these parameters. However, while Cubrinovski and Ishihara (2000) indicated that the correlation was dependent on particle shape (rounded or angular), the results of Cho et al. (2006) and this thesis suggest that it is not. Additionally, the results of Hird and Hassona (1990) Figure 6.4 indicate that the presence of platy particles increases λ. Testing programmes including formal measurements of particle form would be useful to determine whether particle shape effects can indeed be captured by the limiting void ratios.
3. Chapter 8 presented data that suggests TSF-specific correlations between FC and e_{min} can be obtained for hydraulically deposited TSFs. However, data is still lacking to confirm whether this correlation exists or not and it is recommended that this correlation is explored further to improve our understanding of TSFs.

Appendix A Slope stability models used to implement the Olson and Stark method

A.1 Introduction

Slope stability analyses are required to implement the Olson and Stark method. Due to the uncertainties involved in the case histories considered, several scenarios were modelled for each case to consider different values of parameters such as:

1. Friction angle (φ')
2. Effective cohesion (c')
3. Geometry of the failure surface
4. Location of the water table
5. Capillary head
6. Yield strength ratio (*YSR*)
7. Liquefied strength ratio (*LSR*)
8. Peak horizontal acceleration (a_{max})

This appendix describes the different scenarios considered when analysing the slope stability of the case histories. The scenarios are mostly described with the aid of figures and tabulated data. The figures describe the geometry, soiltypes involved and slip failure surface used. The tables contain the strength parameters, unit weights, q_{c1}* value, factors of safety and, in the case of the seismic case histories, they also contain earthquake moment magnitude (M_w) and peak acceleration (a_{max}). All models were created using module Slope/W of the software package GeoStudio 2007 (Geo-Slope International Ltd.).

For some analyses, the software was allowed to search for a circular critical slip surface and subsequently optimise it to find sliding surfaces that may be weaker but do not have a circular geometry. The 'grid and radius' method described in Geo-Slope (2010) was used to find the critical circular slip surface. The optimisation consisted of small modifications to the slip surface that were conducive to a smaller factor of safety. There were also some scenarios for which non-critical slip surfaces were used. This was done either because such a slip surface had been suggested by another author or because it was considered convenient to force a slip surface to intersect a region of the tailings that had not been intersected by the critical slip surface. The latter motivation is suggested by Olson (2001).

A.2 Hokkaido Dam – Japan, 1968

Seven scenarios were considered when modelling the slope stability of the Hokkaido Dam (Figure A.1 to Figure A.7 and Table A.1). Critical slip surfaces were not used in three of the scenarios:

For scenarios 3 and 4, the slip surfaces suggested by Olson (2001) were used, whereas for scenario 7 a planar critical slip surface was considered.

A.3 Mochikoshi Dam – Japan, 1978

Dyke 1: Four scenarios were considered when modelling the slope stability of Dyke 1 of the Mochikoshi Dam (Figure A.8 to Figure A.11 and Table A.2). Scenarios 1 and 2 used an optimised critical slip surface and differed only on the location of the water table. Given that the same factor of safety was obtained regardless of the location of the water table, scenarios 3 and 4 only considered water table at ground level in the beach. For scenarios 3 and 4, the slip surfaces suggested by Olson (2001) were used.

Dyke 2: Five scenarios were considered when modelling the slope stability of Dyke 2 of the Mochikoshi Dam (Figure A.12 to Figure A.16 and Table A.3). Scenarios 1 and 2 used an optimised critical slip surface and differed only on the location of the water table. Given that the same factor of safety was obtained regardless of the location of the water table, scenarios 3, 4 and 5 only considered water table at ground level in the beach. For scenarios 3, 4 and 5 the slip surfaces suggested by Olson (2001) were used.

A.4 Dashihe Iron Tailings Dam – China, 1990

The slope stability models of the Dashihe tailings dam used in this research were based on the model reported by Amante (1993). Only three types of soil were considered in this research: tailings above and below the water table, and a foundation material that was modelled as clay with a total strength c = 164 kPa. In the model used by Amante (1993), the tailings above and below the water table are further subdivided into different types of soils. However, since there are only small variations of unit weight and shear strength within these two major groups, it was considered reasonable to disregard the subdivisions for the purpose of the slope stability analyses. Furthermore, Amante (1993) reports that the foundation material is not composed entirely of clay, but rather that the clay with c = 164 kPa represents a weak layer in the foundation. Therefore in this study, it was conservatively assumed that the entire foundation layer was made of clay. Figure A.17 and Figure A.19 show that the slip surfaces do not intersect the foundation material, hence this assumption has no effect on the analysis.

Beach: Four scenarios were considered when modelling the slope stability of the beach at the Dashihe Dam (Figure A.17 to Figure A.20 and Table A.4). For scenarios 1 and 2 a capillary rise of 5 m was adopted, whereas no capillary rise was adopted for scenarios 3 and 4. Scenarios 1 and 3 used an optimised critical slip surface and scenarios 2 and 4 used the slip surface suggested by Amante (1993).

Outer Wall: Four scenarios were considered when modelling the slope stability of the outer wall at the Dashihe Dam (Figure A.21 to Figure A.24 and Table A.5). For scenarios 1 and 2 a capillary rise of 5 m was adopted, whereas no capillary rise was adopted for scenarios 3 and 4. Scenarios 1 and 3

used an optimised critical slip surface and scenarios 2 and 4 used the slip surface suggested by Amante (1993). The results in Table A.5 show that when considering the slip surface suggested by Amante (1993), the shear strength of the liquefiable tailings cannot be reduced enough to obtain a factor of safety equal to 1.

A.5 Sullivan Tailings Dam – Canada, 1991

Four scenarios were considered when modelling the slope stability of the outer wall at the Dashihe Dam (Figure A.25 to Figure A.28 and Table A.6). Optimised critical slip surfaces were used in scenarios 1 and 2, and non-critical slip surfaces were used in scenarios 3 and 4. There was uncertainty regarding the strength of the dyke material, therefore a strong dyke was assumed in scenarios 1 and 3, and a weak dyke was assumed in scenarios 2 and 4.

A.6 Merriespruit Tailings Dam – South Africa, 1994

The static shear stress that triggered the liquefaction of the tailings was a function of the eroded geometry created by the overtopping of water (see Section 3.6). An analysis of the retrogressive failure is included in the files of Jones and Wagener Consulting Civil Engineers (J&W), a firm hired to conduct an investigation to determine the causes of the Merriespruit failure. The geometries used in the J&W analysis were based on field evidence and accounts from eyewitnesses. The retrogressive failure was modelled by J&W in four stages. Given that the first three stages mainly involved failure of the consolidated tailings in the outer wall, it is reasonable to assume that it was only in the fourth stage that the impounded tailings were subjected to the static shear stress that triggered liquefaction. The geometry of this fourth stage was used here to analyse the slope stability.

Four scenarios were considered (Figure A.29 to Figure A.32 and Table A.7). A non-critical slip surface was used in scenario 2, in which a slip surface used in the analyses conducted by J&W was adopted. All other scenarios used a critical slip surface. Scenario 4 considers that the foundation soil is impenetrable.

A.7 Tables and Figures

Note: For Table A.1 to Table A.7, FS_T = factor of safety against triggering of liquefaction and FS_F = factor of safety against flow failure.

Table A.1 Scenarios used to analyse Hokkaido Dam.

Scenario	Liquefiable tailings			Non-liquefiable tailings			Dyke material			M_w	a_{max}	q_{c1}*	Slip surface	FS_T	FS_F
	φ'	c'	γ_t	φ'	c'	γ_t	φ'	c'	γ_t	(--)	(m/s^2)	(MPa)			
1	0	24.3	19.8	30	0	19.8	Impenetrable bedrock			8	2.3	0.47	Critical slip surface was searched.	0.45	0.15
2		24.0		35										0.46	0.15
3		12.9		32.5									Shallowest slip surface suggested by Olson (2001).	0.59	0.23
4		17.9		32.5									Deepest slip surface suggested by Olson (2001).	0.48	0.16
5		23.4		30									Critical slip surface was searched.	0.46	0.15
6		23.3		35										0.46	0.15
7		5.2		--	--	--							Slip surface taken as planar.	0.59	0.35

Table A.2 Scenarios used to analyse Mochikoshi Dyke 1

Scenario	Liquefiable tailings			Dyke material			M_w	a_{max}	q_{c1}*	Slip surface	FS_T	FS_F
	φ'	c'	γ_t	φ'	c'	γ_t	(--)	(m/s^2)	(MPa)			
1	0	30.5	17.6	35	0	16.6	7.7	2.5	0.23	Critical slip surface was searched.	0.45	0.15
2		30.5									0.46	0.15
3		19								Shallowest slip surface suggested by Olson (2001).	0.59	0.23
4		28								Deepest slip surface suggested by Olson (2001).	0.48	0.16

Table A.3 Scenarios used to analyse Mochikoshi Dyke 2.

Scenario	Liquefiable tailings			Dyke material			M_w	a_{max}	q_{c1}*	Slip surface	FS_T	FS_F
	φ'	c'	γ_t	φ'	c'	γ_t	(--)	(m/s^2)	(MPa)			
1	0	20.9	17.6	35	0	15.1	7.7	2.5	0.23	Critical slip surface was searched.	0.48	0.16
2		20.9						2.5			0.48	0.16
3		3.2						2.5		Slip surface is upper one suggested by Olson (2001).	0.74	0.60
4		11.8						2.5		Slip surface is middle one suggested by Olson (2001).	0.53	0.20
5		14.0						2.5		Slip surface is lower one suggested by Olson (2001).	0.47	0.18

Table A.4 Scenarios used to analyse Dashihe Beach.

Scenario	Liquefiable tailings			Non-liquefiable tailings			Clay			M_w	a_{max}	q_{c1}*	Slip surface	FS_T	FS_F
	φ'	c'	γ_t	φ'	c'	γ_t	φ'	c'	γ_t	(--)	(m/s^2)	(MPa)			
1	0	10.2	19.6	39	0	15.9	0	164	18.9	7.5	1.2	4.5	Critical slip surface was searched.	2.51	--
2		3.9											Slip surface is as suggested by Amante (1993).	1.84	--
3		9.4											Critical slip surface was searched.	2.31	--
4		2.7											Slip surface is as suggested by Amante (1993).	1.66	--

Table A.5 Scenarios used to analyse Dashihe Outer Wall.

Scenario	Liquefiable tailings			Non-liquefiable tailings			Clay			M_w	a_{max}	q_{c1}*	Slip surface	FS_T	FS_F
	φ'	c'	γ_t	φ'	c'	γ_t	φ'	c'	γ_t	(--)	(m/s^2)	(MPa)			
1	0	75	19.6	39	0	15.9	0	164	18.9	7.5	1.2	5.6	Critical slip surface was searched.	1.22	--
2		0											Slip surface is as suggested by Amante (1993).	--	--
3		77.1											Critical slip surface was searched.	1.19	--
4		0											Slip surface is as suggested by Amante (1993).	--	--

Table A.6 Scenarios used to analyse Sullivan Dam.

Scenario	Liquefiable tailings			Dyke material			q_{c1}*	Slip surface	FS_T	FS_F
	φ'	c'	γ_t	φ'	c'	γ_t	(MPa)			
1	0	43.6	24	35	15	22.4	1.4	Critical slip surface was searched.	0.85	0.19
2		43.6		30	5				0.83	0.18
3		23.7		35	15			Slip surface was forced to intersect different portion of tailings.	0.95	0.21
4		25.3		30	5				0.89	0.20

Table A.7 Scenarios used to analyse Merriespruit Dam.

Scenario	Liquefiable tailings			Natural soil			q_{c1}*	Slip surface	FS_T	FS_F
	φ'	c'	γ_t	φ'	c'	γ_t	(MPa)			
1	0	83.3	20	40	40	20	0.92	Critical slip surface was searched.	0.42	0.08
2		55						Slip surface is as suggested by Jones & Wagener.	0.36	0.07
3		83.6						Critical slip surface was searched controlling entry and exit angles.	0.42	0.08
4		83		Impenetrable bedrock				Critical slip surface was searched.	0.43	0.09

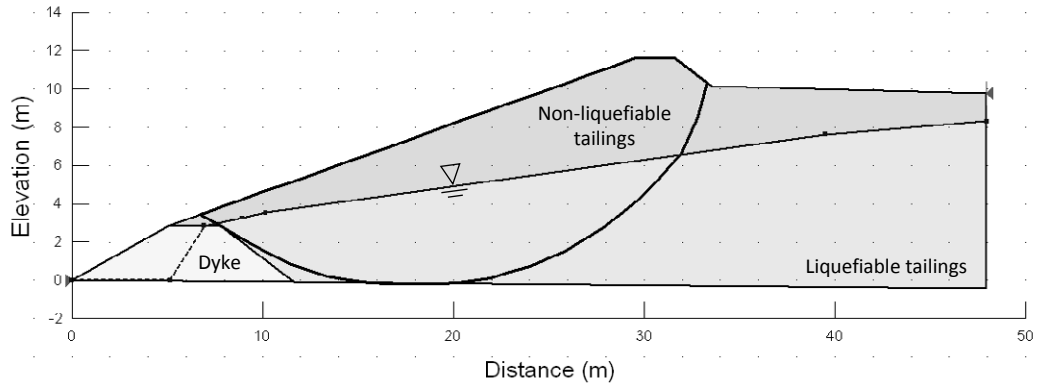


Figure A.1 Hokkaido Dam: Geometry of model used in scenario 1.

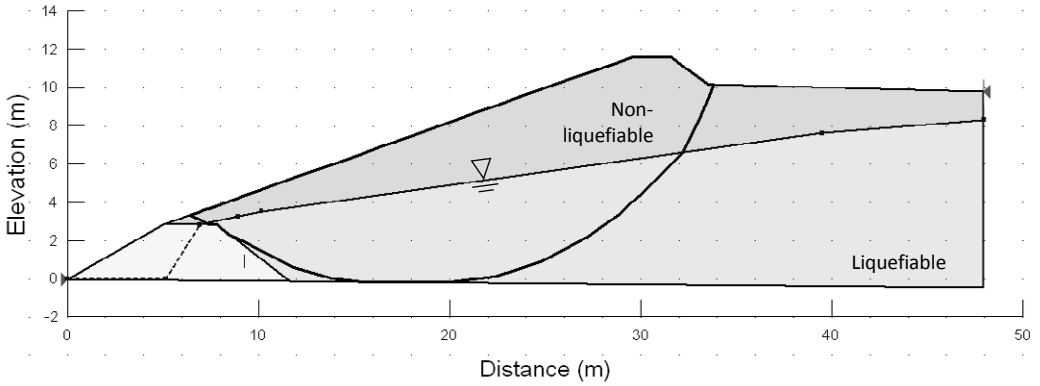


Figure A.2 Hokkaido Dam: Geometry of model used in scenario 2.

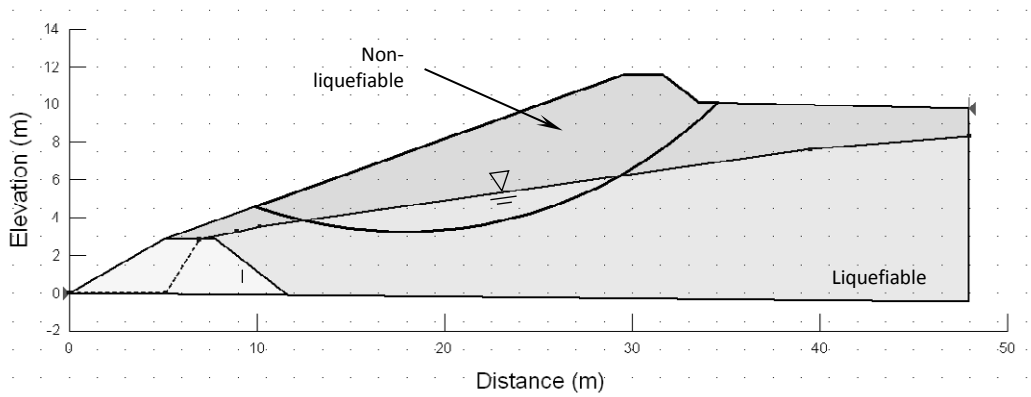


Figure A.3 Hokkaido Dam: Geometry of model used in scenario 3.

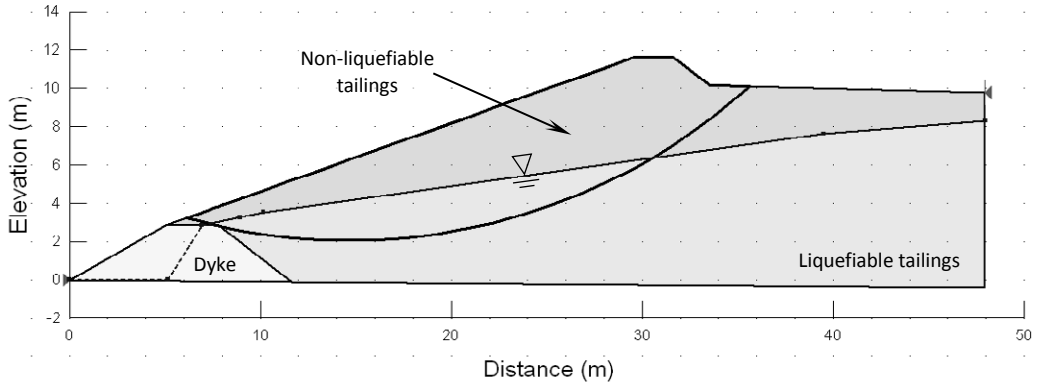


Figure A.4 Hokkaido Dam: Geometry of model used in scenario 4.

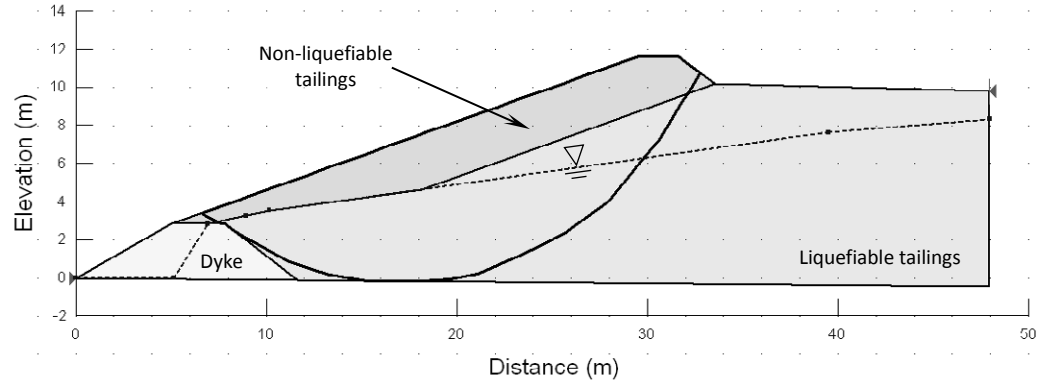


Figure A.5 Hokkaido Dam: Geometry of model used in scenario 5.

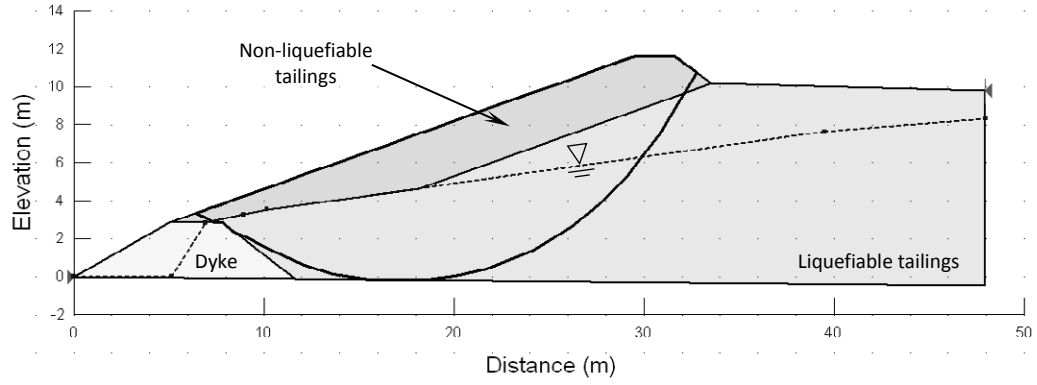


Figure A.6 Hokkaido Dam: Geometry of model used in scenario 6.

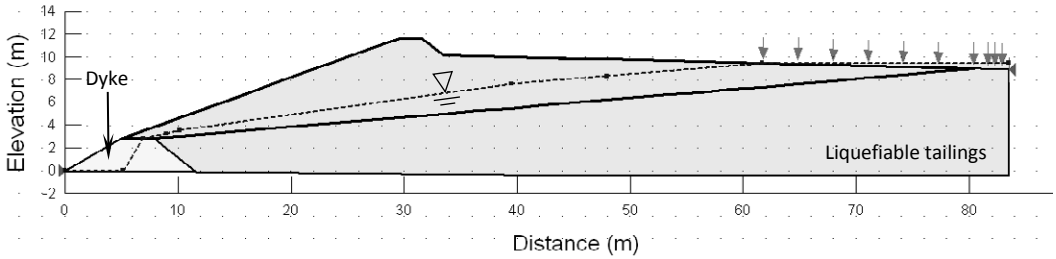


Figure A.7 Hokkaido Dam: Geometry of model used in scenario 7.

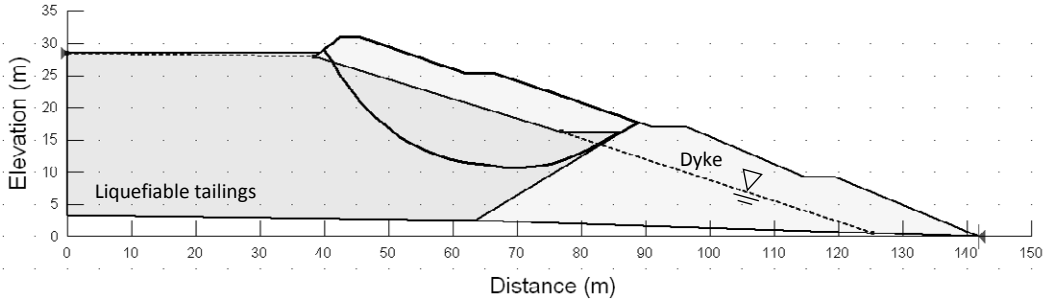


Figure A.8 Mochikoshi Dyke 1: Geometry of model used in scenario 1.

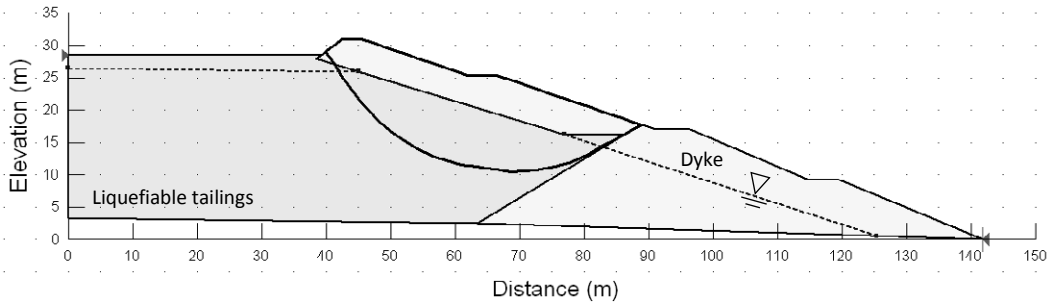


Figure A.9 Mochikoshi Dyke 1: Geometry of model used in scenario 2.

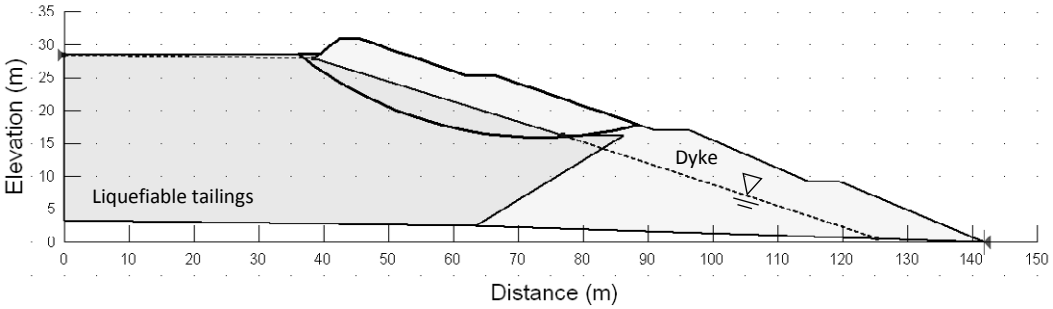


Figure A.10 Mochikoshi Dyke 1: Geometry of model used in scenario 3.

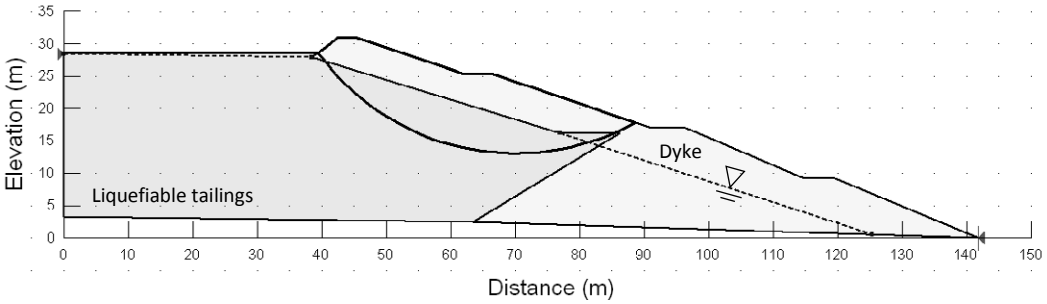


Figure A.11 Mochikoshi Dyke 1: Geometry of model used in scenario 4.

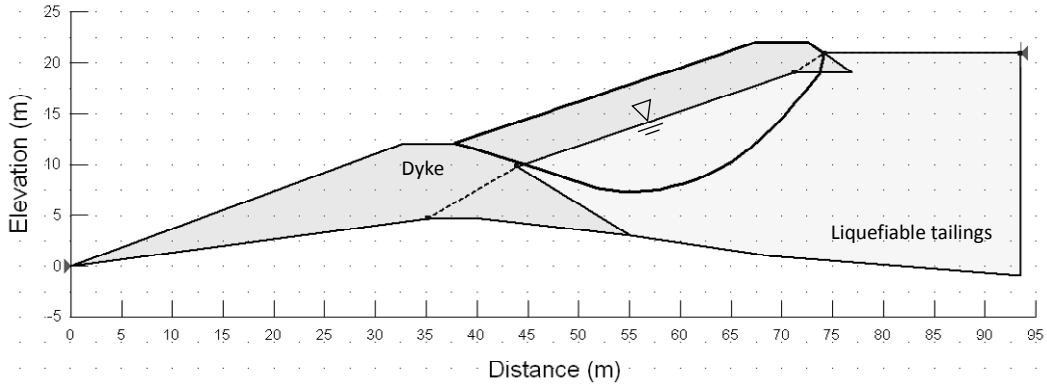


Figure A.12 Mochikoshi Dyke 2: Geometry of model used in scenario 1.

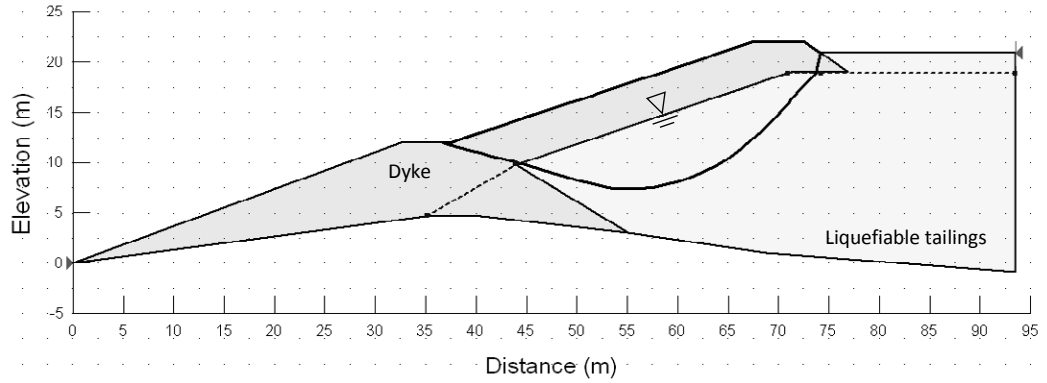


Figure A.13 Mochikoshi Dyke 2: Geometry of model used in scenario 2.

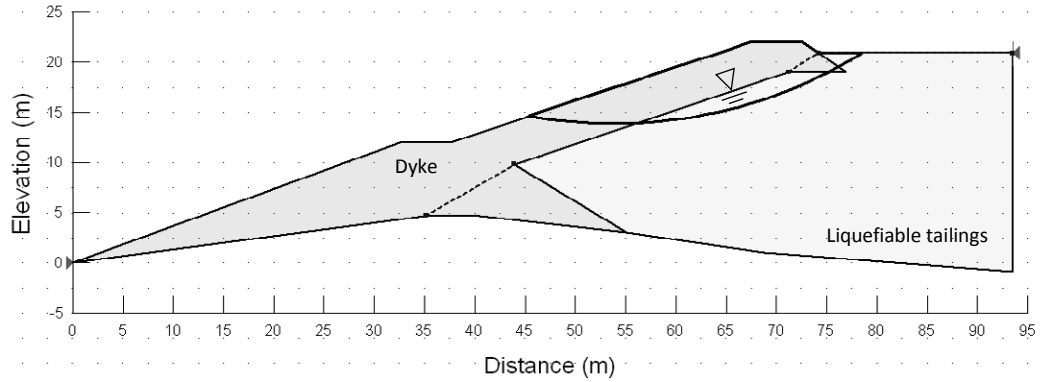


Figure A.14 Mochikoshi Dyke 2: Geometry of model used in scenario 3.

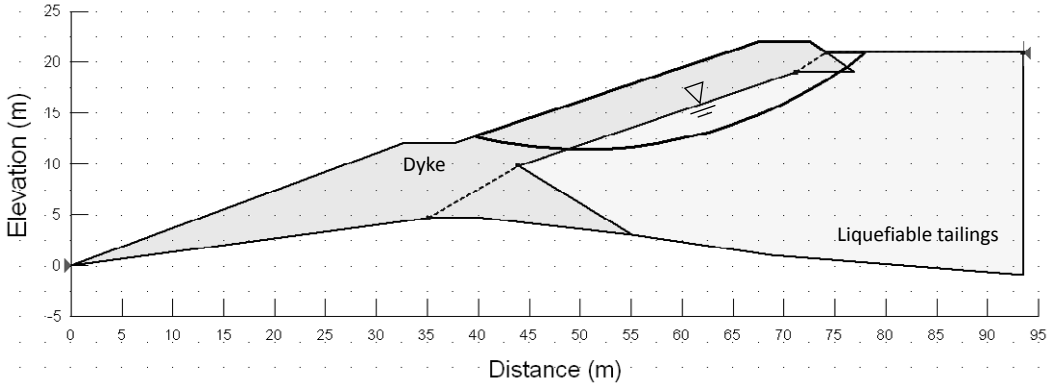


Figure A.15 Mochikoshi Dyke 2: Geometry of model used in scenario 4.

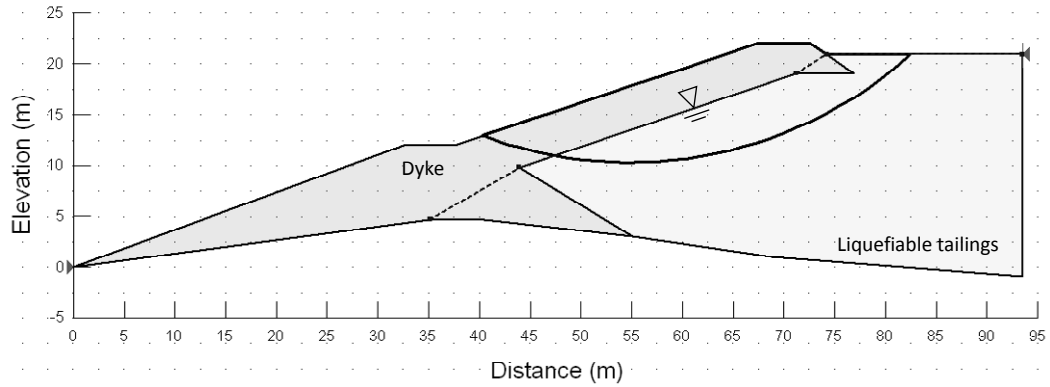


Figure A.16 Mochikoshi Dyke 2: Geometry of model used in scenario 5.

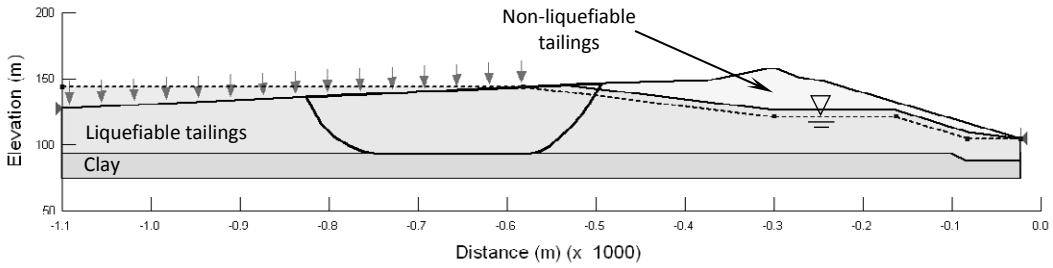


Figure A.17 Dashihe Beach: Geometry of model used in scenario 1.

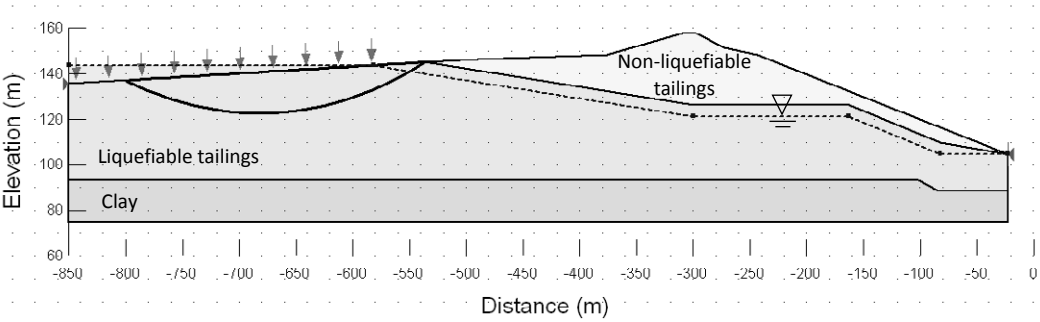


Figure A.18 Dashihe Beach: Geometry of model used in scenarios 2.

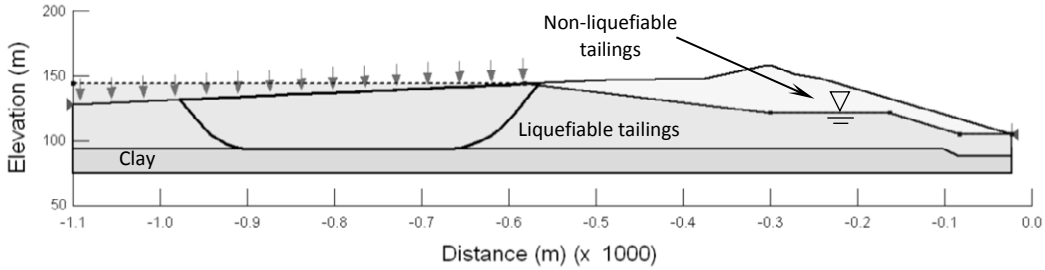


Figure A.19 Dashihe Beach: Geometry of model used in scenario 3.

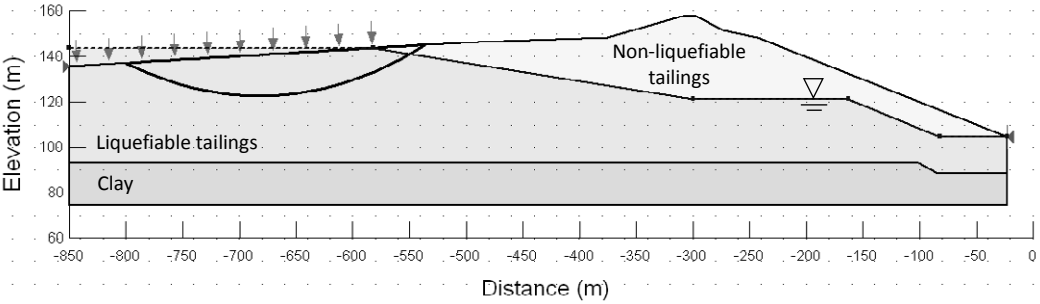


Figure A.20 Dashihe Beach: Geometry of model used in scenario 4.

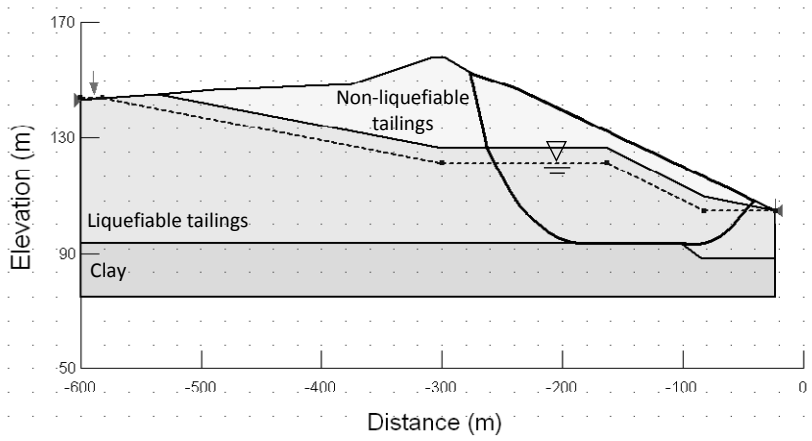


Figure A.21 Dashihe Outer Wall: Geometry of model used in scenario 1.

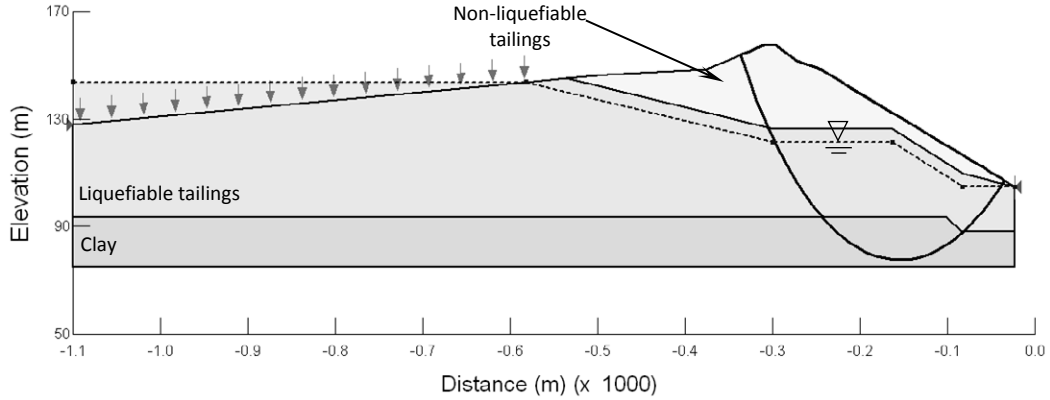


Figure A.22 Dashihe Outer Wall: Geometry of model used in scenario 2.

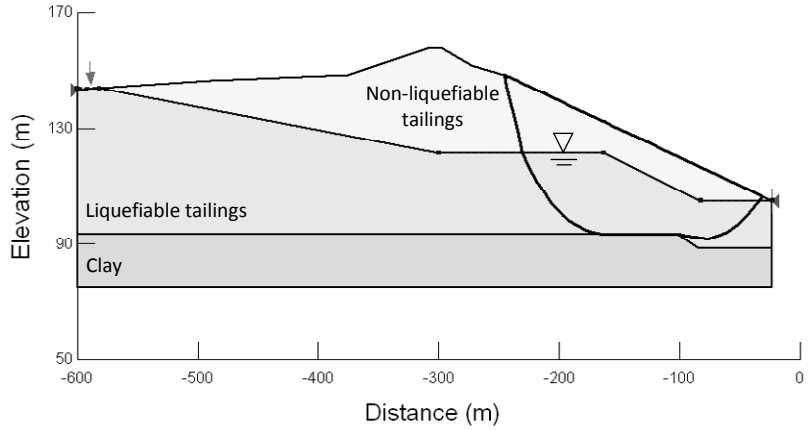


Figure A.23 Dashihe Outer Wall: Geometry of model used in scenario 3.

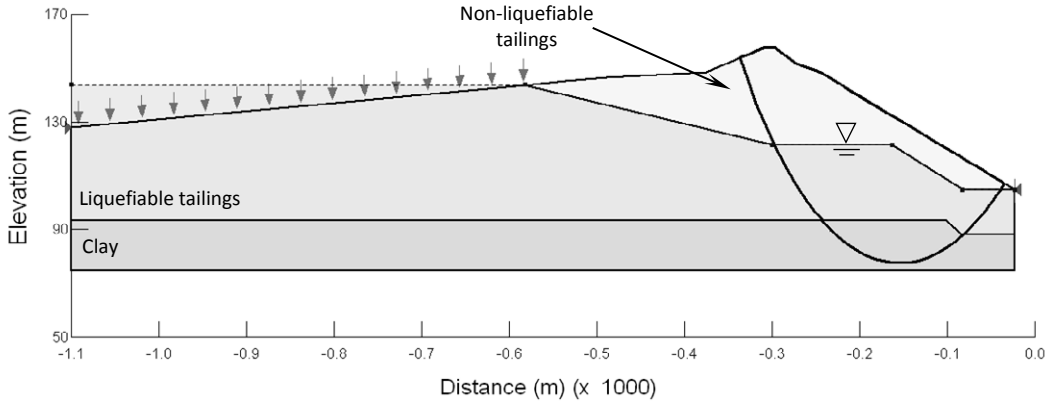


Figure A.24 Dashihe Outer Wall: Geometry of model used in scenario 4.

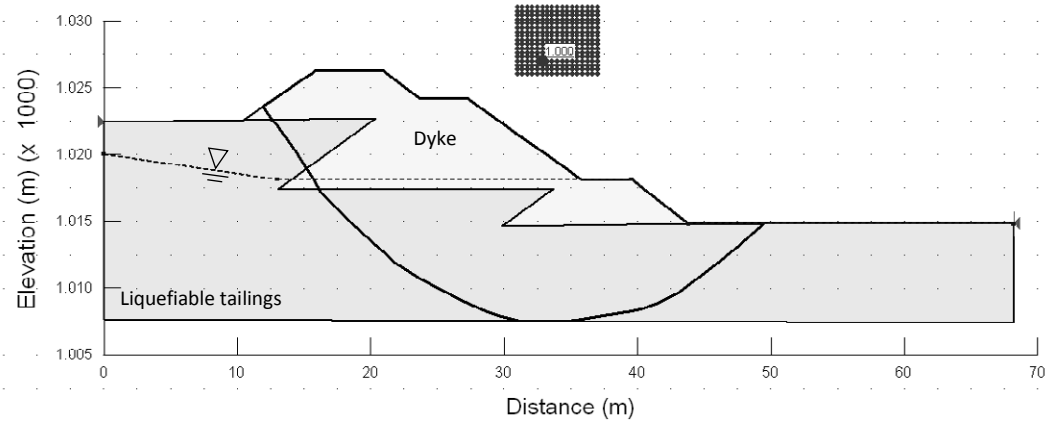


Figure A.25 Sullivan Dam: Geometry of model used in scenario 1.

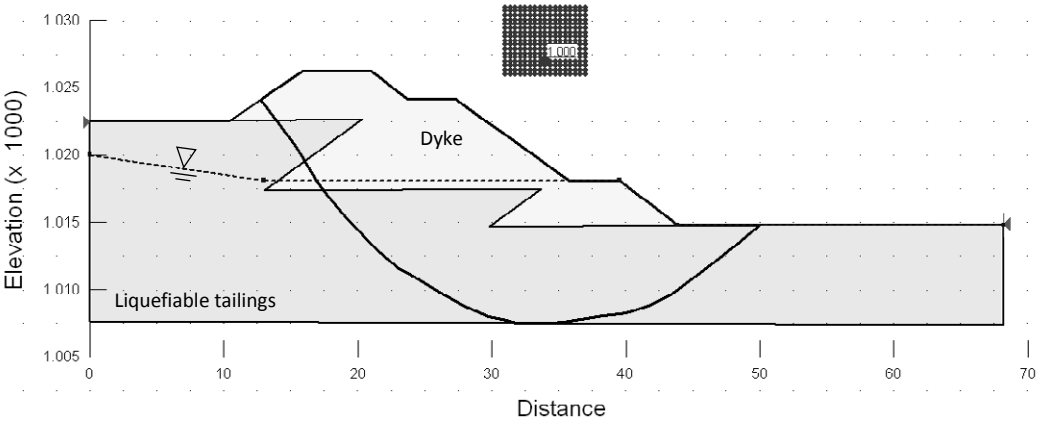


Figure A.26 Sullivan Dam: Geometry of model used in scenario 2.

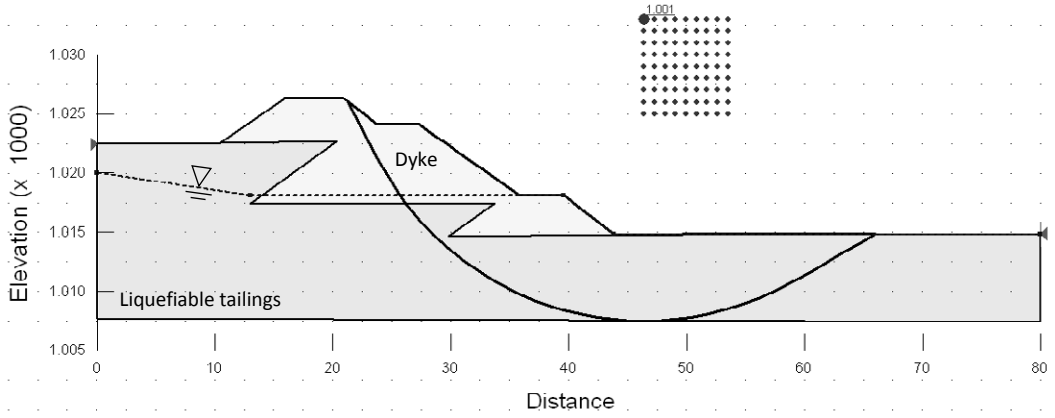


Figure A.27 Sullivan Dam: Geometry of model used in scenario 3.

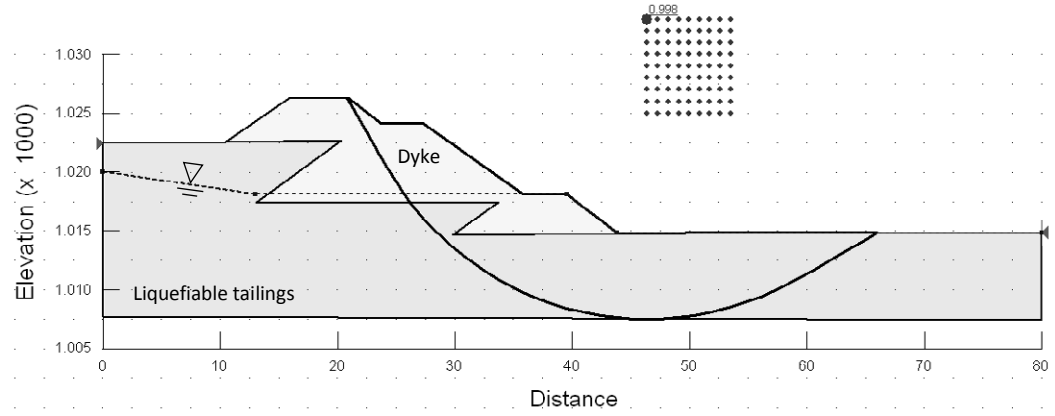


Figure A.28 Sullivan Dam: Geometry of model used in scenario 4.

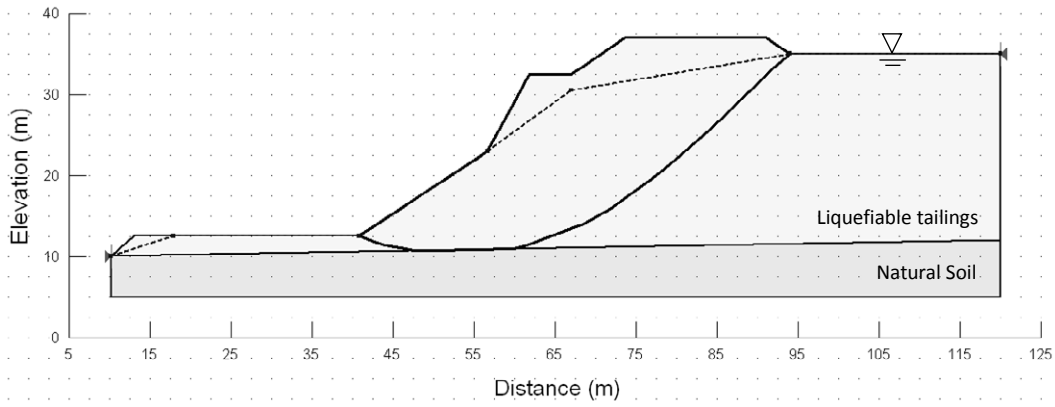


Figure A.29 Merriespruit Dam: Geometry of model used in scenario 1.

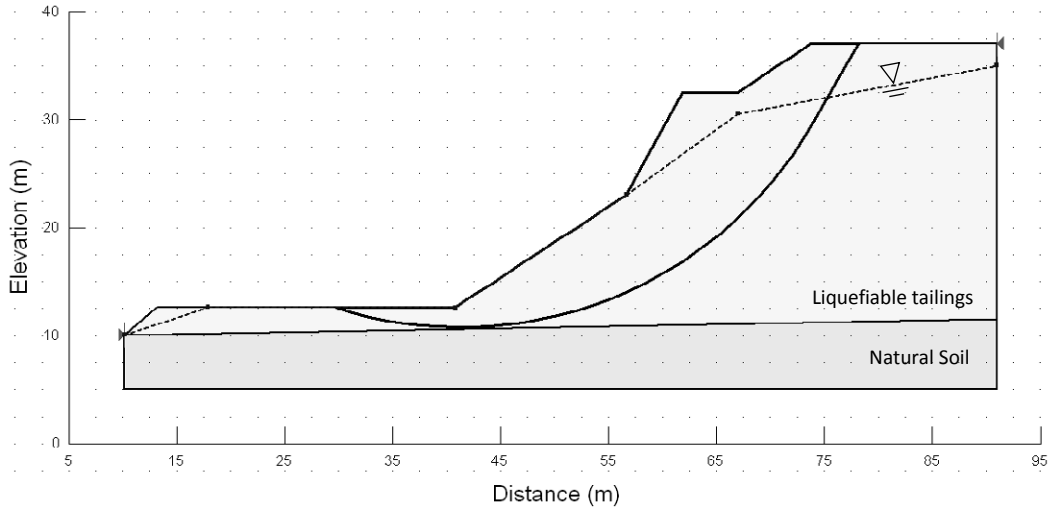


Figure A.30 Merriespruit Dam: Geometry of model used in scenario 2.

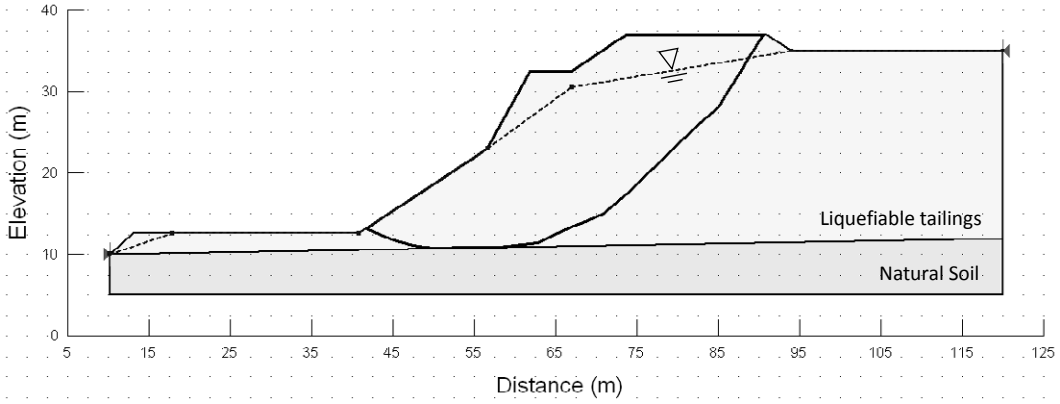


Figure A.31 Merriespruit Dam: Geometry of model used in scenario 3.

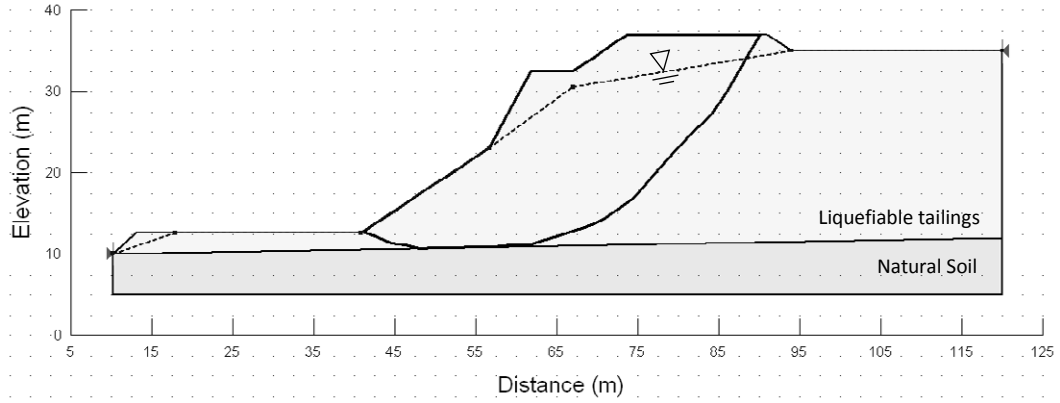


Figure A.32 Merriespruit Dam: Geometry of model used in scenario 4.

Appendix B Additional inputs and results corresponding to the Robertson-based method

B.1 Hokkaido TSF

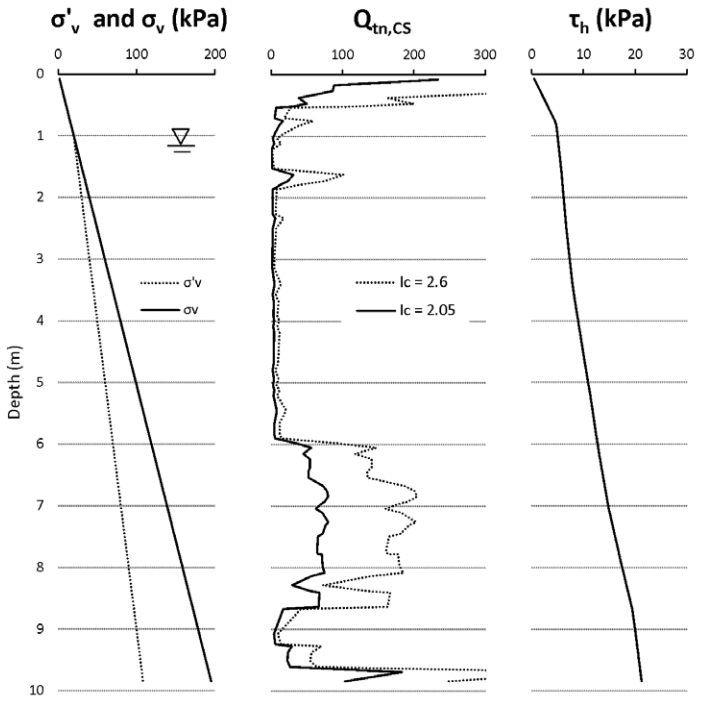


Figure B.1 σ'_v, σ_v, $Q_{tn,cs}$, and τ_h profiles of the Hokkaido TSF.

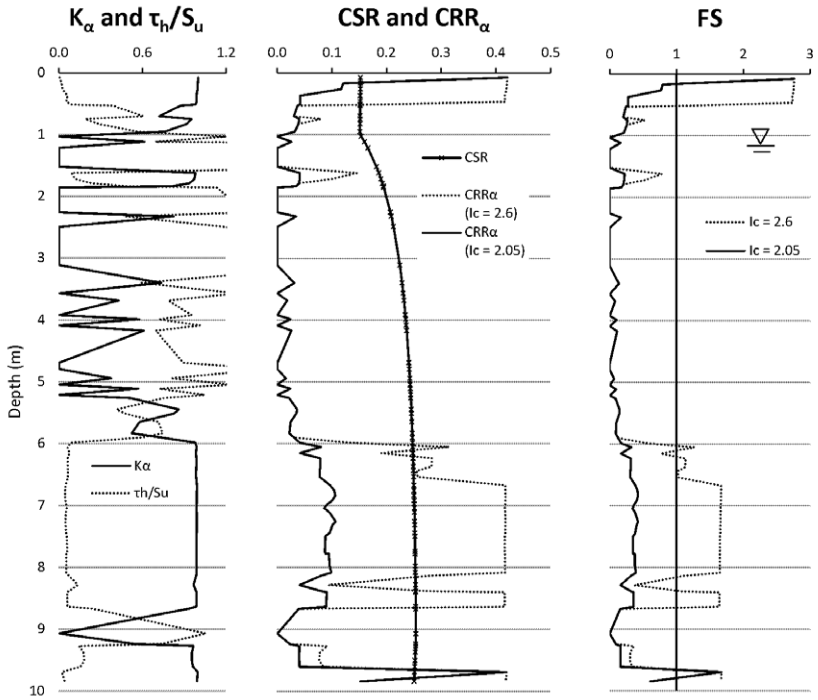


Figure B.2 K_α, τ_h/S_u, CSR, CRR_α, and FS profiles of the Hokkaido TSF.

B.2 Mochikoshi TSF

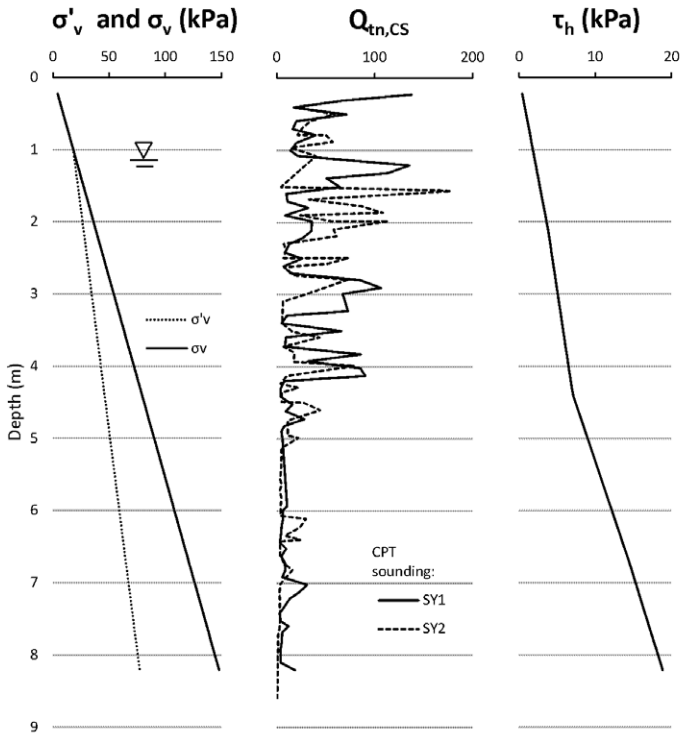


Figure B.3 σ'_v, σ_v, $Q_{tn,cs}$, and τ_h profiles of the Mochikoshi TSF - Dyke 1.

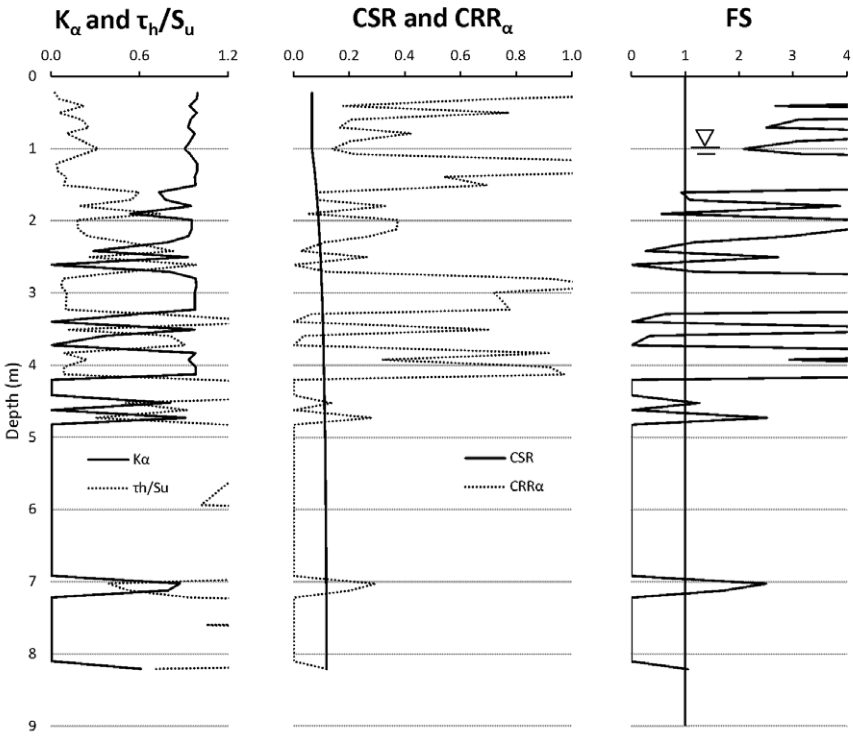


Figure B.4 K_α, τ_h/S_u, CSR, CRR_α, and FS profiles of the Mochikoshi TSF - Dyke 1. Values computed using CPT sounding SY1.

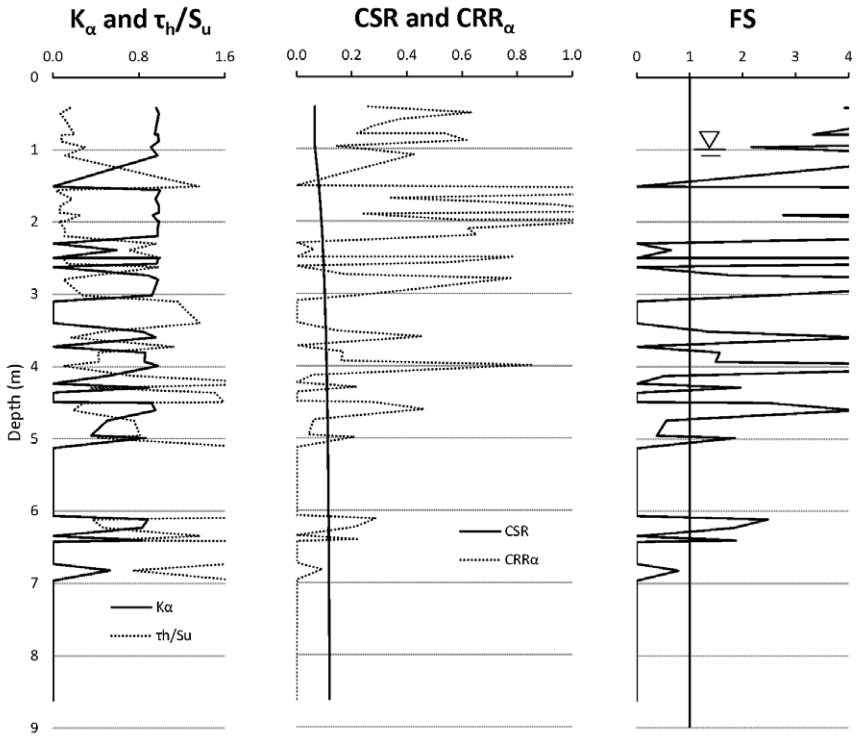


Figure B.5 K_α, τ_h/S_u, CSR, CRR_α, and FS profiles of the Mochikoshi TSF - Dyke 1. Values computed using CPT sounding SY2.

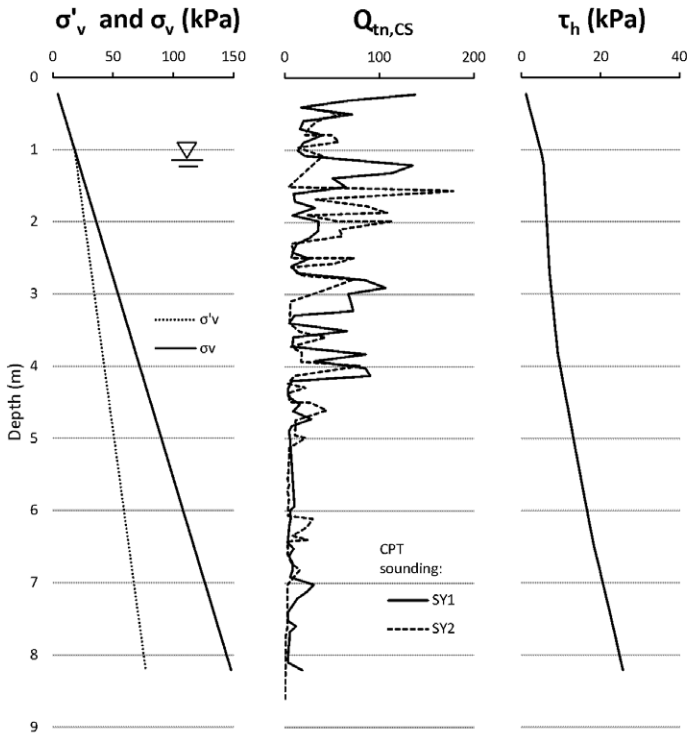


Figure B.6 σ'_v, σ_v, $Q_{tn,cs}$, and τ_h profiles of the Mochikoshi TSF - Dyke 2.

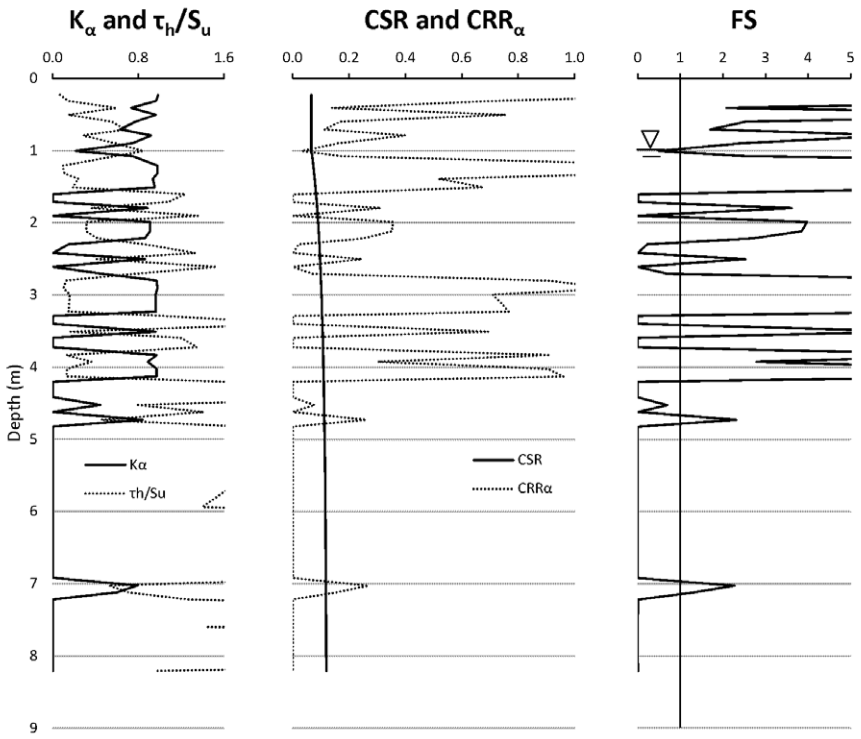


Figure B.7 K_α, τ_h/S_u, CSR, CRR_α, and FS profiles of the Mochikoshi TSF - Dyke 2. Values computed using CPT sounding SY1.

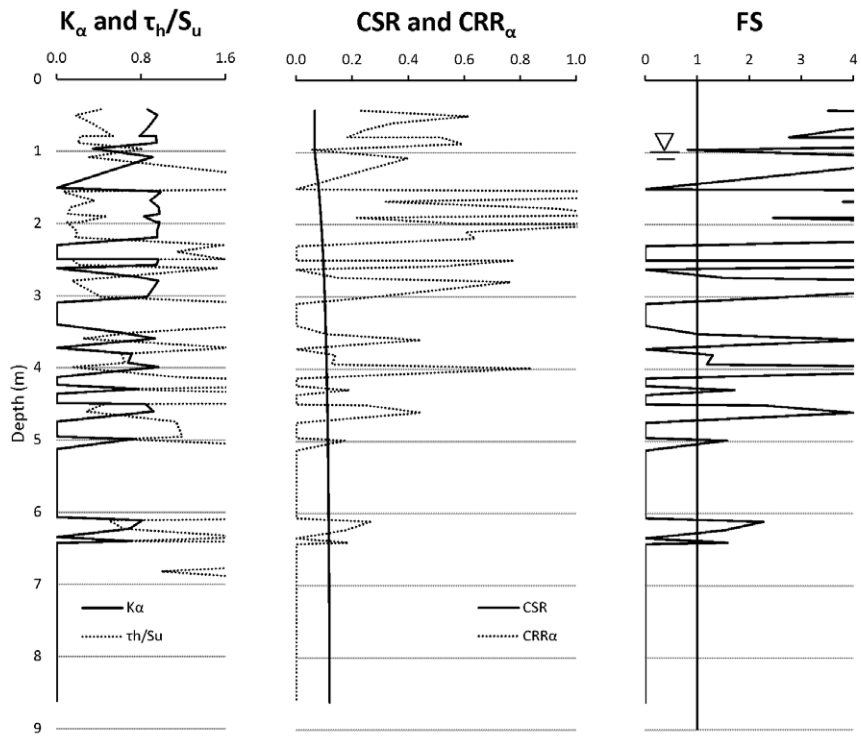


Figure B.8 K_α, τ_h/S_u, CSR, CRR_α, and FS profiles of the Mochikoshi TSF - Dyke 2. Values computed using CPT sounding SY2.

B.3 Dashihe Iron TSF

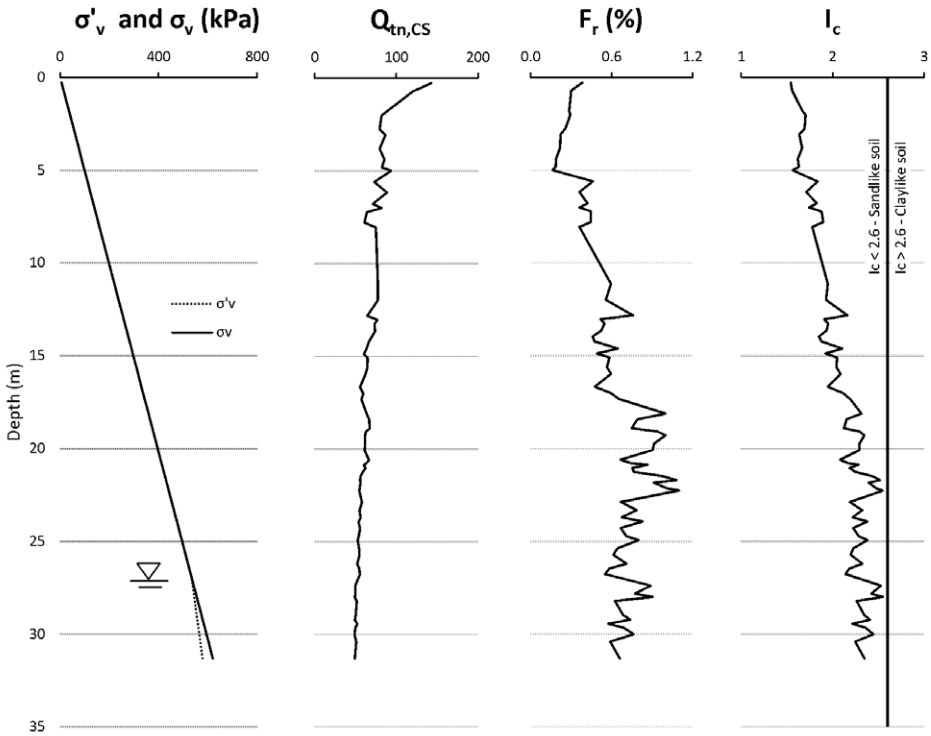


Figure B.9 σ'_v, σ_v, $Q_{tn,cs}$, F_r, and I_c profiles of the Dashihe TSF beach. Values computed with CPT sounding I8.

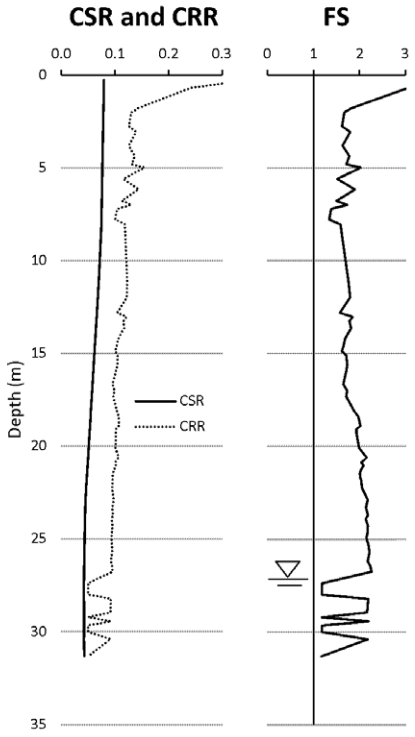


Figure B.10 CSR, CRR, and FS profiles of the Dashihe TSF beach. Values computed with CPT sounding I8.

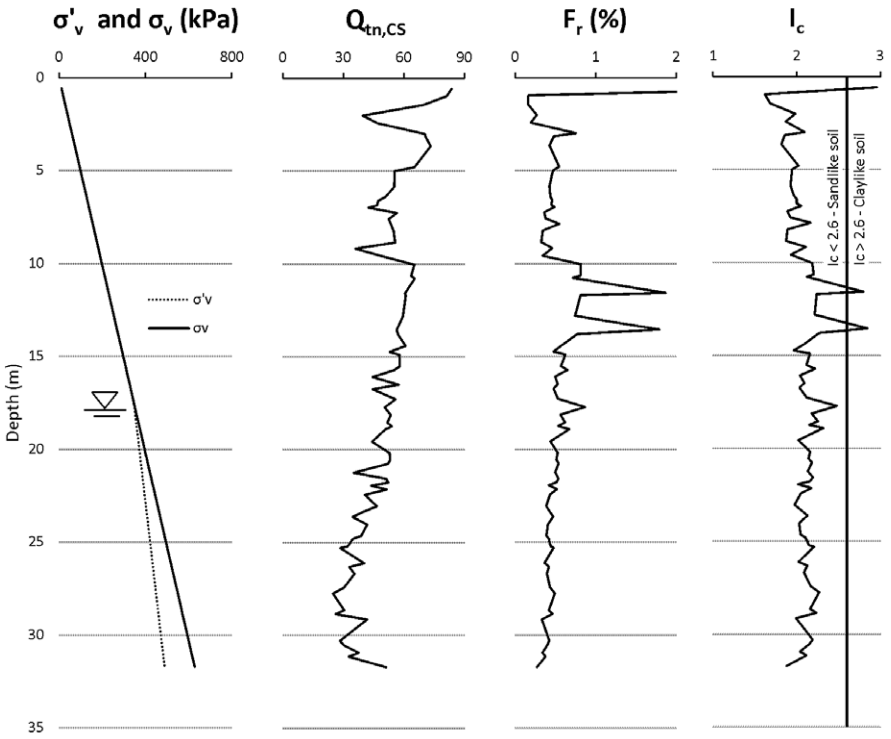


Figure B.11 σ'_v, σ_v, $Q_{tn,cs}$, F_r, and I_c profiles of the Dashihe TSF beach. Values computed with CPT sounding I9.

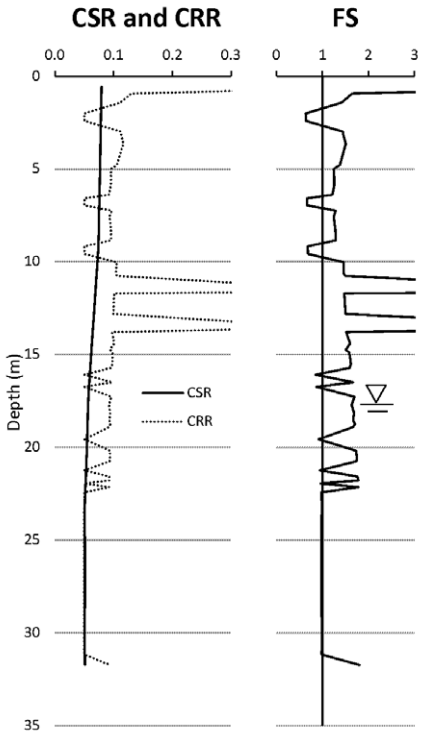


Figure B.12 CSR, CRR, and FS profiles of the Dashihe TSF beach. Values computed with CPT sounding I9.

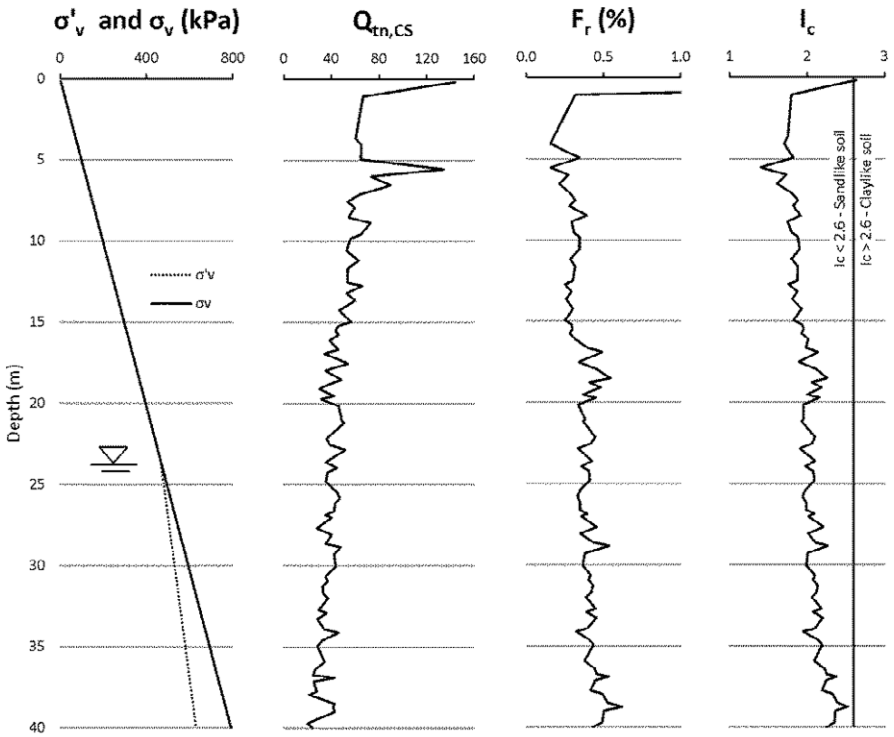


Figure B.13 σ'_v, σ_v, $Q_{tn,cs}$, F_r, and I_c profiles of the Dashihe TSF beach. Values computed with CPT sounding II6.

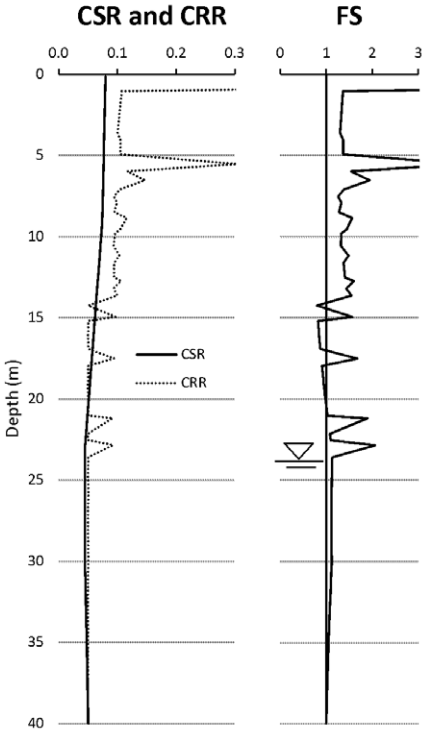


Figure B.14 CSR, CRR, and FS profiles of the Dashihe TSF beach. Values computed with CPT sounding II6.

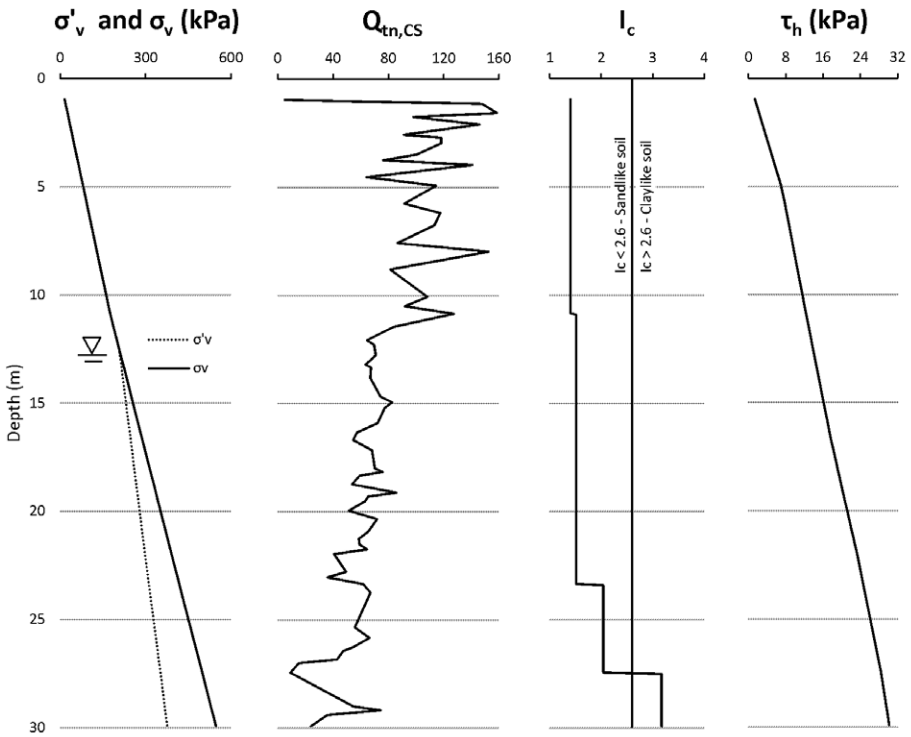


Figure B.15 σ'_v, σ_v, $Q_{tn,cs}$, I_c, and τ_h profiles of the Dashihe TSF outer wall. Values computed with CPT sounding I4.

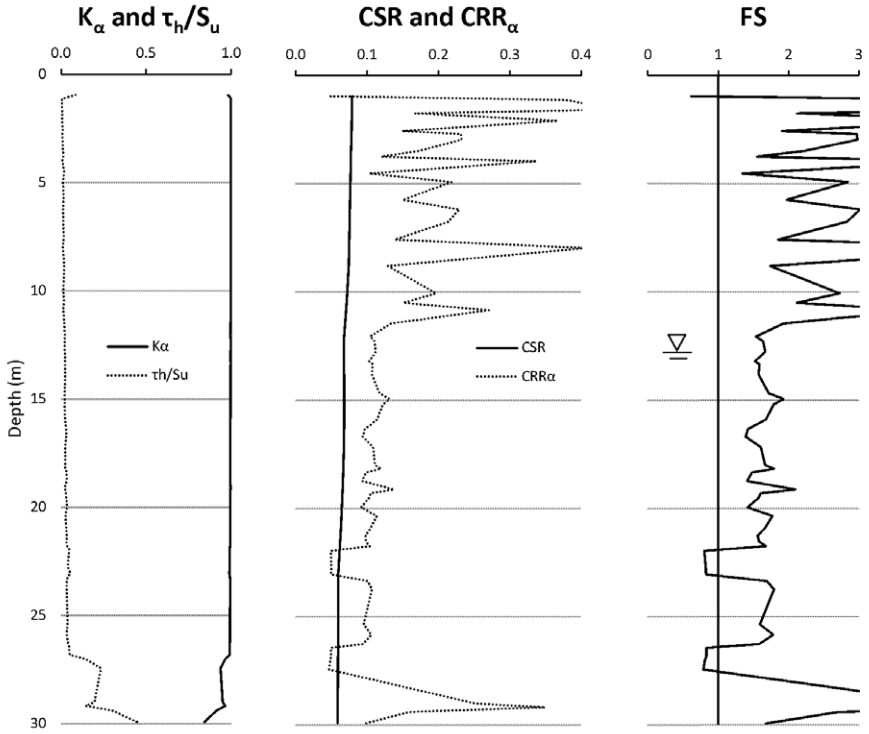


Figure B.16 K_α, τ_h/S_u, CSR, CRR_α, and FS profiles of the Dashihe TSF outer wall. Values computed with CPT sounding I4.

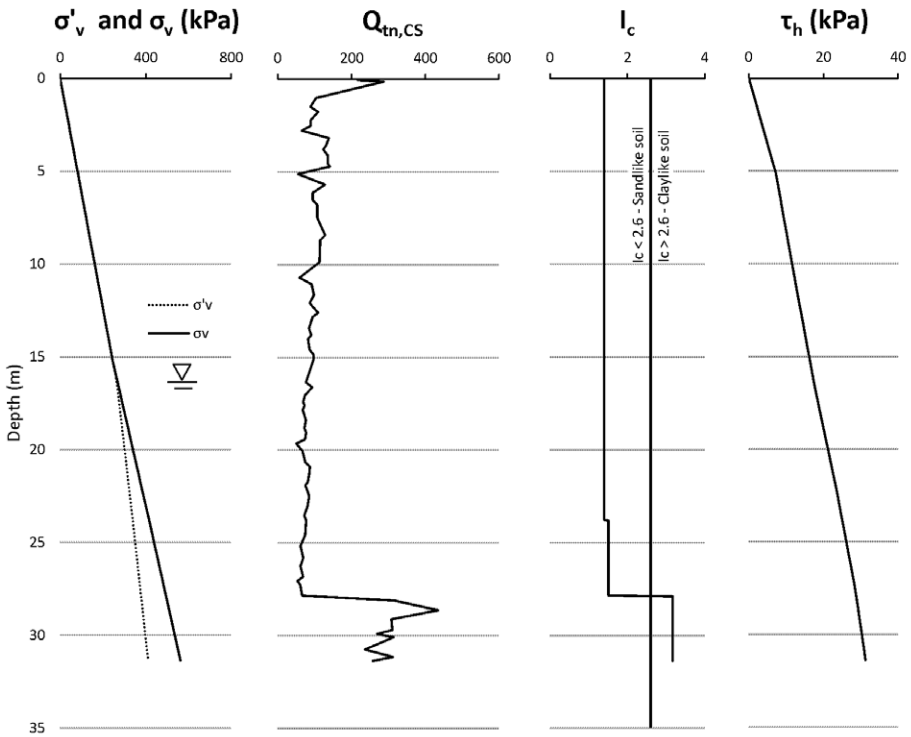


Figure B.17 σ'_v, σ_v, $Q_{tn,cs}$, I_c, and τ_h profiles of the Dashihe TSF outer wall. Values computed with CPT sounding I5.

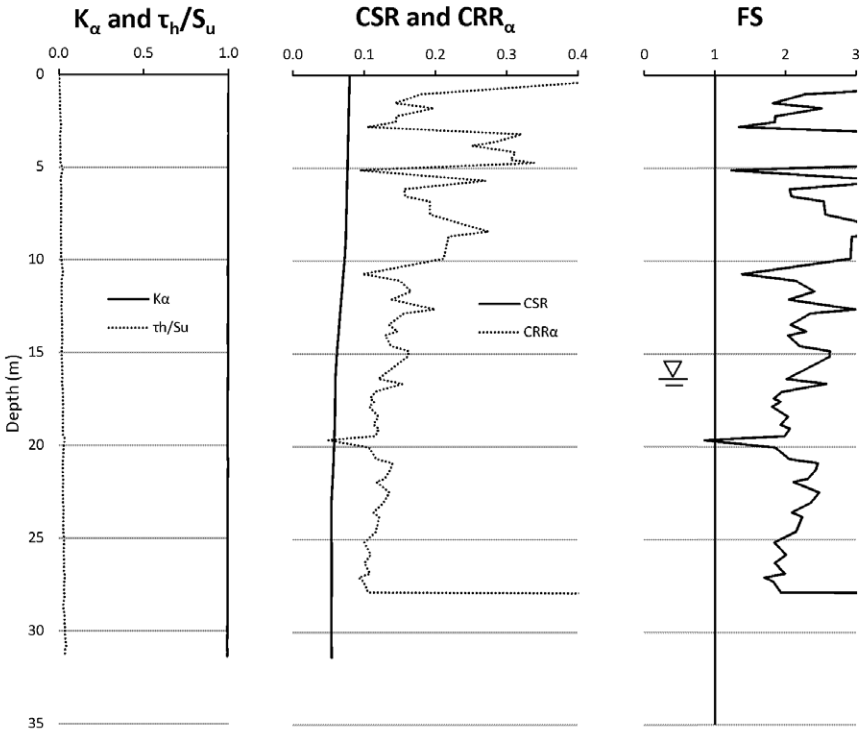


Figure B.18 K_α, τ_h/S_u, CSR, CRR_α, and FS profiles of the Dashihe TSF outer wall. Values computed with CPT sounding I5.

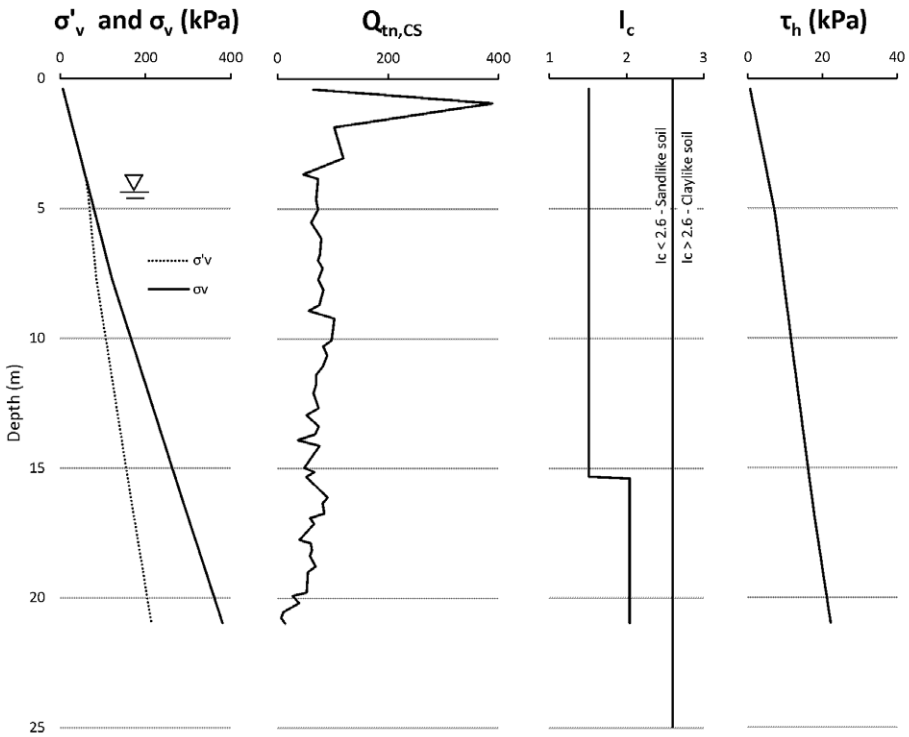


Figure B.19 σ'_v, σ_v, $Q_{tn,cs}$, I_c, and τ_h profiles of the Dashihe TSF outer wall. Values computed with CPT sounding II2.

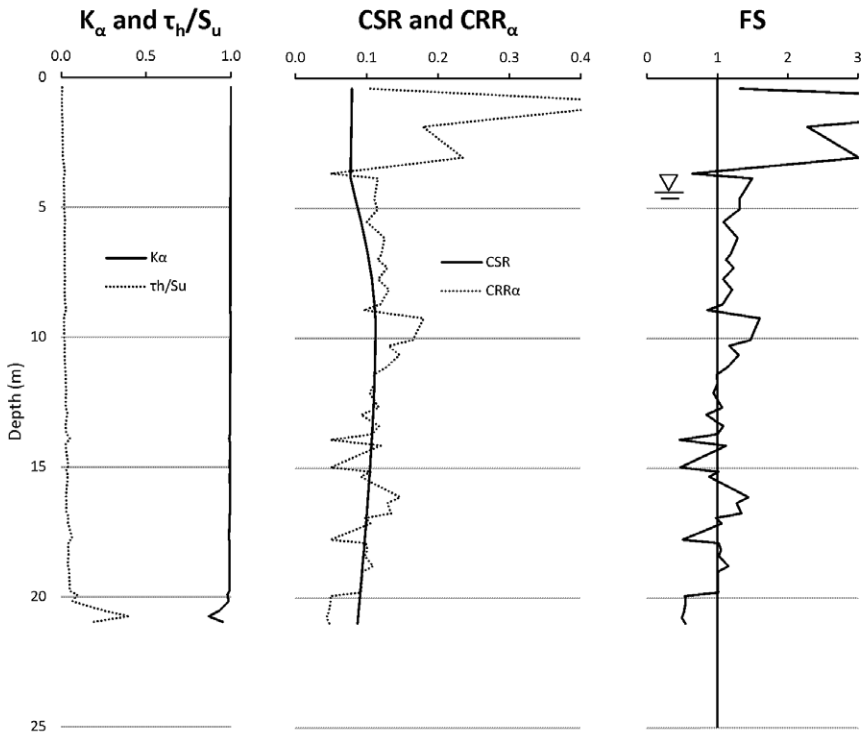


Figure B.20 K_α, τ_h/S_u, CSR, CRR_α, and FS profiles of the Dashihe TSF outer wall. Values computed with CPT sounding II2.

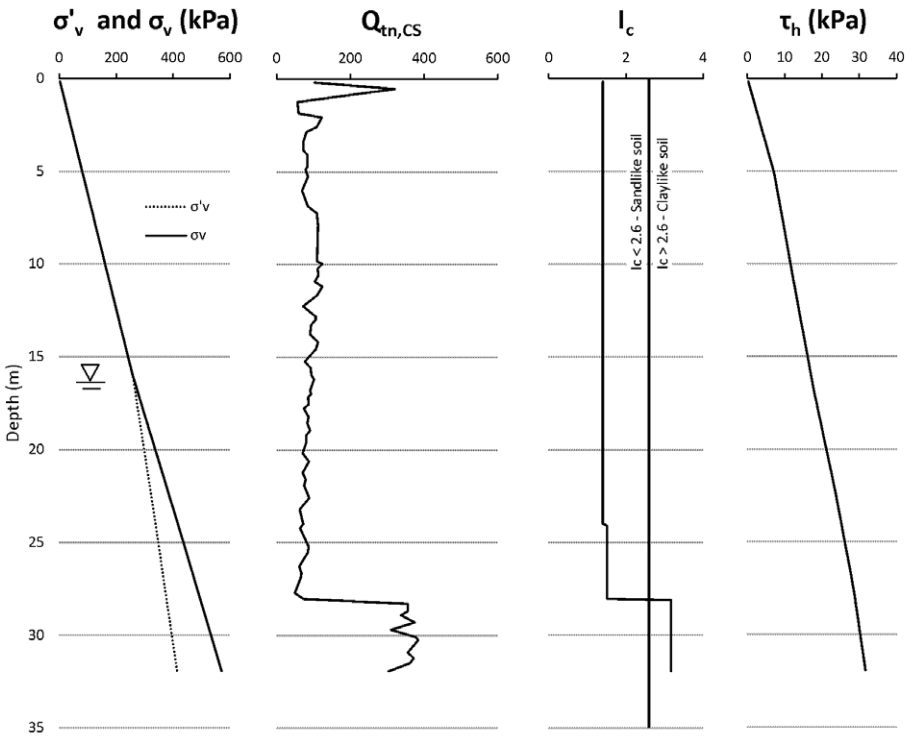


Figure B.21 σ'_v, σ_v, $Q_{tn,cs}$, I_c, and τ_h profiles of the Dashihe TSF outer wall. Values computed with CPT sounding II4.

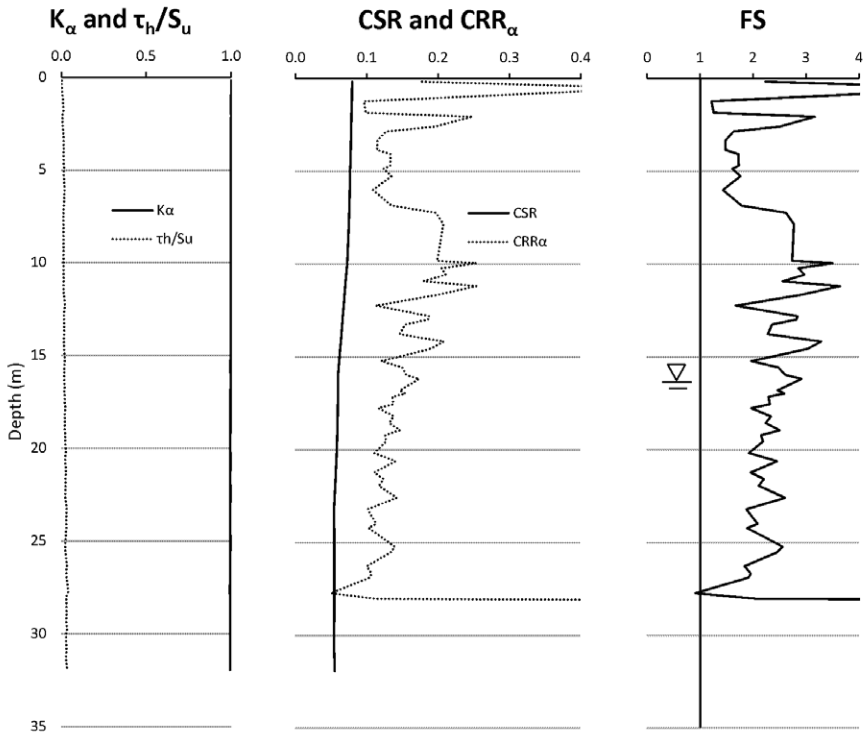


Figure B.22 K_α, τ_h/S_u, CSR, CRR_α, and FS profiles of the Dashihe TSF outer wall. Values computed with CPT sounding II4.

B.4 Sullivan TSF

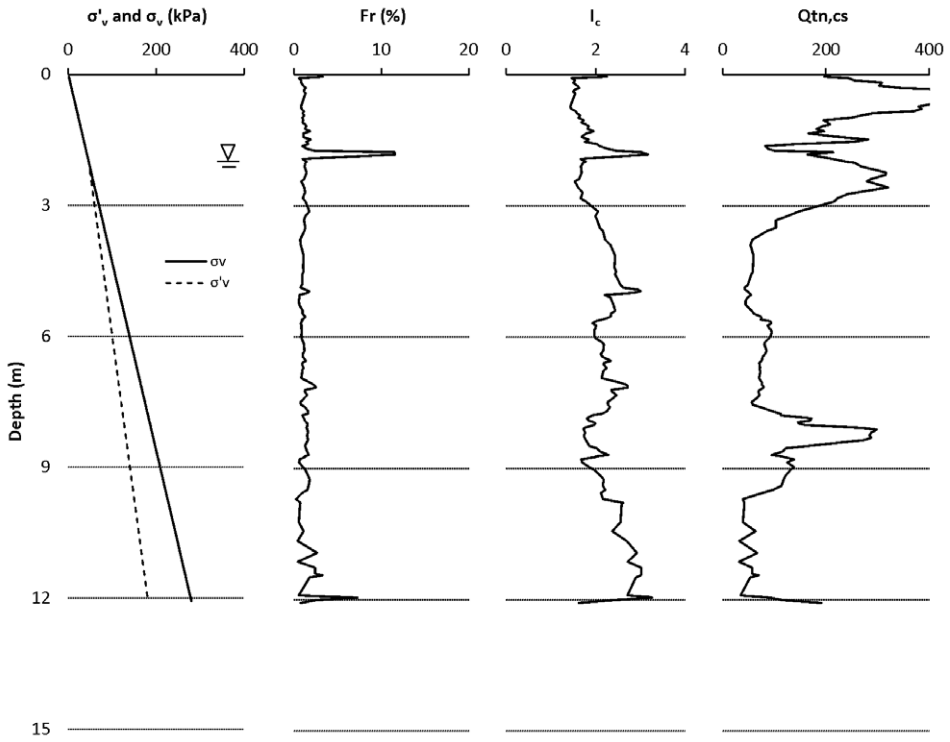


Figure B.23 σ'_v, σ_v, F_r, I_c, and $Q_{tn,cs}$ profiles of the Sullivan TSF. Values computed with CPT sounding CP91-29.

B.5 Merriespruit TSF

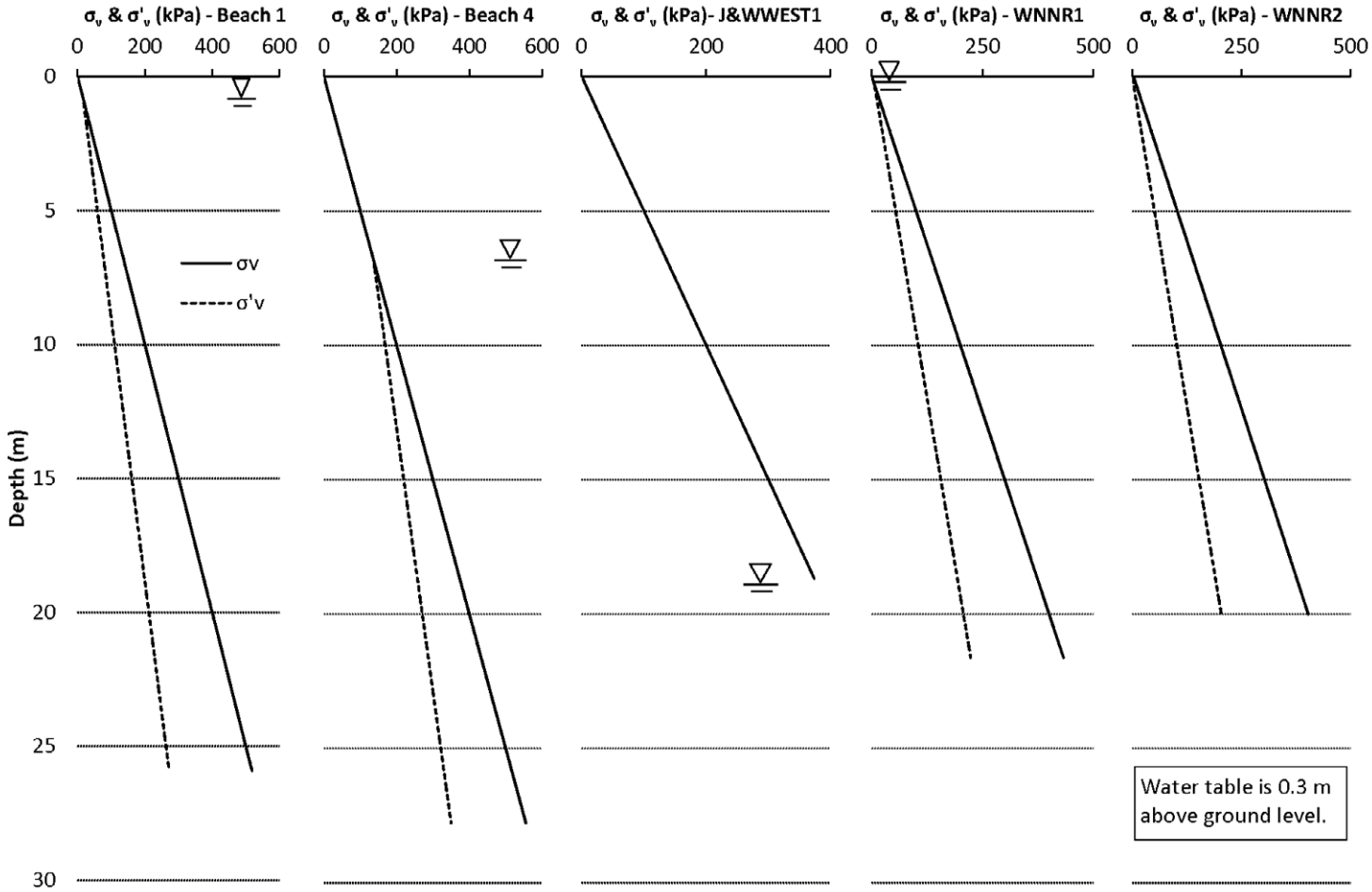


Figure B.24 Profiles of total vertical stress (σ_v) and effective vertical stress (σ'_v) for the different CPTu soundings conducted at the Merriespruit TSF.

Appendix C Values of mean effective stress (p'), deviator stress (q), and void ratio (e) used to calculate the SSL parameters in Table 6.3

The soiltype symbols used in this appendix are the same as those used in Table 6.2. When q and p' coordinates were available, M was calculated by fitting Eq. 2.2 to the data. Otherwise M was estimated as indicated below. When the data was extracted from a figure, the figure was first digitised and the pixel coordinates were then converted to coordinates in the relevant units. Cells with grey shading contain values that were not considered in the calculation of SSL parameters as they defined a curved SSL that could not be modelled with Eq. 2.1. The SSL parameters of soiltypes with symbols CDS 1 and CDS 2 are reported in Cho et al. (2006), and the SSL parameters of soiltypes with symbols JB1, JB2 and JB3 are reported in Jefferies and Been (2006). Nonetheless, an independent calculation of these SSL parameters was done herein when data was available to do so.

C.1 Soiltypes ARM

All data was collected from Naeini and Baziar (2004). Values of σ'_3 and e were taken from Figure 4 (only data corresponding to the static tests were considered). Values of q were read off Table 2 by taking S_{us} = q/2. This interpretation of S_{us} is based on the caption of Figure 6 which refers to S_{us} as a shear stress; hence it is half of the deviator stress.

Ardebil sand-silt mix (0)		
e	σ'_3 (kPa)	q (kPa
1.049	39.8	191.2
0.991	85.7	288.6
0.941	141.9	441.2
Γ_{50} = 1.13; λ = 0.242; M = 1.57		

Ardebil sand-silt mix (10)		
e	σ'_3 (kPa)	q (kPa)
1.033	37.9	152.8
0.975	79.8	247.0
0.905	139.9	372.8
Γ_{50} = 1.10; λ = 0.269; M = 1.46		

Ardebil sand-silt mix (20)		
e	σ'_3 (kPa)	q (kPa)
0.920	36.2	129.6
0.888	71.1	220.4
0.818	141.2	311.2
Γ_{50} = 0.97; λ = 0.205; M = 1.36		

Ardebil sand-silt mix (30)		
e	σ'_3 (kPa)	q (kPa)
0.902	28.0	116.4
0.843	79.8	175.6
0.765	172.5	275.6
Γ_{50} = 0.93; λ = 0.227; M = 1.12		

Ardebil sand-silt mix (35)		
e	σ'_3 (kPa)	q (kPa)
0.866	29.9	100.6
0.786	89.8	166.8
0.706	178.4	234.4
Γ_{50} = 0.90; λ = 0.261; M = 1.00		

Ardebil sand-silt mix (50)		
e	σ'_3 (kPa)	q (kPa)
0.880	32.0	110.6
0.803	104.1	170.6
0.737	183.5	255.4
Γ_{50} = 0.92; λ = 0.239; M = 1.01		

Ardebil sand-silt mix (100)		
e	σ'_3 (kPa)	q (kPa)
0.946	34.0	172.4
0.885	92.0	247.6
0.858	121.9	350.6
Γ_{50} = 1.00; λ = 0.214; M = 1.49		

C.2 Soiltypes ASM

All data was collected from Papadopoulou and Tika (2008). Values of p' and e were taken from Figure 7. Values of M were read off Table 2.

Assyros sand-silt mix (0)			
p' (kPa)	e	p' (kPa)	e
74	0.771	1071	0.635
107	0.745	1178	0.648
125	0.736	1273	0.650
158	0.752	1333	0.632
210	0.730	1405	0.615
809	0.679	--	--
Γ_{50} = 0.79; λ = 0.108; M = 1.3553			

Assyros sand-silt mix (5)			
p' (kPa)	e	p' (kPa)	e
250	0.710	1230	0.609
1035	0.667	1431	0.604
Γ_{50} = 0.76; λ = 0.069; M = 1.4123			

Assyros sand-silt mix (10)			
p' (kPa)	e	p' (kPa)	e
43	0.700	190	0.644
45	0.690	1797	0.535
Γ_{50} = 0.69; λ = 0.099; M = 1.4469			

Assyros sand-silt mix (15)			
p' (kPa)	e	p' (kPa)	e
40	0.614	1091	0.528
153	0.576	1337	0.445
191	0.570	1366	0.433
874	0.551	1609	0.376
Γ_{50} = 0.60; λ = 0.046; M = 1.5441			

Assyros sand-silt mix (25)			
p' (kPa)	e	p' (kPa)	e
16	0.503	1038	0.399
33	0.500	1700	0.384
185	0.492	--	--
Γ_{50} = 0.49; λ = 0.061; M = 1.4083			

Assyros sand-silt mix (35)			
p' (kPa)	e	p' (kPa)	e
5	0.456	252	0.405
38	0.443	742	0.384
61	0.404	1084	0.385
154	0.431	1422	0.365
Γ_{50} = 0.43; λ = 0.035; M = 1.4390			

Assyros sand-silt mix (60)			
p' (kPa)	e	p' (kPa)	e
10	0.550	785	0.462
169	0.515	1223	0.442
479	0.489	--	--
Γ_{50} = 0.52; λ = 0.048; M = 1.4398			

Assyros sand-silt mix (100)			
p' (kPa)	e	p' (kPa)	e
158	0.752	901	0.647
685	0.688	--	--
Γ_{50} = 0.82; λ = 0.125; M = 1.5147			

C.3 Soiltypes CP

Values of p' and e were extracted from Figure 12 of Kikumoto et al. (2010). Value of M is reported in Muir-Wood and Maeda (2008) as 16 degrees.

DEM discs 1 (0)			
p' (kPa)	e	p' (kPa)	e
71	0.238	689	0.231
74	0.241	693	0.225
135	0.231	2709	0.204
149	0.240	2821	0.190
Γ_{50} = 0.25; λ = 0.025; M = 0.61			

DEM discs 2 (0)			
p' (kPa)	e	p' (kPa)	e
74	0.232	679	0.223
81	0.224	696	0.217
142	0.233	2632	0.192
145	0.223	2858	0.186
Γ_{50} = 0.24; λ = 0.024; M = 0.61			

DEM discs 3 (0)			
p' (kPa)	e	p' (kPa)	e
71	0.210	672	0.202
81	0.214	2584	0.181
149	0.211	2861	0.174
635	0.199	--	--
Γ_{50} = 0.22; λ = 0.022; M = 0.61			

DEM discs 4 (0)			
p' (kPa)	e	p' (kPa)	e
81	0.190	693	0.178
81	0.188	696	0.181
149	0.188	2828	0.159
152	0.186	2929	0.155
Γ_{50} = 0.20; λ = 0.020; M = 0.61			

C.4 Soiltype DUZ

All data was collected from Papadopoulou and Tika (2008). Values of p' and e were taken from Figure 17. Values of M were read off Table 2.

Duzce-1 (13)			
p' (kPa)	e	p' (kPa)	e
35	0.533	580	0.482
47	0.608	926	0.440
Γ_{50} = 0.56; λ = 0.085; M = 1.5013			

C.5 Soiltypes GB

All data was read off Table 3.7 in Li et al. (2013).

Glass balls 1 (0)		
e	p' (kPa)	q (kPa
0.671	138.05	112.11
0.663	275.61	225.27
0.655	556.48	449.52
0.645	1363.73	1253.52
Γ_{50} = 0.68; λ = 0.026; M = 0.90		

Glass balls 2 (0)		
e	p' (kPa)	q (kPa
0.643	119.88	96.84
0.633	252.60	199.41
0.623	498.31	403.15
0.621	1254.83	1142.17
Γ_{50} = 0.65; λ = 0.022; M = 0.89		

Glass balls 3 (0)		
e	p' (kPa)	q (kPa
0.586	138.16	113.22
0.577	277.94	227.23
0.566	543.22	445.39
0.559	840.30	760.28
Γ_{50} = 0.60; λ = 0.035; M = 0.87		

Glass balls 4 (0)		
e	p' (kPa)	q (kPa
0.470	131.63	102.94
0.460	268.63	212.35
0.462	360.44	327.34
0.448	545.95	450.04
Γ_{50} = 0.48; λ = 0.032; M = 0.84		

Glass balls 5 (0)		
e	p' (kPa)	q (kPa
0.421	136.62	109.38
0.413	144.84	131.64
0.404	271.05	227.42
0.392	572.55	453.40
Γ_{50} = 0.44; λ = 0.042; M = 0.81		

Glass balls 6 (10)		
e	p' (kPa)	q (kPa
0.342	75.12	65.83
0.332	131.02	106.35
0.321	274.61	222.82
0.304	579.13	477.66
Γ_{50} = 0.35; λ = 0.042; M = 0.82		

C.6 Soiltypes HCM

All data was collected from Yang et al. (2006). Values of p' and e were taken from Figures 10 and 11. Values of M were calculated from Figure 14.

HKS sand & CHB silt mix (0)			
p' (kPa)	e	p' (kPa)	e
14	0.854	215	0.825
29	0.850	268	0.807
77	0.842	335	0.809
111	0.828	--	--
Γ_{50} = 0.84; λ = 0.035; M = 1.64			

HKS sand & CHB silt mix (5)			
p' (kPa)	e	p' (kPa)	e
9	0.789	236	0.760
54	0.771	275	0.756
98	0.781	306	0.752
121	0.779	--	--
Γ_{50} = 0.78; λ = 0.022; M = n/a			

HKS sand & CHB silt mix (10)			
p' (kPa)	e	p' (kPa)	e
51	0.715	221	0.650
64	0.693	286	0.665
111	0.675	495	0.679
115	0.709	--	--
Γ_{50} = 0.70; λ = 0.043; M = n/a			

HKS sand & CHB silt mix (15)			
p' (kPa)	e	p' (kPa)	e
7	0.678	109	0.633
7	0.670	226	0.607
61	0.658	283	0.615
70	0.636	314	0.584
Γ_{50} = 0.64; λ = 0.046; M = n/a			

HKS sand & CHB silt mix (20)			
p' (kPa)	e	p' (kPa)	e
1.4	0.650	115	0.560
2.5	0.638	221	0.543
7	0.624	268	0.556
32	0.579	515	0.482
83	0.534	--	--
Γ_{50} = 0.57; λ = 0.056; M = n/a			

HKS sand & CHB silt mix (30)			
p' (kPa)	e	p' (kPa)	e
0.1	0.626	22	0.477
0.1	0.612	108	0.544
0.5	0.603	209	0.536
0.7	0.588	272	0.530
1.0	0.532	528	0.448
Γ_{50} = 0.52; λ = 0.032; M = 1.73			

HKS sand & CHB silt mix (50)			
p' (kPa)	e	p' (kPa)	e
0.1	0.758	109	0.683
0.4	0.727	139	0.567
1.2	0.746	165	0.523
1.8	0.667	208	0.673
3	0.635	262	0.673
Γ_{50} = 0.64; λ = 0.038; M = 1.66			

HKS sand & CHB silt mix (70)			
p' (kPa)	e	p' (kPa)	e
1.0	0.981	12	0.748
1.3	1.006	105	0.900
2.2	0.958	126	0.723
3	0.815	194	0.877
4	0.790	253	0.885
Γ_{50} = 0.85; λ = 0.041; M = n/a			

HKS sand & CHB silt mix (94)			
p' (kPa)	e	p' (kPa)	e
0.7	1.242	6	1.046
2.3	1.267	97	1.150
2.3	1.219	152	0.929
4	0.983	184	1.125
5	1.094	240	1.113
Γ_{50} = 1.09; λ = 0.051; M = 1.52			

C.7 Soiltypes HOS

All data was read off Table 3.3 in Li et al. (2013).

Hostun sand 1 (0)		
e	p' (kPa)	q (kPa
0.779	25.9	29.61
0.732	162.5	187.02
0.719	328.3	384.76
0.700	639.0	712.35
Γ_{50} = 0.76; λ = 0.056; M = 1.13		

Hostun sand 2 (0)		
e	p' (kPa)	q (kPa
0.780	11.48	12.76
0.726	158.40	174.29
0.727	159.15	177.46
0.723	160.62	176.62
0.720	224.33	240.99
0.720	249.45	271.34
0.713	316.40	339.08
0.700	497.45	542.40
0.690	544.12	603.38
0.691	629.93	650.90
Γ_{50} = 0.75; λ = 0.051; M = 1.08		

Hostun sand 3 (0)		
e	p' (kPa)	q (kPa
0.774	10	10.21
0.770	13	13.77
0.743	61	72.96
0.714	160	176.75
0.695	321	354.58
0.675	640	701.48
Γ_{50} = 0.74; λ = 0.054; M = 1.10		

Hostun sand 4 (0)		
e	p' (kPa)	q (kPa
0.694	162	183.08
0.671	323	370.13
0.681	326	368.57
0.662	644	714.06
Γ_{50} = 0.72; λ = 0.053; M = 1.12		

Hostun sand 5 (0)		
e	p' (kPa)	q (kPa
0.618	164.66	190.97
0.608	324.70	374.11
0.606	651.96	755.89
Γ_{50} = 0.63; λ = 0.020; M = 1.16		

Hostun sand 6 (0)		
e	p' (kPa)	q (kPa
0.602	164.52	190.55
0.595	325.07	375.22
0.586	645.21	738.64
Γ_{50} = 0.62; λ = 0.027; M = 1.15		

Hostun sand 7 (0)		
e	p' (kPa)	q (kPa
0.730	158.90	176.71
0.706	315.26	347.79
0.697	632.56	700.67
Γ_{50} = 0.76; λ = 0.055; M = 1.11		

Hostun sand 8 (10)		
e	p' (kPa)	q (kPa
0.723	165.31	178.89
0.710	318.12	351.36
0.698	627.13	669.39
Γ_{50} = 0.75; λ = 0.043; M = 1.08		

C.8 Soiltypes MLM

All data was collected from Huang et al. (2004). Values of p' and e were taken from Figure 5. Values of M were taken from Figure 4c.

Mai Liao sand-silt mix (0)			
p' (kPa)	e	p' (kPa)	e
70	0.894	256	0.815
84	0.887	383	0.772
132	0.849	464	0.777
218	0.862	--	--
Γ_{50} = 0.92; λ = 0.148; M = 1.24			

Mai Liao sand-silt mix (15)			
p' (kPa)	e	p' (kPa)	e
20	0.767	183	0.686
69	0.732	209	0.646
93	0.711	214	0.669
120	0.700	265	0.669
Γ_{50} = 0.73; λ = 0.100; M = 1.24			

Mai Liao sand-silt mix (30)			
p' (kPa)	e	p' (kPa)	e
16	0.669	135	0.588
26	0.669	171	0.572
67	0.591	179	0.561
93	0.625	225	0.538
130	0.568	261	0.536
Γ_{50} = 0.62; λ = 0.114; M = 1.24			

Mai Liao sand-silt mix (50)			
p' (kPa)	e	p' (kPa)	e
35	0.649	109	0.629
37	0.590	130	0.498
37	0.563	242	0.566
38	0.554	297	0.534
41	0.563	285	0.480
Γ_{50} = 0.58; λ = 0.070; M = 1.21			

C.9 Soiltypes MER

Values of p', e, and q of Merriespruit tailings FC = 0% were tabulated in Tshabalala (2003). Values of p', e, and q of the remaining three soiltypes were read off tables in Papageorgiou (2004).

Merriespruit tailings (0)		
e	p' (kPa)	q (kPa
1.137	2	2
1.231	10	13
1.239	36	38
1.146	46	67
1.091	64	86
1.106	113	145
1.101	166	198
1.018	192	237
Γ_{50} = 1.13; λ = 0.061; M = 1.24		

Merriespruit tailings (20)		
e	p' (kPa)	q (kPa
1.23	7	2
1.29	11	2
1.25	15	10
1.18	25	26
1.19	29	32
1.10	53	54
1.14	57	62
1.12	80	86
Γ_{50} = 1.14; λ = 0.157; M = 1.17		

Merriespruit tailings (30)		
e	p' (kPa)	q (kPa
0.95	2	4
1.13	4	4
0.98	13	6
0.97	14	12
0.85	19	26
0.99	24	24
0.90	25	36
0.94	61	72
0.82	62	66
0.90	93	92
0.96	106	124
0.90	130	148
Γ_{50} = 0.92; λ = 0.073; M = 1.12		

Merriespruit tailings (50)		
e	p' (kPa)	q (kPa
0.814	11	10
0.749	12	18
0.780	22	24
0.819	41	48
0.742	47	52
0.708	64	76
0.803	72	90
0.755	76	96
0.703	113	138
0.814	113	132
0.773	125	146
Γ_{50} = 0.77; λ = 0.024; M = 1.19		

C.10 Soiltype MIZ

Values of p', e, and q were taken from figures in Chapter 3 of Vermeulen (2001).

Mizpah dam tailings (72)		
e	p' (kPa)	q (kPa
0.821	22	38
0.728	110	160
0.680	238	350
Γ_{50} = 0.77; λ = 0.136; M = 1.47		

C.11 Soiltype OTM

All data was collected from Murthy et al. (2007). Tests for which q is reported are undrained and their e, p', and q values were read off Table 1. Tests for which q is not reported are drained and their e and p' values were extracted from Figure 6. Values of M were read off Figure 7.

Ottawa sand-silt mix (0)		
e	p' (kPa)	q (kPa
0.714	24	39
0.725	32	39
0.724	37	46
0.711	38	51
0.707	54	68
0.693	62	82
0.707	65	83
0.696	134	174
0.694	158	178
0.701	169	203
0.682	179	227
0.667	584	716
0.645	888	1110
0.652	962	1162
0.643	1037	1223
0.654	1381	1664
0.695	166	--
0.674	332	--
0.660	658	--
0.663	673	--
Γ_{50} = 0.71; λ = 0.044; M = 1.209		

Ottawa sand-silt mix (5)		
e	p' (kPa)	q (kPa
0.720	20	25
0.671	148	205
0.650	272	352
0.650	309	383
0.659	310	385
0.627	910	1103
0.631	917	1120
0.630	1131	1389
0.686	170	--
0.674	168	--
0.664	166	--
0.668	340	--
0.660	329	--
0.640	673	--
0.627	673	--
Γ_{50} = 0.70; λ = 0.055; M = 1.226		

Ottawa sand-silt mix (10)		
e	p' (kPa)	q (kPa
0.622	35	58
0.600	108	134
0.571	276	366
0.581	559	708
0.621	170	--
0.601	336	--
0.569	703	--
Γ_{50} = 0.62; λ = 0.038; M = 1.279		

Ottawa sand-silt mix (15)		
e	p' (kPa)	q (kPa
0.582	30	23
0.556	84	112
0.523	629	886
0.481	1053	1396
0.488	1228	1768
0.525	185	--
0.481	703	--
Γ_{50} = 0.57; λ = 0.061; M = 1.393		

C.12 Soiltype PAY

Values of p', e, and q were taken from figures in Chapter 3 of Vermeulen (2001).

Pay dam tailings (77)		
e	p' (kPa)	q (kPa
0.76	30	32
0.67	105	139
0.63	198	265
0.79	50	77
0.74	100	138
0.65	194	288
Γ_{50} = 0.75; λ = 0.176; M = 1.40		

C.13 Soiltype RIM

All data was collected from Papadopoulou and Tika (2008). Values of p' and e were taken from Figure 17. Values of M were read off Table 2.

Rimnio (37)			
p' (kPa)	e	p' (kPa)	e
53	0.778	1115	0.636
93	0.743	--	--
Γ_{50} = 0.78; λ = 0.105; M = 1.3864			

C.14 Soiltypes SIM

Values of p' and e were taken from Figure 3 of Rahman and Lo (2008). Estimates of M are based on Figures 6 and 10 of Thevanayagam et al. (2002).

Silica sand-silt mix (0)			
p' (kPa)	e	p' (kPa)	e
5	0.801	473	0.718
10	0.796	937	0.668
23	0.774	937	0.645
41	0.774	1099	0.681
48	0.765	1217	0.595
157	0.746	1407	0.606

Γ_{50} = 0.76; λ = 0.042; M = 1.4			
Silica sand-silt mix (7)			
p' (kPa)	e	p' (kPa)	e
5	0.731	434	0.628
14	0.717	547	0.595
216	0.670	1234	0.553
236	0.665	--	--
Γ_{50} = 0.69; λ = 0.047; M = 1.5			

Silica sand-silt mix (15)			
p' (kPa)	e	p' (kPa)	e
1	0.617	124	0.575
17	0.589	306	0.522
42	0.575	306	0.513
94	0.600	1289	0.421
Γ_{50} = 0.58; λ = 0.057; M = 1.6			

Silica sand-silt mix (25)			
p' (kPa)	e	p' (kPa)	e
1	0.477	83	0.430
11	0.461	232	0.404
69	0.430	690	0.357
73	0.416	787	0.357
Γ_{50} = 0.43; λ = 0.058; M = n/a			

Silica sand-silt mix (40)			
p' (kPa)	e	p' (kPa)	e
4	0.410	64	0.390
7	0.401	265	0.363
13	0.390	--	--
Γ_{50} = 0.38; λ = 0.022; M = 1.3			

Silica sand-silt mix (60)			
p' (kPa)	e	p' (kPa)	e
5	0.547	138	0.514
5	0.530	157	0.511
11	0.539	184	0.497
112	0.514	--	--
Γ_{50} = 0.52; λ = 0.022; M = 1.3			

Silica sand-silt mix (100)			
p' (kPa)	e	p' (kPa)	e
10	0.877	157	0.821
13	0.854	315	0.767
Γ_{50} = 0.83; λ = 0.059; M = 1.6			

C.15 Soiltypes STA

All data was collected from Table 1 in Carrera et al. (2011).

Stava tailings (0)		
e	p' (kPa)	q (kPa
0.993	7.8	9.5
0.958	62.8	91.5
0.939	73.8	116.1
0.933	95.3	135.6
0.943	101.2	144.1
0.896	187.1	262.9
0.915	195.0	280.2
0.914	202.9	293.7
0.872	308.0	448.3
0.839	465.0	645
0.820	571.0	813
0.759	900.0	1320
0.751	1045.0	1475
0.716	1078.8	1563.4
Γ_{50} = 1.00; λ = 0.180; M = 1.44		

Stava tailings (30)		
e	p' (kPa)	q (kPa
0.665	44.3	65.6
0.651	65.3	98.4
0.644	153.0	230
0.544	517.0	750
0.459	1350.0	1957.5
Γ_{50} = 0.68; λ = 0.138; M = 1.45		

Stava tailings (50)		
e	p' (kPa)	q (kPa
0.663	12.7	16.8
0.601	23.0	33
0.600	35.0	50
0.535	770.0	1111.7
Γ_{50} = 0.60; λ = 0.061; M = 1.44		

Stava tailings (100)		
e	p' (kPa)	q (kPa
0.775	15.8	18.6
0.725	99.9	138.3
0.695	123.0	167.7
0.657	720.3	959.5
0.614	1220.0	1708
Γ_{50} = 0.74; λ = 0.081; M = 1.38		

C.16 Soiltypes TOM

All p' and e values were taken from Figure 8 of Zlatović and Ishihara (1995). The M values were estimated from Figure 5 of Zlatović and Ishihara (1995).

Toyoura sand-silt mix (0)			
p' (kPa)	e	p' (kPa)	e
No data points given. Only a line from which SSL parameters were inferred. Since this soiltype already appears under CDS 2 as "Toyoura 1 (0)", it was excluded from the soiltypes TOM in Table 6.2 and Table 6.3. However, the SSL parameters reported below were included in Figure 6.41k			
Γ_{50} = 0.92; λ = 0.041; M = n/a			

Toyoura sand-silt mix (5)			
p' (kPa)	e	p' (kPa)	e
31.9	0.886	660.8	0.825
125.1	0.867	--	--
Γ_{50} = 0.88; λ = 0.047; M = 1.3			

Toyoura sand-silt mix (10)			
p' (kPa)	e	p' (kPa)	e
10.9	0.84	262.3	0.78
19.9	0.83	277.0	0.79
27.0	0.81	302.6	0.77
96.0	0.80	376.0	0.77
100.7	0.81	451.7	0.76
163.1	0.80	588.7	0.76
212.5	0.79		
Γ_{50} = 0.81; λ = 0.042; M = 1.3			

Toyoura sand-silt mix (15)			
p' (kPa)	e	p' (kPa)	e
49.0	0.74	227.5	0.70
56.9	0.74	304.6	0.69
90.3	0.72	--	--
Γ_{50} = 0.74; λ = 0.059; M = 1.3			

Toyoura sand-silt mix (30)			
p' (kPa)	e	p' (kPa)	e
33.3	0.505	335.0	0.478
41.4	0.504	402.5	0.479
72.2	0.499	451.7	0.471
86.1	0.492	600.8	0.461
236.9	0.488	731.7	0.451
Γ_{50} = 0.50; λ = 0.034; M = 1.3			

Toyoura sand-silt mix (100)			
p' (kPa)	e	p' (kPa)	e
No data points given. Only a line from which SSL parameters were inferred.			
Γ_{50} = 0.69; λ = 0.040; M = n/a			

C.17 Soiltypes CDS 1

All data was collected from Santamarina and Cho (2001). Values of p' and e were taken from Figure 5 and values of M from Table 3.

Blasting sand (0)			
p' (kPa)	e	p' (kPa)	e
16	0.977	216	0.903
26	0.972	227	0.892
47	0.955	273	0.937
70	0.934	280	0.928
71	0.968	377	0.881
139	0.956	413	0.923
154	0.923	524	0.914
201	0.907	524	0.904
Γ_{50} = 0.95; λ = 0.051; M = 1.3			

Ottawa #20/30 sand (0)			
p' (kPa)	e	p' (kPa)	e
10	0.715	180	0.692
20	0.707	215	0.673
65	0.717	247	0.689
124	0.704	361	0.681
169	0.684	482	0.674
178	0.667	627	0.652
Γ_{50} = 0.70; λ = 0.031; M = 1.1			

Sandboil (4)			
p' (kPa)	e	p' (kPa)	e
73	0.688	280	0.656
102	0.655	423	0.652
143	0.676	565	0.645
178	0.644	608	0.609
211	0.668	689	0.604
212	0.637	--	--
Γ_{50} = 0.69; λ = 0.062; M = 1.3			

C.18 Soiltypes CDS 2

The values of p' and e for Lagunillas (70) and Tia Juana Silty (12) was extracted from Figures 61 and 58, respectively, of Ishihara (1993). The M value of Tia Juana Silty (12) was estimated from Figure 59 of Ishihara (1993).

The p' and e values of Toyoura 1 (0) were taken from Figure 2.25 of Jefferies and Been (2006). The data was downloaded from www.golder.com/liq. SSL points with p' ≤ 50.0 kPa or p' ≥ 853.5 kPa were not considered herein. M was read off from Table 2 of Cho et al. (2006).

Lagunillas (70)			
p' (kPa)	e	p' (kPa)	e
15	0.920	100	0.849
48	0.873	202	0.823
53	0.870	273	0.810
94	0.848	--	--
Γ_{50} = 0.87; λ = 0.086; M = n/a			

Tia Juana Silty (12)			
p' (kPa)	e	p' (kPa)	e
64	0.890	276	0.849
124	0.873	300	0.842
195	0.858	319	0.833
229	0.843	404	0.834
239	0.841	--	--
Γ_{50} = 0.90; λ = 0.076; M = 1.35			

Toyoura 1 (0)			
p' (kPa)	e	p' (kPa)	e
50.0	0.920	304.1	0.885
68.7	0.921	353.2	0.883
86.3	0.915	353.2	0.890
96.1	0.912	355.1	0.883
108.9	0.910	423.8	0.878
114.8	0.911	431.6	0.879
128.5	0.910	431.6	0.870
147.2	0.911	441.5	0.879
176.6	0.901	475.8	0.874
186.4	0.908	495.4	0.870
190.3	0.909	549.4	0.867
196.2	0.896	598.4	0.868
210.9	0.890	608.2	0.857
235.4	0.900	608.2	0.863
245.3	0.899	675.9	0.861
251.1	0.896	696.5	0.857
290.4	0.887	716.1	0.856
291.4	0.889	853.5	0.855
Γ_{50} = 0.94; λ = 0.065; M = 1.24			

C.19 Soiltypes JB1

Data to perform an independent calculation of SSL parameters was only found for Castro Sand B (0). This data was downloaded from www.golder.com/liq which contains the results of the triaxial tests for this soiltype. Steady state values of p', e and q were estimated from each test as listed below. Tests that did not reach steady state were not considered.

Castro Sand B (0)			
Test	e	p' (kPa)	q (kPa)
LIQB1_2	0.778	1.1	1.8
LIQB3_1	0.769	2.3	2.9
LIQB3_2	0.769	3.2	4.5
LIQB4_1	0.770	8	8
LIQB4_2	0.748	18	25
LIQB4_3	0.740	19	27
LIQB1_3	0.733	27	33
LIQB10_1	0.723	34	63
CID_B31	0.729	50	59
CID_B32	0.726	51	63
LIQB4_4	0.714	65	89
CID_B51	0.738	84	104
LIQB10_2	0.699	120	156
CID_B12	0.733	167	206
CID_B11	0.729	170	216
CID_B13	0.713	171	219
LIQB10_3	0.685	312	401
LIQB10_4	0.678	323	394
CID_B41	0.710	643	753
CID_B42	0.691	656	792
CID_B101	0.679	1611	1892
CID_B14	0.620	187	268
CID_B43	0.607	696	911
CID_B102	0.563	1869	2666
Γ_{50} = 0.73; λ = 0.035; M = 1.21			

C.20 Soiltypes JB2

Data to perform an independent calculation of SSL parameters was only found for Erksak (1). This data was downloaded from www.golder.com/liq which contains the results of the triaxial tests for this soiltype. Steady state values of p', e and q were estimated from each test as listed below. Tests that did not reach steady state were not considered.

Erksak (1)			
Test	e	p' (kPa)	q (kPa)
Liq_G506	0.848	6.2	1.5
Liq_G503	0.812	10.5	2.7
Liq_G505	0.838	11.5	6.6
Liq_G502	0.863	30.3	1.3
Liq_G504	0.802	32.4	29.7
Liq_D02	0.811	59.2	4.2
Liq_D01	0.782	73.2	10.6
Liq_D04	0.76	113.9	55.5
Liq_D03	0.753	209.6	158.2
Liq_D05	0.736	372.7	343.4
CID_G563	0.693	721.9	965.6
CID_G562	0.623	801.5	1204.5
Γ_{50} = 0.80; λ = 0.086; M = 1.19			

Appendix D Correlations of Γ_n vs e_{min} in which each soiltype was included

In the table below, "1" indicates that a soiltype was included in a given Γ_n vs e_{min} correlation and "0" indicates that the soiltype was not included in that correlation. The Γ_n vs e_{min} correlations are presented in Figure 6.36.

Table D.1 Correlations of Γ_n vs e_{min} in which each soiltype was included.

Soiltype	p'_{min} (kPa)	p'_{max} (kPa)	Value of n in kPa:						Soiltype	p'_{min} (kPa)	p'_{max} (kPa)	Value of n in kPa:					
			50	90	150	250	450	800				50	90	150	250	450	800
Ardebil sand-silt mix (0)	104	289	0	0	1	1	0	0	Glass balls 6 (10)	75	579	0	1	1	1	1	0
Ardebil sand-silt mix (10)	89	264	0	1	1	1	0	0	HKS sand & CHB silt mix (0)	14	335	1	1	1	1	0	0
Ardebil sand-silt mix (20)	79	245	0	1	1	1	0	0	HKS sand & CHB silt mix (5)	9.3	306	1	1	1	1	0	0
Ardebil sand-silt mix (30)	67	264	0	1	1	1	0	0	HKS sand & CHB silt mix (10)	51	495	1	1	1	1	1	0
Ardebil sand-silt mix (35)	63	256	0	1	1	1	0	0	HKS sand & CHB silt mix (15)	7.0	314	1	1	1	1	0	0
Ardebil sand-silt mix (50)	69	269	0	1	1	1	0	0	HKS sand & CHB silt mix (20)	1.4	515	1	1	1	1	1	0
Ardebil sand-silt mix (100)	91	239	0	1	1	1	0	0	HKS sand & CHB silt mix (30)	0.1	528	1	1	1	1	1	0
Assyros sand-silt mix (0)	74	1405	0	1	1	1	1	1	HKS sand & CHB silt mix (50)	0.1	262	1	1	1	1	0	0
Assyros sand-silt mix (5)	250	1035	0	0	0	1	1	1	HKS sand & CHB silt mix (70)	1.0	253	1	1	1	1	0	0
Assyros sand-silt mix (10)	43	1797	1	1	1	1	1	1	HKS sand & CHB silt mix (94)	0.7	240	1	1	1	1	0	0
Assyros sand-silt mix (15)	40	874	1	1	1	1	1	1	Hostun sand 1 (0)	26	639	1	1	1	1	1	0
Assyros sand-silt mix (25)	16	1700	1	1	1	1	1	1	Hostun sand 2 (0)	11	630	1	1	1	1	1	0
Assyros sand-silt mix (35)	5.2	1422	1	1	1	1	1	1	Hostun sand 3 (0)	9.6	640	1	1	1	1	1	0
Assyros sand-silt mix (40)	3.3	777	1	1	1	1	1	1	Hostun sand 4 (0)	162	644	0	0	0	1	1	0
Assyros sand-silt mix (60)	9.6	1223	1	1	1	1	1	1	Hostun sand 5 (0)	165	652	0	0	0	1	1	0
Assyros sand-silt mix (100)	158	901	0	0	1	1	1	1	Hostun sand 6 (0)	165	645	0	0	0	1	1	0
DEM discs 1 (0)	71	2821	0	1	1	1	1	1	Hostun sand 7 (0)	159	633	0	0	1	1	1	0
DEM discs 2 (0)	74	2858	0	1	1	1	1	1	Hostun sand 8 (0)	165	627	0	0	0	1	1	0
DEM discs 3 (0)	71	2861	0	1	1	1	1	1	Leighton Buzzard 1 (0)	90	900	0	1	1	1	1	1
DEM discs 4 (0)	81	2929	0	1	1	1	1	1	Leighton Buzzard 1 (0)	6.0	400	1	1	1	1	0	0
Duzce-1 (13)	35	926	1	1	1	1	1	1	Mai Liao sand-silt mix (0)	70	464	0	1	1	1	1	0
Glass balls 1 (0)	138	1364	0	0	1	1	1	1	Mai Liao sand-silt mix (15)	20	265	1	1	1	1	0	0
Glass balls 2 (0)	120	1255	0	0	1	1	1	1	Mai Liao sand-silt mix (30)	16	261	1	1	1	1	0	0
Glass balls 3 (0)	138	840	0	0	1	1	1	1	Mai Liao sand-silt mix (50)	35	297	1	1	1	1	0	0
Glass balls 4 (0)	132	546	0	0	1	1	1	0	Merriespruit tailings (0)	2.2	192	1	1	1	0	0	0
Glass balls 5 (0)	137	573	0	0	1	1	1	0	Merriespruit tailings (20)	7.0	80	1	1	0	0	0	0

Soiltype	p'_{min} (kPa)	p'_{max} (kPa)	Value of n in kPa:						Soiltype	p'_{min} (kPa)	p'_{max} (kPa)	Value of n in kPa:					
			50	90	150	250	450	800				50	90	150	250	450	800
Merriespruit tailings (30)	2.0	130	1	1	1	0	0	0	Banding sand 1 (0)	10	400	1	1	1	1	0	0
Merriespruit tailings (60)	11	125	1	1	1	0	0	0	Banding sand 5 (0)	10	400	1	1	1	1	0	0
Mizpah dam tailings (72)	22	238	1	1	1	1	0	0	Banding sand 6 (0)	10	400	1	1	1	1	0	0
Ottawa sand - silt mix (0)	24	1381	1	1	1	1	1	1	Banding sand 9 (0)	10	400	1	1	1	1	0	0
Ottawa sand - silt mix (5)	20	1131	1	1	1	1	1	1	Brenda sand (0)	0.0	200	1	1	1	0	0	0
Ottawa sand - silt mix (10)	35	703	1	1	1	1	1	1	Chonan silty sand (18)	20	100	1	1	0	0	0	0
Ottawa sand - silt mix (15)	30	1228	1	1	1	1	1	1	Dune sand (6)	40	700	1	1	1	1	1	0
Pay dam tailings (77)	30	198	1	1	1	0	0	0	Fraser River sand (0)	10	800	1	1	1	1	1	1
Rimnio (37)	53	1115	1	1	1	1	1	1	Hostun RF sand (0)	20	400	1	1	1	1	0	0
Silica sand-silt mix (0)	4.9	473	1	1	1	1	1	0	Kogyuk 350 (0)	25	1000	1	1	1	1	1	1
Silica sand-silt mix (7)	4.9	434	1	1	1	1	1	0	Lagunillas (70)	15	273	1	1	1	1	0	0
Silica sand-silt mix (15)	17	306	1	1	1	1	0	0	Likan (0)	10	700	1	1	1	1	1	0
Silica sand-silt mix (25)	11	787	1	1	1	1	1	1	Lornex (0)	20	400	1	1	1	1	0	0
Silica sand-silt mix (40)	4.0	265	1	1	1	1	0	0	Mailiao (5)	20	400	1	1	1	1	0	0
Silica sand-silt mix (60)	5.1	184	1	1	1	0	0	0	Mailiao (10)	20	400	1	1	1	1	0	0
Silica sand-silt mix (100)	9.8	315	1	1	1	1	0	0	Mailiao (15)	20	400	1	1	1	1	0	0
Stava tailings (0)	63	1079	0	1	1	1	1	1	Massey tunnel (3)	100	400	0	0	1	1	0	0
Stava tailings (30)	44	1350	1	1	1	1	1	1	Monterey #0 (0)	1.0	200	1	1	1	0	0	0
Stava tailings (50)	13	770	1	1	1	1	1	1	Monterey #16 (0)	1.0	1000	1	1	1	1	1	1
Stava tailings (100)	16	1220	1	1	1	1	1	1	Nerlerk (2)	60	600	0	1	1	1	1	0
Toyoura sand (5)	32	661	1	1	1	1	1	0	Nevada fine (5)	2.0	26	1	1	0	0	0	0
Toyoura sand (10)	11	589	1	1	1	1	1	0	Ottawa C109 (0)	10	800	1	1	1	1	1	1
Toyoura sand (15)	49	305	1	1	1	1	0	0	S (12)	20	400	1	1	1	1	0	0
Toyoura sand (30)	33	732	1	1	1	1	1	1	S (20)	20	400	1	1	1	1	0	0
Toyoura silt (100)	30	500	1	1	1	1	1	0	Sacramento (0)	1.0	600	1	1	1	1	1	0
ASTM graded sand (0)	20	100	1	1	0	0	0	0	Sydney (0)	20	400	1	1	1	1	0	0
Blasting sand (0)	16	524	1	1	1	1	1	0	Syncrude (12)	7.0	800	1	1	1	1	1	1
Glass beads (0)	20	100	1	1	0	0	0	0	Tia Juana Silty (12)	8.0	656	1	1	1	1	1	0
Granite powder (44)	20	100	1	1	0	0	0	0	Toyoura 1 (0)	70	720	0	1	1	1	1	1
Nevada sand (2.2)	20	100	1	1	0	0	0	0	Unimin 2010 (0)	20	450	1	1	1	1	1	0
Ottawa #20/30 sand (0)	10	627	1	1	1	1	1	0	Castro Sand B (0)	10	700	1	1	1	1	1	0
Ottawa F-110 sand (6)	20	100	1	1	0	0	0	0	Castro Sand C (0)	10	80	1	1	0	0	0	0
Sandboil (4)	73	689	0	1	1	1	1	0	Hokksund (0)	11	750	1	1	1	1	1	1
Ticino sand (0)	20	100	1	1	0	0	0	0	Monterey (0)	9.0	700	1	1	1	1	1	0

Soiltype	p'_{min} (kPa)	p'_{max} (kPa)	Value of n in kPa:						Soiltype	p'_{min} (kPa)	p'_{max} (kPa)	Value of n in kPa:					
			50	90	150	250	450	800				50	90	150	250	450	800
Ottawa (0)	4.0	800	1	1	1	1	1	1	Erksak (3)	8.0	1100	1	1	1	1	1	1
Reid Bedford (0)	6.0	1050	1	1	1	1	1	1	Fraser River (Massey) (<5)	1.0	250	1	1	1	1	0	0
Ticino-4 (0)	11	800	1	1	1	1	1	1	Isserk (2)	7.0	990	1	1	1	1	1	1
Toyoura 2 (0)	30	500	1	1	1	1	1	0	Isserk (5)	6.0	700	1	1	1	1	1	0
Toyoura 3 (0)	8.0	1050	1	1	1	1	1	1	Isserk (10)	17	400	1	1	1	1	0	0
Alaskan Beaufort (5)	7.0	160	1	1	1	0	0	0	Nerlerk (1.9)	7.0	300	1	1	1	1	0	0
Alaskan Beaufort (10)	5.0	150	1	1	1	0	0	0	Nerlerk (12)	9.0	400	1	1	1	1	0	0
Chek Lap Kok (0.5)	2.0	900	1	1	1	1	1	1	Highland Valley Copper (8)	1.0	220	1	1	1	1	0	0
Duncan Dam (6.5)	1.0	220	1	1	1	1	0	0	Hilton Mines (2.5)	50	985	1	1	1	1	1	1
Erksak (0.7)	6.0	500	1	1	1	1	1	0	Syncrude (Mildred Lake) (10)	1.0	370	1	1	1	1	0	0
Erksak (1)	10	720	1	1	1	1	1	1	Syncrude Oil Sand Tailings (3.5)	10	620	1	1	1	1	1	0

10 References

Amante CV. (1993). *Seismic response and post-liquefaction analysis of the 1990 Dashihe Tailings Dam*. MSc Thesis. Department of Civil Engineering. University of British Columbia. Canada.

Anderson D, Byrne P, DeVall R, Naesgaard E, Wijewickreme D, Adebar P, Atukorala U, Finn W, Gohl B, and Henderson P. (2007). *Geotechnical design guidelines for buildings on liquefiable sites in accordance with NBC 2005 for Greater Vancouver Region*. Greater Vancouver Task Force Report. Vancouver, Canada.

Been K, Crooks JHA, Becker DE, and Jefferies MG. (1986). *Cone penetration test in sands: Part I, State parameter interpretation*. Géotechnique 36(2):239-249.

Been K, and Jefferies M. (1992). *Towards systematic CPT interpretation*. Predictive Soil Mechanics - Proceedings Of The Wroth Memorial Symposium, 27-29 July 1992. Oxford, England.

Been K, and Jefferies MG. (1985). *A state parameter for sands*. Géotechnique 35(2):99-112.

Been K, Jefferies MG, Crooks JHA, and Rothenberg L. (1987). *The cone penetration test in sands: Part II, general inference of state*. Géotechnique 37(3):285-299.

Been K, Jefferies MG, and Hachey J. (1991). *The critical state of sands*. Géotechnique 41(3):365-381.

Been K, Romero S, Obermeyer J, and Hebeler G. (2012). *Determining in situ state of sand and silt tailings from the CPT*. Tailings and Mine Waste 2012. Keystone, Colorado, USA.

Biarez J, and Hicher PY. (1994). *Elementary mechanics of soil behaviour: saturated remoulded soils*. CRC Press Taylor & Francis Group.

Bishop AW, and Henkel DJ. (1957). *The measurement of soil properties in the triaxial test*. Edward Arnold Publishers Limited. London, England.

Blight G. (2010). *Geotechnical engineering for mine waste storage facilities*. CRC Press Taylor & Francis Group.

Boone MD, and Freitas MJ. (2010). *A site-specific fines content correlation using cone penetration test data*. CPT'10 Second International Symposium on Cone Penetration Testing. Huntington Beach, California, USA.

Bouckovalas GD, Andrianopoulos KI, and Papadimitriou AG. (2003). *A critical state interpretation for the cyclic liquefaction resistance of silty sands*. Soil Dynamics and Earthquake Engineering 23(2):115-125.

Boulanger R, and Idriss I. (2007). *Evaluation of cyclic softening in silts and clays*. Journal of Geotechnical and Geoenvironmental Engineering 133(6):641-652.

Campanella R, and Robertson PK. (1988). *Current status of the piezocone test*. Proceedings of the First International Symposium on Penetration Testing: ISOPT-1. pp. 93-116. Balkema, Rotterdam.

Carrera A, Coop M, and Lancellota R. (2011). *Influence of grading on the mechanical behaviour of Stava tailings*. Géotechnique. 61(11):935-946.

Casagrande A. (1936). *Characteristics of cohesionless soils affecting the stability of slopes and earth fills*. Harvard University.

Casagrande A. (1975). *Liquefaction and Cyclic Deformation of Sands: A Critical Review*. Proceedings of the Fifth Panamerican Conference on Soil Mechanics and Foundation Engineering. November 1975. Buenos Aires, Argentina. Pierce Hall.

Castro G. (1969). *Liquefaction of sands*. PhD Thesis. Division of Engineering and Applied Mechanics. Harvard University. USA.

Cetin KO, and Ozan C. (2009). *CPT-based probabilistic soil characterization and classification*. Journal of Geotechnical and Geoenvironmental Engineering 135(1):84-107.

Cetin KO, and Seed RB. (2004). *Nonlinear shear mass participation factor (r_d) for cyclic shear stress ratio evaluation*. Soil Dynamics and Earthquake Engineering 24(2):103-113.

Cho G, Dodds J, and Santamarina J. (2006). *Particle shape effects on packing density, stiffness, and strength: natural and crushed sands*. Journal of Geotechnical and Geoenvironmental Engineering 132(5):591-602.

Clayton C, Abbireddy C, and Schiebel R. (2009). *A method of estimating the form of coarse particulates*. Géotechnique 59(6):493-501.

Cubrinovski M, and Ishihara K. (2000). *Flow potential of sandy soils with different grain compositions*. Soils and Foundations 40(4):103-119.

Cubrinovski M, and Ishihara K. (2002). *Maximum and minimum void ratio characteristics of sands*. Soils and Foundations 42(6):65-78.

Cunning JC, Robertson PK, and Sego DC. (1995). *Shear wave velocity to evaluate in situ state of cohesionless soils*. Canadian Geotechnical Journal 32(5):848-858.

Davies MP, Martin TE, and PC Lighthall. (2001). *Tailings dam stability: essential ingredients for success*. Chapter 40, Slope stability in surface mining. Society for Mining, Metallurgy, and Exploration.

Davies MP. (1999). *Piezocone technology for the geoenvironmental characterization of mine tailings.* PhD Thesis. Department of Civil Engineering. University of British Columbia. Canada.

Davies MP. (2002). *Tailings impoundment failures: are geotechnical engineers listening?*. Geotechnical News 21(3):31-36.

Desrues J, Chambon R, Mokni M, and Mazerolle F. (1996). *Void ratio evolution inside shear bands in triaxial sand specimens studied by computed tomography*. Géotechnique 46(3):529-546.

Dodds JS. (2003). *Particle Shape and Stiffness: Effects on soil behaviour.* MSc Thesis. Georgia Institute of Technology. USA.

Fear CE, and Robertson PK. (1995). *Estimating the undrained strength of sand: A theoretical framework*. Canadian Geotechnical Journal 32(5):859-870.

Finn WDL, Yogendrakumar M, Yoshida N, and Yoshida H. (1986). *TARA-3: A program to compute the response of 2-D embankments and soil-structure interaction systems to seismic loadings.* Department of Civil Engineering. University of British Columbia. Canada.

Fourie AB, Blight GE, and Papageorgiou G. (2001). *Static liquefaction as a possible explanation for the Merriespruit tailings dam failure*. Canadian Geotechnical Journal 38(4):707-719.

Fourie AB, and Papageorgiou G. (2001). *Defining an appropriate steady state line for Merriespruit gold tailings*. Canadian Geotechnical Journal 38(4):695-706.

Gao JS, Robertson PK, and Morgenstern NR. (1991). *Site data analysis on Dashihe tailings dam.* Report 3-2-1 for the Sino-Canadian joint investigation on earthquake safety of Chinese tailings dams.

Geo-Slope. (2010). *Stability modelling with Slope/W 2007 version*. Geo-Slope International Ltd.

Germaine JT, and Germaine AV. (2009). *Geotechnical laboratory measurements for engineers*. John Wiley & Sons.

Graham J, and Jefferies M. (1986). *Some examples of in situ lateral stress determinations in hydraulic fills using the self-boring pressuremeter*. Proceedings of the 39th Canadian Geotechnical Conference. Ottawa, Canada.

Henian L, Yuqing W, Zhiping W, Zhejun L, Wansheng L, Jiansheng G, Hongbo X, Zhilin L, and Ying W. (1990). *Report 3-2 for the Sino-Canadian joint investigation on earthquake safety of Chinese tailings dams*.

Hird CC, and Hassona FAK. (1990). *Some factors affecting the liquefaction and flow of saturated sands in laboratory tests*. Engineering Geology 28(1–2):149-170.

Huang Y-T, Huang A-B, Kuo Y-C, and Tsai M-D. (2004). *A laboratory study on the undrained strength of a silty sand from Central Western Taiwan*. Soil Dynamics and Earthquake Engineering 24(9):733-743.

Ishihara K. (1993). *Liquefaction and flow failure during earthquakes.* Géotechnique 43(3):351-415.

Ishihara K, and Nagao A. (1983). *Analysis of landslides during the 1978 Izu-Ohshima-Kinkai Earthquake*. Soils and Foundations 23(1):19-37.

Ishihara K, Yasuda S, and Yoshida Y. (1990). *Liquefaction-induced flow failure of embankments and residual strength of silty sands*. Soils and Foundations 30(3):69-80.

ISSMFE. (1989). *Appendix A: International reference test procedure for cone penetration test (CPT).* Report of the ISSMFE Technical Comittee on Penetration Testing of Soils. Swedish Geotechnical Institute.

Jefferies M, Jonsson L, and Been K. (1987). *Experience with measurement of horizontal geostatic stress in sand during cone penetration test profiling*. Géotechnique 37(4):483-498.

Jefferies MG, and Been K. (2006). *Soil liquefaction: A critical state approach*. Taylor & Francis.

Jefferies MG, and Davies MP. (1991). *Soil classification by the cone penetration test: Discussion*. Canadian Geotechnical Journal 28(1):173-176.

Jefferies MG, and Davies MP. (1993). *Use of CPTu to Estimate Equivalent SPT N_{60}*. Geotechnical Testing Journal 16:458-458.

Kanamori H. (1977). *The energy release in great earthquakes*. Journal of Geophysical Research 82(20):2981-2987.

Kanamori H. (2004). *The diversity of the physics of earthquakes*. Proceedings of the Japan Academy: Series B 80(7):297-316.

Kikumoto M, Wood DM, and Russell A. (2010). *Particle crushing and deformation behaviour.* Soils and Foundations 50(4):547-563.

Kim Y, and Lee S. (2000). *Prediction of long-term pore pressure dissipation behavior by short-term piezocone dissipation test*. Computers and Geotechnics 27(4):273-287.

Kolbuszewski J. (1948). *An experimental study of the maximum and minimum porosities of sands*. Proceedings of the 2nd international conference on soil mechanics and foundation engineering. Rotterdam.

Konrad JM. (1997). *In situ sand state from CPT: evaluation of a unified approach at two CANLEX sites.* Canadian Geotechnical Journal 34(1):120-130.

Krumbein WC, and Sloss LL. (1963). *Stratigraphy and sedimentation*. Freeman and Company.

Lade PV, Liggio C, and Yamamuro JA. (1998). *Effects of non-plastic fines on minimum and maximum void ratios of sand*. Geotechnical Testing Journal 21:336-347.

Lambe TW, and Whitman RV. (1979). *Soil Mechanics - SI Version*. John Wiley and Sons.

Lee PY, and Suedkamp RJ. (1972). *Characteristics of irregularly shaped compaction curves of soils.* Compaction and Stabilization. Highway Research Record.

Lee WS, Robertson PK, and Morgenstern NR. (1992). *Laboratory test data analysis on Dashihe tailings sands*. In Report 3-5 for the Sino-Canadian joint investigation on earthquake safety of Chinese tailings dams.

Li G. (2013). *Étude de l'influence de l'étalement granulometrique sur le comportement mecanique des materiaux granulaires*. PhD Thesis. Ecole Centrale de Nantes. France.

Li G, Ovalle C, Dano C, and Hicher P-Y. (2013). *Influence of Grain Size Distribution on Critical State of Granular Materials*. In Constitutive Modeling of Geomaterials. Springer Berlin Heidelberg.

Li SL. (2011). *Effects of particle gradation on static liquefaction behavior of sands.* Master Thesis. Harbin Institute of Technology. China.

Li X-S, and Wang Y. (1998). *Linear representation of steady-state line for sand*. Journal of geotechnical and geoenvironmental engineering 124(12):1215-1217.

Long H. (2007). *Interpreting pore pressure in marine mudstones with pore pressure penetrometers, in situ data, and laboratory measurements*. College of Earth and Mineral Sciences. Pennsylvania State University. USA.

Lunne T, Robertson P, and Powell J. (1997). *Cone Penetration Testing in Geotechnical Practice*. Blackie Academic & Professional.

Maeda K, Fukuma M, and Nukudani E. (2009). *Macro and micro critical states of granular materials with different grain shapes*. AIP Conference Proceedings. July 2009. Golden, Colorado, USA.

Marsland A, and Quarterman R. (1982). *Factors affecting the measurements and interpretation of quasi static penetration tests in clays*. Proceedings of the 2nd European Symposium on Penetration Testing ESOPT II. AA Balkema. Amsterdam, The Netherlands.

Morgenstern NR, Vick SG, and Van Zyl D. (2015). *Report on Mount Polley Tailings Storage Facility Breach*. Government of British Columbia, Canada.

Muir-Wood D, and Maeda K. (2008). *Changing grading of soil: effect on critical states*. Acta Geotechnica 3(1):3-14.

Murthy TG, Loukidis D, Carraro JAH, Prezzi M, and Salgado R. (2007). *Undrained monotonic response of clean and silty sands*. Géotechnique. 57(3):273-288.

Naeini SA, and Baziar MH. (2004). *Effect of fines content on steady-state strength of mixed and layered samples of a sand.* Soil Dynamics and Earthquake Engineering 24(3):181-187.

Okusa S, and Anma S. (1980). *Slope failures and tailings dam damage in the 1978 Izu-Ohshima-Kinkai earthquake*. Engineering Geology 16(3–4):195-224.

Olson SM. (2001). *Liquefaction analysis of level and sloping ground using field case histories and penetration resistance*. PhD Thesis. University of Illinois at Urbana-Champaign. USA.

Olson SM. (2009). *Strength ratio approach for liquefaction analysis of tailings dams.* Proceedings of the 57th Annual Geotechnical Engineering Conference. Minneapolis, Minnesota, USA.

Olson SM, and Stark TD. (2002). *Liquefied strength ratio from liquefaction flow failure case histories.* Canadian Geotechnical Journal 39(3):629-647.

Olson SM, and Stark TD. (2003). *Yield strength ratio and liquefaction analysis of slopes and embankments.* Journal of Geotechnical and Geoenvironmental Engineering 129(8):727-737.

Papadopoulou A, and Tika T. (2008). The effect of fines on critical state and liquefaction resistance characteristics of non-plastic silty sands. Soils and Foundations 48(5):713-725.

Papageorgiou G. (2004). *Liquefaction assessment and flume modelling of the Merriespruit gold and Bafokeng platinum tailings*. PhD Thesis. Department of Civil and Environmental Engineering. University of the Witwatersrand. South Africa.

Plewes H, Davies M, and Jefferies M. (1992). *CPT based screening procedure for evaluating liquefaction susceptibility.* Proceedings of the 45th Canadian Geotechnical Conference. Toronto, Canada.

Poulos SJ, Castro G, and France JW. (1985). *Liquefaction evaluation procedure*. Journal of Geotechnical Engineering 111(6):772-792.

Psarropoulos PN, and Tsompanakis Y. (2008). *Stability of tailings dams under static and seismic loading*. Canadian Geotechnical Journal 45(5):663-675.

Rahman MM, and Lo S. (2012). *Predicting the Onset of Static Liquefaction of Loose Sand with Fines*. Journal of Geotechnical and Geoenvironmental Engineering 138(8):1037-1041.

Rahman MM, and Lo SR. (2008). *The prediction of equivalent granular steady state line of loose sand with fines*. Geomechanics and Geoengineering 3(3):179-190.

Rees SD. (2010). *Effects of fines on the undrained behaviour of Christchurch sandy soils*. PhD Thesis. Department of Civil and Natural Resources Engineering. University of Canterbury. New Zealand.

Reid D. (2012). *Update on the Plewes method for liquefaction screening*. Tailings and Mine Waste 2012. Keystone, Colorado, USA.

Reid D. (2014). *Estimating slope of critical state line from cone penetration test—an update*. Canadian Geotechnical Journal 52(1):46-57.

Robertson P, Sasitharan S, Cunning J, and Sego D. (1995). *Shear-Wave Velocity to Evaluate In-Situ State of Ottawa Sand*. Journal of Geotechnical Engineering 121(3):262-273.

Robertson PK, and Wride C. (1998). *Evaluating cyclic liquefaction potential using the cone penetration test*. Canadian Geotechnical Journal 35(3):442-459.

Robertson PK. (1990). *Soil classification using the cone penetration test*. Canadian Geotechnical Journal 27(1):151-158.

Robertson PK. (1991). *Soil classification using the cone penetration test: Reply*. Canadian Geotechnical Journal 28(1):176-178.

Robertson PK. (2009a). *Interpretation of cone penetration tests — a unified approach*. Canadian Geotechnical Journal 46(11):1337-1355.

Robertson PK. (2009b). *Performance based earthquake design using the CPT*. International conference on performance-based design in earthquake geotechnical engineering. Tokyo, Japan.

Robertson PK. (2010). *Evaluation of Flow Liquefaction and Liquefied Strength Using the Cone Penetration Test*. Journal of Geotechnical & Geoenvironmental Engineering 136(6):842-853.

Rowe PW. (1962). *The Stress-Dilatancy Relation for Static Equilibrium of an Assembly of Particles in Contact.* Proceedings of the Royal Society of London A: Mathematical, Physical and Engineering Sciences 269(1339):500-527.

Rust E, and Clayton C. (1999). *Interpretation of incomplete dissipation data from piezocone tests.* Proceedings of the ICE-Geotechnical Engineering 137(2):97-103.

Sadrekarimi A, and Olson S. (2011). *Critical state friction angle of sands*. Géotechnique 61(9):771-783.

Santamarina JC, and Cho GC. (2001). *Determination of critical state parameters in sandy soils-simple procedure*. Geotechnical testing journal 24(2):185-192.

Schofield AN, and Wroth P. (1968). *Critical state soil mechanics*. McGraw-Hill.

Seed HB. (1981). *Earthquake-resistant design of earth dams*. First International Conference on Recent Advances in Geotechnical Earthquake Engineering & Soil Dynamics. Paper 23.

Seed HB, and Idriss IM. (1971). *Simplified procedure for evaluating soil liquefaction potential*. Journal of the Soil Mechanics and Foundations Division. Proceedings of the ASCE. 97(9):1249-1273.

Seed HB, and Idriss IM. (1982). *Ground motions and soil liquefaction during earthquakes*. Earthquake Engineering Research Institute Monograph.

Shuttle D, and Jefferies M. (1998). *Dimensionless and unbiased CPT interpretation in sand*. International Journal for Numerical and Analytical Methods in Geomechanics 22(5):351-391.

Shuttle DA, and Cunning J. (2007). *Liquefaction potential of silts from CPTu*. Canadian Geotechnical Journal 44(1):1-19.

Sladen JA. (1989). *Problems with interpretation of sand state from cone penetration test.* Géotechnique 39(2):323-332.

Sladen JA, D'Hollander RD, and Krahn J. (1985). *The liquefaction of sands, a collapse surface approach*. Canadian Geotechnical Journal 22(4):564-578.

Strydom JH, and Williams AAB. (1999). *A review of important and interesting technical findings regarding the tailings dam failure at Merriespruit*. Journal of the South African Institute of Civil Engineering 41(4):1-9.

Sully JP, Robertson PK, Campanella RG, and Woeller DJ. (1999). *An approach to evaluation of field CPTu dissipation data in overconsolidated fine-grained soils*. Canadian geotechnical journal 36(2):369-381.

Tavenas F, and Rochelle PL. (1972). *Accuracy of relative density measurements*. Géotechnique 22(4):549-562.

Taylor JR. (1997). *An introduction to error analysis: The study of uncertainties in physical measurements*. University Science Books.

Teh C, and Houlsby G. (1991). *An analytical study of the cone penetration test in clay*. Géotechnique 41(1):17-34.

Thevanayagam S, Shenthan T, Mohan S, and Liang J. (2002). *Undrained Fragility of Clean Sands, Silty Sands, and Sandy Silts*. Journal of Geotechnical and Geoenvironmental Engineering 128(10):849-859.

Thomas D. (1965). *Static Penetration Tests in London Clay*. Géotechnique 15(2):174-179.

Torres-Cruz LA. (2015). *CPT-Based Soil Type Classification in a Platinum Tailings Storage Facility.* XV Panamerican Conference on Soil Mechanics and Geotechnical Engineering. Buenos Aires, Argentina.

Tshabalala L. (2003). *The Effect of Consolidation and Loading Stress Paths on the Static Liquefaction of Mine Tailings*. MSc Thesis. Department of Civil and Environmental Engineering. University of the Witwatersrand. South Africa.

Unno T, Kazama M, Uzuoka R, and Sento N. (2008). *Liquefaction of unsaturated sand considering the pore air pressure and volume compressibility of the soil particle skeleton.* Soils and Foundations 48(1):87-99.

Verdugo R, and Ishihara K. (1996). *The steady state of sandy soils*. Soils and foundations 36(2):81-91.

Vermeulen N, Rust E, and Clayton C. (2002). *Variations in composition on SA gold tailings dams.* Tailings and Mine Waste 2002. Fort Collins, Colorado, USA.

Vermeulen NJ. (2001). *The composition and state of gold tailings*. PhD Thesis. Faculty of Engineering, Built Environment and Information Technology. University of Pretoria. South Africa.

Wagener F, Strydom K, Craig H, and Blight G. (1997). *The tailings dam flow failure at Merriespruit, South Africa: causes and consequences.* Proceedings of the Fourth International Conference on Tailings and Mine Waste, Fort Collins, Colorado, USA.

Wagener FvM, Craig H, Blight G, McPhail G, Williams A, and Strydom J. (1998). *The Merriespruit tailings dam failure*. Tailings and Mine Waste '98.

Williams AAB, and Strydom JH. (1994). *Third report on Merriespruit Slimes Dam: Laboratory Tests, field trials, analyses and conclusions*. Internal Report from Jones & Wagener Engineering & Environmental Consultants.

Wride CE, Hofmann BA, Sego DC, Plewes HD, Konrad JM, Biggar KW, Robertson PK, and Monahan PA. (2000). *Ground sampling program at the CANLEX test sites*. Canadian Geotechnical Journal 37(3):530-542.

www.mountpolleyreviewpanel.ca. *Mount Polley Independent Expert Investigation and Review Report*. Accessed: 10 January 2016.

Yang J, and Luo X. (2015). *Exploring the relationship between critical state and particle shape for granular materials*. Journal of the Mechanics and Physics of Solids 84:196-213.

Yang J, Wei LM, and Dai BB. (2015). *State variables for silty sands: Global void ratio or skeleton void ratio?* Soils and Foundations 55(1):99-111.

Yang SL, Sandven R, and Grande L. (2006). *Steady-state lines of sand–silt mixtures*. Canadian Geotechnical Journal 43(11):1213-1219.

Yi F. (2014). *Estimating soil fines contents from CPT data*. 3rd International Symposium on Cone Penetration Testing. Las Vegas, Nevada, USA.

Yoshimi Y, and Akagi T. (1968). *Tokachioki Earthquake of 1968*. Soils and Foundations 8(3):87-95.

Youd T, Idriss I, Andrus R, Arango I, Castro G, Christian J, Dobry R, Finn W, Harder L, Hynes ME, Ishihara K, Koester JP, Liao SC, Marcuson WF, Martin GR, Mitchell JK, Moriwaki Y, Power MS, Robertson PK, Seed RB, Stokoe KH. (2001). *Liquefaction Resistance of Soils: Summary Report from the 1996 NCEER and 1998 NCEER/NSF Workshops on Evaluation of Liquefaction Resistance of Soils*. Journal of Geotechnical and Geoenvironmental Engineering 127(10):817-833.

Zandarín MT, Oldecop LA, Rodríguez R, and Zabala F. (2009). *The role of capillary water in the stability of tailing dams*. Engineering Geology 105(1–2):108-118.

Zardari MA. (2011). *Stability of tailings dams focus on numerical modelling*. PhD Thesis. Department of Civil, Environmental and Natural Resources Engineering. Lulea University of Technology. Sweden.

Zlatović S, and Ishihara K. (1995). *On the influence of nonplastic fines on residual strength*. Proceedings of the first international conference on earthquake geotechnical engineering. Tokyo, Japan.